Jens Petter Bergerud
Håvard Morvik Torød

Shape optimization of an aluminium girder for a long-span suspension bridge

Aerodynamic stability, buffeting response and suppression of vortex induced vibrations

Master's thesis

NTNU
Norwegian University of
Science and Technology

Jens Petter Bergerud
Håvard Morvik Torød

Shape optimization of an aluminium girder for a long-span suspension bridge

Aerodynamic stability, buffeting response and suppression of vortex induced vibrations

NTNU

Norwegian University of
Science and Technology

Department of Structural Engineering
Faculty of Engineering
NTNU – **Norwegian University of Science and Technology**

MASTER THESIS 2021

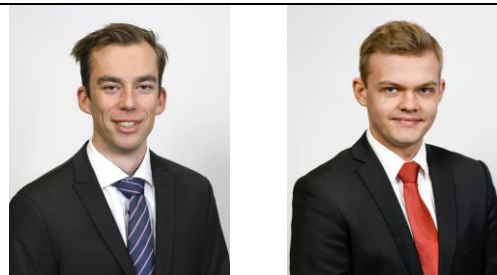| SUBJECT AREA:	DATE:	NO. OF PAGES:
Structural Dynamics	10.06.2021	20 + 96 + 69 = 185

TITLE:

Shape optimization of an aluminium girder for a long-span suspension bridge
Aerodynamic stability, buffeting response and suppression of vortex induced vibrations

BY:

Jens Petter Bergerud and Håvard Morvik Torød

SUMMARY:
This thesis studies optimization of an aluminium girder for the Langenuen Suspension Bridge with respect to aerodynamic properties and buffeting response, and methods for vibration suppression during wind tunnel tests. A parameterization method was chosen for the design of the cross-sections to limit the possible design options. The girders were designed as symmetric closed box girders with a fixed width of the top deck. In order to describe the cross-sections with only one defining parameter, the height H of the girders, parameterizations of the cross-sections were based on a fixed torsion constant I_T.

Eleven different cross-sections have been investigated for the bridge; five with $I_T = 26$ m^4 and six with $I_T = 31$ m^4. The girder heights varied from $H = 4.9 – 6.1$ m and $H = 5.5 – 7.0$ m for the cross-sections with $I_T = 26$ m^4 and $I_T = 31$ m^4, respectively. Cross-sectional properties were calculated with simplified methods based on effective thickness of a thin-walled cross-section. The results were implemented in finite element models of the bridge to extract modal properties. The aerodynamic properties of each cross-section were found by performing wind tunnel tests on section models. Actions were taken to suppress vortex induced vibrations of the section models during wind tunnel testing. Ultimately, calculations of stability limits and buffeting response were executed based on the modal and aerodynamic properties.

The critical wind velocity for all cross-sections varied from 81.06 m/s to 92.98 m/s, which was above the design critical wind velocity of 76 m/s. Multi-modal flutter was the instability mode for all sections.
A machine learning algorithm was implemented to predict the aerodynamic derivatives for girder heights which were not tested in the wind tunnel. The predicted surfaces allow for prediction of stability limits of additional cross-sections without performing wind tunnel tests. The produced results had low prediction uncertainty when interpolating.

By evaluating the aerodynamic properties and buffeting response of the cross-sections, it was found that several of the proposed designs are interesting for further analysis. The recommended girders include $H = 5.2 - 5.8$ m and $H = 5.8 - 6.1$ m for the cross-sections with $I_T = 26$ m^4 and $I_T = 31$ m^4, respectively.

Abstract

A suspension bridge over Langenuen is planned to achieve the goal of a ferry-free coastal highway E39 along the western coast of Norway. The proposed design of the bridge includes a main span length of 1220 m, which will make it the second longest in Norway after the Hardanger Bridge. It has been suggested that building the box girder in aluminium will be cost-effective compared to the traditional steel box girder. Building the bridge in aluminium will also stimulate the Norwegian aluminium industry. If this is realized, the bridge will be the first of its kind. This thesis studies girder optimization of such a bridge with respect to aerodynamic properties and buffeting response, and methods for vibration suppression during wind tunnel tests.

A parameterization method was chosen for the design of the cross-sections to limit the possible design options. The girders were designed as symmetric closed box girders with a fixed width of the top deck. In order to describe the cross-sections with only one defining parameter, the height H of the girders, parameterizations of the cross-sections were based on a fixed torsion constant I_T.

Eleven different cross-sections have been investigated for the bridge; five with $I_T = 26$ m^4 and six with $I_T = 31$ m^4. The girder heights varied from H = 4.9 - 6.1 m and H = 5.5 - 7.0 m for the cross-sections with $I_T = 26$ m^4 and $I_T = 31$ m^4, respectively. Analysing eleven different cross-sections allow for comparison of the girders. Optimization of cross-sectional shape is more easily and effectively done when several cross-sections are assessed. Girders without promising results in the preliminary design phase can be omitted in later studies. Cross-sectional properties were calculated with simplified methods based on effective thickness of thin-walled cross-sections. The results were implemented in finite element models of the bridge to extract modal properties. The aerodynamic properties of each cross-section were found by performing wind tunnel tests on section models. These tests were performed due to the lack of analytical methods that provide results of the aerodynamic properties of sufficient quality. Actions were taken to suppress vortex induced vibrations of the section models during wind tunnel testing. This included instalment of guide vanes and tuned mass dampers. These proved to be effective. Ultimately, calculations of stability limits and buffeting response were executed based on the modal and aerodynamic properties.

The critical wind velocity for all cross-sections varied from 81.06 m/s to 92.98 m/s, which was above the design critical wind velocity of 76 m/s. Multi-modal flutter was the instability mode for all sections, dominated by the first torsional symmetric and the second vertical symmetric modes. The mounting of guide vanes on the section models changed the instability mode for the sections with $H = 6.7$ - 7.0 m and $I_T = 31$ m^4 from galloping to multi-modal flutter. This caused a significant increase in critical wind velocity.

A machine learning algorithm was implemented to predict the aerodynamic derivatives for girder heights which were not tested in the wind tunnel. This was used as an interpolation method, thus, aerodynamic derivatives were only predicted for heights between $H = 4.9$ - 6.1 m and $H = 5.5$ - 7.0 m for the cross-sections with $I_T = 26$ m^4 and $I_T = 31$ m^4, respectively. The produced results had low prediction uncertainty. The predicted surfaces allow for prediction of stability limits of additional cross-sections without performing wind tunnel tests.

The buffeting response calculations revealed that an increase of girder height was not strictly concordant with a decrease in buffeting response. Several factors were believed to affect the results, such as static coefficients, aerodynamic derivatives and stiffness properties. For lateral and torsional displacement response, the standard deviation was largest at the mid-span of the bridge. It was largest at the quarter- and three-quarter-spans for the vertical response.

By evaluating the aerodynamic properties and buffeting response of the cross-sections, it was found that several of the proposed designs are interesting for further analysis. The recommended girders include $H = 5.2$ - 5.8 m and $H = 5.8$ - 6.1 m for the cross-sections with $I_T = 26$ m^4 and $I_T = 31$ m^4, respectively.

The obtained results showed that further optimization of the cross-sectional shape with respect to aerodynamic properties and stability limits is possible. This includes reduction of I_T to get lower streamlined girders or changing the parameterization method such that material usage is reduced.

Sammendrag

Det er planlagt å bygge en hengebro over Langenuen som en del av målsetningen om å bygge ferjefri E39 langs kysten av Vest-Norge. Det planlagte konseptet av broen inkluderer et hovedspenn på 1220 m, som vil gjøre den til den nest lengste i Norge etter Hardangerbrua. Som et kostnadsreduserende tiltak har det blitt foreslått å bygge brokassen i aluminium i stedet for stål, som er det tradisjonelle valget. Bygging av brokassen i aluminium vil også stimulere den norske aluminiumsindustrien. Hvis dette realiseres vil broen bli den første langspennsbroen i verden som er bygget med aluminium. Denne masteroppgaven undersøker optimalisering av tverrsnittet til en slik bro med tanke på aerodynamiske egenskaper og buffetingrespons, altså turbulensindusert respons. Metoder for å redusere virvelinduserte vibrasjoner i vindtunneltester er også undersøkt.

En parameteriseringsmetode ble valgt for utforming av tverrsnitt slik at antall muligheter ble redusert. Brokassene ble utformet som symmetriske, lukkede kassetverrsnitt med konstant bredde på det øvre dekket. For å kunne bestemme utformingen av tverrsnittene med kun en parameter, høyden H til brokassene, ble parameteriseringene basert på konstant torsjonskonstant I_T.

Elleve ulike tverrsnitt har blitt undersøkt for broen; fem med $I_T = 26$ m^4 og seks med $I_T = 31$ m^4. Kassehøydene varierte fra $H = 4.9$ - 6.1 m og $H = 5.5$ - 7.0 m, for henholdsvis $I_T = 26$ m^4 og $I_T = 31$ m^4. Gjennomføring av analyser for elleve ulike tverrsnitt muliggjør sammenligning av de ulike brokassenes egenskaper. Optimalisering av tverrsnittsutforming blir dermed enklere og mer effektivt. Tverrsnitt uten lovende resultater kan bli utelatt for senere analyser. Tverrsnittsegenskaper ble funnet ved å benytte effektiv tykkelse av tynnveggede tverrsnitt. Resultatene ble implementert i elementmodeller av broen for å finne modale egenskaper. De aerodynamiske egenskapene til hvert tverrsnitt ble funnet ved å gjennomføre vindtunneltester på seksjonsmodeller. Testene ble gjennomført på grunn av mangelen på analytiske metoder som gir de aerodynamiske egenskapene med tilstrekkelig kvalitet. Det ble gjort tiltak for å redusere virvelinduserte svingninger av seksjonsmodellene under vindtunneltestene. Dette inkluderte installering av ledeskovler og svingningsdempere. Disse tiltakene viste seg å være effektive. Til slutt ble det gjennomført beregning av stabilitetsgrenser og buffetingrespons basert på de modale og aerodynamiske egenskapene.

Den kritiske vindhastigheten for alle tverrsnittene varierte fra 81.06 m/s til 92.98 m/s, som var over designkravet på 76 m/s. Flermodal flutter, kobling av vertikale og torsjonelle svingemoder, viste seg å være instabilitetsbevegelsen for alle tverrsnittene. Bevegelsen ble dominert av den første symmetriske torsjonsmoden og den andre symmetriske vertikalmoden. Installasjonen av ledeskovler på seksjonsmodellene endret instabilitetsbevegelsen for tverrsnittene med $H = 6.7 - 7.0$ m og $I_T = 31$ m^4 fra galloping, vertikal instabilitet, til flermodal flutter. Dette ga en markant økning i kritisk vindhastighet.

En maskinlæringsalgoritme ble implementert for å forutsi de aerodynamiske deriverte for kassehøyder som ikke ble testet i vindtunnelen. Dette ble brukt som en interpolasjonsmetode, altså ble de aerodynamiske deriverte bare forutsagt for høyder mellom $H = 4.9 - 6.1$ m og $H = 5.5 - 7.0$ m for tverrsnittene med henholdsvis $I_T = 26$ m^4 og $I_T = 31$ m^4. Resultatene hadde lav usikkerhet. Interpolasjonsflatene åpner for beregning av stabilitetsgrenser for øvrige tverrsnitt uten å måtte gjennomføre vindtunneltester.

Beregningen av buffetingrespons avslørte at en økning i tverrsnittshøyde ikke nødvendigvis førte til en reduksjon i buffetingrespons. Det er grunn til å tro at flere parametere påvirket resultatene, blant annet statiske koeffisienter, aerodynamiske deriverte og stivheten til tverrsnittene. For horisontal og torsjonell deformasjonsrespons var standardavviket størst i midtspennet til broen. Det var størst i vertikal retning rundt fjerdedels- og trefjerdelsspennet til broen.

Ved evaluering av aerodynamiske egenskaper og buffetingrespons ble det funnet at flere av de foreslåtte tverrsnittsutformingene egner seg godt for videre analyse. De anbefalte tverrsnittene er $H = 5.2 - 5.8$ m og $H = 5.8 - 6.1$ m for tverrsnittene med henholdsvis $I_T = 26$ m^4 og $I_T = 31$ m^4.

Resultatene viser at videre optimalisering av tverrsnittene med tanke på aerodynamiske egenskaper og stabilitetsgrenser er mulig. Dette inkluderer reduksjon av torsjonskonstanten I_T for å få lavere strømlinjede kasser eller å endre parameteriseringsmetode slik at materialbruket reduseres.

Preface

This master's thesis is the dissertation for the M. Sc. degree at the Department of Structural Engineering at the Norwegian University of Science and Technology (NTNU). It concludes 20 weeks of work during the spring of 2021.

We want to thank our supervisor Professor Ole Øiseth and our co-supervisors Postdoc Øyvind Wiig Petersen and PhD candidate Oddbjørn Kildal for their guidance and feedback throughout this semester. Their expertise in bridge aerodynamics, finite element modelling and wind tunnel testing have been invaluable. We are also thankful for the assistance of Staff Engineer Gøran Loraas during the manufacturing of the section models.

Jens Petter Bergerud and Håvard Morvik Torød
Trondheim 10.06.2021

Contents

Figures

Tables

Abbreviations

Acronyms

AD	Aerodynamic Derivative
FEA	Finite Element Analysis
FRF	Frequency Response Function
GPR	Gaussian Process Regression
MDOF	Multi Degree of Freedom
NPRA	The Norwegian Public Roads Administration
NTNU	The Norwegian University of Science and Technology
SDOF	Single Degree of Freedom
TMD	Tuned Mass Damper
VIV	Vortex Induced Vibration

Chapter 1

Introduction

As part of the long-term goal of building a ferry-free highway E39 along the western coast of Norway, several long-span suspension bridges are planned. Today, travelling by car from Kristiansand to Trondheim, crossing the many fjords requires ferry connections. Replacing these ferry connections with bridges and tunnels will lead to a heavy reduction in travelling time and improve the connection between cities along the highway.

One of the planned long-span bridges is Langenuen Suspension Bridge. As a cost-saving measure, it has been proposed to build this bridge with a box girder made out of aluminium instead of steel, which is the common choice of material. Aluminium is more expensive than steel, thus, the price of an aluminium girder will be increased compared to a steel girder. For a suspension bridge, the self-weight is the main load. The density of aluminium is lower than the density of steel, hence, the load on other structural elements of the suspension bridge will be reduced if the girder is built in aluminium. This will allow for reduced dimensions of other structural elements, which will reduce the cost. The ambition is that the reduced cost of other structural elements will outweigh the increased cost of an aluminium girder, and lead to a reduction of total cost.

Norway has a prominent aluminium industry, and several aluminium plants are located along the west coast of the country. Building a suspension bridge with an aluminium girder will stimulate this industry. Even if a suspension bridge with an aluminium girder might be more expensive than the steel girder alternative, the choice of an aluminium girder will be advantageous for the local industry. Successfully building a suspension bridge with aluminium might also make aluminium competitive as a material for similar structures in the future.

Although aluminium is a popular choice of material in offshore structures, no long-span suspension bridges have ever been built in aluminium. Feasibility and cost analyses have been performed in the past years to validate if aluminium is a competitive material compared to steel for these structures, and the research is ongoing. One of the areas of concern is the aerodynamic stability of the structures.

The slenderness of long-span suspension bridges means that the dynamic response might be critical for the design. Due to the reduction in self-weight and stiffness of the bridge girder when replacing steel with aluminium, the challenge regarding aerodynamic stability increases. This thesis is a continuation of work previously done. A master's thesis written at NTNU in 2020 investigated aerodynamic properties and stability limits of several cross-sections [1]. A parameterization which constrained the torsion constant I_T to a constant value was developed. This was done in order to produce models with as few varying parameters as possible. By doing this, the influence of the remaining varying parameters could be more easily studied. Four girders with torsion constant $I_T = 31$ m^4 were found to have sufficient capacity regarding critical wind velocity. It was therefore suggested to perform analyses for cross-sections with a lower torsion constant in order to further optimize the design.

Progress has been made in the field of numerical estimation of the aerodynamic behaviour of a bridge girder, but it remains a challenge to obtain results of acceptable quality. Therefore, wind tunnel testing of section models, taut-strip models or full-bridge models is necessary to obtain reliable results. The aerodynamic properties of a bridge girder are dependent on its shape. Thus, to optimize the shape of a girder, several girders must be tested.

This thesis studies the aerodynamic properties and buffeting response of an aluminium suspension bridge with respect to girder optimization. Eleven girders are evaluated, five with torsion constant $I_T = 26$ m^4 and the six with torsion constant $I_T = 31$ m^4 which were produced the year prior to this thesis. The parameterization method developed in 2020 is adopted in this thesis. Wind tunnel tests are conducted prior to the analyses, where actions are taken to suppress vortex induced vibrations. Results from wind tunnel testing and finite element modelling are used to numerically estimate the buffeting response and flutter stability limit of each cross-section. The flutter stability limit of each girder is compared to the design critical wind speed at the building site. Aerodynamic properties of the tested girders are implemented in a machine learning algorithm in order to predict the aerodynamic properties of untested girders.

The theory needed for the calculations is presented in Chapter 2. A brief summary of basic structural dynamics, bridge aerodynamics and a short introduction to Gaussian process regression are among the subjects covered in this chapter. Chapter 3 presents the crossing of Langenuen, different design proposals and the box girder parameterization used in this thesis. The finite element models used for calculating the modal properties of the bridge models are presented in Chapter 4, along with the corresponding results. Production of section models and the tests performed in the wind tunnel are described in Chapter 5. The results from the wind tunnel tests are presented in Chapter 6. This chapter also includes the calculated stability limits and discussions of the obtained results. Conclusions of this thesis are presented in Chapter 7, along with proposals for further work.

Chapter 2

Theory

The theory needed for this thesis is presented in this chapter, where bridge aerodynamics is the area given the most attention.

2.1 Suspension bridges

Over the past centuries, the development of bridges has led to suspension bridges covering spans up to almost 2000 m. Although these bridges are impressive, the basic structural concepts behind them are quite simple. There are, in general, four elements contributing to the main characteristics of the bridge, namely the bridge deck, cable system, pylons and anchoring system. Effective load-carrying through tension in the cable system is one reason why cable supported bridges are popular choices for crossing large spans. The pylons are mostly subjected to axial compression due to the connection to the main cables. Figure 2.1 shows the main components of a suspension bridge.

The bridge deck is the bridge component that is subjected to the largest part of the external loads, which is why the deck must contribute with considerable stiffness in the lateral, vertical and torsional directions. The design
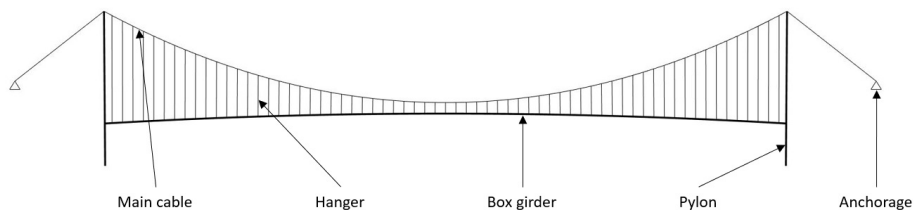
Figure 2.1: A two-dimensional model of a typical suspension bridge, showing its main components.

of the cross-section will therefore be of importance. Axial stiffness is in most traditional suspension bridges no concern since the transfer of load from the deck to the main cables takes place without introducing axial forces in the deck [2]. Most of the long-span suspension bridges built today are made with either truss or closed box girders. The closed box design has superior torsional stiffness, which is vital for instability phenomena like flutter. This is one of the reasons why the closed box girder is considered the most modern design.

Long-span suspension bridges are normally characterized as slender constructions. This means that the dynamic response of the structure might be critical for the design. Tacoma Narrows Bridge is one of the best known bridge collapses [2]. Dynamic response from wind action was its reason for failure [3]. Natural frequencies and aerodynamic properties are therefore important subjects when designing a bridge. The first eigenfrequencies of long-span bridges are low, which makes them exposed to oscillations resulting from wind loading, which is dominated by low frequencies [4]. To correctly determine the response and stability limits of the bridge deck, the modal and aerodynamic properties of the bridge must be calculated. This is done using analytical methods and model testing, where the aerodynamic properties of the cross-sections are determined.

2.2   Basic structural dynamics

Displacements of a suspension bridge can be described using the equation of motion for a multi degree of freedom (MDOF) system,

$$\mathbf{M}\ddot{\mathbf{r}}(t) + \mathbf{C}\dot{\mathbf{r}}(t) + \mathbf{K}\mathbf{r}(t) = \mathbf{q}(t), \tag{2.1}$$

where $\mathbf{M}$, $\mathbf{C}$ and $\mathbf{K}$ are matrices for mass, damping and stiffness, respectively. The displacement vector $\mathbf{r}$ contains the response of the structure, while $\mathbf{q}$ represents the loading applied to the structure. An overdot indicates the time derivative. By finding the non-trivial solutions of the matrix eigenvalue problem,

$$\left[\mathbf{K} - \omega_n^2\mathbf{M}\right]\boldsymbol{\phi}_n = 0, \tag{2.2}$$

the natural frequencies, ω_n, and corresponding mode shapes, $\boldsymbol{\phi}_n$, can be found [5]. The solution of the equation of motion is based on superposition,

$$\mathbf{r}(t) = \sum_{n=1}^{N} \boldsymbol{\phi}_n \eta_n(t) = \boldsymbol{\Phi}\boldsymbol{\eta}(t) \tag{2.3}$$

where the mode shapes $\boldsymbol{\Phi} = \begin{bmatrix} \boldsymbol{\phi}_1 & \boldsymbol{\phi}_2 & ... & \boldsymbol{\phi}_N \end{bmatrix}$ are weighted by time-dependent functions $\eta_n(t)$, also known as modal coordinates [5, 6]. N is the number of degrees of freedom. The time-dependent weighting functions can be found by generalizing the equation of motion using the acquired mode shapes, such that the equation system becomes decoupled. Each equation can

therefore be solved as a single degree of freedom (SDOF) system. Detailed descriptions of this procedure is covered extensively in the literature, for example [5]. This will not be further described in this thesis.

By applying the Fourier transform to the equation of motion, the relation between response $\mathbf{R}(\omega)$ and load $\mathbf{Q}(\omega)$ in the frequency domain can be expressed with the frequency response function (FRF) $\mathbf{H}(\omega)$ [7],

$$\mathbf{R}(\omega) = \mathbf{H}(\omega)\mathbf{Q}(\omega). \tag{2.4}$$

The FRF is given as

$$\mathbf{H}(\omega) = \frac{1}{-\omega^2\mathbf{M} + i\omega\mathbf{C} + \mathbf{K}}, \tag{2.5}$$

where ω is the angular frequency and i is the imaginary unit. The only component preventing the FRF to increase towards infinity at a natural frequency is the damping term. Resonance occurs when a structure is subjected to loading with a frequency equal to one of the structure's natural frequencies. This causes large deformations.

2.2.1 Complex eigenvalue problem

When the generalized damping matrix is diagonal, each equation is solvable as a damped SDOF problem, as explained above. However, in a general case, the generalized damping matrix is not diagonal. Thus, the matrix eigenvalue problem is expanded into the quadratic eigenvalue problem,

$$(\lambda^2\mathbf{M} + \lambda\mathbf{C} + \mathbf{K})\boldsymbol{\psi} = \mathbf{0}, \tag{2.6}$$

also referred to as the complex eigenvalue problem [5, 6]. The eigenvalues exist as real-valued or complex conjugate pairs,

$$\lambda_n, \bar{\lambda}_n = -\zeta_n\omega_n \pm i\omega_{nD}, \tag{2.7}$$

where

$$\omega_{nD} = \omega_n\sqrt{1 - \zeta_n^2} \tag{2.8}$$

is the damped natural frequency and ζ_n is the damping ratio of the nth mode. The natural frequencies and damping ratios are related to the eigenvalues with the following expressions:

$$\omega_n = |\lambda_n| \tag{2.9}$$

and

$$\zeta_n = -\frac{\text{Re}(\lambda_n)}{|\lambda_n|}. \tag{2.10}$$

For each pair of eigenvalues, there is an associated eigenvector. These vectors are also separated into real and imaginary parts,

$$\boldsymbol{\psi}_n, \bar{\boldsymbol{\psi}}_n = \boldsymbol{\phi}_n \pm i\boldsymbol{\chi}_n, \tag{2.11}$$

where $\boldsymbol{\phi}_n$ and $\boldsymbol{\chi}_n$ are real-valued vectors with N elements.
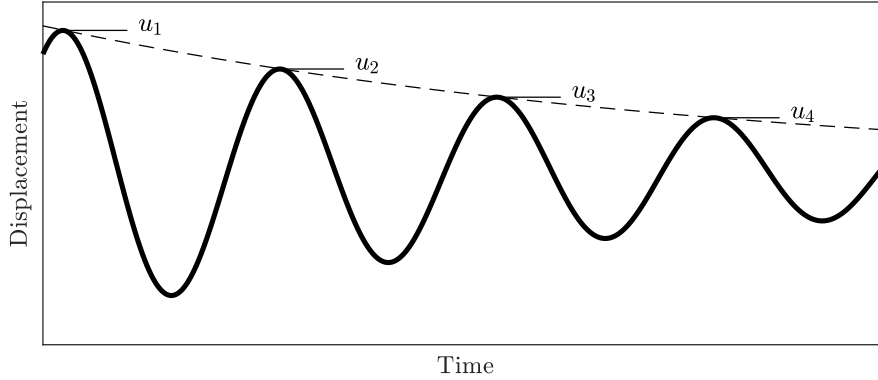
Figure 2.2: Displacement of a damped free vibration system. The dashed line represents the decay in amplitude over time, while the peaks in each cycle are denoted by u_n, where n are all positive integers.

2.2.2   Damping of free vibration

Figure 2.2 shows displacement of a typical damped free vibration system. The peaks in each cycle of motion are denoted by u_n, where n are all positive integers. The dashed line represents the decay in amplitude. Logarithmic decrement δ is defined as

$$\delta = \ln \frac{u_n}{u_{n+1}} = \frac{2\pi\zeta}{\sqrt{1-\zeta^2}}. \tag{2.12}$$

When ζ is small, the relation between ζ and δ can be approximated by

$$\delta \approx 2\pi\zeta. \tag{2.13}$$

Damping ratio ζ is for most structures below 0.2 [5]. The dashed damping curve is given by

$$\rho \cdot e^{-\zeta\omega_n\Delta t}, \tag{2.14}$$

where ρ can be approximated as u_1 and $\Delta t = t$ - t_0, where t_0 is the time corresponding to u_1.

2.2.3   Tuned mass damper

In order to effectively damp out natural frequencies, a tuned mass damper (TMD) can be installed. The TMD, also referred to as vibration absorber [5], is installed to decrease the amplitude of vibrations. The device is designed as an SDOF system consisting of a mass and a spring connected to the structure. The idea is that the damper system is designed with an eigenfrequency close to the frequency where vibration limitation is desired. Thus, when the structure is excited, the vibration of the TMD will absorb energy such that vibrations of the system are reduced. TMDs are effective for a certain frequency range. The size of the frequency range will be dependent on the mass ratio, defined as the

mass of the damper divided by the mass of the structure. As the mass ratio decreases, the operating frequency range becomes narrower [5, 8]. However, there are practical limitations to the mass of the damper. The amount of additional mass which can practically be added to the structure is usually no more than 1-2% [9].

2.3 Buffeting theory

Buffeting forces are the wind forces caused by pressure fluctuations in the oncoming flow [10]. These pressure fluctuations are known as turbulence. The physical mechanism caused by buffeting on suspension bridges is vibration [2]. For a particular time and position in space, the instantaneous wind velocity pressure is a stochastic process. The short-term statistics of this process are assumed to be stationary and homogeneous. The main flow direction of the wind is assumed perpendicular to the main span axis of the structure. Further assumptions regarding the buffeting theory are [11]:

- Loads may be calculated from the instantaneous velocity pressure and appropriate load coefficients obtained from static tests.
- Linearization of any fluctuating parts will render results with sufficient accuracy.
- Structural displacements and rotations are small.

It is also assumed that the instantaneous wind velocity pressure is given by Bernoulli's equation

$$q_U(t) = \frac{1}{2}\rho \left[U(t)\right]^2,\qquad(2.15)$$

where ρ is the air density and U is the instantaneous wind velocity.

The total buffeting load on a structure $\mathbf{q}_{tot}$ is a function of a time independent mean static component $\bar{\mathbf{q}}$, a dynamic component due to turbulence ($\mathbf{B}_q \cdot \mathbf{v}$) and motion induced loads associated with the velocity ($\mathbf{C}_{ae} \cdot \dot{\mathbf{r}}$) and displacement ($\mathbf{K}_{ae} \cdot \mathbf{r}$) of a structure

$$\mathbf{q}_{tot}(x,t) = \begin{bmatrix} \bar{q}_y(x) \\ \bar{q}_z(x) \\ \bar{q}_\theta(x) \end{bmatrix} + \begin{bmatrix} q_y(x,t) \\ q_z(x,t) \\ q_\theta(x,t) \end{bmatrix} = \bar{\mathbf{q}} + \mathbf{B}_q \cdot \mathbf{v} + \mathbf{C}_{ae} \cdot \dot{\mathbf{r}} + \mathbf{K}_{ae} \cdot \mathbf{r}. \qquad(2.16)$$

The vector $\mathbf{r} = \begin{bmatrix} r_y & r_z & r_\theta \end{bmatrix}^T$ contains the structural displacement. The vector $\mathbf{v} = \begin{bmatrix} u & w \end{bmatrix}^T$ contains the turbulence components in the along-wind and the vertical wind direction. Further are

$$\bar{\mathbf{q}}(x) = \begin{bmatrix} \bar{q}_y(x) \\ \bar{q}_z(x) \\ \bar{q}_\theta(x) \end{bmatrix} = \frac{\rho V^2 B}{2} \begin{bmatrix} (D/B)\bar{C}_D \\ \bar{C}_L \\ B\bar{C}_M \end{bmatrix} = \frac{\rho V^2 B}{2} \cdot \hat{\mathbf{b}}_q, \qquad(2.17)$$
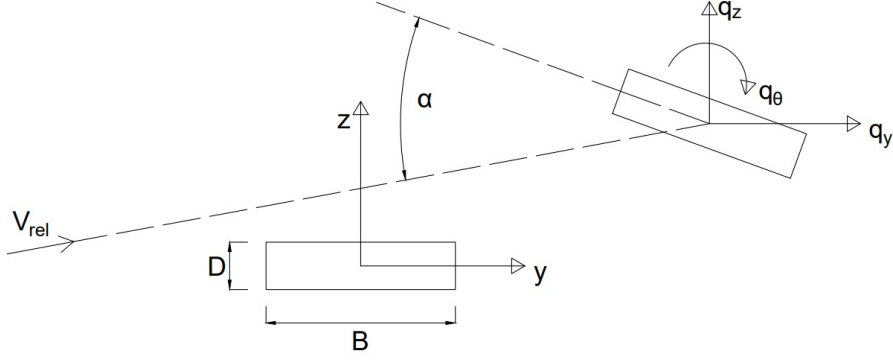
Figure 2.3: Total buffeting load on a structure where V_{rel} is the instantaneous relative wind velocity and α is the angle of flow incidence.

$$\mathbf{B}_q(x) = \frac{\rho V B}{2} \begin{bmatrix} 2(D/B)\bar{C}_D & \left((D/B)C_D' - \bar{C}_L\right) \\ 2\bar{C}_L & \left(C_L' + (D/B)\bar{C}_D\right) \\ 2B\bar{C}_M & BC_M' \end{bmatrix} = \frac{\rho V B}{2}\hat{\mathbf{B}}_q, \qquad (2.18)$$

$$\mathbf{C}_{ae}(x) = -\frac{\rho V B}{2} \begin{bmatrix} 2(D/B)\bar{C}_D & \left((D/B)C_D' - \bar{C}_L\right) & 0 \\ 2\bar{C}_L & \left(C_L' + (D/B)\bar{C}_D\right) & 0 \\ 2B\bar{C}_M & BC_M' & 0 \end{bmatrix} \qquad (2.19)$$

and

$$\mathbf{K}_{ae}(x) = \frac{\rho V^2 B}{2} \begin{bmatrix} 0 & 0 & (D/B)C_D' \\ 0 & 0 & C_L' \\ 0 & 0 & BC_M' \end{bmatrix}. \qquad (2.20)$$

The mean wind velocity is given as V. $\mathbf{B}_q$, $\mathbf{C}_{ae}$ and $\mathbf{K}_{ae}$ are all functions of $C_D(\alpha)$, $C_L(\alpha)$ and $C_M(\alpha)$, which are the static coefficients of drag, lift and moment, respectively. These coefficients are again functions of the angle of flow incidence α corresponding to the instantaneous relative wind velocity V_{rel}, illustrated in Figure 2.3. The prime on the coefficients indicates the derivative with respect to α, and the overbar indicates the mean value of the coefficient. Further explanation of these coefficients are covered in the literature, see for example [11–15]. Also shown in the figure are B and D, which are the width and height of the cross-section, respectively, and $\mathbf{q}_{tot}(x,t)$. The static coefficients introduced in Equations 2.17 to 2.20 can be found by performing quasi-steady wind tunnel tests. By slowly rotating the angle α and measuring

the forces at the bridge section, the coefficients are found for different angles
using

$$
\begin{bmatrix} C_D(\alpha) \\ C_L(\alpha) \\ C_M(\alpha) \end{bmatrix} = \frac{2}{\rho V^2 DL} \begin{bmatrix} F_D \\ (D/B)F_L \\ (D/B^2)M \end{bmatrix}.
\tag{2.21}
$$

F_D and F_L are the drag and lift forces, respectively, measured during the tests,
while M is the torsional moment.

The buffeting theory expands the FRF to be a function of $\mathbf{C}_{ae}$ and $\mathbf{K}_{ae}$

$$
\mathbf{H}(\omega) = \frac{1}{-\omega^2 \mathbf{M} + i\omega\,(\mathbf{C} - \mathbf{C}_{ae}) + (\mathbf{K} - \mathbf{K}_{ae})}.
\tag{2.22}
$$

The introduction of $\mathbf{C}_{ae}$ prevents the generalized damping matrices from being
diagonalizable, such that the eigenvalues and eigenvectors resulting from the
flutter analyses become complex. Flutter is presented later in this chapter.

2.3.1 Buffeting response

Consideration of the flow induced part $\mathbf{q}_b = \mathbf{B}_q \cdot \mathbf{v}$ is sufficent for develop-
ment of a modal buffeting load [11]. The cross-spectral density matrix of the
generalized load is

$$
\mathbf{S}_b(\omega) = \int_0^L \int_0^L \boldsymbol{\Phi}^T(x_1) \mathbf{B}_q(x_1) \mathbf{S_v}(\omega, \Delta x) \mathbf{B}_q^T(x_2) \boldsymbol{\Phi}(x_2) dx_1 dx_2,
\tag{2.23}
$$

where L is the length of the structure and $\mathbf{S_v}$ is the cross-spectral density
matrix of the turbulence components of the wind velocity

$$
\mathbf{S_v} = \begin{bmatrix} S_{uu} & S_{uv} & S_{uw} \\ S_{vu} & S_{vv} & S_{vw} \\ S_{wu} & S_{wv} & S_{ww} \end{bmatrix}.
\tag{2.24}
$$

As wind measuremens are not available for this bridge, the wind spectrum
must be estimated. The Norwegian Public Roads Administration (NPRA)
propose a procedure for this in Handbook N400 [16]. The wind spectrum is a
Kaimal spectrum [17], where the single point autospectral density is

$$
S_n(\omega) = \frac{\sigma_n^2\,{}^x L_n(z)}{2\pi V} \frac{A_n}{(1 + 1.5 A_n \hat{\omega}_n)^{5/3}}, \quad n = u, v, w
\tag{2.25}
$$

where σ_n is the standard deviation of turbulence component n, ${}^x L_n$ is the
integral length scale, the value of the coefficients A_n are given in N400 and $\hat{\omega}_n$
is

$$
\hat{\omega}_n = \frac{\omega\,{}^x L_n(z)}{2\pi V}.
\tag{2.26}
$$

This procedure introduces the turbulence length scale L_n. These are meas-
ures of the average eddy size of the turbulence [14]. Estimation of this para-
meter can be done by several different methods, each producing different res-
ults [18]. Studies performed on the Hardanger Bridge concluded that the use

of a turbulence length scale with a stationary wind model should be avoided, due to the wide range of results [19, 20].

To avoid the use of the turbulence length scale, another Kaimal spectrum is used [21]

$$\frac{S_n\omega}{2\pi\sigma_n^2} = \frac{A_n\omega_z}{(1 + 1.5A_n\omega_z)^{5/3}}, \quad \omega_z = \frac{\omega z}{2\pi V} \tag{2.27}$$

where z is the height above the ground. The cross-spectrum follows Davenport's exponential format [22]

$$C_{nm}(\omega, \Delta x) = \exp\left(-K_{nm}\frac{\omega\Delta x}{2\pi V}\right) \tag{2.28}$$

where K_{nm} are decay coefficients and the normalized cross-spectrum is defined as [15]

$$C_{nm}(\omega, \Delta x) = \frac{S_{nm}(\omega)}{\sqrt{S_n(\omega)S_m(\omega)}}, \tag{2.29}$$

where $n, m = u, v, w$.

The cross-spectral density of the modal response is found by using the generalized FRF

$$\mathbf{S}_\eta(\omega) = \tilde{\mathbf{H}}^*(\omega)\mathbf{S}_{\tilde{\mathbf{Q}}_b}(\omega)\tilde{\mathbf{H}}^T(\omega), \tag{2.30}$$

where the superscript $*$ denotes the complex conjugate and a tilde above a symbol refers to the modal quantity. Subsequently, the cross-spectral density of the response is

$$\mathbf{S}_r(\omega) = \mathbf{\Phi}\mathbf{S}_\eta(\omega)\mathbf{\Phi}^T. \tag{2.31}$$

The covariance matrix, containing the variances for each DOF and the correlation between the DOFs, is given by

$$\mathbf{Cov}_{rr}(x) = \int_0^L \mathbf{S}_r(\omega)d\omega = \begin{bmatrix} \sigma_{r_y}^2 & \rho_{r_y r_z}\sigma_{r_y}\sigma_{r_z} & \rho_{r_y r_\theta}\sigma_{r_y}\sigma_{r_\theta} \\ \rho_{r_z r_y}\sigma_{r_z}\sigma_{r_y} & \sigma_{r_z}^2 & \rho_{r_z r_\theta}\sigma_{r_z}\sigma_{r_\theta} \\ \rho_{r_\theta r_y}\sigma_{r_\theta}\sigma_{r_y} & \rho_{r_\theta r_z}\sigma_{r_\theta}\sigma_{r_z} & \sigma_{r_\theta}^2 \end{bmatrix}, \tag{2.32}$$

where ρ_{ij} are the correlation coefficients

$$\boldsymbol{\rho}_{rr}(x) = \frac{\mathbf{Cov}_{rr}(x)}{\sigma_{r_i} \cdot \sigma_{r_j}}, \tag{2.33}$$

and $\sigma_{r_i r_j}$ are the standard deviation of the DOFs, with $i, j = y, z, \theta$ [7].

2.4   Aerodynamic derivatives

The theory of aerodynamic derivatives (ADs) is an extension of the buffeting theory which includes frequency in the load description. This theory was first developed by Theodorsen in 1935 [23] and later applied to the field of bridge

aerodynamics in 1971 [24]. The frequency domain versions of $\mathbf{C}_{ae}$ and $\mathbf{K}_{ae}$ are given as

$$\mathbf{C}_{ae} = \begin{bmatrix} P_1 & P_5 & P_2 \\ H_5 & H_1 & H_2 \\ A_5 & A_1 & A_2 \end{bmatrix} \quad \text{and} \quad \mathbf{K}_{ae} = \begin{bmatrix} P_4 & P_6 & P_3 \\ H_6 & H_4 & H_3 \\ A_6 & A_4 & A_3 \end{bmatrix}. \quad (2.34)$$

The coefficients can be made non-dimensional by normalising $\mathbf{C}_{ae}$ and $\mathbf{K}_{ae}$ with $\rho B^2 \omega_n / 2$ and $\rho B^2 \omega_n^2 / 2$ respectively, where ω_n is the in-wind resonance frequency associated with mode n from which they have been extracted [11]. This results in

$$\mathbf{C}_{ae} = \frac{\rho B^2}{2} \cdot \omega_n \cdot \hat{\mathbf{C}}_{ae} \quad \text{and} \quad \mathbf{K}_{ae} = \frac{\rho B^2}{2} \cdot \omega_n^2 \cdot \hat{\mathbf{K}}_{ae} \quad (2.35)$$

where

$$\hat{\mathbf{C}}_{ae} = \begin{bmatrix} P_1^* & P_5^* & BP_2^* \\ H_5^* & H_1^* & BH_2^* \\ BA_5^* & BA_1^* & B^2 A_2^* \end{bmatrix} \quad \text{and} \quad \hat{\mathbf{K}}_{ae} = \begin{bmatrix} P_4^* & P_6^* & BP_3^* \\ H_6^* & H_4^* & BH_3^* \\ BA_6^* & BA_4^* & B^2 A_3^* \end{bmatrix}. \quad (2.36)$$

It is the coefficients P_i^*, H_i^* and A_i^*, $i = 1, 2, ..., 6$ which are referred to as aerodynamic derivatives. In bridge engineering, these are used to measure motion-related aerodynamic damping, and detect possible aerodynamic coupling between mechanical modes of the structural system [25]. P_i^*, H_i^* and A_i^* are related to drag, heaving and torsional forces, respectively.

All 18 ADs are seen in relation to the self-excited forces for bridge decks. The unsteady self-excited aerodynamic forces for a section in a single harmonic motion are

$$q_y^{Se} = \frac{1}{2}\rho V^2 B \left(KP_1^* \frac{\dot{r}_y}{V} + KP_2^* \frac{B\dot{r}_\theta}{V} + K^2 P_3^* r_\theta + K^2 P_4^* \frac{r_y}{B} + KP_5^* \frac{\dot{r}_z}{V} + K^2 P_6^* \frac{r_z}{B} \right)$$

$$q_z^{Se} = \frac{1}{2}\rho V^2 B \left(KH_1^* \frac{\dot{r}_z}{V} + KH_2^* \frac{B\dot{r}_\theta}{V} + K^2 H_3^* r_\theta + K^2 H_4^* \frac{r_z}{B} + KH_5^* \frac{\dot{r}_y}{V} + K^2 H_6^* \frac{r_y}{B} \right)$$

$$q_\theta^{Se} = \frac{1}{2}\rho V^2 B^2 \left(KA_1^* \frac{\dot{r}_z}{V} + KA_2^* \frac{B\dot{r}_\theta}{V} + K^2 A_3^* r_\theta + K^2 A_4^* \frac{r_z}{B} + KA_5^* \frac{\dot{r}_y}{V} + K^2 A_6^* \frac{r_y}{B} \right)$$

$$(2.37)$$

where $K = V_{red}^{-1} = B\omega/V$ is the reduced frequency of motion and V_{red} is reduced velocity [26].

The role of the aerodynamic derivatives and their influence on critical velocities is a subject under research. It has been concluded that galloping and torsional flutter only is possible for $H_1^* > 0$ and $A_2^* > 0$, respectively [27]. In cases where these variables are negative, the self-excited forces will cause positive aerodynamic damping. This dissipates energy from the system [28]. An iteration method for flutter analysis, referred to as the step-by-step analysis, has been presented for a better understanding of the influence of ADs on coupled flutter [29]. Some of the results have been summarized, and are presented in Table 2.1, which shows the influence of the ADs H_1^*, H_3^*, A_1^*, A_2^*

Table 2.1: The influence of critical aerodynamic derivatives on coupled flutter stability.

Derivative	Stabilizing	Destabilizing
A_1^*	Low absolute values	High absolute values
A_2^*	Negative values	Positive values
A_3^*	Low absolute values	High absolute values
H_1^*	Negative values	Positive values, low absolute values
H_3^*	Low absolute values	High absolute values

and A_3^*. These ADs have been identified as the critical ADs [30]. It has been concluded that A_2^*, A_1^* and H_3^* are dominating for torsional flutter, while H_1^*, A_1^* and H_3^* are dominating vertical flutter, galloping. A_1^* has been identified as the most critical aerodynamic derivative regarding coupled flutter instability [31].

A drawback with ADs is that they only capture linear contribution [26]. This can be problematic when studying the self-excited drag forces mainly, where the presence of higher-order terms have been observed [32].

2.4.1 Aerodynamic derivatives by Theodorsen

It has been suggested to compare the values of the ADs to those developed by Theodorsen for a flat plate when discussing the limits of low and high absolute values [30]. These ADs are given by

$$\begin{bmatrix} H_1^* & A_1^* \\ H_2^* & A_2^* \\ H_3^* & A_3^* \\ H_4^* & A_4^* \end{bmatrix} = \begin{bmatrix} -2\pi F \hat{V}_i & -\frac{\pi}{2} F \hat{V}_i \\ \frac{\pi}{2}(1 + F + 4G\hat{V}_i)\hat{V}_i & -\frac{\pi}{8}(1 - F - 4G\hat{V}_i)\hat{V}_i \\ 2\pi(F\hat{V}_i - G/4)\hat{V}_i & \frac{\pi}{2}(F\hat{V}_i - G/4)\hat{V}_i \\ \frac{\pi}{2}(1 + 4G\hat{V}_i) & \frac{\pi}{2}G\hat{V}_i \end{bmatrix}, \qquad (2.38)$$

where

$$F\left(\frac{\hat{\omega}_i}{2}\right) = \frac{J_1 \cdot (J_1 + Y_0) + Y_1 \cdot (Y_1 - J_0)}{(J_1 + Y_0)^2 + (Y_1 - J_0)^2} \qquad (2.39)$$

$$G\left(\frac{\hat{\omega}_i}{2}\right) = \frac{J_1 \cdot J_0 + Y_1 \cdot Y_0}{(J_1 + Y_0)^2 + (Y_1 - J_0)^2}. \qquad (2.40)$$

J_n and Y_n, $n = 0$, 1 are Bessel functions of first and second kind, respectively, with order n. The ADs given by Theodorsen are not applicable for the bridge decks designed in this thesis and should only be used as a comparison to the results obtained in wind tunnel testing.

2.4.2 Identification of aerodynamic derivatives

There are several approaches to the identification of ADs for a suspension bridge. As the power of modern computers increase, computational fluid dy-

namics techniques become a more attractive tool in the computation of aero-dynamic behaviour of bridge decks [33]. Although studies have shown computational results in accordance with results from section models [34–37], it remains a challenge to obtain results of acceptable quality. For example, discrepancies in ADs for high reduced velocities have been reported [34]. Therefore, to determine the ADs, wind tunnel testing is necessary to obtain reliable results [26].

ADs can be identified by different methods from the forced vibration test data. The forced vibration test is covered later in this chapter. One way to determine the ADs is to study the phase angle between the self-excited forces and the motion of the section [38, 39]. Another is to study how the complex Fourier amplitudes of the self-excited forces are related to the ADs [40, 41]. However, uncertainties in the estimation of the phase angle [38, 42] or spectral leakage caused by the frequency domain truncation [43] can result in significant estimation error.

To eliminate these uncertainties a time domain method was developed [43]. In this method, the model for the self-excited forces is fitted to the time series of the self excited forces by least squares. Further extension of this method allows for consideration of a more complex motion [44]. Equation 2.37 can be written on the more compact matrix form

$$\mathbf{q}_{Se}(t, K, V) = \mathbf{X}\mathbf{E}, \tag{2.41}$$

where

$$\mathbf{q}_{Se} = \begin{bmatrix} q_{Se,y,1} & q_{Se,z,1} & q_{Se,\theta,1} \\ q_{Se,y,2} & q_{Se,z,2} & q_{Se,\theta,2} \\ \vdots & \vdots & \vdots \\ q_{Se,y,n} & q_{Se,z,n} & q_{Se,\theta,n} \end{bmatrix}, \tag{2.42}$$

$$\mathbf{X} = \begin{bmatrix} \dot{r}_{y,1} & \dot{r}_{z,1} & \dot{r}_{\theta,1} & r_{y,1} & r_{z,1} & r_{\theta,1} \\ \dot{r}_{y,2} & \dot{r}_{z,2} & \dot{r}_{\theta,2} & r_{y,2} & r_{z,2} & r_{\theta,2} \\ \vdots & \vdots & \vdots & \vdots & \vdots & \vdots \\ \dot{r}_{y,n} & \dot{r}_{z,n} & \dot{r}_{\theta,n} & r_{y,n} & r_{z,n} & r_{\theta,n} \end{bmatrix} \tag{2.43}$$

and

$$\mathbf{E} = \frac{1}{2}\rho V^2 B \begin{bmatrix} K_y P_1^*/V & K_y H_5^*/V & BK_y A_5^*/V \\ K_z P_5^*/V & K_z H_1^*/V & BK_z A_1^*/V \\ BK_\theta P_2^*/V & BK_\theta H_2^*/V & B^2 K_\theta A_2^*/V \\ K_y^2 P_4^*/B & K_y^2 H_6^*/B & K_y^2 A_6^* \\ K_z^2 P_6^*/B & K_z^2 H_4^*/B & K_z^2 A_4^* \\ K_\theta^2 P_3^* & K_\theta^2 H_3^* & BK_\theta^2 A_3^* \end{bmatrix} \tag{2.44}$$

for n samples in the time series. By minimizing the sum of squares, $\mathbf{E}$ and thus the ADs, can be found

$$\mathbf{E} = \left(\mathbf{X}^T\mathbf{X}\right)^{-1}\mathbf{X}^T\mathbf{q}_{Se}. \tag{2.45}$$
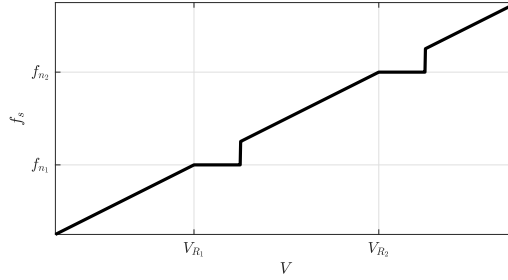
Figure 2.4: Lock-in effect at vortex shedding frequencies.

2.5   Vortex shedding

Vortex shedding is oscillations of the bridge deck in mainly vertical or torsional direction due to separation of the wind flow caused by the bridge deck. The separation of wind causes forces q_z and q_θ on both sides of the deck, which causes oscillations. Vortex shedding frequency f_s is given by

$$f_s = St \cdot \frac{V}{D}, \tag{2.46}$$

where St is the Strouhal number. The Strouhal number measures the ratio of inertial forces caused by a local acceleration of the wind flow to inertial forces caused by acceleration due to change of position in the wind flow [45]. Vortex shedding is characterized as narrow banded, and resonance will occur for every velocity where f_s is equal to one of the eigenfrequencies in vertical or torsional direction of the respective structure [11]. For velocities causing these vibrations, a lock-in effect is normally observed. This means that for a certain increase in velocity, the vibration will not change. In these ranges, Equation 2.46 will not be valid. Vortex shedding will therefore be visible for a range of velocities. This is shown in Figure 2.4.

The Scruton number of a structure is critical for the vortex shedding response [46]. It is defined as

$$Sc = \frac{2\delta \tilde{m}_n}{\rho b_{ref}^2}, \tag{2.47}$$

where b_{ref} is the cross-wind width and $\tilde{m}_n$ is effective mass per unit length

$$\tilde{m}_n = \frac{\tilde{M}_n}{\int_L \phi_n^2(x)dx}, \quad n = z, \theta \tag{2.48}$$

where $\tilde{M}_n$ is the modal mass and the mass moment of inertia from the vertical and torsional still-air mode shapes, respectively. For increasing Scruton numbers, vortex shedding response is reduced.

2.5.1   Guide vanes

Guide vanes installed at suspension bridges have proven to be an efficient way of mitigating vortex shedding excitation [47]. The effect of guide vanes has
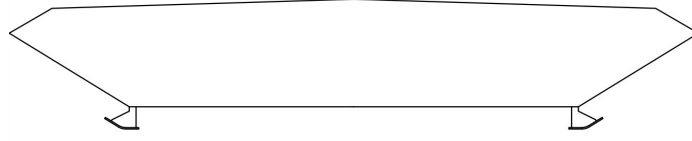
Figure 2.5: Guide vanes mounted on cross-section.

also been observed for section models experiencing galloping. The objective of the guide vanes is to prevent the separation of wind flow from causing transverse forces on the bridge deck [48]. Bridge decks where galloping occurs often experience what is known as full separation of flow, which means that the wind flow is not reattached to the surface of the bridge deck. The guide vanes reduce the amount of vortices under the bridge deck such that the wind flow is reattached to the bridge deck faster. One of the bridges where the effect of guide vanes has been proven is the Storebælt suspension bridge [49]. During the last stages of construction, it was decided to design and manufacture guide vanes to mitigate vortex induced vibrations (VIV) that could be of disturbance for users of the bridge. With the aid of wind tunnel testing, guide vanes were designed and installed at the bridge. After a period of 18 months, no vortex-induced oscillations had been observed [49]. The same was observed at Osterøy Bridge, where no vibrations were reported the year following the installation of guide vanes [50]. Guide vanes have also been installed underneath the deck at several other Norwegian suspension bridges, among others the Hardanger Bridge [19] and the Bømla Bridge [51]. Figure 2.5 shows how the guide vanes are mounted on a girder.

2.6 Motion induced instabilities

Instability phenomena are characterized as situations where a small increase in loading will cause a large increase in structural response. These phenomena will occur for bridges when the wind velocity reaches critical wind velocity V_{cr}, similar to the traditional buckling phenomena, where the axial compression force exceeds the critical load. Instabilities are mathematically defined by the absolute value of the impedance function being equal to zero,

$$\left| \det\left(\hat{\mathbf{E}}_\eta(\omega, V) \right) \right| = 0 \tag{2.49}$$

where the impedance function is the inverse of the FRF

$$\hat{\mathbf{E}}_\eta(\omega, V) = \left\{ \mathbf{I} - \boldsymbol{\kappa}_{ae} - \left(\omega \cdot \mathrm{diag}\left[\frac{1}{\omega_n} \right] \right)^2 + 2i\omega \cdot \mathrm{diag}\left[\frac{1}{\omega_n} \right] \cdot (\boldsymbol{\zeta} - \boldsymbol{\zeta}_{ae}) \right\}, \tag{2.50}$$

where $\mathbf{I}$ is the identity matrix. The unstable effects are caused by changes to $\boldsymbol{\zeta}_{ae}$ and $\boldsymbol{\kappa}_{ae}$, where these are the normalized modal quantities of aerodynamic damping and stiffness, respectively. Each solution to the eigenvalue problem represented in Equation 2.49 will contain a pair of ω and V. The values of interest will always be the ones with the lowest critical wind velocity.

There are four different instability phenomena of interest for a long span suspension bridge:

- Static divergence.
- Galloping.
- Dynamic stability limit in torsion.
- Flutter.

For all instability phenomena, the variable of interest is the vertical or torsional displacement or both. The mathematical expressions for finding the critical wind velocity and corresponding frequencies can be simplified by assuming mode shapes where the dominant structural response is vertical or torsional. Thus, the simplified impedance function is given by

$$
\hat{\mathbf{E}}_\eta(\omega_r, V_{cr}) = \begin{bmatrix} 1 & 0 \\ 0 & 1 \end{bmatrix} - \begin{bmatrix} \kappa_{ae_{11}} & \kappa_{ae_{12}} \\ \kappa_{ae_{21}} & \kappa_{ae_{22}} \end{bmatrix} - \begin{bmatrix} (\omega_r/\omega_1)^2 & 0 \\ 0 & (\omega_r/\omega_2)^2 \end{bmatrix}
$$
$$
+ 2i \begin{bmatrix} \omega_r/\omega_1 & 0 \\ 0 & \omega_r/\omega_2 \end{bmatrix} \cdot \begin{bmatrix} \zeta_1 - \zeta_{ae_{11}} & -\zeta_{ae_{12}} \\ -\zeta_{ae_{21}} & \zeta_2 - \zeta_{ae_{22}} \end{bmatrix}. \tag{2.51}
$$

The matrix entries are given by

$$
\kappa_{ae_{11}} = \kappa_{ae_{zz}} = \frac{\rho B^2}{2\tilde{m}_z} \left(\frac{\omega_z(V)}{\omega_z} \right)^2 H_4^* \frac{\int_{L_{exp}} \phi_z^2 dx}{\int_L \phi_z^2 dx} \tag{2.52a}
$$

$$
\kappa_{ae_{12}} = \kappa_{ae_{z\theta}} = \frac{\rho B^3}{2\tilde{m}_z} \left(\frac{\omega_z(V)}{\omega_z} \right)^2 H_3^* \frac{\int_{L_{exp}} \phi_z \phi_\theta dx}{\int_L \phi_z^2 dx} \tag{2.52b}
$$

$$
\kappa_{ae_{22}} = \kappa_{ae_{\theta\theta}} = \frac{\rho B^4}{2\tilde{m}_\theta} \left(\frac{\omega_\theta(V)}{\omega_\theta} \right)^2 A_3^* \frac{\int_{L_{exp}} \phi_\theta^2 dx}{\int_L \phi_\theta^2 dx} \tag{2.52c}
$$

$$
\kappa_{ae_{21}} = \kappa_{ae_{\theta z}} = \frac{\rho B^3}{2\tilde{m}_\theta} \left(\frac{\omega_\theta(V)}{\omega_\theta} \right)^2 A_4^* \frac{\int_{L_{exp}} \phi_\theta \phi_z dx}{\int_L \phi_\theta^2 dx} \tag{2.52d}
$$

$$
\zeta_{ae_{11}} = \zeta_{ae_{zz}} = \frac{\rho B^2}{4\tilde{m}_z} \frac{\omega_z(V)}{\omega_z} H_1^* \frac{\int_{L_{exp}} \phi_z^2 dx}{\int_L \phi_z^2 dx} \tag{2.52e}
$$

$$
\zeta_{ae_{12}} = \zeta_{ae_{z\theta}} = \frac{\rho B^3}{4\tilde{m}_z} \frac{\omega_z(V)}{\omega_z} H_2^* \frac{\int_{L_{exp}} \phi_z \phi_\theta dx}{\int_L \phi_z^2 dx} \tag{2.52f}
$$

$$
\zeta_{ae_{22}} = \zeta_{ae_{\theta\theta}} = \frac{\rho B^4}{4\tilde{m}_\theta} \frac{\omega_\theta(V)}{\omega_\theta} A_2^* \frac{\int_{L_{exp}} \phi_\theta^2 dx}{\int_L \phi_\theta^2 dx} \tag{2.52g}
$$

$$
\zeta_{ae_{21}} = \zeta_{ae_{\theta z}} = \frac{\rho B^3}{4\tilde{m}_\theta} \frac{\omega_\theta(V)}{\omega_\theta} A_1^* \frac{\int_{L_{exp}} \phi_\theta \phi_z dx}{\int_L \phi_\theta^2 dx}, \tag{2.52h}
$$

where L_{exp} is the wind exposed length.

2.6.1 Static divergence

Since static divergence is a static stability problem, the corresponding frequency ω_r is equal to zero. Instability occurs because of lost torsional stiffness as an effect of motion induced loading. The mode shape can be described with a dominant structural response in torsional direction only,

$$\phi_2 \approx \begin{bmatrix} 0 & 0 & \phi_\theta \end{bmatrix}^T. \tag{2.53}$$

Inserting these simplifications into the impedance function reduces the equation to

$$\hat{\mathbf{E}}_\eta(\omega_r = 0, V_{cr}) = 1 - \kappa_{ae_{\theta\theta}}. \tag{2.54}$$

It follows that instability for static divergence occurs when $\kappa_{ae_{\theta\theta}}$ is equal to 1. By inserting the quasi-static value for A_3^*, the critical wind velocity for static divergence can be expressed as

$$V_{cr} = B \cdot \omega_\theta \cdot \sqrt{\frac{2\tilde{m}_\theta}{\rho B^4 C_M'} \cdot \frac{\int_L \phi_\theta^2 dx}{\int_{L_{exp}} \phi_\theta^2 dx}}. \tag{2.55}$$

2.6.2 Galloping

Galloping is a dynamic stability problem with the main structural response in vertical direction. The mode shape describing the deformation is expressed as

$$\phi_1 \approx \begin{bmatrix} 0 & \phi_z & 0 \end{bmatrix}^T, \tag{2.56}$$

with a corresponding frequency $\omega_r = \omega_z(V_{cr})$. The impedance function is simplified to

$$\hat{E}_\eta(\omega_r, V_{cr}) = 1 - \kappa_{ae_{zz}} - (\omega_r/\omega_z)^2 + 2i(\zeta_z - \zeta_{ae_{zz}})\omega_r/\omega_z. \tag{2.57}$$

The equation contains both real and imaginary parts. By setting both parts equal to zero, the frequency and damping properties corresponding to galloping can be found,

$$\omega_r = \omega_z \left(1 + \frac{\rho B^2}{2\tilde{m}_z} H_4^* \frac{\int_{L_{exp}} \phi_z^2 dx}{\int_L \phi_z^2 dx} \right)^{-1/2} \tag{2.58}$$

and

$$\zeta_z = \zeta_{ae_{zz}} = \frac{\rho B^2}{4\tilde{m}_z} \frac{\omega_r}{\omega_z} H_1^* \frac{\int_{L_{exp}} \phi_z^2 dx}{\int_L \phi_z^2 dx}. \tag{2.59}$$

A structure can only experience galloping instability if it has positive H_1^*-values.

2.6.3   Dynamic stability limit in torsion

The dynamic stability limit in torsion is similar to that of galloping, however the dominant structural response is in torsional direction. The mode shape is described in the same manner as static divergence,

$$\phi_2 \approx \begin{bmatrix} 0 & 0 & \phi_\theta \end{bmatrix}^T, \tag{2.60}$$

but with a corresponding frequency $\omega_r = \omega_\theta(V_{cr})$. The approach for deriving resonance frequency and damping properties follows the same steps as for galloping,

$$\hat{E}_\eta(\omega_r, V_{cr}) = 1 - \kappa_{ae_{\theta\theta}} - (\omega_r/\omega_\theta)^2 + 2i(\zeta_\theta - \zeta_{ae_{\theta\theta}})\omega_r/\omega_\theta, \tag{2.61}$$

where

$$\omega_r = \omega_\theta \left(1 + \frac{\rho B^4}{2\tilde{m}_\theta} A_3^* \frac{\int_{L_{exp}} \phi_\theta^2 dx}{\int_L \phi_\theta^2 dx} \right)^{-1/2} \tag{2.62}$$

and

$$\zeta_\theta = \zeta_{ae_{\theta\theta}} = \frac{\rho B^4}{4\tilde{m}_\theta} \frac{\omega_r}{\omega_\theta} A_2^* \frac{\int_{L_{exp}} \phi_\theta^2 dx}{\int_L \phi_\theta^2 dx}. \tag{2.63}$$

A structure can only experience dynamic instability in torsion if it has positive A_2^*-values.

2.6.4   Flutter

Contrary to the mentioned stability problems where there is only one direction with dominant response, flutter introduces a coupling between vertical and torsional modes. The structural displacements r_z and r_θ connect via the off-diagonal terms in the impedance function. Normally flutter happens for vertical and torsional modes that are shape-wise similar, where the modes previously used, Equations 2.56 and 2.60 are connected with a joint resonance frequency

$$\omega_r = \omega_z(V_{cr}) = \omega_\phi(V_{cr}). \tag{2.64}$$

The coupling between modes makes the impedance function more mathematically complex, which is why it is preferable to rewrite the expression as

$$\hat{\mathbf{E}}_\eta = \hat{\mathbf{E}}_1 + \hat{\mathbf{E}}_2 + 2i\left(\hat{\mathbf{E}}_3 + \hat{\mathbf{E}}_4\right), \tag{2.65}$$

where $\hat{\mathbf{E}}_1$, $\hat{\mathbf{E}}_2$, $\hat{\mathbf{E}}_3$ and $\hat{\mathbf{E}}_4$ are given as

$$\hat{\mathbf{E}}_1 = \begin{bmatrix} 1 - \kappa_{ae_{zz}} - (\omega_r/\omega_z)^2 & 0 \\ -\kappa_{ae_{\theta z}} & 0 \end{bmatrix} \qquad \hat{\mathbf{E}}_3 = \begin{bmatrix} (\zeta_z - \zeta_{ae_{zz}}) \cdot \omega_r/\omega_z & 0 \\ -\zeta_{ae_{\theta z}} \cdot \omega_r/\omega_\theta & 0 \end{bmatrix}$$

$$\hat{\mathbf{E}}_2 = \begin{bmatrix} 0 & -\kappa_{ae_{z\theta}} \\ 0 & 1 - \kappa_{ae_{\theta\theta}} - (\omega_r/\omega_\theta)^2 \end{bmatrix} \qquad \hat{\mathbf{E}}_4 = \begin{bmatrix} 0 & -\zeta_{ae_{z\theta}} \cdot \omega_r/\omega_z \\ 0 & (\zeta_\theta - \zeta_{ae_{\theta\theta}}) \cdot \omega_r/\omega_\theta \end{bmatrix}. \tag{2.66}$$

The stability limit is found by calculating the determinant of the impedance function and setting both the real and imaginary part to be equal to zero.

It is common to separate between bi-modal and multi-modal flutter calculations. Bi-modal flutter analysis include two still-air modes only, while multi-modal include interaction between several vibration modes. It has been shown that the inclusion of several modes in flutter analysis can be both stabilizing and destabilizing. Which modes that couple in flutter motion is dependent on the shape-wise similarity between the modes and the separation of the corresponding natural frequencies [52]. The shape-wise similarity between two modes i and j is defined by

$$\psi_{ij} = \frac{\int_L \phi_i \phi_j dx}{\int_L \phi_i^2 dx} \cdot \frac{\int_L \phi_j \phi_i dx}{\int_L \phi_j^2 dx}. \tag{2.67}$$

The coefficient ψ_{ij} is equal to one for a perfect match, while it is zero for shape-wise dissimilar modes [53].

2.6.5 Calculation of critical wind velocity

Since the aerodynamic derivatives are dependent on frequency and wind velocity, iterations are required to obtain the stability limits for the dynamic instability motions.

In the analyses, complex eigenvalues and eigenmodes are calculated based on the still-air mode shapes. The iteration procedure starts at an initial wind velocity. It is repeated for changing velocities until the real part of one of the complex eigenvalues is zero, meaning that there is no damping in this mode. The critical wind velocity is found when the velocity increment is below a specific tolerance level. Critical mode is the one with an eigenvalue with no real part. The influence of the still-air modes can be found by investigating the critical mode.

In this thesis, this method is referred to as complex flutter analysis, as the method includes complex eigenvalues and eigenmodes. This is done in order to separate between results of different solution methods.

2.6.6 Closed-form solution of flutter stability

Simplified solution methods of the flutter stability limit of cable supported bridges are a valuable tool in the preliminary design phase. The strength of these methods is their reduced computational time compared to less approximate solutions. Several methods have been developed [54, 55]. In this thesis, a method for estimating critical bi-modal flutter velocity with vertical and torsional modes is used [53].

The method introduces the dimensionless coefficients

$$\chi_z = \frac{\rho B^2}{\tilde{m}_z} \quad \chi_\theta = \frac{\rho B^4}{\tilde{m}_\theta} \quad \gamma = \frac{\omega_\theta}{\omega_z} \tag{2.68}$$

to make expressions simpler, where $\omega_n, n = z, \theta$ are still-air natural frequencies. Further are H_3^*, A_1^*, A_2^* and A_3^* identified as the critical ADs in this solution method. It is assumed that these can be approximated by polynomials which provide a description of the self excited forces which is frequency-independent. This is done by assuming

$$X_i^*(K) = x_i(1/K), \quad i = 1, 2, 5$$
$$X_i^*(K) = x_i(1/K)^2, \quad i = 3, 4, 6 \tag{2.69}$$

where $X = P, H, A$ and $x = p, h, a$. Torsional motion is important for coupled flutter as it generates large coupling forces compared to vertical motion. Therefore, it is assumed that the critical frequency is on the torsional branch of the solution. The critical frequency can thus be approximated by an uncoupled system of equations.

Neglecting the torsion damping because it often is very low results in the following expression for the critical velocity

$$V_{cr,cf} = B\omega_\theta \cdot \sqrt{\frac{2a_2(\gamma^2 - 1)}{\gamma^2 \Omega}}, \tag{2.70}$$

where

$$\Omega = \chi_z \psi_{z\theta} h_3 a_1 + \chi_\theta a_2 a_3. \tag{2.71}$$

As the torsion damping is neglected, the estimated critical wind velocity is expected to be lower than estimates done with the complex flutter analysis. Given this closed-form equation for the prediction of critical wind velocity, the influence of the ADs is more easily understood.

An iteration process is required for the closed-form solution. The ADs, used to calculate the critical wind velocity, are extracted for a certain K. The critical velocity corresponds to a specific value of K, which differs from the K used initially. The calculation process must be repeated until the difference between consecutive reduced frequencies is below a certain tolerance level.

2.7   Wind tunnel testing

Four approaches are available when assessing the response of long-span suspension bridges [56]. Section modelling, taut-strip modelling and full-bridge modelling are all applicable to the design phase, while full-scale measurements are used in calibrating modelling approaches. Section modelling is the most widely used method, as it can be performed in reasonably sized wind tunnels at a low cost, on a large scale and in a short lead time [57].

Two methods are available to determine ADs from wind tunnel tests, forced vibration and free vibration tests. In a free vibration test, the model is suspended in springs. The movement is caused by initial conditions and mutual interactions between the wind flow and model. In a forced vibration test, the

movement is caused by forcing the model in harmonic oscillations. These can be horizontal, vertical or torsional, or combinations of the three. Due to the forcing motion of the latter approach, the free vibration tests are considered to provide more realistic in-wind motion of the bridge deck, while ADs are more easily obtained from the forced vibration tests [26].

2.7.1 Wind tunnel effects

The laboratory environment may have an effect on the obtained results and should be considered [58]. Uncertainty analyses for the aerodynamic derivatives obtained from wind tunnel testing can be included during the early stages of bridge design [59]. An uncertainty analysis is not included in this thesis; however, wind tunnel effects are discussed.

Compared to full-bridge modelling, which has to be on a small scale to fit inside the wind tunnel, section models can be of large scale, typically between 1:25 and 1:100. In addition to modelling advantages on larger scale section models, they are also less prone to aerodynamic scale effects [2].

The model sections placed in the wind tunnel will obstruct the wind flow, causing what is known as the blockage effect. This obstruction will cause an increase in wind velocity around the section models, causing the forces to increase. However, for small blockage ratios, the effects of blockage will be small. The blockage ratio is defined as S/C, where S is model projected area normal to wind and C is the area of the wind tunnel [60]. Studies concluded that for circular cylinders with a blockage ratio less than 6%, the effects of blockage will be small [61]. Similar studies have been performed for bluff body aerodynamics. For blockage ratios from 3-10%, almost identical results were achieved [62]. The Strouhal number will also be independent of the ratio for such blockage ratios.

Due to friction between the boundaries in the tunnel and the wind, wind flow is disturbed close to the edges. The effect is called boundary layer flow. In the wind tunnel at NTNU, this effect is relevant in a range of 200 mm from the walls, floor and ceiling [63].

End plates are used in wind tunnel testing to secure a two-dimensional wind flow across the whole model. It has been reported that if circular, these end plates must have a diameter larger than 8.5 times the depth of the model normal to the approaching wind flow [64]. By making models span the entire width of the tunnel, the need for end plates is eliminated.

Dependency on Reynolds number should also be considered in the tests. The Reynolds number is defined as the ratio of inertial forces to the viscous forces,

$$Re = \frac{\rho U D}{\mu} = \frac{UD}{\nu}, \tag{2.72}$$

where μ and ν are the shear and kinematic viscosity of the fluid, respectively [65]. By performing wind tunnel tests for different wind velocities, a dependency on Reynolds number can be revealed.

Cross-sectional details like railings can have a significant influence on the results obtained from wind tunnel testing. In a test of a section model of the Hardanger Bridge, the critical wind velocity for flutter instability increased by 9.1 m/s due to the inclusion of bridge deck details. It was suggested that all changes in design and details should be investigated to include the consequences of these changes [66].

2.8   St. Venant torsion

For a thin-walled cross-section, the St. Venant torsion is the shear stress flow in each plate element within the cross-section caused by a torsion moment [67]. The theory of St. Venant torsion is based on the following assumptions [68]:

- The material is elastic and Hooke's law is valid.
- Deformations are small.
- The shape of the cross-section is unchanged during the deformation.
- The cross-section is free to warp.

For a closed, thin-walled cross-section, the torsion constant I_T, can be found by Bredt's 2. formula,

$$I_T = \frac{4A_m^2}{\oint \frac{ds}{t}}. \tag{2.73}$$

The area within the centre line of the cross-section is denoted A_m, and t is the cross-sectional thickness.

2.9   Gaussian process regression

Gaussian process regression (GPR) is a data-driven method to predict behaviour in unmeasured regions and is a popular method of interpolation of spatial data [69]. Due to the purely data-based regression, no model of the underlying physics is necessary. Using the obtained results, referred to as training data, the goal is to develop a function that predicts the outcome for all possible input values [70, 71]. One of the approaches for finding this function is to give a prior probability to possible functions. GPR is based on this approach, where the Gaussian probability distribution is used to control the properties of the desired function.

A prior Gaussian distribution of the function $f(x)$ is defined

$$p(f) \sim \mathcal{GP}(m(x), K(x, x')), \tag{2.74}$$

where $\mathcal{GP}(\cdot)$ denotes a Gaussian process. The properties of the function are introduced through the applied mean $m(x)$ and covariance $K(x, x')$ functions. The mean is usually set to zero [70], while the covariance function describes

the degree of correlation between two points x and x' [72, 73]. One example of a covariance model used is the squared exponential kernel,

$$K(x, x') = \sigma^2 \cdot \exp\left(-\frac{(x-x')^2}{2L^2}\right), \qquad (2.75)$$

where σ and L are hyperparameters. The squared exponential covariance function is a stationary function, dependent on $x - x'$ [70, 73]. It fulfills the assumption that the correlation between two points decays with the distance between the points [74].

To predict the value of f at points where there are no data $\mathbf{X}_*$, the prior distribution is conditioned on some observations $\mathbf{y}$ at locations $\mathbf{X}$ [75]. The predicted value f_* at the new location x_* is described by [72]

$$\mathrm{E}[f_*|\mathbf{y}, \mathbf{X}] = \mathbf{K}(x_*, \mathbf{X})\mathbf{K}(\mathbf{X}, \mathbf{X})^{-1}\mathbf{y}, \qquad (2.76)$$

and

$$\mathrm{Cov}[f_*|\mathbf{y}, \mathbf{X}] = K(x_*, x_*) - \mathbf{K}(x_*, \mathbf{X})\mathbf{K}(\mathbf{X}, \mathbf{X})^{-1}\mathbf{K}(x_*, \mathbf{X})^T. \qquad (2.77)$$

This result is the posterior distribution which is also Gaussian distributed.

The hyperparameter L is called the length scale and is related to the smoothness of the function [72]. If the length scale is short, local relationships between nearby points dominate the GPR [76]. Consequently, a too short length scale increases the prediction uncertainty away from the data points [70]. In contrast, if the length scale is large, global long-range relationships between data points dominate the GPR. A too long length scale, therefore, results in a slowly varying function with high prediction uncertainty, also near data points.

After choosing a covariance model, the hyperparameters are determined from the data points. They can be guessed but also trained to best fit the data. This can be done by observing the log-likelihood of the data under the chosen prior $\log(p(\mathbf{y}|\mathbf{X}, \theta))$, where θ is a vector of all hyperparameters. The larger the log-likelihood, the better the data fit the model. Thus, by maximizing the log-likelihood, the optimal hyperparameters are found [75].

GPR is effective in interpolation even when the data points are sparse. In extrapolation however, the predictive power drastically deteriorates [77]. As the distance between points increases, the correlation decreases, resulting in an increased prediction uncertainty.

Chapter 3

Langenuen Suspension Bridge

The E39 Coastal Highway Route is the largest infrastructure project ever planned in Norway. The long-term goal is to build a continuous highway between Kristiansand and Trondheim [78]. If the goal is reached, the current travelling time of 21 hours can be cut in half [79]. Today, E39 includes seven ferry crossings, and each one of them must be replaced to reach the long-term goal. Although some new technology must be developed to realize these crossings, most of the technology needed already exists. Possible solutions include tunnels, suspension bridges and floating bridges [80].

3.1   The fjord crossing

Langenuen Suspension Bridge will, after its completion, connect the two islands Tysnes and Stord, in Western Norway. Three locations were considered for the crossing before the southernmost option was decided on in September 2019 [81]. All three alternatives are shown in Figure 3.1. The choice of crossing resulted in a main span length of 1220 m, which will make it the second

Figure 3.1: The three alternatives for crossing Langenuen [82].

Figure 3.2: Illustration of Langenuen Suspension Bridge [82].

longest in Norway after the Hardanger Bridge [83]. The depth below sea level is ca 500 m [84].

The proposed general arrangement of Langenuen Suspension Bridge is similar to other suspension bridges, with the same main components as shown in Figure 2.1. The pylons are A-shaped towers of concrete with a saddle elevation of about 200 m. An illustration of what this may look like is shown in Figure 3.2.

In order to evaluate the results from the aerodynamic stability analysis, a threshold for wind velocity was needed. This was estimated from the expected mean wind velocity for the desired return period. For this suspension bridge, the return period was set to 500 years. This resulted in a mean wind velocity of 47.4 m/s. The design critical wind velocity was found by multiplying the 500-year mean wind velocity by a safety factor of 1.6 [16]. Thus, $V_{cr,d} = 76$ m/s [83].

3.2   Aluminium girder alternative

Aluminium has been introduced as a possible solution for long-span bridges to reduce the cost of these structures. Several large aluminium structures exist, and especially in the offshore industry have the advantages of aluminium been utilized [83]. However, a long-span suspension bridge with a box girder made of aluminium has never been built, which is why this subject has been investigated heavily in previous years. The modulus of elasticity for aluminium is $E = 70\,000$ N/mm^2 and the density $\rho = 2700$ kg/m^3 [85], while the same properties for steel are equal to 210 000 N/mm^2 and 7850 kg/m^3 [68].

The main argument for replacing steel with aluminium for the crossing of Langenuen is the reduction in self-weight. Since the density of aluminium is about one third of steel density, the self-weight of the bridge girder, which is

the primary load for long-span bridges, will be heavily reduced. This reduction in self-weight creates the opportunity of reducing the dimensions of the other components of the bridge. Other advantages that aluminium introduces are the lack of surface treatment needed due to its high resistance to corrosion, the possibility of local production and assembly close to the construction site, and the fact that aluminium is faster to fabricate than steel [86].

It is implied that there are some significant drawbacks to the concept since a long-span bridge has never been built with aluminium. The stiffness of aluminium is about one third of the stiffness of steel. Thus the dimensions of the bridge girder must be increased. Aluminium is also more expensive than steel, which might cause an aluminium bridge girder to be more expensive than the steel alternative. Furthermore, the reduction of self-weight increases the challenge regarding dynamic stability. The reduced bridge weight makes the structure more prone to experience the instability phenomena described in Chapter 2.

In the feasibility and cost analysis performed by Dr. techn. Olav Olsen, several different aluminium concepts were suggested:

- Plate concept.
- Panel concept.
- Transverse panel concept.
- Inverted cable concept.

Langenuen Suspension Bridge with an aluminium box girder was the topic of a master's thesis written at NTNU in 2020 [1]. In that thesis, the panel concept was chosen as the basis for girder shapes tested in the wind tunnel. Later results showed that this design was problematic concerning local fatigue and ultimate limit state. The concept being further investigated at the time of writing this thesis was the transverse panel concept [83]. A principle sketch of the transverse panel concept is shown in Figure 3.3, while the dimensions of the top deck panel and bulkhead panels are shown in Figure 3.4.

3.2.1   Steel concept

Norconsult presented a steel concept in their preliminary design of the crossing of Langenuen [82]. Their design was based on the crossing of Julsundet, and the dimensions of the bridge girder are shown in Figure 3.5. The design also included A-pylons more than 200 meters tall, which are relevant for the aluminium concept as well.

3.3   Box girder parameterization

A parametric approach in designing the cross-sections was chosen to minimize the number of variables that had to be changed for each cross-section. For this type of box girder, seven points were enough to describe the cross-section

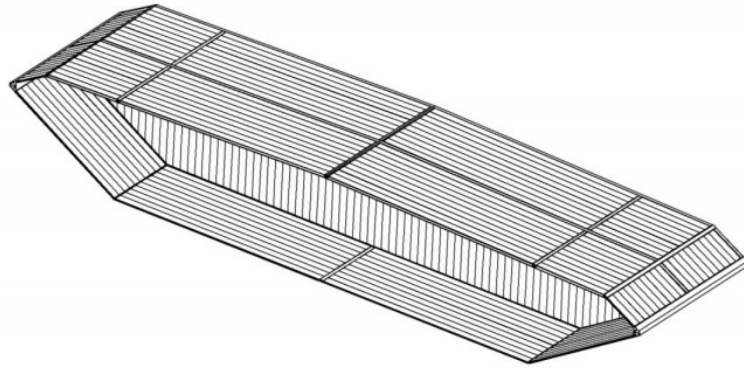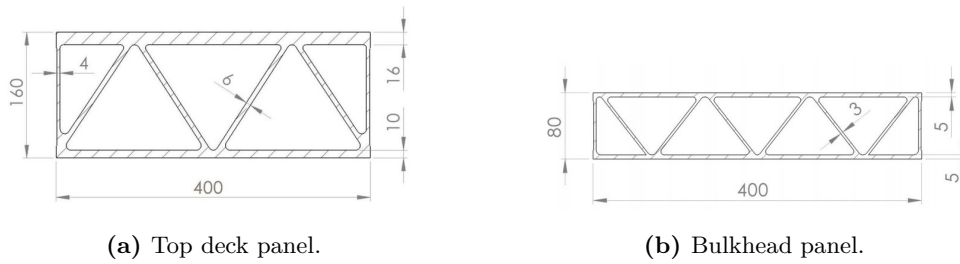**Figure 3.3:** Principle sketch of the transverse panel concept [83].

(a) Top deck panel.   (b) Bulkhead panel.

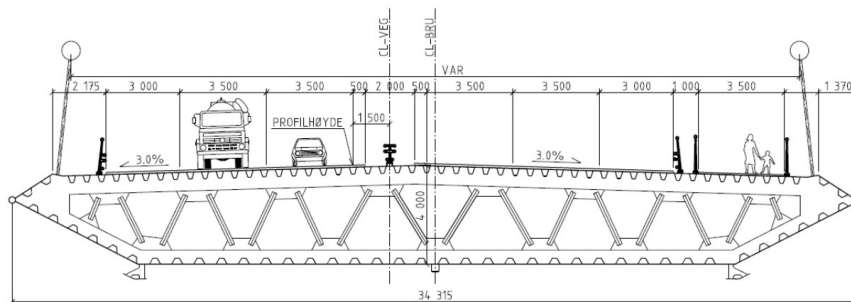**Figure 3.4:** Top panel and bulkhead panel dimensions for transverse panel concept [83].

Figure 3.5: Sketch of a proposed cross-section of Langenuen Suspension Bridge where the box girder is made of steel [82].
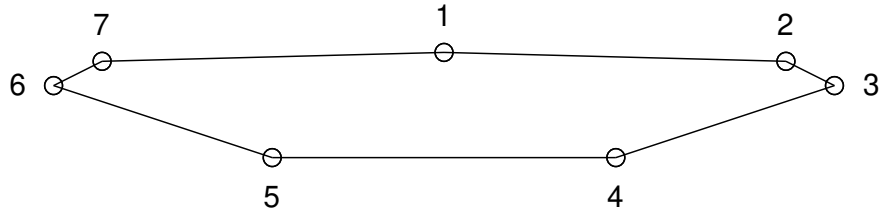
Figure 3.6: The seven points which defines the box girder cross-section.
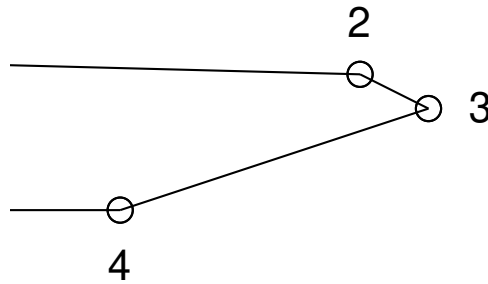

Figure 3.7: The three points which defines the box girder cross-section when it is made symmetric.

uniquely. These points are shown in Figure 3.6. Despite the suggestions of a non-symmetric cross-section [82, 83], the cross-sections used in this thesis were chosen to be symmetric. This, in addition to making point 1 the reference point, reduced the number of points to be chosen to three, shown in Figure 3.7. By constraining both the width and the inclination of the top deck of the box girder, point 2 was fixed. The width and the inclination were set to 31 m and 3%, respectively. This complies with earlier proposals [82].

The last two points were chosen to follow a parameterization similar to the one developed the year prior to this thesis [1]. Two parameters determined the girder shapes; the height of the girder H and the angle below the edge on the girder θ. The horizontal distance between points 2 and 3 was set to $0.4 \cdot H$, and the angle from that horizontal line to the plate between points 2 and 3 was fixed to 30°. This parameterization is shown in Figure 3.8. All seven points were thus uniquely described by the two parameters H and θ.

3.3.1 Torsion constant

In order to narrow down the combinations of the two defining parameters H and θ, the torsion constant was set to be a fixed parameter. The torsion constant was estimated with Bredt's 2. formula (Equation 2.73). This was a simplification of the different concepts suggested, but the same procedure applied by Dr. techn. Olav Olsen [83]. An effective wall thickness of 22.5 mm was used, which was applied in this thesis as well. The choice of effective
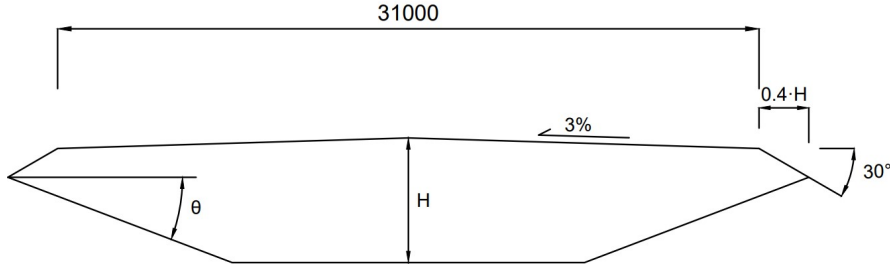
Figure 3.8: Parameterization of the box girder. All points are determined by the two parameters H and θ.

thickness is discussed in Section 4.4.

The study from 2020 reported on four cross-sections with sufficient capacity compared to the design critical wind velocity [1]. It was therefore decided to investigate cross-sections with a lower torsion constant. The cross-sections previously tested had a torsion constant of $I_T = 31$ m^4. For this thesis, cross-sections with a torsion constant of $I_T = 26$ m^4 were produced.

A surface plot using the described parameterization was made to find combinations of H and θ which gave the desired torsion constant. The first value of the torsion constant, which was above the chosen limit, was extracted. The surface plot with the combinations of H and θ which gave $I_T = 26$ m^4 is shown in Figure 3.9. As H increases and θ decreases, points 4 and 5 (Figure 3.6) cross each other. This was defined as an invalid geometry, thus constraining the torsion constant to zero.

The data points where $I_T = 26$ m^4 were extracted. A rational function was fitted to these data points. This is shown in Figure 3.10. The function can be interpreted as a constant torsion constant curve, since all points on the curve give combinations of H and θ with approximately $I_T = 26$ m^4.

The purpose of the curve was to reduce the two defining parameters to one defining parameter. The expression of the curve was

$$\theta = \frac{9.538H - 30.64}{H - 4.451}. \tag{3.1}$$

In this thesis, H was chosen as the defining parameter.

3.3.2   Girder shapes

It was chosen to investigate box girders with the same height as the three lowest studied in 2020. These girders satisfied the critical wind velocity criterion. This includes the heights 5.5, 5.8 and 6.1 m. To accommodate the industry's interest in lower box girders, girders with heights 4.9 and 5.2 m were also tested. This resulted in the angle θ varying from 16.7° to 35.8°, where the smallest angle corresponds to the tallest girder. The cross-sectional shapes are presented in Table 3.1.

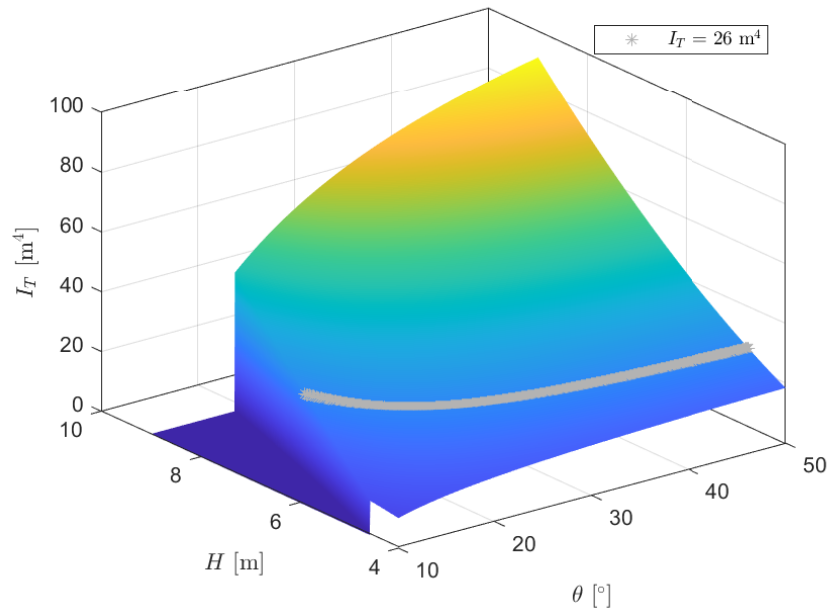**Figure 3.9:** Surface plot of the torsion constant I_T, as functions of the two defining parameters H and θ. Grey stars indicate a torsion constant of 26 m^4. Invalid geometry resulted in a torsion constant equal to zero.
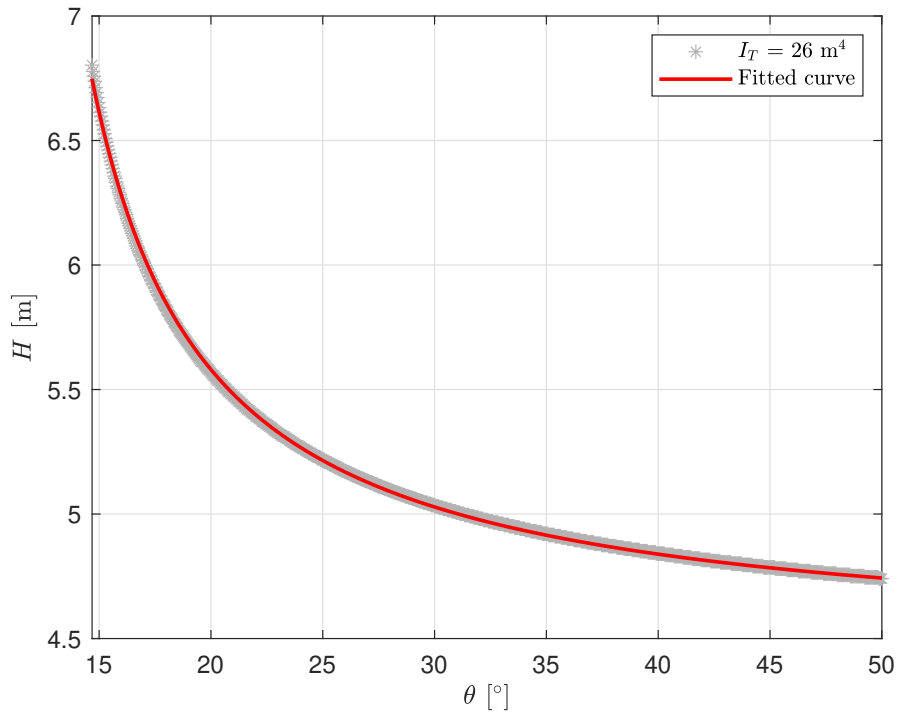
Figure 3.10: Data points showing combinations of H and θ which give $I_T = 26$m^4. A rational function was fitted to the data points.

Table 3.1: Girder shapes for the selected heights with torsion constant $I_T = 26$ m^4.

H [m]	θ [°]	Girder shape
4.9	35.8	
5.2	25.3	
5.5	20.8	
5.8	18.3	
6.1	16.7	

The cross-sections produced in 2020 with $I_T = 31$ m^4 was tested again for this thesis. Although the girder concept investigated in this thesis was different from the girder concept investigated in 2020, the outer shapes of the girders were not changed. These section models were, therefore, still relevant for this thesis. The parameterization used to get $I_T = 31$ m^4 resulted in the following relation of H and θ [1]:

$$\theta = \frac{2.1404H - 7.5532}{0.2062H - 1}.\tag{3.2}$$

It was produced six section models with this parameterization, with girder heights from 5.5 to 7.0 meters. These girder shapes are presented in Table 3.2.

Table 3.2: Girder shapes for the selected heights with torsion constant $I_T = 31$ m^4 [1].

H [m]	θ [°]	Girder shape
5.5	31.4	
5.8	24.8	
6.1	21.3	
6.4	19.2	
6.7	17.8	
7.0	16.7	

Chapter 4

Finite Element Analysis

Finite element analysis (FEA) is a method for numerical solution of field problems [87]. In this thesis, FEA is used to assess the box girders' cross-sectional properties and determine the modal properties of the structure. A brief analysis regarding the effective thickness is also included. The Abaqus [88] software was used to perform the FEA.

4.1 Cross-sectional modelling

The cross-sections were modelled using a simplified cross-section with a constant plate thickness of 22.5 mm. A mesh size of 5 mm and the Abaqus elements WARP2D3 and WARP2D4 were used. These elements are 3- and 4-noded two-dimensional warping elements, respectively. They allow for computation of cross-sectional parameters, such as area A, second moments of area I_y, I_z and torsion constant I_T. As the cross-sections were designed with $I_T = 26$ m^4 and $I_T = 31$ m^4, the latter computation served as a check of what had previously been calculated by Bredt's second formula (Equation 2.73). The results from the cross-sectional analysis are summed up in Table 4.1 for all cross-sections.

4.2 Global element model

Dombu and Gjelstad [89] presented a parametric model of Langenuen Suspension Bridge in their master's thesis in 2019. It was made as a parametric script in Python [90]. This model was also used in 2020 [1], and it allows for finding modal properties necessary to calculate the stability limits and buffeting response of the bridge girder. The parametric design of the model heavily reduced the time needed for calculating the modal properties for all the different bridge girders. The authors were grateful to use their model as a basis in this thesis.

Figure 4.1 shows the global dimensions of the bridge. The parametric model

Table 4.1: Area A, second moments of area I_y, I_z and torsion constant I_T for all cross-sections.

I_T [m^4]	H [m]	A [m^2]	I_y [m^4]	I_z [m^4]	I_T [m^4]
26	4.9	1.63	7.53	175	26.0
	5.2	1.63	7.85	174	26.0
	5.5	1.64	8.14	176	26.1
	5.8	1.65	8.37	179	26.2
	6.1	1.66	8.53	182	26.2
31	5.5	1.66	9.29	181	31.1
	5.8	1.66	9.62	182	31.1
	6.1	1.67	9.91	184	31.1
	6.4	1.68	10.2	187	31.3
	6.7	1.69	10.3	190	31.2
	7.0	1.70	10.4	194	31.1
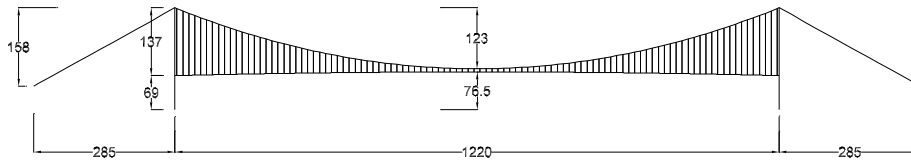
Figure 4.1: Global dimensions of Langenuen Bridge, used in the FEA.

was modified in order to represent the transverse panel concept from Dr. techn. Olav Olsen, with hangers every 12 meters [83]. The x-axis was set along the bridge with $x = 0$ in the centre of the bridge, while y-axis was lateral to the bridge deck and the z-axis was in vertical direction.

The modelling approach utilized for the FEA of Langenuen Bridge was the spine-beam approach. This approach has previously been used to model several suspension bridges and has been proved to be efficient for assessment of the global behaviour of long-span cable supported bridges [91]. The box girder was modelled as a beam girder with one-dimensional elements in the longitudinal direction. These were connected to the hangers with rigid connection elements. This approach is shown in Figure 4.2. The nodal coordinates of the girder elements were given in the centre of the cross-section. Due to the relatively small changes in centre coordinates for the different cross-sections, these differences were neglected when creating the different models. Thus, an identical geometry was used for all models. The calculated cross-sectional parameters were implemented for the beam girder for each of the eleven models. Parameters for the other parts of the models are shown in Table 4.2. The
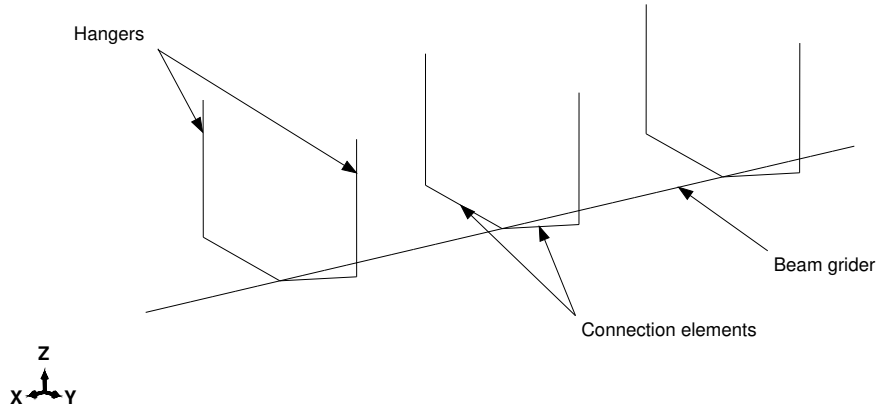
Figure 4.2: The spine-beam approach replaces the box girder with beam and connection elements.

Table 4.2: Cross-sectional parameters used in the FEA for all structural elements of the model, excluding the girder. These parameters were identical for all cross-sections.

Component	Material	A [m^2]	$I_y = I_z$ [m^4]	I_T [m^4]	E [GPa]	ν	ρ [kg/m^3]
Main cables	Steel	0.3257	0.0084	0.0169	200	0.3	7850
Hangers	Steel	0.0017	$2.2 \cdot 10^{-7}$	$4.4 \cdot 10^{-7}$	210	0.3	7850
Pylons	Concrete	-	-	-	35	0.2	2400
Connection elements	-	0.22	1000	1000	200	0.3	0
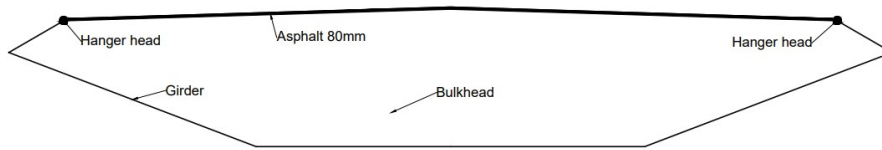
Figure 4.3: Box girder elements which contributed to the added inertia.

pylons were simplified as constant quadratic hollow cross-sections, with outer dimension equal to 5 meters and wall thickness equal to 1 meter. All section properties for the pylons were automatically calculated by the geometric input.

Inertia properties for the beam girder and additional masses were added independently of the section profiles. The contributions from each component were calculated based on the cross-sections' outer shape and a layer of 80 mm asphalt layer as surface. Figure 4.3 shows a simplified drawing of the different parts which were included when calculating additional inertia. Tables 4.3 and 4.4 list the contributions included for the different element models with I_T = 26 m^4 and I_T = 31 m^4, respectively. The contributions from the bulkhead panels were calculated using the dimensions from Figure 3.4b and considering bulkheads every fourth meter. Since Bernoulli beam elements ignore additional inertia added to the elements [92], the beam girder was modelled with B32 elements, 3-noded quadratic Timoshenko elements. Other parts of the model were modelled using cubic Bernoulli elements, B33.

The pylons were clamped to the ground, fixing both translation and rotation in all directions, while the main cables were pinned, which allowed rotation. In order to allow some movement between the pylons and the bridge girder, spring elements were used in both ends of the girder. Tie constraints were applied where elements of different components met, meaning that no relative motion was allowed between these elements [92].

Figure 4.4 shows the global element model. All eleven global element models are appended to this thesis. They are listed in Appendix A.
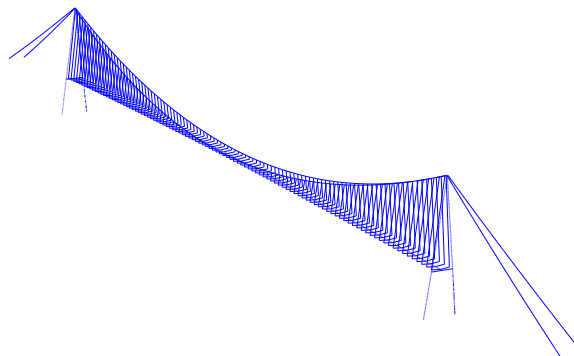
Figure 4.4: Global element model of Langenuen Suspension Bridge.

Table 4.3: Moments of inertia used in the FEA for the cross-sections with $I_T = 26$ m^4. The orientation angle was 0° for all components.

Height [m]	Inertia component	Linear mass [kg/m]	e_y [m]	e_z [m]	I_{11} [kgm^2/m]	I_{22} [kgm^2/m]
4.9	Girder	4401	0	0	20331	472500
	Bulkhead	1515	0	0	2644	31540
	Asphalt	5580	0	2.23	2.976	446865
	Hanger heads	32	±15.5	1.95	0	0
	Other equipment	400	0	0	0	0
5.2	Girder	4401	0	0	21195	469800
	Bulkhead	1515	0	0	2905	30047
	Asphalt	5580	0	2.22	2.976	446865
	Hanger heads	32	±15.5	1.95	0	0
	Other equipment	400	0	0	0	0
5.5	Girder	4428	0	0	21978	475200
	Bulkhead	1521	0	0	3155	29918
	Asphalt	5580	0	2.22	2.976	446865
	Hanger heads	32	±15.5	1.95	0	0
	Other equipment	400	0	0	0	0
5.8	Girder	4455	0	0	22599	483300
	Bulkhead	1527	0	0	3372	30462
	Asphalt	5580	0	2.23	2.976	446865
	Hanger heads	32	±15.5	1.96	0	0
	Other equipment	400	0	0	0	0
6.1	Girder	4482	0	0	23031	491400
	Bulkhead	1532	0	0	3533	31317
	Asphalt	5580	0	2.23	2.976	446865
	Hanger heads	32	±15.5	1.96	0	0
	Other equipment	400	0	0	0	0

Table 4.4: Moments of inertia used in the FEA for the cross-sections with $I_T = 31$ m^4. The orientation angle was 0° for all components.

Height [m]	Inertia component	Linear mass [kg/m]	e_y [m]	e_z [m]	I_{11} [kgm^2/m]	I_{22} [kgm^2/m]
5.5	Girder	4482	0	0	25083	488700
	Bulkhead	1669	0	0	3652	34265
	Asphalt	5580	0	2.43	2.976	446865
	Hanger heads	32	±15.5	2.15	0	0
	Other equipment	400	0	0	0	0
5.8	Girder	4482	0	0	25974	491400
	Bulkhead	1671	0	0	3959	33465
	Asphalt	5580	0	2.42	2.976	446865
	Hanger heads	32	±15.5	2.15	0	0
	Other equipment	400	0	0	0	0
6.1	Girder	4509	0	0	26757	496800
	Bulkhead	1677	0	0	4244	33465
	Asphalt	5580	0	2.43	2.976	446865
	Hanger heads	32	±15.5	2.15	0	0
	Other equipment	400	0	0	0	0
6.4	Girder	4536	0	0	27405	504900
	Bulkhead	1683	0	0	4487	34360
	Asphalt	5580	0	2.43	2.976	446865
	Hanger heads	32	±15.5	2.16	0	0
	Other equipment	400	0	0	0	0
6.7	Girder	4563	0	0	27810	513000
	Bulkhead	1687	0	0	4663	35300
	Asphalt	5580	0	2.44	2.976	446865
	Hanger heads	32	±15.5	2.16	0	0
	Other equipment	400	0	0	0	0
7.0	Girder	4590	0	0	27972	523800
	Bulkhead	1690	0	0	4746	36259
	Asphalt	5580	0	2.44	2.976	446865
	Hanger heads	32	±15.5	2.17	0	0
	Other equipment	400	0	0	0	0

4.3   Modal properties

A modal step was performed on each of the global element models. One hundred modes were extracted with their corresponding natural frequencies. Mode shapes determined to be less relevant for the global response of the girder included modes dominated by oscillations of cables and towers. These were excluded for most of the analyses. Each mode shape was described as either horizontal (H), vertical (V) or torsional (T), as well as symmetric (S) or asymmetric (A). This description complied with the motion of the girder. The natural frequencies of the first symmetric and asymmetric motion, in each of the three directions, are listed in Table 4.5 for all cross-sections.

A list of the first 15 most relevant natural frequencies for all girders can be found in Appendix B. Along with the natural frequencies is a visualization of the mode shapes in three directions. When choosing the most relevant torsional mode shapes, similar mode shapes with almost the same natural frequencies were observed for symmetric and asymmetric shapes. The modes with the largest excitation were chosen as the most relevant modes.

The first 15 most relevant mode shapes of the global element model are shown in Figure B.1. This figure shows the result of the FEA of the cross-section with $H = 5.5$ m and $I_T = 26$ m^4. Mode shapes for other cross-sections were similar.

Natural frequencies of similar modes for different girder heights were compared. This was done by plotting the natural frequencies against the height for both parameterizations. This is shown in Figure 4.5. The measurement points are indicated by a circle. Lines between measurement points are not an interpolation. They give information of which frequencies that have similar

Table 4.5: Natural frequencies in Hz for the first horizontal, vertical and torsional modes, both symmetric and asymmetric, for all models.

I_T [m^4]	H [m]	1HS	1HA	1VS	1VA	1TS	1TA
26	4.9	0.0573	0.1442	0.1439	0.1095	0.4148	0.4756
	5.2	0.0573	0.1438	0.1442	0.1096	0.4142	0.4756
	5.5	0.0574	0.1443	0.1444	0.1097	0.4141	0.4758
	5.8	0.0575	0.1450	0.1446	0.1098	0.4139	0.4758
	6.1	0.0576	0.1457	0.1447	0.1098	0.4135	0.4753
31	5.5	0.0577	0.1450	0.1452	0.1100	0.4239	0.5072
	5.8	0.0577	0.1453	0.1455	0.1101	0.4236	0.5070
	6.1	0.0578	0.1457	0.1457	0.1102	0.4234	0.5071
	6.4	0.0579	0.1464	0.1459	0.1103	0.4230	0.5069
	6.7	0.0580	0.1471	0.1459	0.1103	0.4222	0.5054
	7.0	0.0581	0.1481	0.1460	0.1104	0.4214	0.5037

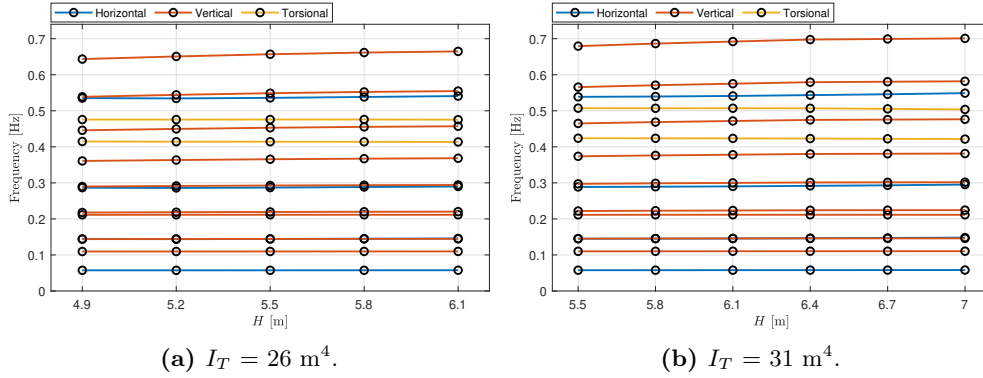(a) $I_T = 26 \text{ m}^4$.   (b) $I_T = 31 \text{ m}^4$.

Figure 4.5: Comparison of natural frequencies of the first 15 most relevant modes. Colour specific lines are not to be interpreted as interpolations.

mode shapes and the direction of that mode shape.

The figures show that the natural frequencies varied little between heights within the same parameterization. Natural frequencies related to the horizontal and vertical motion had a slight increase in value as the cross-section height increased. The trend was opposite for natural frequencies related to torsional motion, which had a slight decrease as the cross-section height increased. These trends were more prevalent for higher natural frequencies. Natural frequencies for the cross-sections with $I_T = 26 \text{ m}^4$ were, in general, lower than natural frequencies for the cross-sections with $I_T = 31 \text{ m}^4$, for girders with the same height.

The percentage increase between the girders with the lowest and highest natural frequencies was calculated to quantify the difference between the natural frequencies. This was done for the first 15 most relevant mode shapes for both parameterizations. Table 4.6 lists these values. The increase was no higher than 2.28%, 3.30% and 0.71% for the horizontal, vertical and torsional directions, respectively. In the vertical direction, the percentage increase tended to increase as the natural frequency increased. The exception was the mode 2VS.

The modal properties of the cross-sections with $I_T = 31 \text{ m}^4$ were compared to the results from 2020 [1] to investigate discrepancies as a result of the change of design concept. For vertical and torsional mode shapes, the differences in modal properties were minor. The changes in design led to larger differences for the horizontal modes. Eigenfrequencies were reduced, especially for higher frequencies.

4.4   Effective thickness of transverse panel concept

The effective thickness of 22.5 mm was the same thickness chosen by Dr. techn. Olav Olsen for the sandwich panel concept. Due to the change in design to the transverse panel concept, simple analyses regarding the axial stiffness of the

Table 4.6: The percentage increase between the girders with the lowest and highest natural frequencies of the first 15 most relevant mode shapes for both parameterizations.

Direction	Description	$I_T = 26$ m^4 [%]	$I_T = 31$ m^4 [%]
Horizontal	1HS	0.49	0.78
	1HA	1.33	2.14
	2HS	1.42	2.28
	2HA	1.23	1.90
Vertical	1VA	0.28	0.29
	1VS	0.53	0.54
	2VS	0.10	0.08
	2VA	1.12	1.14
	3VS	1.49	1.52
	3VA	2.07	2.05
	4VS	2.52	2.47
	4VA	2.95	2.85
	5VS	3.30	3.16
Torsional	1TS	0.31	0.57
	1TA	0.12	0.71

top panel were conducted. Tests were performed with different placement of load and boundary conditions. This allowed for axial stiffness calculations in the longitudinal and transverse directions. The top deck panel was modelled in Abaqus using shell elements with varying thickness, following the dimensions from Figure 3.4a. The section models were 4×4 meters.

Boundary conditions and loading are shown in Figures 4.6 and 4.7 for investigation of axial stiffness in the longitudinal and transverse directions, respectively. For both cases, deformation was allowed in the loading direction only. Pressure load was applied at one end of the section model, while the
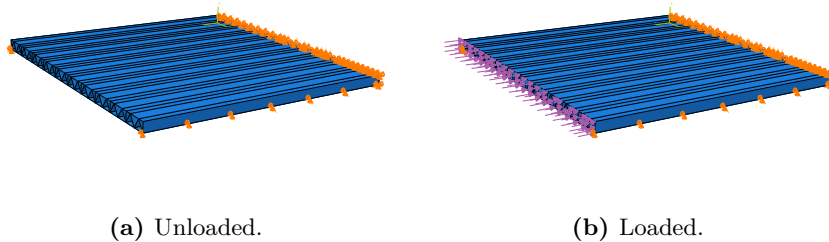

(a) Unloaded. **(b)** Loaded.

Figure 4.6: Placement of boundary conditions and load, in order to investigate axial stiffness in longitudinal direction.
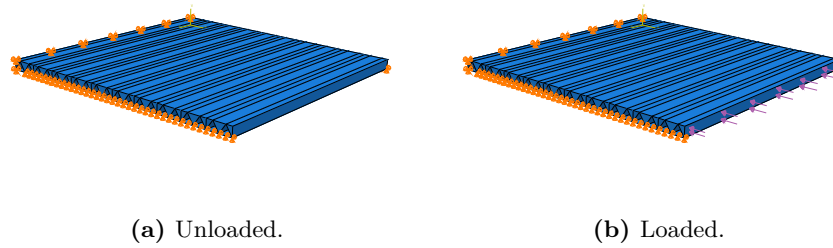
(a) Unloaded.　　　　　　　　　　**(b)** Loaded.

Figure 4.7: Placement of boundary conditions and load, in order to investigate axial stiffness in transverse direction.

opposite end was fixed in all directions.

The test with loading in longitudinal direction revealed an effective thickness of 38.1 mm, while the transverse loading resulted in effective thickness equal to 29.4 mm. The stiffness was lower in the transverse direction, but the calculated effective thickness of 29.4 mm was larger than the thickness used in calculations for the torsion constant. Reaction forces and deformations used in the calculations of effective thickness are given in Appendix C.

The effective thickness of 22.5 mm was conservative for the top panel regarding axial stiffness. This does not guarantee that the choice of torsion constant was conservative. However, Dr. techn. Olav Olsen analysed a section of the transverse panel concept with an outer shape equal to the girder with $H = 5.5$ m and $I_T = 31$ m^4. The torsion constant was found to be 40.6 m^4, considerably larger than the torsion constant used in this thesis [83].

The simplification with effective thickness and the resulting cross-sectional properties was an uncertainty when calculating the modal properties. In order to find the structural properties of the cross-sections more accurately, finite element models of the sections covering a certain span would have been needed, which is what Dr. techn. Olav Olsen did in their report. Although more accurate, this was not included in this thesis as a time-saving measure.

Chapter 5

Wind Tunnel Testing

The experiments presented in this thesis were conducted in the wind tunnel at the fluid mechanics laboratory at NTNU. The processes of producing the section models and performing the tests are described in this chapter.

5.1 Section models

The girders chosen and described in Chapter 3 were produced in a scale of 1:70. In order to achieve section models that were both stiff and light, the material Divinycell H was used, which provided these properties [93]. Each section was made out of two plates of Divinycell, which were glued together. The assembled sections were milled to the desired cross-section shapes. Before assembly, each plate was milled such that an aluminium pipe could be placed inside the models. The aluminium pipes provided extra stiffness to the models. The pipes had an outer diameter of 50 mm, and a wall thickness of 1 mm. In addition, two extra cylinders were carved out of the plates as a weight reduction measure. Figure 5.1 shows one of the models during and after the milling process.
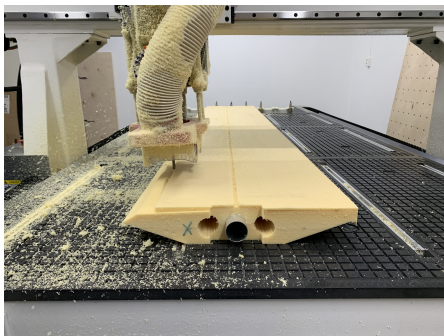
(a) Milling of section model.
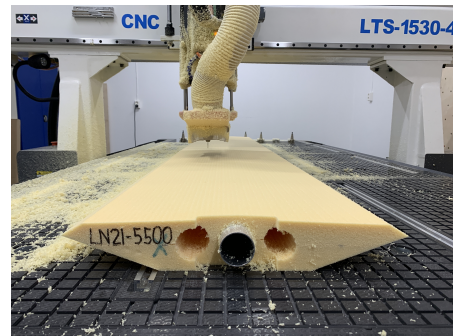
(b) Finished section model.

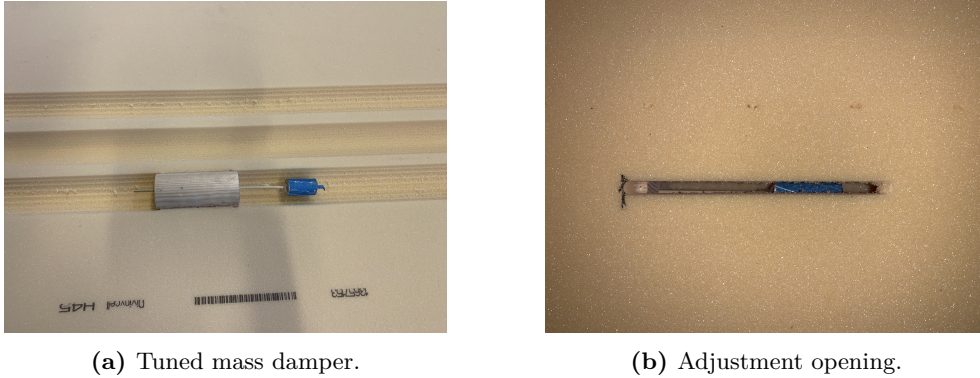**Figure 5.1:** Cross-section model during and after milling.

(a) Tuned mass damper.

(b) Adjustment opening.

Figure 5.2: Tuned mass damper mounted in a section model.

A TMD was placed in the section models with $I_T = 26$ m^4. The damper was built out of a roll of coins connected to a cylindrical timberpiece with a rod. The operating frequency range of the damper could be changed by adjusting the distance from the timberpiece to the coin-mass. The mass ratio of the TMD was 2%. In the top part of the section model, above the TMD, an opening was milled in the section models. This enabled adjustment of the TMD. The TMD is shown in Figure 5.2. Coarse tuning of the damper resulted in a default distance between the timberpiece and the nearest part of the coin-mass of 6 cm. This corresponded to a natural frequency of about 12.5 Hz.

The milling process was performed by a CNC milling machine. The machine used Matlab [94] codes written by our supervisor to produce the section shapes. The input for this code was the coordinates for the seven points which defined the cross-section (Figure 3.6). The process was guided by Gøran Loraas.

5.1.1 Modelling details and guide vanes

Fences were added to the section models in order to increase the reliability of the results. The fences used in this thesis were produced in 2020 for testing of cross-sections with $I_T = 31$ m^4 [1]. These were also milled by the CNC machine.

Guide vanes were designed based on drawings provided by NPRA and previously designed guide vanes for a section model of the Hardanger Bridge. Figure 5.3 shows one of the sections designed in SolidWorks [95]. The guide vanes were 3D-printed, limiting the thickness of the elements to be no smaller than 1 mm. The total length of one element was 295 mm, while the centre distance between each vertical plate was 42.14 mm. Five different designs were made for the guide vanes, such that the angle of the inclined parts was approximately equal to θ for each cross-section. The angles used were 17°, 20°, 25°, 31° and 36°. For each bridge section model, a total of 18 guide vanes were used, nine on each side.
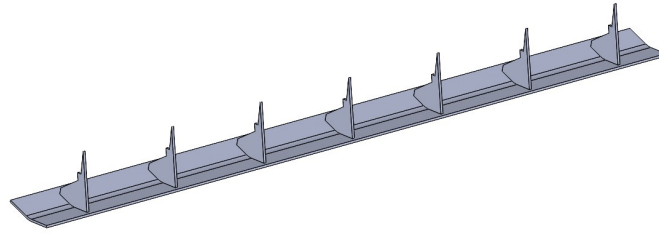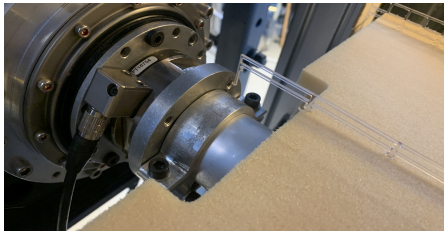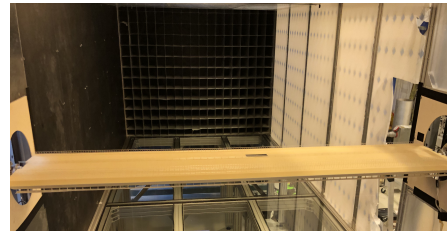
Figure 5.3: 3D-drawing of a guide vane.

(a) Section model clamped to a load cell. The load cell was bolted to an actuator.

(b) Full section model mounted. The air outlet is seen in the back.

Figure 5.4: Mounting of a section model in the wind tunnel.

To investigate the effect of the guide vanes, the cross-sections produced the year prior to this thesis [1] were tested with the inclusion of guide vanes.

5.2 Experimental setup

The rig was a forced vibration rig, similar to a setup developed at the Department of Structural Engineering at NTNU in 2017. It was designed to move a section model in arbitrary motion. Consequently, real bridge motion is more easily imitated, thus reducing the drawbacks of the forced vibration test compared to the free vibration test. It was reported on excellent performance of the rig setup [26].

The movement in the forced vibration setup was caused by two 3-DOF actuators. Two linear motion slides allowed for movement of ± 100 mm in the horizontal and vertical directions, while servo motors drove torsional motion of ± 90 degrees. Bolted to the actuators were load cells. They measured three forces and three moments at each end of the section model. The section models were clamped to the load cell in each end. This setup is shown in Figure 5.4a.

The wind tunnel was a low-speed closed-loop, driven by a 220 kW fan [96]. Its test area was 2.7 m wide, 1.8 m high and 11.1 m long. The height of the test area allowed for section models to be placed outside the area where friction between the air and the boundaries affected the wind velocity. Hence, boundary layer flow on the floor and in the ceiling was not an issue in the experiments. The section models were made to span the entire width of the

Table 5.1: Tests performed on every cross-section in the wind tunnel. Wind speeds were approximate.

Purpose	Motion	Wind speed [m/s]	Amplitude
Vortex shedding	None	0-13	None
Damping	Free decay	0	None
Static coefficients	Angular steps	0, 6, 8, 10	8°
ADs	Horizontal harmonic	0, 6, 8	20 mm
ADs	Vertical harmonic	0, 6, 8	10 mm
ADs	Torsional harmonic	0, 6, 8	1°

test area, which excluded the need for end plates. As the length of the section models was 2.7 m, the boundary layer effect on the walls of the test area was considered negligible.

Thin plates with circular holes were mounted around the load cells to minimize the openings in the wind tunnel. This was done to secure two-dimensional wind flow by preventing wind from flowing in or out of the tunnel. The plates can be seen in Figure 5.4b. They were created thin enough not to reduce the test area, which minimized disturbances of the wind flow.

The blockage ratio was calculated to 5.6% for the tallest section model. Thus, no actions were taken to account for blockage effects.

5.3   Test description

For each section model, four different test types were performed. The tests performed on the section models are summed up in Table 5.1.

Vortex shedding tests were conducted in order to discover wind velocities where VIV occurred. The wind speed was gradually increased while monitoring the movement of the model. No forced motion was prescribed to the model during the vortex shedding tests. Wind speeds where significant vibrations were observed were avoided in the following tests.

Free decay tests were performed to investigate the damping properties of each section model. The movement of the model was initiated by knocking on the top deck in still-air.

Quasi-steady tests were necessary to identify static coefficients. The tests were conducted by slowly rotating the section model about its length axis and monitoring the resulting forces. These tests were performed for several wind speeds in order to investigate a possible dependency on Reynolds number. The amplitude of the torsional rotation was eight degrees. The motion history of this test is shown in Figure 5.5.

Tests with a harmonic motion of the section models were performed in three different directions; horizontal, vertical and torsional. The purpose was to identify the aerodynamic derivatives for each model. Similar to the quasi-
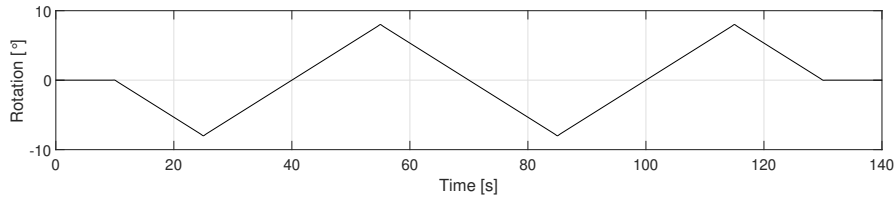
Figure 5.5: Quasi-steady motion history used in the wind tunnel for the purpose of estimating static coefficients.

steady tests, the harmonic vibration tests were performed for different wind speeds, including a still-air test. The still-air tests were performed in order to subtract inertia forces from the calculations. Thus, the wind forces were isolated. The time series of the harmonic movements included movement with several different frequencies to acquire results for a broader band of reduced frequencies. These frequencies were 0.25, 0.50, 0.77, 1.1, 1.4, 1.7, 2.0 and 2.5 Hz. The motion histories of the harmonic vibration tests are shown in Figure 5.6.
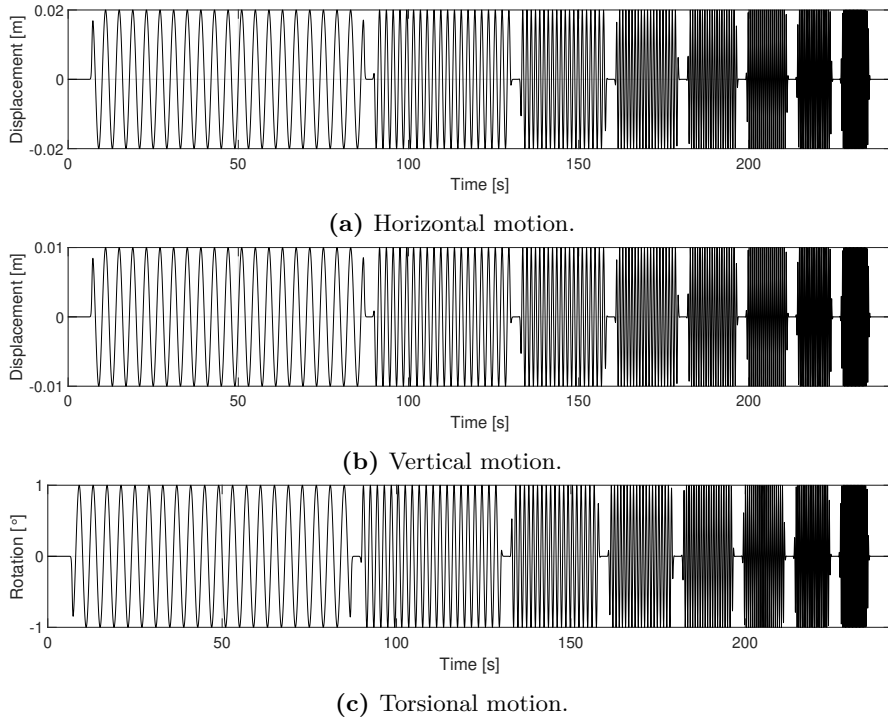

(a) Horizontal motion.

(b) Vertical motion.

(c) Torsional motion.

Figure 5.6: Harmonic motion histories used in the wind tunnel for the purpose of estimating ADs.

Chapter 6

Results and Discussion

Processed results from the wind tunnel tests are presented in this chapter. Gaussian process regression has been utilized to predict the behaviour of aerodynamic derivatives in areas without data points. Stability limit calculations have been performed on all cross-sections to estimate the critical wind velocity of each cross-section. The buffeting response was calculated at three locations on the bridge. Matlab scripts provided by our supervisors aided the analyses. Discussion of results is included.

6.1 Vortex induced vibrations

Vortex induced vibrations were observed for some of the section models, especially those with lower girder heights. Wind speed, vertical forces, and standard deviation of vertical forces and normalized lateral forces of all sections are seen in Appendix D. The plots for the cross-sections with $I_T = 31$ m^4 include the forces measured both with and without guide vanes installed, where the latter results are from the tests performed in 2020 [1]. Instalment of guide vanes was seen to be effective for all cross-sections with $I_T = 31$ m^4, except the girder with $H = 5.5$ m. For all other girders, VIV was reduced compared to the results from 2020. The results showed that VIV was a more significant problem for the cross-sections with $I_T = 31$ m^4, particularly the two lowest girders. Lower cross-sections were less streamlined than taller cross-sections, which likely led to larger transverse forces due to the separation of wind flow. This explains the larger presence of VIV observed for the lower girders. The reason for the relatively small vibrations observed for the cross-sections with $I_T = 26$ m^4 was likely the instalment of TMDs. Since the TMDs were installed in the sections with $I_T = 26$ m^4 only, their influence could be observed. It is believed that this influence was significant, which is supported by the observations done during free decay tests. The influence of the TMDs should only be considered for the section models and not the full scale bridge design. A full-scale TMD design for the Langenuen Suspension bridge is far more complex than the simple installation made for the section models. In most cases, the
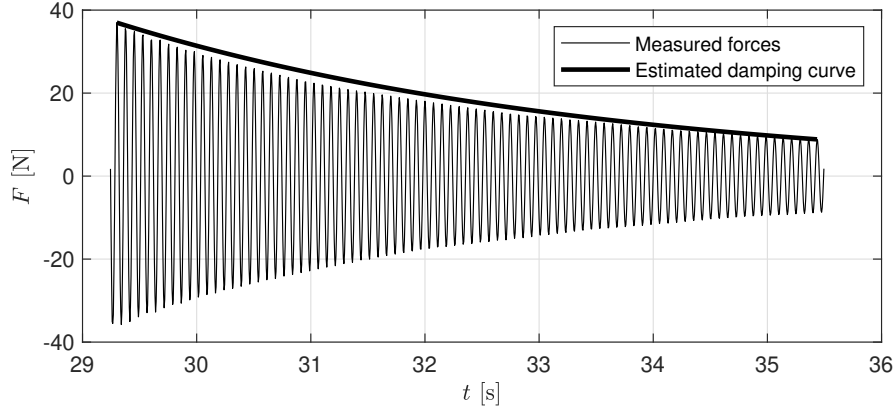
51

Figure 6.1: Measured forces during the free decay test of a section model and the estimated corresponding damping curve.

Table 6.1: Damping ratio and logarithmic decrement of section models estimated from the free decay tests in the wind tunnel.

I_T [m^4]	H [m]	δ [-]	ζ [%]
26	4.9	0.0565	0.90
	5.2	0.0415	0.66
	5.5	0.0369	0.59
	5.8	0.0333	0.53
	6.1	0.0364	0.58
31	5.5	0.0158	0.25
	5.8	0.0175	0.28
	6.1	0.0206	0.33
	6.4	0.0195	0.31
	6.7	0.0183	0.29
	7.0	0.0210	0.33

actions taken to suppress VIV in the wind tunnel were considered effective.

The later tests were performed successfully for all section models by varying the wind speed such that VIV was avoided. The gathered data was considered to be of a quality that was satisfactory for further analyses.

Figure 6.1 shows a part of a time series from the free decay test of one section model, with the estimated damping curve plotted along with the measured forces. The theory presented for estimation of damping properties based on displacement measurements is valid for forces as well. Thus, damping properties of the section models were extracted. The logarithmic decrement and damping ratio of all section models are listed in Table 6.1.

Some uncertainty was related to the estimation of these parameters since the time series chosen varied between cross-sections. Decreasing or increasing

the part of the time series used to estimate the damping properties would have led to small changes in the results. Nevertheless, the section models with TMDs installed had a larger damping ratio than those without TMDs. The logarithmic decrement was the only parameter in the equation for Scruton number, which differed significantly for the section models. Therefore, the Scruton number of the cross-sections without TMDs was lower than that of the cross-sections with TMDs. This result partially explained the more significant VIV problem observed for the section models with $I_T = 31$ m^4.

The Scruton number was estimated for the girder with $H = 5.5$ m and $I_T = 31$ m^4 for both the section model and the global bridge model. This was the cross-section where the greatest VIV-problem was observed. For the bridge, ζ was assumed to be equal to 0.5%. The calculated Scruton number was equal to 7.25 and 30.30 for the section model and the bridge, respectively. The higher Scruton number calculated for the bridge means that the vibrations observed in the wind tunnel are less likely to occur for the bridge. Calculations were performed for the other cross-sections as well, where the same trend was observed.

6.2   Static coefficients

The static coefficients were obtained with the quasi-steady test displayed in Figure 5.5. Figures 6.2 and 6.3 display the static coefficients of the cross-sections with $I_T = 26$ m^4 and $I_T = 31$ m^4, respectively. The coefficients of drag, lift and moment were plotted as functions of the flow of incidence α, with a maximal inclination of eight degrees. All coefficients were plotted for three different wind speeds. The wind speeds varied for each model to avoid VIV.

There were some differences for the considered section models, but the static coefficient curves were shape-wise similar for different heights. The drag coefficients showed a close to parabolic behaviour, while the lift and moment coefficients were close to linear functions. There were some disturbances to the linearity, especially for the lift coefficients at $\alpha \approx 0$, and these disturbances became more significant for taller cross-sections.

The lift coefficient was negative for all sections when the flow of incidence was below zero. For a specific positive value of α, the lift coefficient got positive. This value varied between cross-sections, but it increased when the height increased. The reason for the negative lift coefficient is the same effect that causes positive lift for airfoils. Lift is caused when a solid object in a fluid deflects the flow around it. The cross-sectional shape of the bridge girder and the relative angle to the flow α causes the flow to deflect from its original path. When the flow is curved in one direction, lift is generated in the opposite direction. The net curvature was upwards at $\alpha = 0$, causing the lift force to act downwards, defined as negative lift. At some point, α got so large that the flow was deflected the other way around the section models. The net curvature
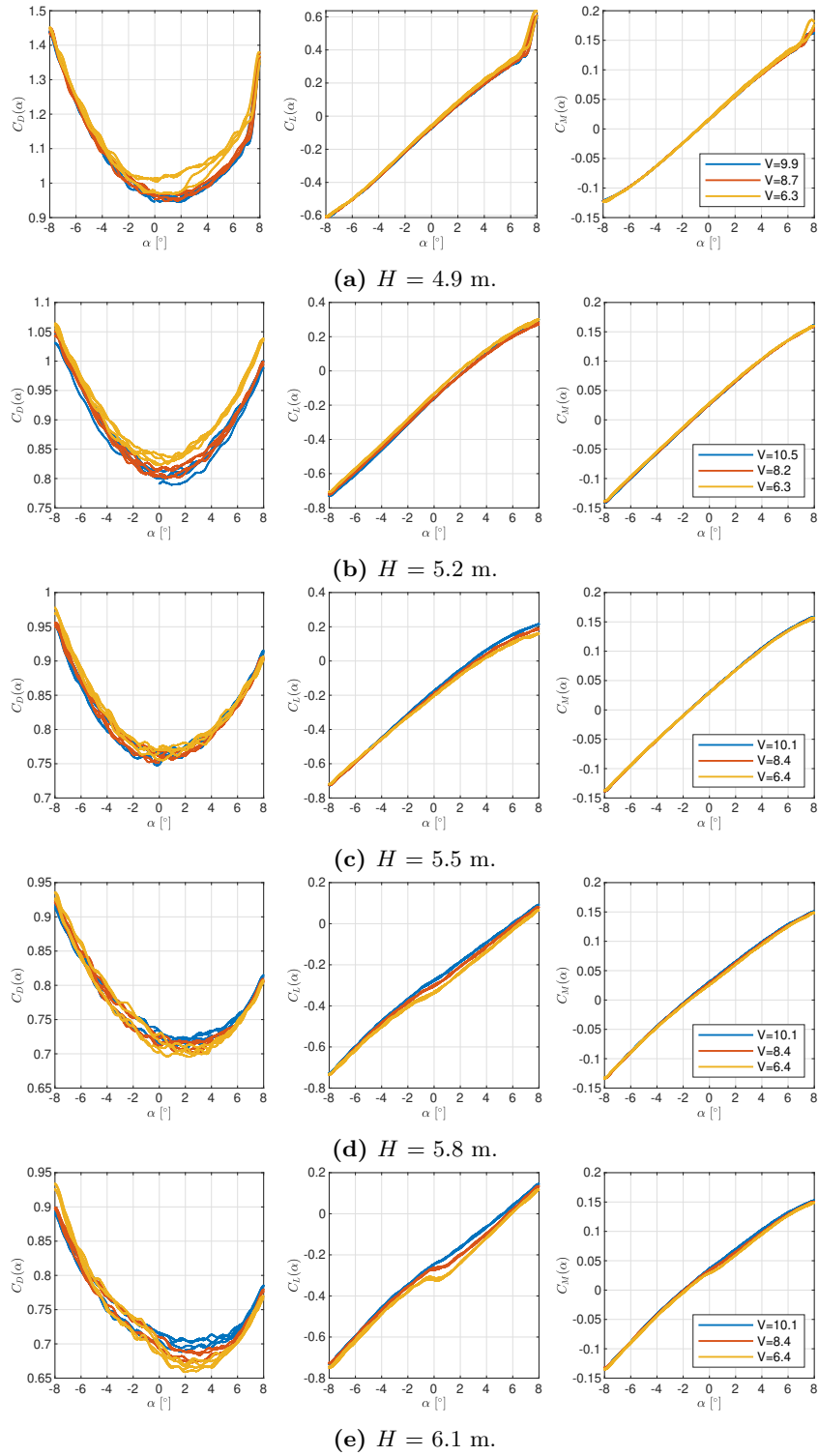
(a) $H = 4.9$ m.

(b) $H = 5.2$ m.

(c) $H = 5.5$ m.

(d) $H = 5.8$ m.

(e) $H = 6.1$ m.

Figure 6.2: Static coefficients measured at three different wind speeds for the cross-sections parameterized with $I_T = 26$ m^4.
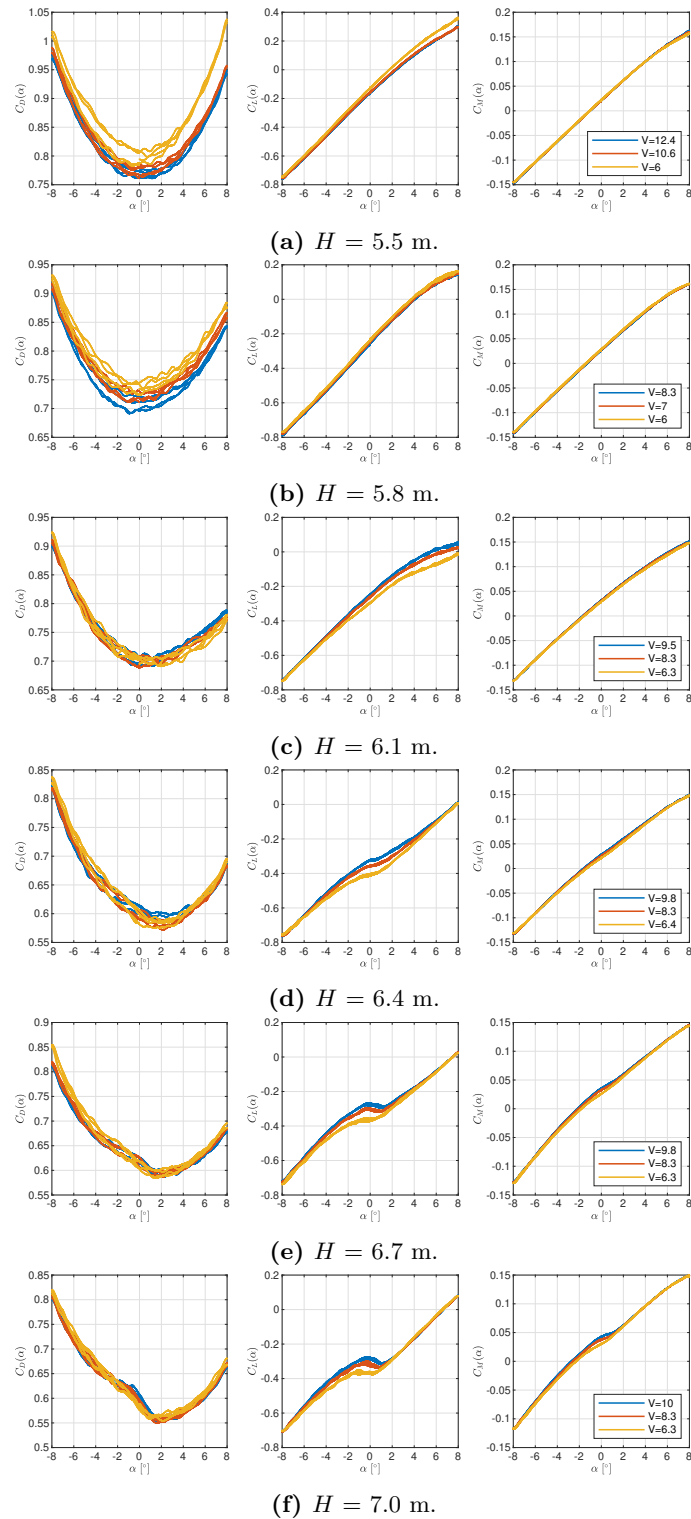
(a) $H = 5.5$ m.

(b) $H = 5.8$ m.

(c) $H = 6.1$ m.

(d) $H = 6.4$ m.

(e) $H = 6.7$ m.

(f) $H = 7.0$ m.

Figure 6.3: Static coefficients measured at three different wind speeds for the cross-sections parameterized with $I_T = 31$ m^4.

was changed from upwards to downwards; thus, the direction of the lift force changed to act upwards, defined as positive lift [97–99].

The static coefficients used in the analyses were extracted for $\alpha = 0$. The drag coefficients decreased for taller girders, varying from 0.95 to 0.59. In general, the lift coefficients became more negative for taller girders, from -0.16 to -0.34. C_M was slightly above zero for all sections, varying from 0.01 to 0.04.

Some differences for different wind velocities were observed, which implied a dependency on Reynolds number. This was most clear for C_D, where the parabolic shapes showed shifts for different wind velocities. The dependency on Reynolds number meant that results from the wind tunnel tests could not be scaled up to higher velocities without introducing uncertainty. Differences were also observed for C_L and C_M of taller section models, where minor discrepancies were seen when α was close to zero degrees.

6.3   Aerodynamic derivatives

The harmonic tests displayed in Figure 5.6 resulted in 16 data points of all 18 ADs for each cross-section. These data points are plotted against its reduced frequency K in Appendix E. For each of the ADs, a third-degree polynomial was fitted to the data points. The polynomials are also plotted in the figures. Outside the area of experimental observations, the polynomials were constrained to a constant value. This limitation was applied to avoid prediction of the ADs in areas where no data points had been observed.

The fitted polynomials of both parameterizations were plotted against each other to illustrate how the ADs varied between cross-sections. This is shown in Figures 6.4 and 6.5 for the cross-sections with $I_T = 26$ m^4 and $I_T = 31$ m^4, respectively.

The shape of the polynomial functions of A_1^*, identified as the most critical AD regarding coupled flutter, changed as the height increased. The polynomials were almost linear or downward-sloping parabolas for the lower girder heights. Higher girders had upward-sloping parabolic functions of A_1^*. This tendency was visible for both parameterizations. Despite these differences, the values of A_1^* were similar for all cross-sections when K was larger than 0.5.

Changes in the polynomial shapes were also observed for H_3^*. The polynomials were linear or slightly upward-sloping parabolic functions for the lower girders, while the functions were downward-sloping parabolas for higher girders. This was seen for girder heights equal to 6.4 - 7.0 m with $I_T = 31$ m^4, and for heights 5.8 - 6.1 m with $I_T = 26$ m^4. This type of development, where the shape of the polynomial changed for higher girders, was visible for other ADs as well, including the other critical ADs; A_2^*, A_3^* and H_1^*.

H_1^* was negative for all girder heights with a torsion constant $I_T = 26$ m^4. The only exception was $H = 6.1$ m for low values of K, where H_1^* was slightly positive. A change in the polynomial shape of $H = 5.8$ - 6.1 m was observed. This change was also present for the taller cross-sections with $I_T = 31$ m^4, but
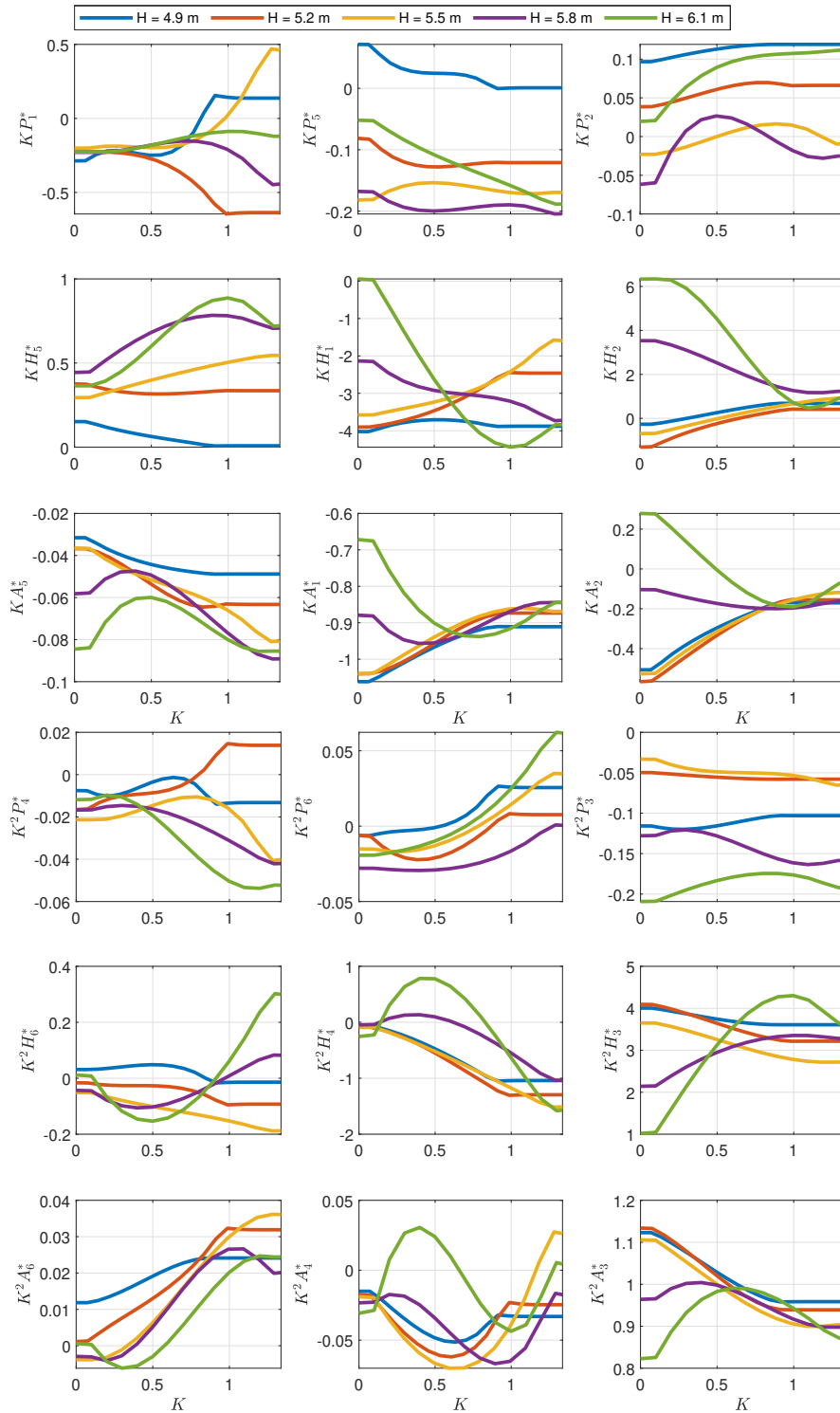
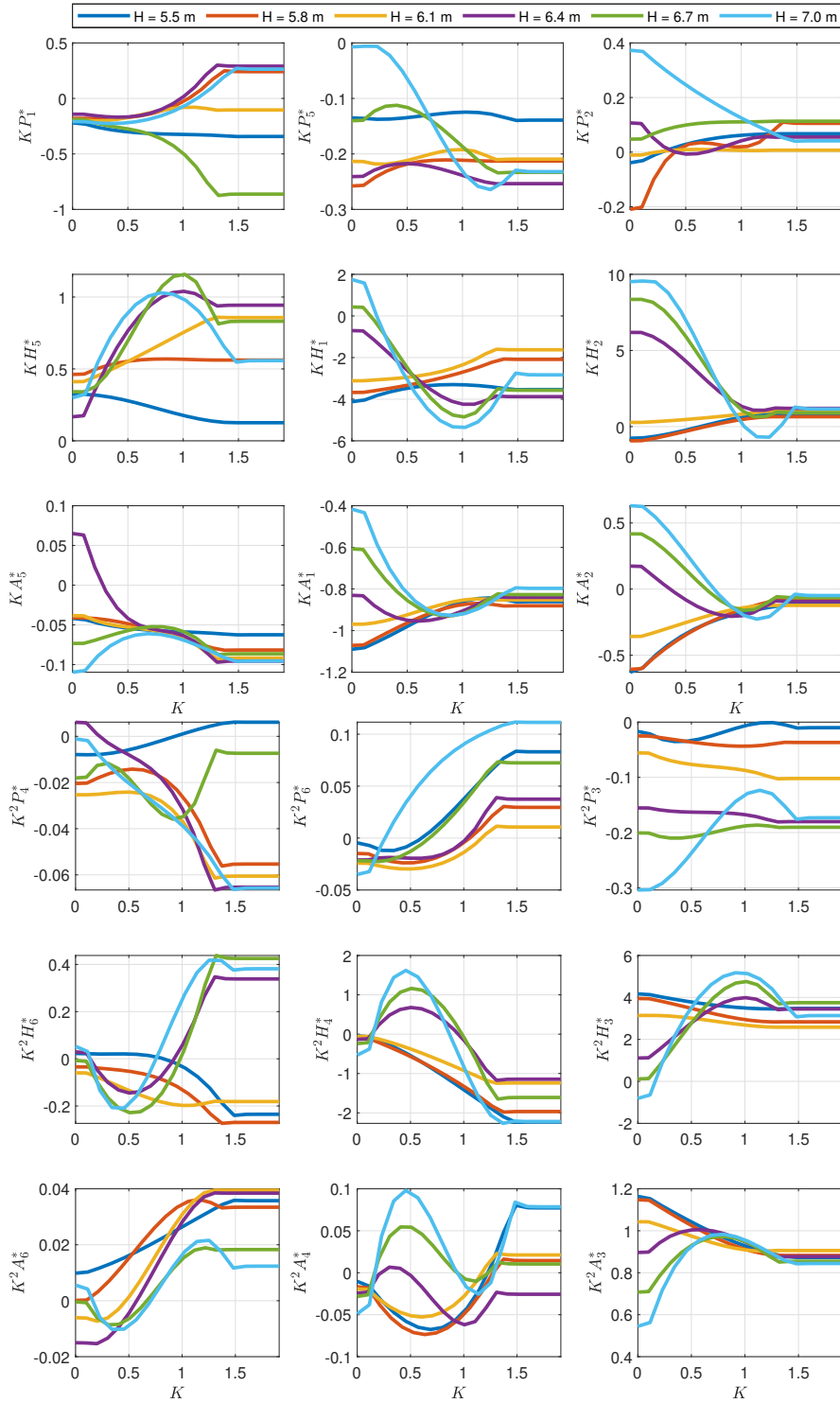**Figure 6.4:** Comparison of ADs of the cross-sections parameterized with $I_T = 26$ m^4.

Figure 6.5: Comparison of ADs of the cross-sections parameterized with $I_T = 31$ m^4.

the values differed compared to the values of the cross-sections with $I_T = 26$ m^4. For $H = 6.7$ - 7.0 m, H_1^* attained larger positive values for low reduced frequencies. Galloping occurs for $H_1^* > 0$ only, meaning that galloping might occur for these cross-sections. Compared to the results from 2020, the positive values of H_1^* were reduced for the cross-sections with $H = 6.7$ and 7.0 m.

The results of A_2^* were similar to the results of H_1^*. A_2^* was positive for $H = 6.4$ - 7.0 m with $I_T = 31$ m^4 when K was low. It was also positive for $H = 6.1$ m with $I_T = 26$ m^4 for low reduced frequencies. Positive values of A_2^* is destabilizing regarding coupled flutter stability, and dynamic instability in torsion can only occur for positive A_2^*-values.

A_1^*, A_3^* and H_3^* have either stabilizing or destabilizing effects on flutter stability depending on their absolute values. The fitted polynomials of all ADs are plotted in Appendix F along with the ADs given by Theodorsen for flat plates as a comparison to what can be regarded as high or low absolute values. For A_1^*, the polynomials obtained from wind tunnel testing attained lower absolute values than A_1^* given by Theodorsen for all section models. The AD polynomials had therefore a more stabilizing effect than the one provided for flat plates. The same results were observed for A_3^* and H_3^*, although not for the entire range of reduced frequencies. For $K \approx 1$, the polynomials of A_3^* and H_3^* for all section models attained values similar to, or above the ones given by Teodorsen. However, for lower reduced frequencies, the polynomials obtained from wind tunnel testing had lower absolute values than Theodorsen ADs, and therefore a more stabilizing effect.

From the plots in Appendix E, it is seen that there was a larger amount of scatter in the obtained data points related to drag (P_1^* - P_6^*) than for the heaving (H_1^* - H_6^*) and torsional (A_1^* - A_6^*) derivatives. This was likely because ADs only capture linear contributions. Drag coefficients were not linear functions, which can be observed for the static drag coefficients in Figures 6.2 and 6.3. Since the lift and moment coefficients had a more linear tendency, the corresponding ADs' scatter was less than for drag. The critical ADs, A_1^*-A_3^*, H_1^* and H_3^* had only small amounts of scatter. Other than for the coefficients related to drag, the polynomials captured the trend of the obtained data. Therefore, it was believed that the fitted polynomials represented the behaviour of the critical ADs well in the range where data points were gathered.

For some of the drag derivatives, the trend of the measured data developed differently at different wind velocities. This has also been observed previously [1, 100], and implied a dependency on Reynolds number, which caused uncertainty in the results due to the same scaling effect mentioned in Section 6.2.

6.4 Gaussian process regression

GPR was implemented on the ADs with height H and reduced frequency K as varying parameters. The squared exponential function was used as the covariance function. This read

$$K\left(\begin{bmatrix} \Delta K \\ \Delta H \end{bmatrix}\right) = \sigma_p^2 \cdot \exp\left(-\frac{1}{2}\begin{bmatrix} \Delta K \\ \Delta H \end{bmatrix}^T \begin{bmatrix} L_1^{-2} & 0 \\ 0 & L_2^{-2} \end{bmatrix} \begin{bmatrix} \Delta K \\ \Delta H \end{bmatrix}\right) + \sigma_n^2, \quad (6.1)$$

where $\theta = \begin{bmatrix} \sigma_p & L_1 & L_2 & \sigma_n \end{bmatrix}$ are hyperparameters.

Initially, the upper bound of all hyperparameters was set to 10, while the lower bound of all hyperparameters was set to 0. Some ADs experienced large amount of scatter, the most prevalent being P_1^* for both parameterizations. The predicted surfaces of this AD were dominated by local relations between nearby points, due to L_1 being low. To prevent the local relations from being too dominant, the lower bound of L_1 was changed to 0.1 for all cross-sections. Thus, the lower and upper bound were $\theta_{lb} = \begin{bmatrix} 0 & 0.1 & 0 & 0 \end{bmatrix}$ and $\theta_{ub} = \begin{bmatrix} 10 & 10 & 10 & 10 \end{bmatrix}$, respectively. The hyperparameters were trained to best fit the data by maximizing the log-likelihood. All hyperparameters calculated in the GPR are listed in Appendix G.

The predicted surfaces and the prediction uncertainties were plotted for both parameterizations. For the cross-section with $I_T = 26$ m^4, Figures 6.6 and 6.7 show the predicted surfaces and the prediction uncertainties, respectively. For the cross-section with $I_T = 31$ m^4, Figures 6.8 and 6.9 show the predicted surfaces and the prediction uncertainties, respectively. The z-axes of the uncertainty plots are labelled by the AD the uncertainty belongs to.

Most of the predicted surfaces were smooth. Least smooth were the surfaces predicted for P_1^*, where local relations dominated. This was reflected by L_1, which, as seen in Tables G.1 and G.2, attained the lowest values for P_1^*. The prediction uncertainties of P_1^* were affected by the low values of L_1, as they varied noticeably between heights with and without data.

Disregarding P_1^*, the prediction uncertainty of all ADs was most prominent in the region where H was small and K was large, for the cross-sections with $I_T = 26$ m^4. The reason became clear when studying the data points in Figure 6.6. There were no data points in that region. GPR is effective in interpolation even when the data points are sparse, just as it was in the region where both H and K are large. However, in extrapolation, the predictive power deteriorates.

The same effect was seen for the cross-sections with $I_T = 31$ m^4. In Figure 6.8, data points for the largest values of K were situated at the lowest and tallest heights. In many cases, this resulted in larger uncertainties for large values of K and heights from 6.0 - 6.5 m. This can for example be seen for H_2^* in Figure 6.9. However, the area with no data points was less prevalent than for the cross-sections with $I_T = 26$ m^4. Thus, if the predicted surface did not

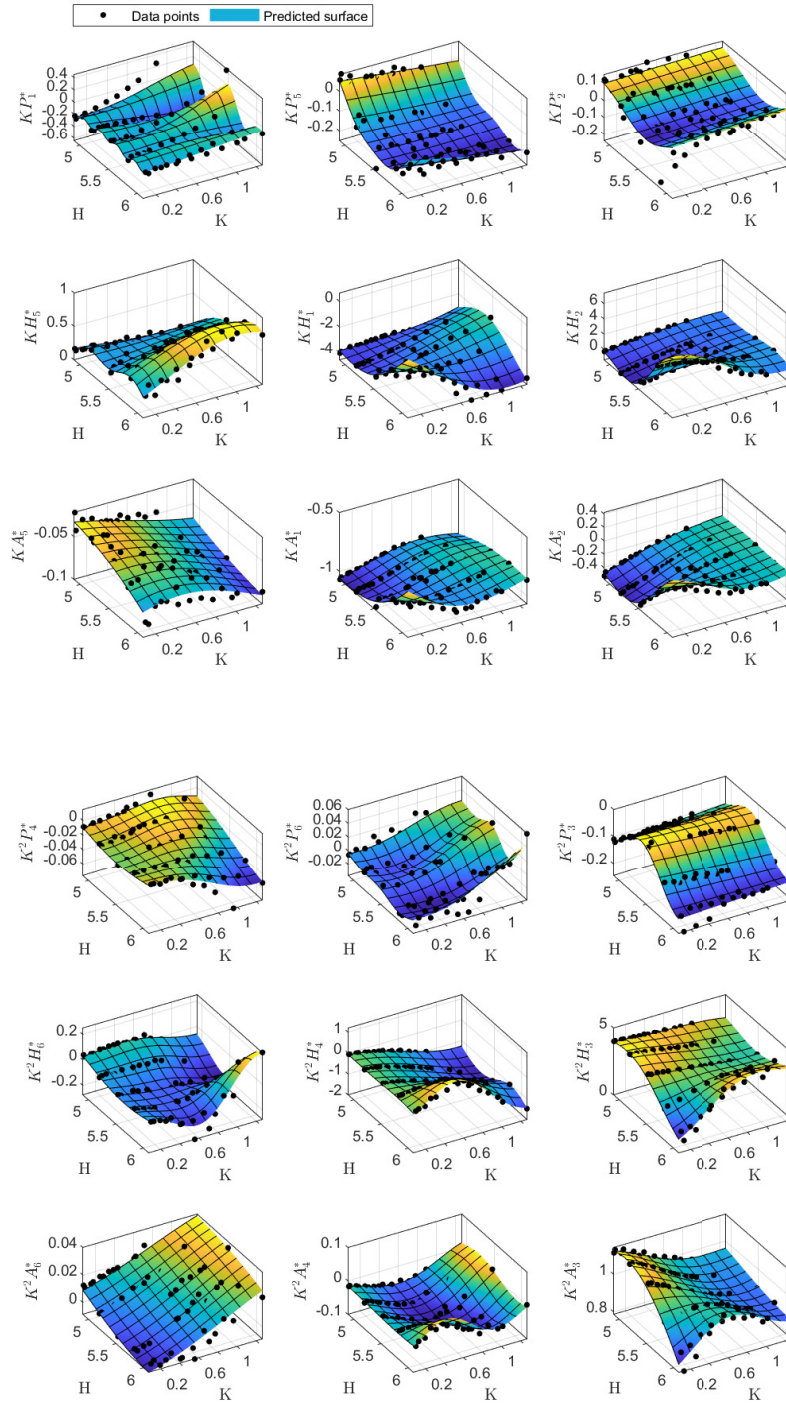**Figure 6.6:** Surface predicted by GPR of the measurement points from the AD analysis of the cross-section with $I_T = 26$ m^4.
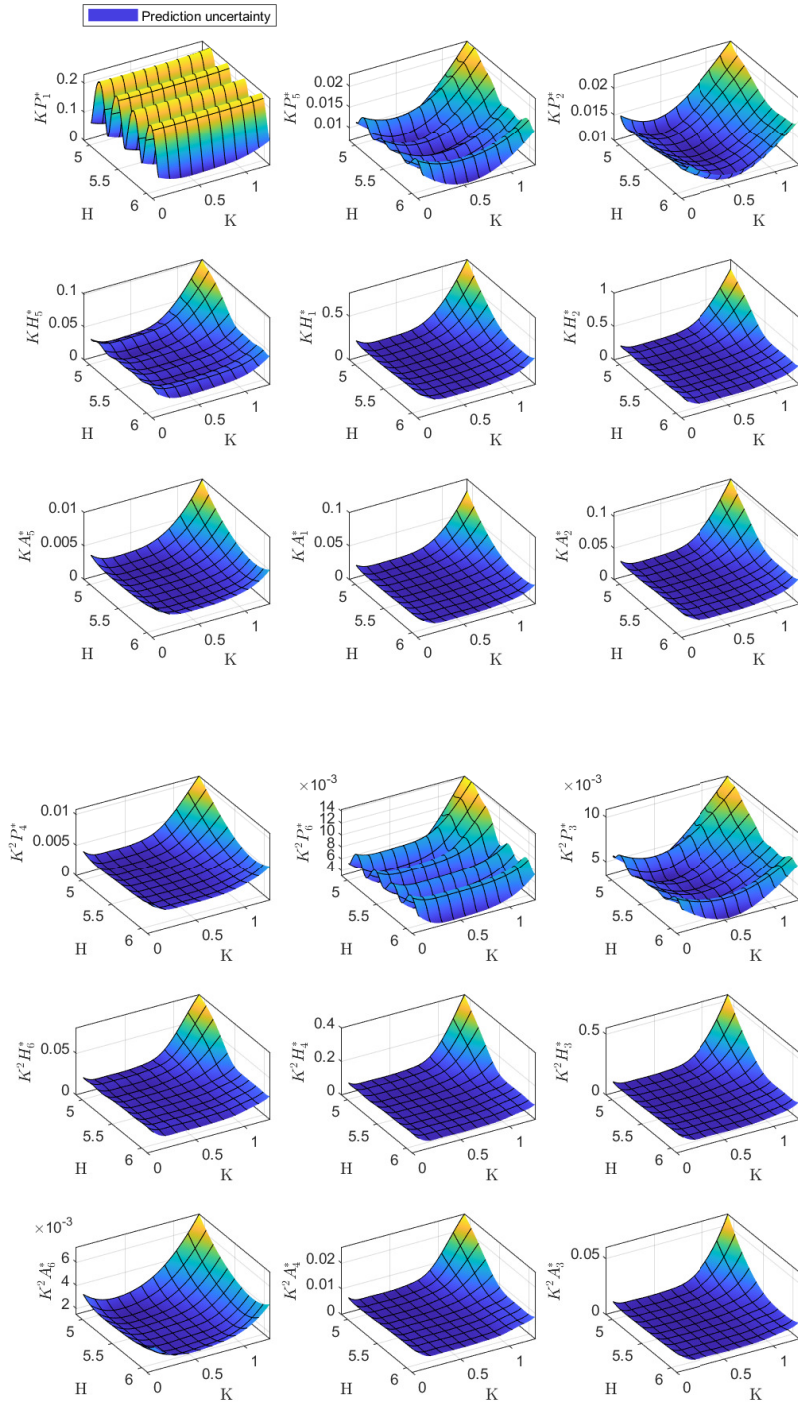
Figure 6.7: Prediction uncertainty by GPR of the predicted surface from the ADs of the cross-section with $I_T = 26$ m^4. The label on the z-axis indicate which AD the prediction uncertainty belongs to.
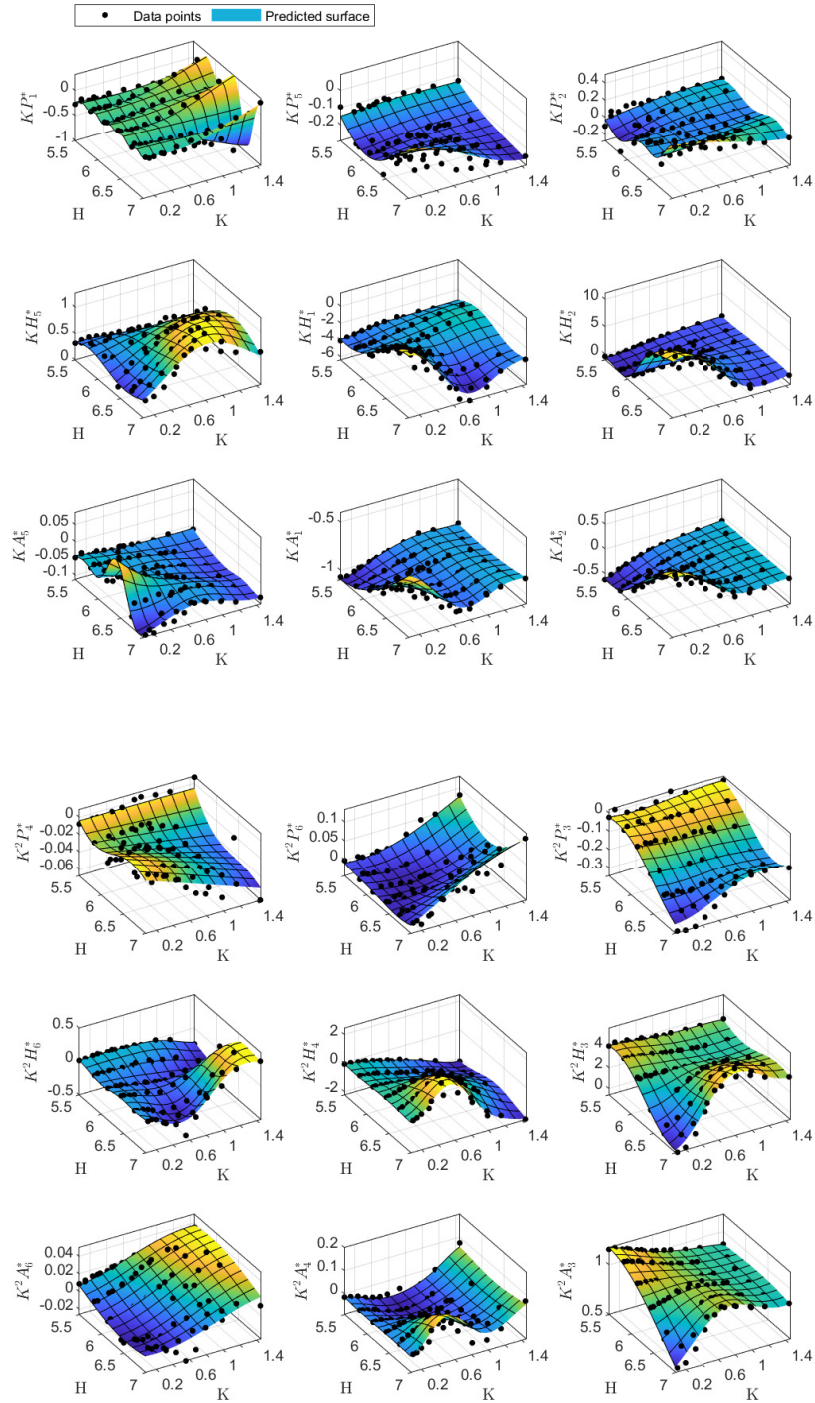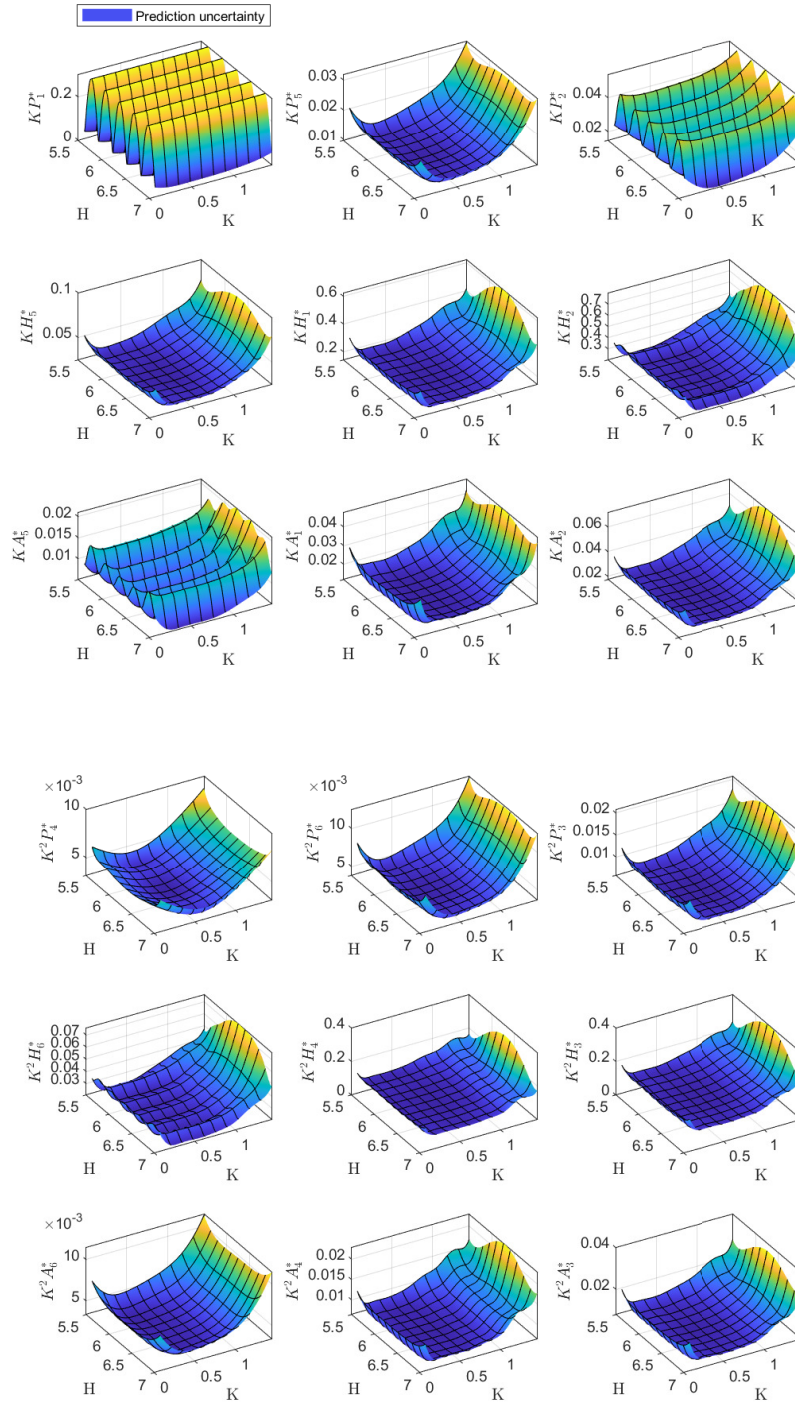
Figure 6.8: Surface predicted by GPR of the measurement points from the AD analysis of the cross-section with $I_T = 31$ m^4.

Figure 6.9: Prediction uncertainty by GPR of the predicted surface from the ADs of the cross-section with $I_T = 31$ m^4. The label on the z-axis indicate which AD the prediction uncertainty belongs to.

capture local relations well, as for P_4^*, the uncertainty would not necessarily follow this trend.

Prediction of ADs allow for stability calculations of cross-sections without performing wind tunnel tests. Estimated ADs can be extracted for any desired height in the range of tested heights. This can also be done for the static coefficients by predicting their behaviour in a similar manner. Thus, after a FEA, all inputs needed for flutter and buffeting analyses are known. Doing a flutter analysis with the predicted ADs for new cross-sections, followed by wind tunnel testing of corresponding section models, will serve as the best test of the quality of the results from the GPR. This was not in the scope of this thesis; thus, the quality of the surfaces predicted by GPR is discussed based on the smoothness of surfaces and the prediction uncertainty.

The ADs were predicted satisfactorily, considering the smoothness of the predicted surface and the low prediction uncertainty. For most ADs, both global and local relations were well preserved. ADs related to drag experienced dependency on Reynolds number to a greater extent than those related to heaving and torsion. This influenced the predicted surfaces, which, in some cases, could not retain both global and local relations as well.

6.5   Stability limits

The results from the wind tunnel tests and the FEA were used to calculate critical wind velocities V_{cr} for each cross-section. Calculations were performed with the complex flutter analysis. Several mode combinations were tested; the 50 first modes, the first 15 of the most relevant modes, and different combinations of symmetric and asymmetric mode shapes. Critical wind velocity of each mode combination for all cross-sections is listed in Appendix H. The mode combination with the lowest critical wind velocity for each cross-section is listed in Table 6.2.

It is seen that all section models fulfilled the design criterion $V_{cr,d} = 76$ m/s for critical wind velocity. The calculations also showed that the critical mode combination was the same for all cross-sections; the three first symmetrical vertical mode shapes, along with the first symmetrical torsional mode shape.

The tables in Appendix H show that the mode combinations which included the first 50 still-air modes resulted in critical wind velocities lower than the values listed in Table 6.2, for all cross-sections. The reason for ignoring these results when deciding the critical wind velocities was uncertainty related to these results. As mentioned in Section 4.2, tie constraints were applied between the connection elements and the hanger elements. Thus, no rotation was allowed between these elements. Some rotation would have been more realistic. Therefore, mode shapes that included large excitations in cables and hangers might have led to unrealistic contributions in the stability calculations. However, most of the sections passed the critical wind velocity design criterion of 76 m/s even with the 50 first modes included. The exceptions were

Table 6.2: Critical wind velocities of the critical mode combination for all cross-sections.

I_T [m^4]	H [m]	Mode combination	Critical wind velocity V_{cr} [m/s]
26	4.9	1-3VS, 1TS	90.56
	5.2	1-3VS, 1TS	85.30
	5.5	1-3VS, 1TS	91.69
	5.8	1-3VS, 1TS	92.98
	6.1	1-3VS, 1TS	85.65
31	5.5	1-3VS, 1TS	86.98
	5.8	1-3VS, 1TS	88.27
	6.1	1-3VS, 1TS	90.17
	6.4	1-3VS, 1TS	90.34
	6.7	1-3VS, 1TS	81.06
	7.0	1-3VS, 1TS	82.04

$H = 5.5$ m with $I_T = 26$ m^4 and $H = 7.0$ m with $I_T = 31$ m^4. For the latter model, the complex critical mode when combining all still-air modes was dominated by large cable excitation in the side-spans and was therefore not relevant for the global response of the bridge girder.

For the section model with $H = 5.5$ m and $I_T = 26$ m^4, the mode combinations with the first 50 modes and the first 15 most relevant modes showed considerably lower stability limits than the other combinations. For these mode combinations, the critical mode was dominated by the second symmetric horizontal mode. This was believed to have been caused by the polynomials fitted to the drag-related ADs. The reduced frequencies corresponding to these wind velocities were outside the range of obtained data. The uncertainty in these results was therefore considerably increased. This was the main reason for excluding these combinations when determining the critical mode combination. Additional uncertainty was related to the scatter in data points and the possible dependency on Reynolds number mentioned in Section 6.3. Due to the considerable uncertainty related to these critical wind velocities and the fact that the results deviated heavily from the other cross-sections, it was decided that they were not relevant for the assessment of stability limits.

Critical in-wind eigenfrequency ω_{cr}, critical reduced wind velocity $V_{cr,red}$ and critical reduced frequency K_{cr} of all cross-sections are presented in Table 6.3. The values showed that the calculated critical wind velocities corresponded to reduced frequencies which were within the range of obtained data.

Knowing the reduced frequencies of the calculated critical velocities resulted in an easier comparison of the results between different girders. Approximate values of the ADs taken from Figures 6.4 and 6.5 were used to explain differences and similarities in the results. Similarities of the critical wind ve-

Table 6.3: Critical in-wind eigenfrequency, critical reduced velocity and critical reduced frequency of all cross-sections.

I_T [m^4]	H [m]	ω_{cr} [rad/s]	$V_{cr,red}$	K_{cr}
26	4.9	2.31	1.12	0.89
	5.2	2.23	1.09	0.92
	5.5	2.19	1.18	0.85
	5.8	2.21	1.18	0.85
	6.1	2.28	1.05	0.95
31	5.5	2.24	1.10	0.91
	5.8	2.22	1.12	0.89
	6.1	2.22	1.13	0.88
	6.4	2.24	1.12	0.89
	6.7	2.33	0.96	1.04
	7.0	2.34	0.96	1.04

(a) $I_T = 26$ m^4. **(b)** $I_T = 31$ m^4.
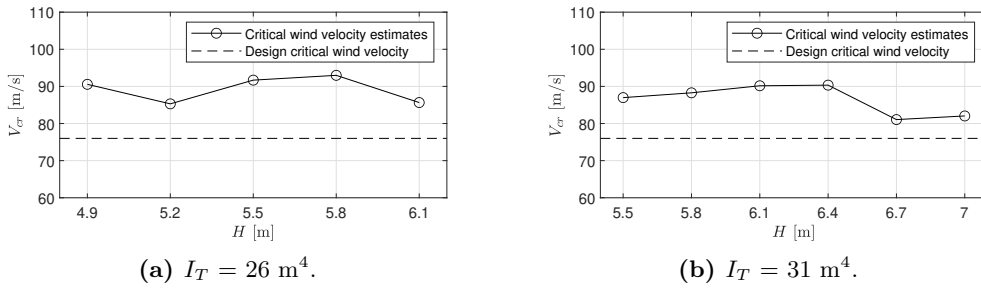
Figure 6.10: Estimated critical wind velocity of all cross-sections compared with the design critical wind velocity of $V_{cr,d} = 76$ m/s. The line between estimated points is not to be interpreted as an interpolation.

locities could partly be explained by investigating A_1^*, identified as the most critical AD regarding coupled flutter instability. The plots of A_1^* showed only minor variations between the cross-sections for relevant reduced frequencies. The same was seen for A_2^* and A_3^*. Larger differences were observed for the critical ADs related to heaving. These ADs were therefore more likely to explain differences between cross-sections than the torsional derivatives.

It was observed that the highest critical wind velocities were found for the cross-sections with $I_T = 26$ m^4. The explanation is likely to be the mentioned differences in aerodynamic derivatives, and therefore slightly better aerodynamic properties for the cross-sections with $I_T = 26$ m^4. The differences between critical wind velocities were however small.

The critical wind velocities listed in Table 6.2 were above the design critical wind velocity $V_{cr,d} = 76$ m/s. This is plotted in Figure 6.10 for both parameterizations. The line between estimated critical wind velocities indicates the development of the critical wind velocity and is not to be interpreted
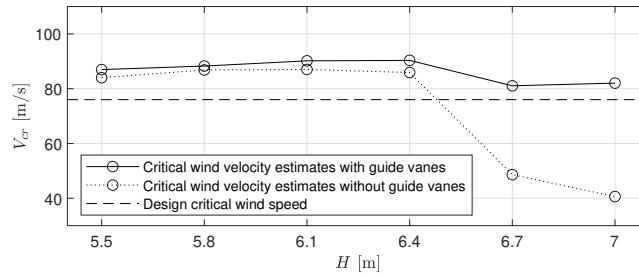
Figure 6.11: Comparison of stability limits for the cross-sections with I_T = 31 m^4, with and without guide vanes. Tests without guide vanes were performed in 2020 [1] and tests with guide vanes were performed for this thesis. The line between estimated points is not to be interpreted as an interpolation.

as an interpolation. The trend was slightly increasing until a certain height, where the critical wind velocity estimate decreased. This happened at $H = 6.1$ m and $H = 6.7$ m for the cross-sections with $I_T = 26$ m^4 and $I_T = 31$ m^4, respectively. The exception from this trend was $H = 5.2$ m with $I_T = 26$ m^4. This cross-section had an estimated critical wind velocity which was 94.2% and 93.0% of that of the cross-sections with $H = 4.9$ m and $H = 5.5$ m, respectively.

The critical wind velocity estimates of the cross-sections with $I_T = 31$ m^4 were compared with estimates from the previous study [1]. This is shown in Figure 6.11. For the four lower cross-sections, the critical wind velocity estimates were slightly larger when the cross-sections were tested with guide vanes. The cross-sections with guide vanes had an estimated critical wind velocity that was 1.7 - 5.2% larger than those without guide vanes. This may indicate that the guide vanes had a small contribution to the flutter stability. However, the finite element models used when estimating the critical wind velocity had minor differences compared to the models used in 2020. Thus, conclusions of the influence of guide vanes on flutter stability for these cross-sections can not be deduced.

Cross-sections with $H = 6.7$ and $H = 7.0$ m had an increase in estimated critical wind velocity of 67% and 102%, respectively. It is not likely that these large increases can be explained by the relatively small changes applied to the finite element models. Without guide vanes, the motion instability was galloping while it was multi-modal flutter with guide vanes. The guide vanes successfully managed to prevent the separation of wind flow from causing transverse forces on the section models large enough to cause galloping. This changed the critical motion instability to multi-modal flutter, which had an estimated critical wind velocity above the design critical wind velocity. The result was that all girders with $I_T = 31$ m^4 passed the critical wind velocity criterion.

Figures 6.12 and 6.13 show Argand diagrams for the instability modes of cross-sections with $I_T = 26$ m^4 and $I_T = 31$ m^4, respectively. The diagrams

(a) $H = 4.9$ m.
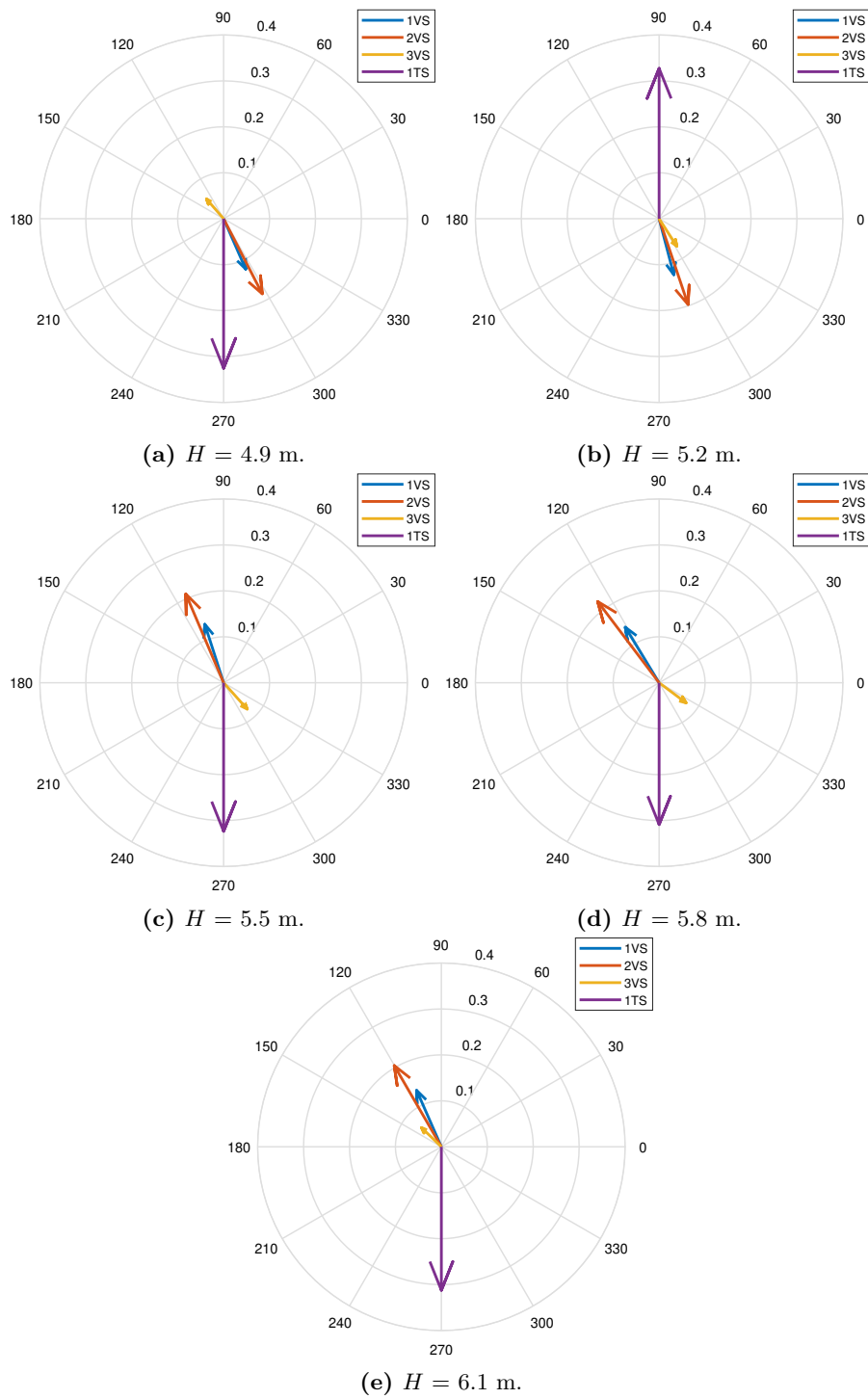
(b) $H = 5.2$ m.

(c) $H = 5.5$ m.

(d) $H = 5.8$ m.

(e) $H = 6.1$ m.

Figure 6.12: Argand diagrams of instability modes of the cross-sections parameterized with $I_T = 26$ m^4.

(a) $H = 5.5$ m.

(b) $H = 5.8$ m.

(c) $H = 6.1$ m.

(d) $H = 6.4$ m.

(e) $H = 6.7$ m.

(f) $H = 7.0$ m.
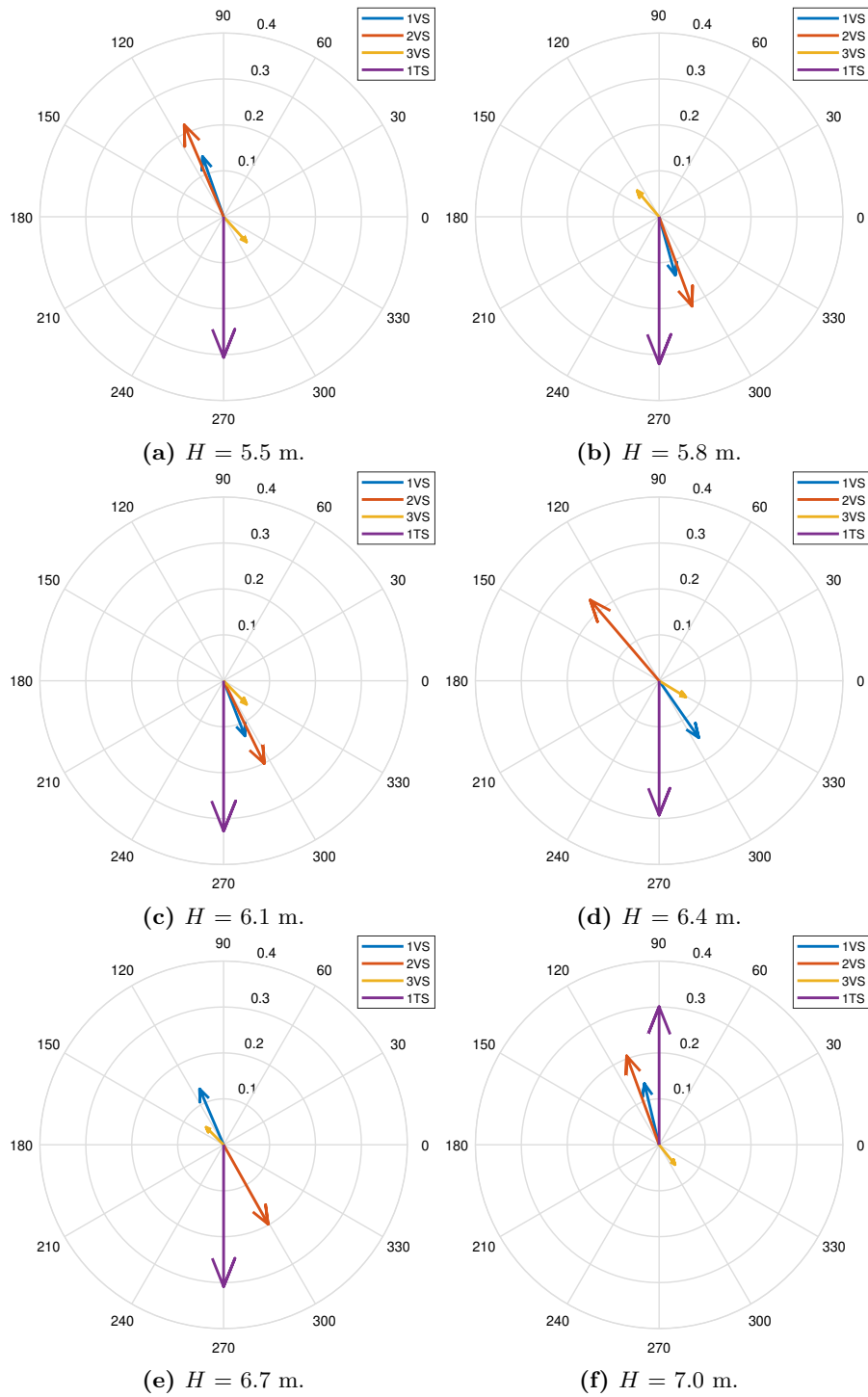
Figure 6.13: Argand diagrams of instability modes of the cross-sections parameterized with $I_T = 31$ m^4.

(a) $I_T = 26$ m^4. **(b)** $I_T = 31$ m^4.
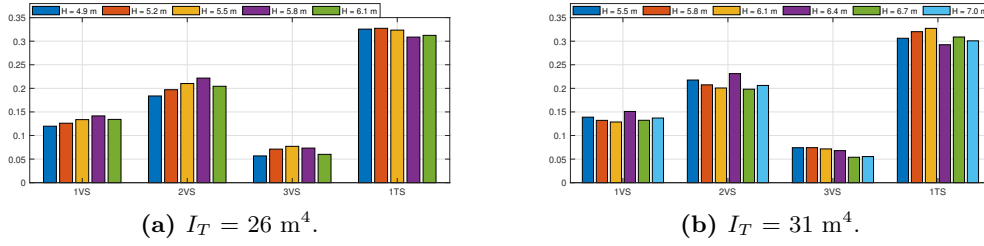
Figure 6.14: Bar diagrams visualizing the contributions from the included still-air modes in the critical instability mode for all cross-sections.

show the contributions of the included still-air modes in the critical complex mode. The non-horizontal direction of the contributions in the diagrams shows that their values were complex. This was interpreted as shifts between the modes, causing complex modes where the deformation pattern was not fixed. The changing pattern occurs due to energy transfer between still-air modes [101].

The absolute values of the still-air mode contributions in the complex instability modes are shown as bar diagrams in Figure 6.14 for both parameterizations. The first symmetrical torsional mode and the second symmetrical vertical mode were the two modes that contributed the most to the instability modes. This is also visualized by the size of the arrows in the Argand diagrams. A greater contribution from the second vertical mode than the first vertical mode was also reported for the Hardanger Bridge [52].

To better understand the contributions from the still-air modes, the shapewise similarities of modes were checked for all cross-sections. The similarities of the first, second and third vertical symmetric modes to the first torsional symmetric mode were 0.39 - 0.40, 0.59 and 0.01 - 0.02, respectively. Thus, the second symmetric vertical mode is expected to contribute more in the flutter mode than the first and third. This complied with the results.

Figures 6.15 and 6.16 show the damped eigenfrequency and damping ratio of the different modes, for the cross-sections with $I_T = 26$ m^4 and $I_T = 31$ m^4, respectively. The legend entries in the plots were named based on the still-air mode that dominated the complex modes. They should not be interpreted as pure torsional or vertical modes since all the complex modes were affected by several still-air modes. Damping ratio equal to zero determined the critical mode. There are only small differences in the plots. This was expected, as the instability modes were multi-modal flutter with contributions from the same still-air modes for all cross-sections. However, for the tallest cross-sections, the damping ratio of the vertical modes started to decrease as the wind velocity increased. This was most visible for $H = 6.7$ - 7.0 m with $I_T = 31$ m^4, but was also observed for $H = 6.1$ m with $I_T = 26$ m^4. This was likely due to the already discussed differences for H_1^* between the cross-sections. A similar development of the damping ratio of vertical modes was observed in 2020 for

the cross-section with $H = 6.4$ m [1]. It was suggested that this indicated a transition from multi-modal flutter to galloping, since galloping was observed for the two tallest girders.
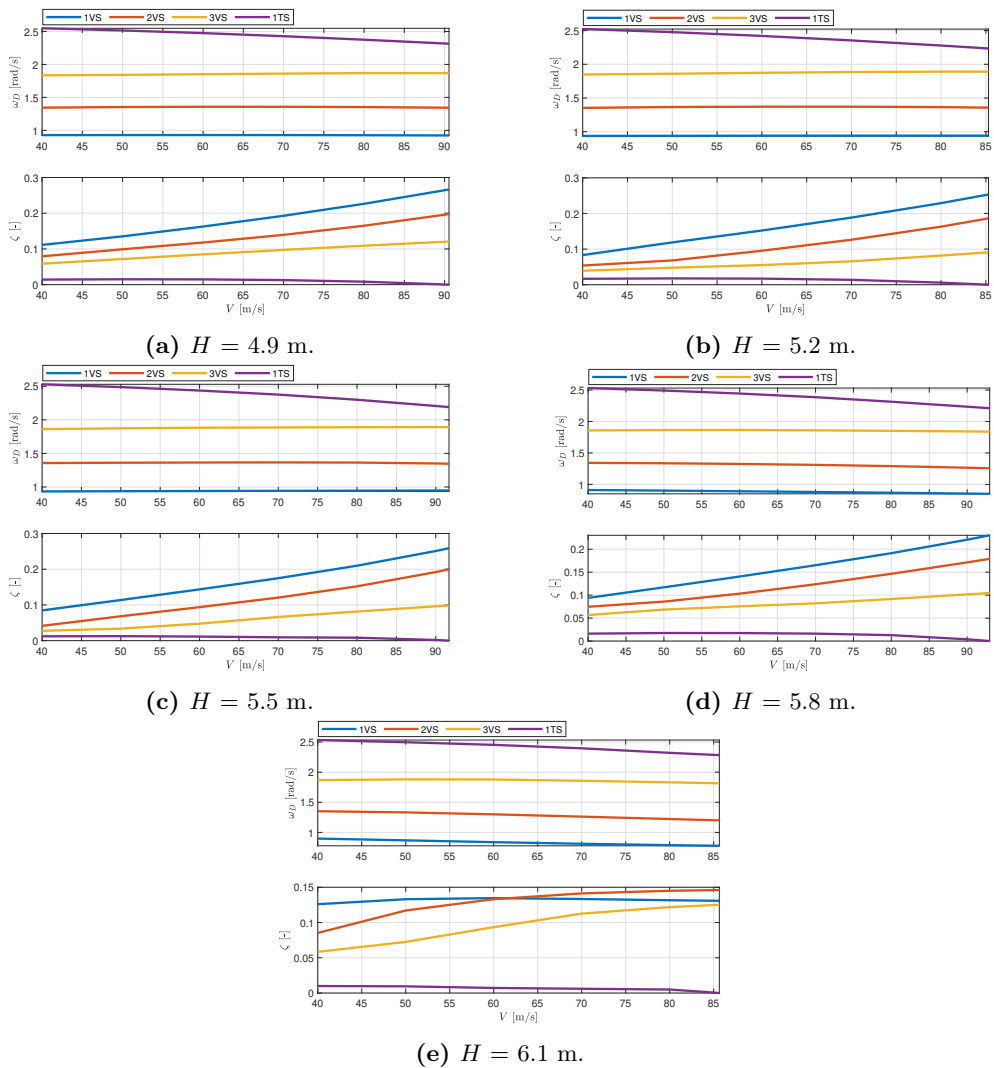

(a) $H = 4.9$ m.

(b) $H = 5.2$ m.

(c) $H = 5.5$ m.

(d) $H = 5.8$ m.

(e) $H = 6.1$ m.

Figure 6.15: Damping ratio and damped eigenfrequency for the cross-sections parameterized with $I_T = 26$ m^4.

(a) $H = 5.5$ m.

(b) $H = 5.8$ m.

(c) $H = 6.1$ m.

(d) $H = 6.4$ m.

(e) $H = 6.7$ m.

(f) $H = 7.0$ m.
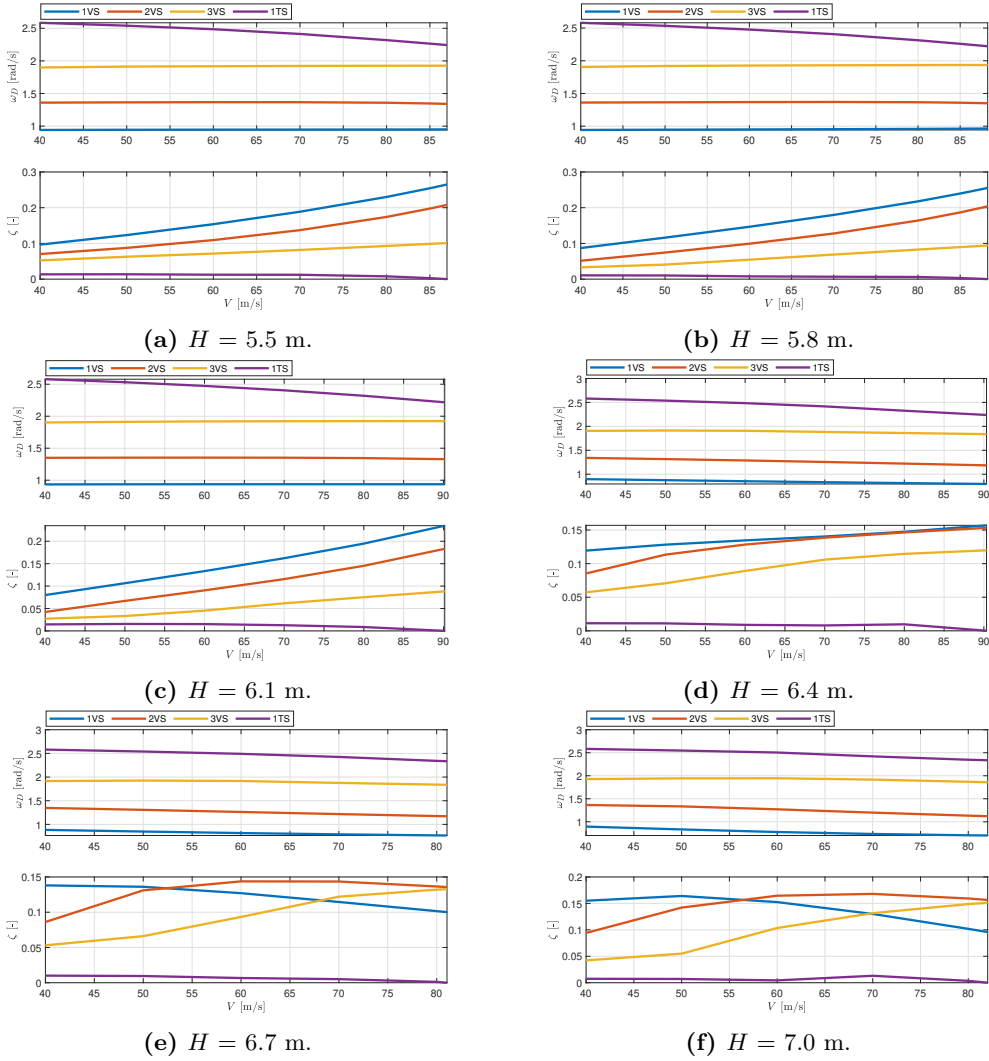
Figure 6.16: Damping ratio and eigenfrequency for the cross-sections parameterized with $I_T = 31$ m^4.

6.5.1 Closed-form solution

The same inputs used in the complex flutter analysis were used in the closed-form solution of the bi-modal flutter analysis. This included ADs and static coefficients from the wind tunnel tests and the results from the FEA.

The iteration process described for the closed-form solution was used, and the critical wind velocity was calculated by Equation 2.70. The tolerance level of two consecutive reduced frequencies was $\epsilon = 10^{-4}$. Critical wind velocities $V_{cr,cf}$ and corresponding critical reduced frequencies $K_{cr,cf}$ found with this method are listed in Table 6.4. A logical statement is listed, which indicates if $K_{cr,cf}$ was in the range of the observed data of K. Lastly, the critical wind

Table 6.4: The critical wind velocity $V_{cr,cf}$ calculated with the closed-form solution with modes 2VS and 1TS. The reduced frequency which corresponds to the critical wind velocity is listed as $K_{cr,cf}$. It is listed whether or not $K_{cr,cf}$ is in range of the reduced frequencies where there were observed data. Lastly, the critical wind velocity from the complex flutter analysis V_{cr} with modes 2VS and 1TS is listed for comparison.

I_T [m^4]	H [m]	$V_{cr,cf}$	$K_{cr,cf}$	In range	V_{cr}
26	4.9	91.66	0.99	False	113.23
	5.2	88.71	1.03	False	102.35
	5.5	94.74	0.97	True	106.57
	5.8	95.56	0.97	True	106.94
	6.1	86.00	1.08	True	100.52
31	5.5	90.66	1.04	True	100.26
	5.8	90.32	1.05	True	102.86
	6.1	92.58	1.03	True	104.13
	6.4	89.05	1.08	True	104.46
	6.7	65.11	1.48	False	92.82
	7.0	88.66	1.09	True	91.24

velocity from the complex flutter analysis V_{cr} is listed for comparison. The results correspond to the mode combination with the first symmetric torsional mode (1TS) and the second vertical symmetric mode (2VS). For all cross-sections, these modes had a shape-wise similarity of $\psi_{z\theta} = 0.59$.

If $K_{cr,cf}$ was not in range, the solution of the closed-form analysis had not converged in an area where data points described the AD functions. It had converged in the area where the functions were constrained to a constant value. This made uncertainties of these results too large for them to be considered as critical wind velocities. The two lowest cross-sections with $I_T = 26$ m^4 converged just outside the region of measured K, while the cross-section with $H = 6.7$ m and $I_T = 31$ m^4 converged further away from the measured reduced frequencies. Thus, uncertainties were larger for the latter, which was the only cross-section with a critical wind velocity from the closed-form solution below the design critical wind velocity.

For all cross-sections where the critical frequency was in range, $V_{cr,cf}$ was higher than the design critical wind velocity $V_{cr,d} = 76$ m/s. The critical wind velocity from the closed-form solution was lower than the critical wind velocity from the complex analysis V_{cr}. This was expected, as the torsion damping was neglected. The closed-form critical wind velocities were from 85.2% - 97.2% of the critical wind velocities from the complex flutter analyses.

The cross-section with $H = 6.1$ m and $I_T = 26$ m^4 had a critical wind velocity from the closed-form solution which was 9.2% and 10.0% lower than the critical wind velocities for the cross-section with $H = 5.5$ m and 5.8 m,

respectively. This was likely the result of a larger value of h_3 for the section with $H = 6.1$ m. The other parameters a_1, a_2 and a_3 were similar for all these cross-sections. The absolute value of Ω (Equation 2.71) was therefore larger for $H = 6.1$ m, resulting in a lower critical wind velocity. This effect of h_3 is in compliance with Table 2.1.

Results from the complex flutter analysis, both with the critical mode combination and with modes 2VS and 1TS, showed a decrease in critical wind velocity for the cross-section with $H = 5.2$ m and $I_T = 26$ m^4 compared to the two nearby cross-sections. The results from the closed-form solution complied with these results, as the cross-section had a critical wind velocity $V_{cr,cf}$ which was 96.8% and 93.6% of that of the cross-sections with $H = 4.9$ m and $H = 5.5$ m, respectively.

The three other bi-modal mode combinations analysed with the complex flutter analysis (Appendix H) were also analysed with the closed-form method. This resulted in critical wind velocities which were larger than for the mode combination with 2VS and 1TS.

6.6 Buffeting response

The buffeting response of the bridge deck was calculated by a method similar to the one described in N400 [16]. The single-point autospectra were calculated by Equation 2.27, which did not include the turbulence length scale. All the still-air modes from Abaqus were included in the calculations, and the mean wind velocity was set to 30 m/s, perpendicular to the length axis of the bridge.

The autospectral densities of each cross-section were studied in the lateral, vertical and torsional directions. This was done at three locations along the bridge; at the quarter-span ($\frac{x}{L} = 0.25$), at the half-span ($\frac{x}{L} = 0.50$) and at the three-quarter-span ($\frac{x}{L} = 0.75$). The correlation coefficients and autospectral density plots at these locations are shown in Appendix I. Figures 6.17 and 6.18 show the buffeting response at half-span for the cross-sections parameterized with $I_T = 26$ m^4 and $I_T = 31$ m^4, respectively.

The autospectral densities indicate frequencies that dominate the response. The peaks in the spectral densities can thus be related to the natural frequencies of the system, listed in Appendix B. Since Figures 6.17 and 6.18 show the spectral density at the half-span, the asymmetric mode shapes were expected not to be visible, as they have little to no excitation at this location. This complied with the autospectral densities.

All the natural frequencies related to symmetric motion from the tables in Appendix B were found as peaks in Figures 6.17 and 6.18. Some additional peaks were found in the spectra of lateral and torsional motion. The natural frequencies related to the symmetric lateral motion were found in the autospectrum for torsional motion and vice versa. The horizontal motion in torsional mode shapes was seen in the table and was therefore expected. Although not visible in the tables in Appendix B, closer evaluation of the mode
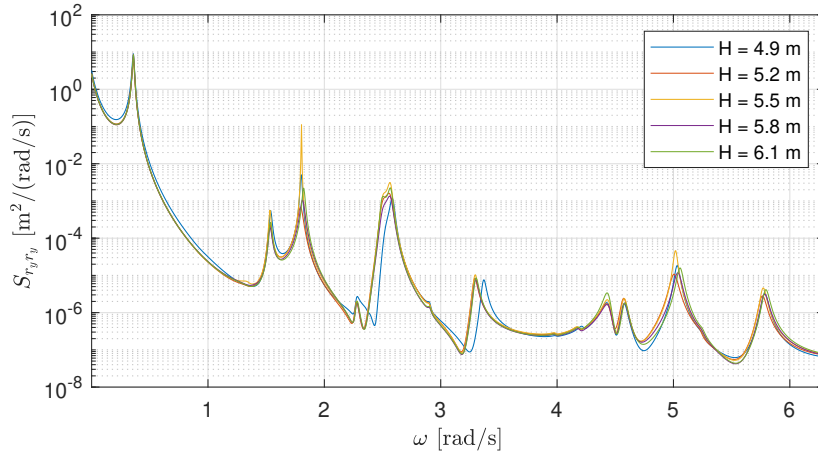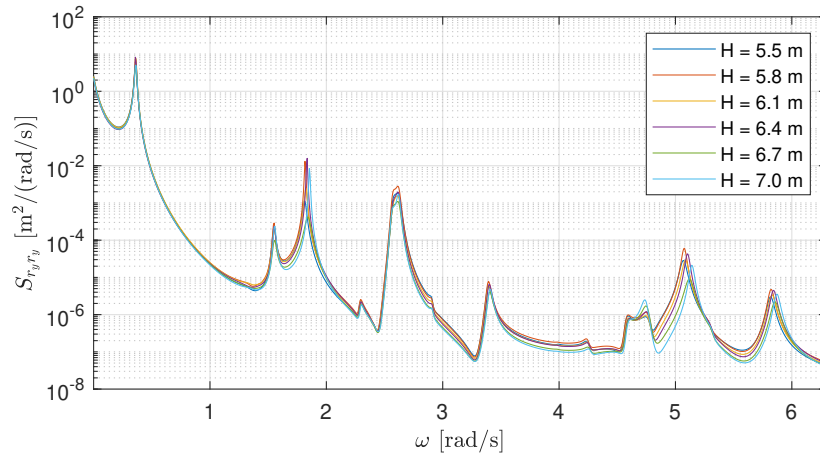
(a) Lateral direction.
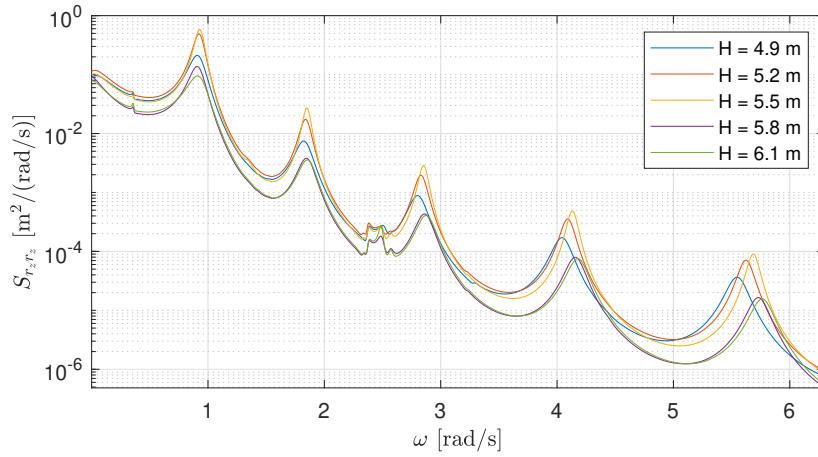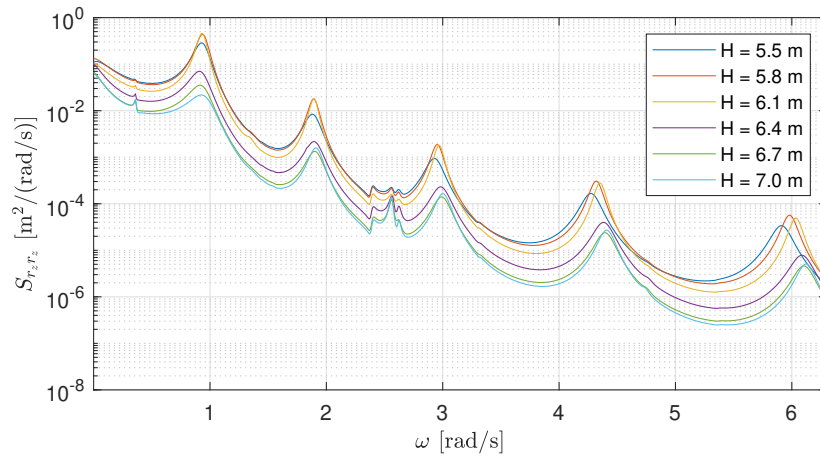

(b) Vertical direction.
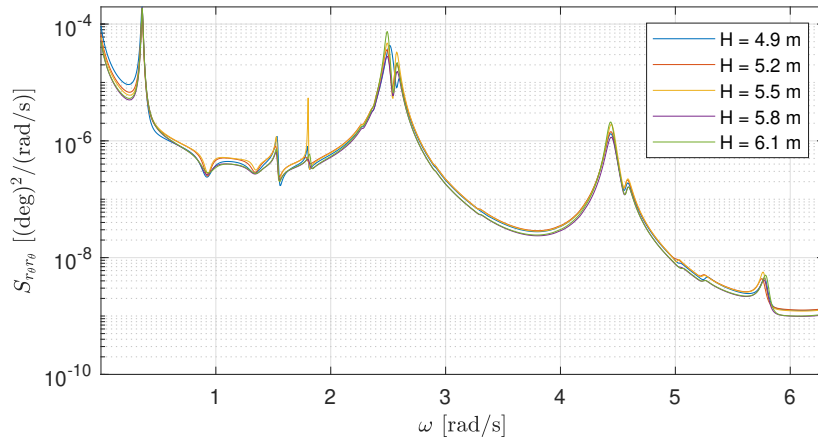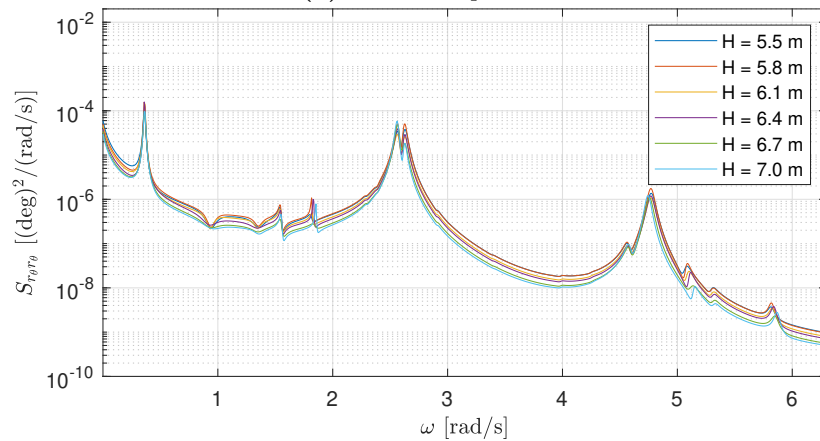

(c) Torsional direction.

Figure 6.17: Autospectral densities of the buffeting response in three directions at the half-span, for the cross-sections parameterized with $I_T = 26$ m^4.

(a) Lateral response.

(b) Vertical response.

(c) Torsional response

Figure 6.18: Autospectral densities of the buffeting response in three directions at the half-span, for the cross-sections parameterized with $I_T = 31$ m^4.

shapes revealed that the horizontal modes had a torsional contribution. The peaks at the lateral eigenfrequencies observed in the torsional spectra were therefore reasonable. At the frequency of mode 1TS (2.60 - 2.66 rad/s), two peaks were found in the autospectral densities of the torsional direction. This complied with observations from the FEA. As mentioned in Section 4.3, two modes with similar motion were found, where one had less excitation than the other, only separated by about 0.08 rad/s. This explained the two peaks. This was also the case at the frequency of mode 1TA, where two peaks are visible in the spectral density plots at the quarter-span and the three-quarter-span in Appendix I.

The peaks in the autospectra at the quarter-span and the three-quarter-span from Appendix I corresponded well to the natural frequencies and mode shapes from Appendix B. Most of the asymmetric mode shapes were visible as peaks in these plots. Exceptions were modes with little or no excitation at these locations, for example 2VA and 2HA. The mode 2HA had a natural frequency of about 3.37 rad/s. There were no peaks at this frequency in the spectral densities at the quarter-span and the three-quarter-span, as expected.

At all three locations, a peak was found in the autospectrum for both the lateral and torsional directions, at a frequency of about 1.53 rad/s. At the half-span, there was a peak at 3.29 rad/s in the lateral direction. Neither of these frequencies corresponded to any of the natural frequencies in Appendix B. Oscillation of the main cables, which led to excitation of the girder, was believed to cause these peaks. Such modes were found in the FEA but not included as the most relevant mode shapes for the global response of the girder.

The autospectral densities were similar for all cross-sections with the same parameterization. This was expected, since the differences in natural frequencies were small. Larger peaks in the autospectral density of the lateral response were observed for the cross-section with $H = 5.5$ m and $I_T = 26$ m^4 than for the other cross-sections. The reason for these observations was likely the polynomials fitted to the drag-related ADs, which also caused low stability limits when including horizontal mode shapes in the complex flutter analysis for this cross-section.

The differences of spectral densities within the same parameterization were most prominent in the vertical direction, as seen in Figures 6.17 and 6.18. Since the variance of the response is the integral of the spectral density, this difference was expected to be seen in the plots of the standard deviation of the displacement response.

The standard deviation of the displacement response in the lateral, vertical and torsional directions for both parameterizations are shown in Figure 6.19. Lateral displacement and torsional rotation had the largest standard deviation in the center of the bridge deck at $x = 0$, while the standard deviation in the vertical direction was largest for x close to the quarter- and three-quarter-spans. This was likely due to the lack of a symmetric vertical mode shape with only one half-wave. Thus, the first vertical mode shape has little contri-
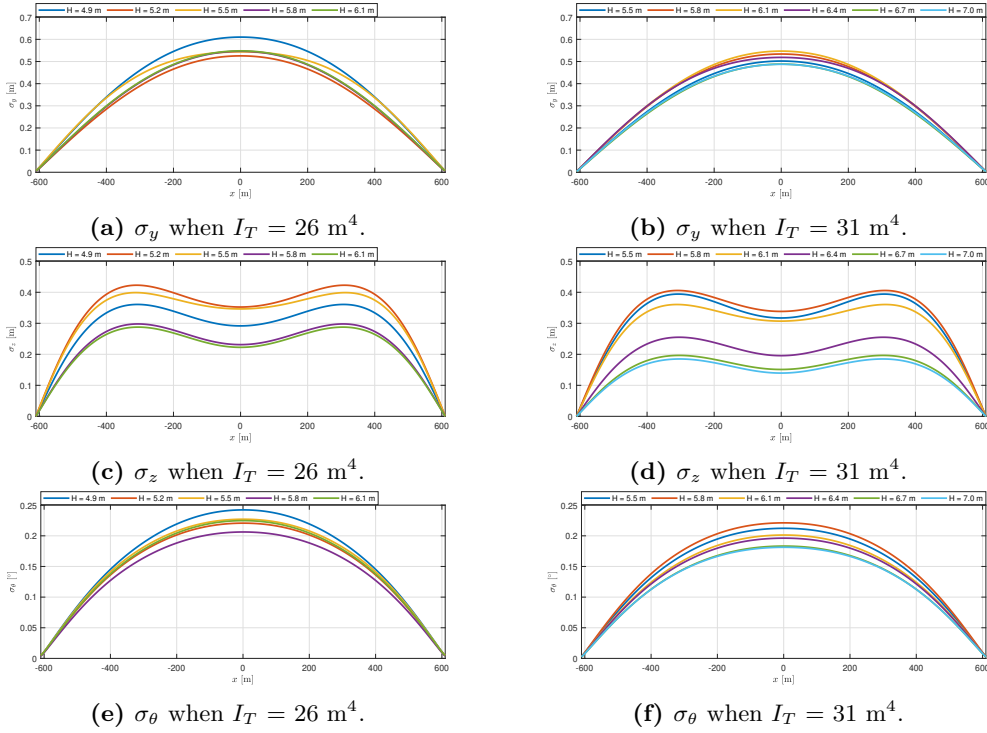
(a) σ_y when $I_T = 26$ m^4.

(b) σ_y when $I_T = 31$ m^4.

(c) σ_z when $I_T = 26$ m^4.

(d) σ_z when $I_T = 31$ m^4.

(e) σ_θ when $I_T = 26$ m^4.

(f) σ_θ when $I_T = 31$ m^4.

Figure 6.19: The standard deviation of the displacement response in the lateral, vertical and torsional directions, for all cross-sections.

bution to vertical displacement at $x = 0$. This shape of the standard deviation curve for vertical response has been observed previously, for example for the Lysefjord Bridge [102].

The largest standard deviation in lateral direction $\sigma_y = 0.61$ m was observed for $H = 4.9$ m with $I_T = 26$ m^4. The lowest value was equal to 0.49 m for $H = 7.0$ m with $I_T = 31$ m^4, which was a reduction of 19.7% from the maximum value. In the vertical direction, the standard deviation was smaller than in the lateral direction for all cross-sections. The largest value of σ_z was found to be 0.42 m for $H = 5.2$ m with $I_T = 26$ m^4, while σ_z was smallest for $H = 7.0$ m with $I_T = 31$ m^4, equal to 0.18 m. This was a reduction of 57.1% compared to the largest value, thus a much larger reduction than for lateral displacement. The results of the standard deviation in the torsional direction were similar to the results of the lateral direction. The standard deviation was largest for $H = 4.9$ m with $I_T = 26$ m^4 and smallest for $H = 7.0$ m with $I_T = 31$ m^4, where σ_θ was 0.24° and 0.18°, respectively. Thus, a reduction of 25%.

The results showed that the standard deviation of displacements, especially in the lateral direction, was not strictly decreasing as the girder height increased. Although I_y and I_z increased as the girder height increased, these changes mainly contributed to the differences in modal properties. It is seen in Section 4.3 that these differences were small. Therefore, the main contrib-

(a) $I_T = 26$ m^4.

(b) $I_T = 31$ m^4.
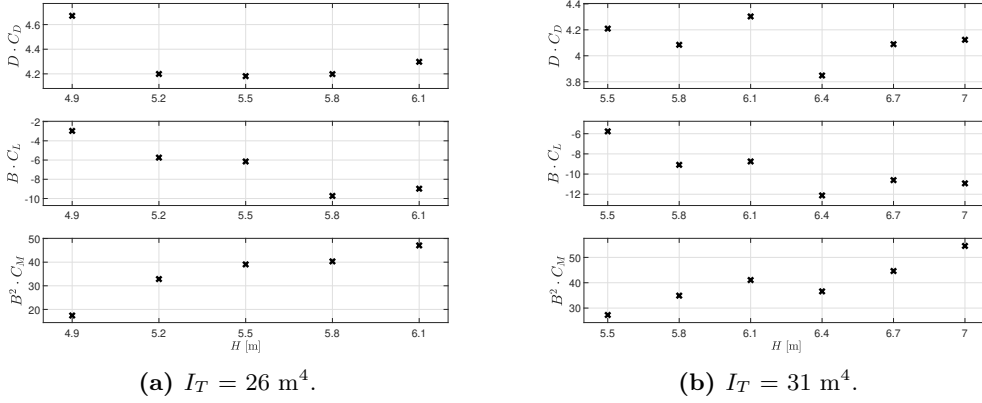
Figure 6.20: Normalized static forces for all cross-sections.

utors to the differences in standard deviation were likely the static coefficients included in $\mathbf{B}_q$, and the ADs included in $\mathbf{C}_{ae}$ and $\mathbf{K}_{ae}$.

The static coefficients C_D, C_L and C_M were multiplied with H, B and B^2, respectively, and plotted in Figure 6.20. This was done to compare the drag, lift and torsional wind forces acting on the different cross-sections. The plots of the normalized drag forces supported the explanation that the large standard deviation in lateral displacement response for $H = 4.9$ m with $I_T = 26$ m^4 partly was caused by the large drag coefficient. The static drag coefficient at $\alpha = 0$ was largest for $H = 4.9$ m with $I_T = 26$ m^4, $C_D = 0.95$. It was smallest for $H = 7.0$ m with $I_T = 31$ m^4, $C_D = 0.59$. The other sections with $I_T = 26$ m^4 had little variation in normalized drag forces and standard deviation in the lateral direction. It was also observed that the cross-section with $H = 6.1$ m, which had the largest σ_y of the sections with $I_T = 31$ m^4, had the largest normalized drag forces of these sections.

The same pattern was not observed for the normalized lift and moment forces. If this was the case, $H = 4.9$ m with $I_T = 26$ m^4 should have been the cross-section with the largest standard deviation in the vertical direction.

For vertical displacement, a much larger relative difference in standard deviation was observed between the largest and smallest value. One of the reasons was likely the larger variation of I_y than of I_z between the cross-sections, seen in Table 4.1. I_y for $H = 7.0$ m with $I_T = 31$ m^4 was 138.1% of I_y for $H = 4.9$ m with $I_T = 26$ m^4. The difference of I_z was only 110.8%.

Another observation from σ_z was that some of the girders with $I_T = 31$ m^4 had a larger standard deviation than the girders with the same height and $I_T = 26$ m^4. This was the case for girders with $H = 5.8$ m. The girder with $I_T = 31$ m^4 and the girder with $I_T = 26$ m^4 had σ_z equal to 0.41 m and 0.30 m, respectively. A combination of several factors was believed to be the explanation behind this observation. The derivative of the static lift coefficient $C_L^{'}$ was larger for the girder with $I_T = 31$ m^4 than for the girder with $I_T = 26$ m^4. Thus, the buffeting lift force became larger. However, if this was the

only explanation, the cross-section with $H = 5.5$ m and $I_T = 31$ m^4 would have had larger σ_z than the cross-section with $H = 5.8$ m and $I_T = 31$ m^4, since C'_L was smaller for the latter cross-section. Another possible contribution to this observation was the differences in H_1^*, contributing to the damping of vertical modes. For the girders with $H = 5.8$ m, H_1^* was more negative with $I_T = 26$ m^4 than with $I_T = 31$ m^4, when K was larger than 0.75. Thus, the aerodynamic damping of vertical motion was larger for the section with $I_T = 26$ m^4 in this range of K.

The correlation coefficients in Appendix I are measures of the linear dependency between the response in different directions [6]. When comparing the values of the coefficients, only the absolute values were studied. The coefficients ρ_{yz} and $\rho_{z\theta}$ were in general low, usually lower than 0.2 and 0.3, respectively. For all cross-sections except $H = 7.0$ m with $I_T = 31$ m^4, ρ_{yz} was lower than $\rho_{z\theta}$. The absolute value of $\rho_{y\theta}$ was 0.5 - 0.6 for all cross-sections. The coefficients were largest at the half-span. This was true for all coefficients and cross-sections.

The cross-sections with $I_T = 31$ m^4 experienced a significant increase of ρ_{yz} for the three tallest cross-sections. It was largest at half-span for the cross-section with $H = 7.0$, where $\left| \rho_{yz} \right|_{H=7.0\text{m}}^{\frac{x}{L}=0.5} \right| = 0.35$. The cross-sections with $I_T = 26$ m^4 also experienced an increase of ρ_{yz} for the two tallest cross-sections, but this increase was smaller than that of the cross-sections with $I_T = 31$ m^4. The increase occurred between $H = 5.5$ - 5.8 m, whereas for the cross-sections with $I_T = 31$ m^4, the increase was gradual from $H = 6.1$ m.

For any given cross-section, $\boldsymbol{\rho}_{rr}$ at the quarter- and three-quarter-spans were close to identical. The maximum increase or decrease of any entry was 0.1%. This was expected due to symmetry.

The low correlation between lateral and vertical response is regarded as positive when evaluating the cross-sections. Large correlation coefficients would have meant significant displacements in both directions simultaneously, which would cause bending about both axes.

6.7 Further discussions

When comparing the quality of different cross-sections, one can not only consider displacements and critical wind velocities. The stresses are also important. Since the distance from the cross-sectional neutral axis is further away from the top and bottom of the girder for the taller cross-sections, the stresses they experience might be higher than what the lower cross-sections experience. Detailed calculations regarding the standard deviation of the moment for the cross-sections were not in the scope of this thesis. However, the elastic moment capacities about the y-axis of all cross-sections are listed in Table 6.5. These results confirmed that moments of the same magnitude cause higher stresses in the taller cross-sections than for the lower ones. Stress calculations will also

Table 6.5: Elastic moment capacity $M_{Rk,el}$ of all cross-sections. The calculations were based on the simplified cross-sections with effective thickness $t = 22.5$ mm.

I_T [m^4]	H [m]	$M_{Rk,el}$ [MNm]
26	4.9	652.6
	5.2	605.3
	5.5	567.3
	5.8	532.5
	6.1	499.1
31	5.5	693.4
	5.8	649.6
	6.1	612.1
	6.4	580.8
	6.7	543.9
	7.0	511.8

be essential for fatigue, which was problematic for the sandwich panel concept.

For further analyses of the produced models, it would be preferable to focus on the cross-sections made with $I_T = 26$ m^4. The material usage is slightly lower for these cross-sections, although the differences are small between cross-sections due to the fixed width of the girders. The main argument for choosing the cross-sections with lower I_T is that girders with the same height can be designed with a more streamlined shape. Thus, the aerodynamic properties of the girders can be improved. From the industry's interest in lower box girders, it is reasonable to avoid the tallest girder. The reason for this interest is the desire to reduce stresses in the girders, which is seen by the elastic moment capacities in Table 6.5. The box girder with $H = 4.9$ m should be avoided due to large drag forces and the buffeting response in the lateral direction. The critical wind velocity showed an unexpected drop for the section with $H = 5.2$ m. $H = 5.8$ m had a lower standard deviation than $H = 5.5$ m in vertical and torsional directions. In addition, some uncertainty was related to the stability limits for $H = 5.5$ m when lateral modes were included in the calculations. The cross-section with $H = 5.8$ m and $I_T = 26$ m^4 may therefore be the best option, but the girders with height equal to 5.2 and 5.5 m are also considered as possible designs.

In the study of girders with torsion constant $I_T = 31$ m^4, it was suggested that the girder with $H = 6.1$ m was the best alternative due to the experienced VIV for the lower girders. The calculations of Scruton numbers implied that these vibrations are less likely to occur for the entire bridge. Thus, the girder with $H = 5.8$ m is therefore recommended for further analyses, along with the girder with $H = 6.1$ m. The three lowest girders had similar results from the buffeting response analysis. $H = 6.1$ m had the largest standard deviation

in lateral response, but lower than the two other alternatives in vertical and torsional response. The girder with $H = 6.1$ m had slightly higher critical wind velocity. The cross-section with $H = 5.5$ m was not of the recommended cross-sections as it might be considered to be too bluff.

Analyses of a cross-section parameterized with $I_T = 31$ m^4 revealed that the simplified method used to calculate the torsion constant underestimated the value of this parameter. It showed that the transverse panel concept with a cross-section parameterized with $I_T = 31$ m^4 had a torsion constant of $I_T = 40.9$ m^4 [83]. The same simplified method used to make cross-sections with $I_T = 31$ m^4 was used to make cross-sections with $I_T = 26$ m^4. Thus, a transverse panel concept girder with an outer shape equal to one cross-section with $I_T = 26$ m^4 will likely have a torsion constant larger than $I_T = 26$ m^4.

The flutter analyses of the cross-sections with $I_T = 26$ m^4 resulted in estimations of critical wind velocities 12.2 - 22.3% above the design critical wind velocity. This implies that the torsion constant, which was reduced from $I_T = 31$ m^4 to $I_T = 26$ m^4, can be further reduced.

Prior to the wind tunnel tests performed in the spring of 2021, a new wind tunnel was mounted in the fluid mechanics laboratory at NTNU. This meant that the test performed for this thesis, and the tests performed in 2020, were executed in different wind tunnels. Both the test area, and the achievable wind speeds of the two wind tunnels were similar. Any other discrepancies of the two wind tunnels were not accounted for in this thesis.

Chapter 7

Conclusions

A dynamic analysis of different cross-sections for an aluminium design of Langenuen Suspension Bridge with a main span length of 1220 m has been performed in this thesis. This has been a continuation of work previously done for the crossing of Langenuen. The main focuses have been aerodynamic stability and buffeting response of the bridge deck, and suppression of vortex induced vibrations during wind tunnel tests. In order to describe the cross-sections with only one defining parameter, the height H of the girders, parameterizations of the cross-sections were based on a fixed torsion constant I_T. Eleven different cross-sections have been investigated for the bridge; five with $I_T = 26$ m^4 and six with $I_T = 31$ m^4. Wind tunnel tests were performed on section models to extract aerodynamic properties of the cross-sections, and suppression of vortex induced vibrations in the wind tunnel was given special consideration. Mechanical properties of the cross-sections were implemented in a parametric model of the bridge to extract modal properties. The global design was based on the transverse panel concept developed by Dr. techn. Olav Olsen in their cost and feasibility analysis of an aluminium bridge for the fjord crossing. Stability calculations were performed with a complex eigenvalue analysis, which allowed for multi-modal flutter instability. A closed-form solution method for bi-modal flutter instability was introduced as comparison.

All eleven bridge decks, $H = 4.9$ - 6.1 m with $I_T = 26$ m^4 and $H = 5.5$ - 7.0 m with $I_T = 31$ m^4, passed the design criterion of critical wind velocity of 76 m/s. The critical instability mode was multi-modal flutter for all cross-sections. The main contributors to the instability modes were the first symmetric torsional and the second symmetric vertical still-air modes. For the cross-sections with $I_T = 26$ m^4, the critical wind velocities were 85.30 - 92.98 m/s. The critical wind velocities were 81.06 - 90.34 m/s for the cross-sections with $I_T = 31$ m^4.

Compared to results from 2020, where the sections with $I_T = 31$ m^4 were tested without the instalment of guide vanes, the two tallest cross-sections showed a significant increase in critical wind velocity. This increase was from 48.60 to 81.06 and 40.63 m/s to 82.04 m/s for the cross-sections with $H = 6.7$

m and $H = 7.0$ m, respectively. It is believed that the guide vanes prevented full separation of the wind flow, such that the flow was reattached to the bridge deck. This explains the change in instability mode from galloping, which was observed in 2020, to multi-modal flutter. This conclusion is supported by the aerodynamic derivative H_1^*, which had negative values for a larger range of reduced frequencies for $H = 6.7$ - 7.0 m this year than the previous results.

The closed-form solution method resulted in lower critical wind velocities compared to the results of the complex eigenvalue analysis. This was expected as this method neglected the torsion damping of the structure. The critical wind velocities estimated by the closed-form approach were 85.2% - 97.2% of the critical wind velocities estimated with the complex eigenvalue analysis. For three of the cross-sections, the solution did not converge in the range of observed data. The remaining eight cross-sections all had a higher critical wind velocity than the design critical wind velocity.

The instalment of guide vanes and tuned mass dampers in order to suppress vortex induced vibrations were effective. The exception was the girder with $H = 5.5$ m and $I_T = 31$ m^4, where little to no effect of the guide vanes was seen. Vibrations observed during the wind tunnel tests were significantly smaller for the cross-sections where tuned mass dampers were installed. During the processing of the free decay tests, it was observed that these cross-sections had larger damping ratios. The tuned mass dampers were only designed for application in the wind tunnel tests, and conclusions of the effect for full scale design should therefore not be drawn.

The aerodynamic properties of the cross-sections were successfully found during the wind tunnel tests. It is believed that the polynomials fitted to the aerodynamic derivatives represented the behaviour of the properties well in the range of measured reduced frequencies. The exceptions are some of the drag-related aerodynamic derivatives, mainly P_1^*, where a large amount of scatter and dependency on Reynolds number was observed. Reynolds number dependency was seen for some static coefficients as well, but only with minor differences between different wind velocities. In general, the obtained data from wind tunnel tests was believed to be of satisfying quality.

Gaussian process regression was implemented on each aerodynamic derivative. Interpolated surfaces were predicted, for which the prediction uncertainty was low, in general. The predicted surfaces managed to describe the trends from the measured data points. The most significant uncertainties were seen for the aerodynamic derivatives related to drag, and especially P_1^*. Increasing the lower bound of the hyperparameter L_1 might reduce the uncertainty in areas between data points but increase the uncertainty in areas where there are data points. The prediction uncertainty was large when extrapolating, as expected, due to a rapid deterioration of predictive power in extrapolation.

The peaks in the autospectral density plots complied with the natural frequencies from the finite element analysis. It revealed coupling of lateral

and torsional movements. Some modes classified as less relevant for the global response of the girder were identified as peaks in the autospectral densities. All cross-sections with the same torsion constant had similar autospectral densities, as expected due to the similarities of natural frequencies.

The standard deviation of the displacement response in the vertical direction was smaller than in the lateral direction. The differences between cross-sections were affected by the static coefficients, aerodynamic derivatives and stiffness properties. However, taller girder height did not necessarily result in a smaller standard deviation of the response. For lateral and torsional response, the maximum standard deviation was at the mid-span of the bridge, while it was largest near the quarter- and three-quarter-spans of the bridge for the vertical response.

Based on the aerodynamic properties and stability limits of the cross-sections, several of the tested girders are relevant for further analysis of the bridge, both cross-sections with $I_T = 26$ m^4 and $I_T = 31$ m^4. Due to the results obtained in this thesis, further recommended cross-sections include $H = 5.2$ - 5.8 m and $H = 5.8$ - 6.1 m with $I_T = 26$ m^4 and $I_T = 31$ m^4, respectively. It is suggested that the cross-section with $H = 5.8$ m and $I_T = 26$ m^4 may be the best option.

As all girders had a critical wind velocity above the design critical wind velocity, further optimization of cross-sections is possible. It is believed that a lower torsion constant is possible. This will allow for streamlined girders which are lower than the girders produced with $I_T = 26$ m^4 and $I_T = 31$ m^4. Girder with lower torsion constants can be produced with a similar parameterization as the already produced girders. Optimization of the cross-section can also be done with a new parameterization.

7.1 Further work

The surfaces predicted in the Gaussian process regression may be used to find predicted aerodynamic derivatives for heights not studied in this thesis. This will allow for stability limit calculations of cross-sections without doing wind tunnel tests. If cross-sections in the predicted area are produced and tested, the accuracy of the predicted surfaced could be evaluated. The regions where the development of the estimated critical wind velocity changes are of special interest. This occurs between $H = 5.8$ - 6.1 m and $H = 6.4$ - 6.7 m for the cross-sections with $I_T = 26$ m^4 and $I_T = 31$ m^4, respectively. Also interesting is the area around $H = 5.2$ m with $I_T = 26$ m^4 where the development of the critical wind velocity was unexpected.

Investigation of cross-sections with a lower torsion constant is possible with respect to aerodynamic stability. This will allow for streamlined girders which are lower than the already produced cross-sections. Changing the parameterization method is also a possible solution for optimization of the cross-section. An asymmetric girder has been suggested by previous reports, and could there-

fore be investigated with regards to aerodynamic stability and buffeting response.

Wind tunnel testing of section models with wind flow in both directions is possible. The symmetric cross-sections tested in this thesis had an asymmetric railing configuration. Thus, the results from wind flow in the opposite direction could vary from the results presented in this thesis. If asymmetrical sections are produced, wind tunnel testing with wind flow in both directions is of interest.

Due to the simplification of the cross-sections as thin-walled, which was deemed as conservative, a closer evaluation of the transverse panel concept could be useful. Accurate calculations of the cross-sectional properties could allow for further optimization of the cross-sectional shape.

The girder behaviour with regard to other areas can be investigated. In particular will stress calculations from dynamic response be important. Static analyses of the different cross-sections will also be decisive for design of the girder shape.

Studies of a stabilization plate have shown that the critical wind velocity of the bridge can be increased with such an instalment [103]. The plate is a thin vertical box mounted at the centre of the top deck of the girder. This is in use as a control measure on several long-span bridges, including the Akashi Kaikyo Bridge [104] and the Runyang Bridge [105]. The influence of such a stabilizer on the critical wind velocity can be studied for Langenuen Suspension Bridge.

Bibliography

[1]   D. K. Bang and E. Ekern, 'Aerodynamic stability of a suspension bridge with an aluminum girder: Wind tunnel testing and numerical predictions,' Master's thesis, NTNU, Jun. 2020.

[2]   N. J. Gimsing and C. T. Georgakis, *Cable Supported Bridges: Concept and Design*, Third Edition. Wiley, 2012.

[3]   Y. Ge and H. Tanaka, 'Long-span bridge aerodynamics,' in *Advanced Structural Wind Engineering*, Y. Tamura and A. Kareem, Eds., First Edition, Springer, 2013, pp. 85–120.

[4]   M. Brorsen, 'Wind structure and wind loading,' DCE Lecture notes No. 12, Department of Civil Engineering, Aalborg University, 2007.

[5]   A. K. Chopra, *Dynamics of Structures*, Fifth Edition. Pearson, 2017.

[6]   G. Müller, *Compendium of lecture notes for structural dynamics*, Technical University of Munich, 2020.

[7]   D. E. Newland, *An Introduction to Random Vibrations, Spectral & Wavelet Analysis*, Third Edition. Dover Publications, 1993.

[8]   G. Bekdaş and S. M. Nigdeli, 'Mass ratio factor for optimum tuned mass damper strategies,' *International Journal of Mechanical Sciences*, vol. 71, pp. 68–84, 2013.

[9]   K. C. S. Kwok and B. Samali, 'Performance of tuned mass dampers under wind loads,' *Engineering Structures*, vol. 17, pp. 655–667, 1995.

[10]   C. Mannini, 'Flutter vulnerability assessment of flexible bridges,' Ph.D. dissertation, Technische Universität Carolo-Wilhelmina zu Braunschweig and University of Florence, 2006.

[11]   E. N. Strømmen, *Theory of Bridge Aerodynamics*, Second Edition. Springer, 2010.

[12]   R. G. J. Flay, 'Bluff body aerodynamics,' in *Advanced Structural Wind Engineering*, Y. Tamura and A. Kareem, Eds., First Edition, Springer, 2013, pp. 59–84.

[13]   T. Stathopoulos and C. C. Baniotopoulos, *Wind Effects on Buildings and Design of Wind-Sensitive Structures*, First Edition. Springer, 2007.

[14] E. Simiu and R. H. Scanlan, *Wind Effects on Structures: Fundamentals and Applications to Design*, Third Edition. Wiley, 1996.

[15] C. Dyrbye and S. O. Hansen, *Wind Loads on Structures*, First Edition. Wiley, 1997.

[16] Norwegian Public Roads Administration, *Bridge Projecting Handbook N400 (in Norwegian)*, 2015.

[17] J. C. Kaimal, J. C. J. Wyngaard, Y. Izumi and O. R. Coté, 'Special characteristics of surface-layer turbulence,' *Quarterly Journal of the Royal Meteorological Society*, vol. 98, pp. 563–589, 1972.

[18] G. Solari and G. Piccardo, 'Probabilistic 3-D turbulence modeling for gust buffeting of structures,' *Probabilistic Engineering Mechanics*, vol. 16, pp. 73–86, 2001.

[19] A. Fenerci, O. Øiseth and A. Rønnquist, 'Long-term monitoring of wind field characteristics and dynamic response of a long-span suspension bridge in complex terrain,' *Engineering Structures*, vol. 147, pp. 269–284, 2017.

[20] A. Fenerci and O. Øiseth, 'Strong wind characteristics and dynamic response of a long-span suspension bridge during a storm,' *Journal of Wind Engineering & Industrial Aerodynamics*, vol. 172, pp. 116–138, 2018.

[21] A. Fenerci and O. Øiseth, 'Measured buffeting response of a long-span suspension bridge compared with numerical predictions based on design wind spectra,' *Journal of Structural Engineering*, vol. 143, p. 04 017 131, 2017.

[22] A. G. Davenport, 'The spectrum of horizontal gustiness near the ground in high winds,' *Quarterly Journal of the Royal Meteorological Society*, vol. 87, pp. 194–211, 1961.

[23] T. Theodorsen, *General theory of aerodynamic instability and the mechanism of flutter*, NACA Report No. 496, Washington DC, 1935.

[24] R. H. Scanlan and J. J. Tomko, 'Airfoil and bridge deck flutter derivatives,' *Journal of the Engineering Mechanics Division*, vol. 97, pp. 1717–1737, 1971.

[25] R. H. Scanlan, 'Wind dynamics of long-span bridges,' in *Aerodynamics Of Large Bridges*, A. Larsen, Ed., First Edition, Balkema, 1992, pp. 47–57.

[26] B. Siedziako, O. Øiseth and A. Rønnquist, 'An enhanced forced vibration rig for wind tunnel testing of bridge deck section models in arbitrary motion,' *Journal of Wind Engineering & Industrial Aerodynamics*, vol. 164, pp. 152–163, 2017.

[27] X. Chen, 'Improved understanding of bimodal coupled bridge flutter based on closed-form solutions,' *Journal of Structural Engineering*, vol. 133, pp. 22–31, 2007.

[28] A. G. Davenport, 'The treatment of wind loading on tall buildings,' in *Tall Buildings: The Proceedings of a Symposium on Tall Buildings with Particular Reference to Shear Wall Structures, Held in the Department of Civil Engineering, University of Southampton*, A. Coull and B. S. Smith, Eds., First Edition, Pergamon Press, 1967, pp. 3–45.

[29] M. Matsumoto, Y. Kobayashi and H. Shirato, 'The influence of aerodynamic derivatives on flutter,' *Journal of Wind Engineering & Industrial Aerodynamics*, vol. 60, pp. 227–239, 1996.

[30] C. A. Trein and H. Shirato, 'Coupled flutter stability from the unsteady pressure characteristics point of view,' *Journal of Wind Engineering & Industrial Aerodynamics*, vol. 99, pp. 114–122, 2011.

[31] M. Matsumoto, K. Okubo, Y. Ito, H. Matsumyia and G. Kim, 'The complex branch characteristics of coupled flutter,' *Journal of Wind Engineering & Industrial Aerodynamics*, vol. 96, pp. 1843–1855, 2008.

[32] F. Xu, T. Wu, X. Ying and A. Kareem, 'Higher-order self-excited drag forces on bridge decks,' *Journal of Engineering Mechanics*, vol. 142, p. 06 015 007, 2016.

[33] L. Patruno, 'Accuracy of numerically evaluated flutter derivatives of bridge deck sections using RANS: Effects on the flutter onset velocity,' *Engineering Structures*, vol. 89, pp. 49–65, 2015.

[34] T. A. Helgedalsrud, Y. Bazilevs, A. Korobenko, K. M. Mathisen and O. A. Øiseth, 'Using ALE-VMS to compute aerodynamic derivatives of bridge sections,' *Computers and fluids*, vol. 179, pp. 820–832, 2019.

[35] L. Huang, H. Liao, B. Wang and Y. Li, 'Numerical simulation for aerodynamic derivatives of bridge deck,' *Simulation Modelling Practice and Theory*, vol. 17, pp. 719–729, 2009.

[36] M. W. Sarwar, T. Ishihara, K. Shimada, Y. Yamasaki and T. Ikeda, 'Prediction of aerodynamic characteristics of a box girder bridge section using LES turbulence model,' *Journal of Wind Engineering & Industrial Aerodynamics*, vol. 96, pp. 1895–1911, 2008.

[37] Z.-w. Zhu, M. Gu and Z.-q. Chen, 'Wind tunnel and CFD study on identification of flutter derivatives of a long-span self-anchored suspension bridge,' *Computer-Aided Civil and Infrastructure Engineering*, vol. 22, pp. 541–554, 2007.

[38] C. Neuhaus, S. Roesler, R. Höffer, M. Hortmanns and W. Zahlten, 'Identification of 18 flutter derivatives by forced vibration tests - a new experimental rig,' in *Proceedings of the 5th European and African Conference on Wind Engineering*, Vancouver, Jul. 2015.

[39] M. Matsumoto, N. Shiraishi, H. Shirato, K. Shigetaka and Y. Niihara, 'Aerodynamic derivatives of coupled/hybrid flutter of fundamental structural sections,' *Journal of Wind Engineering & Industrial Aerodynamics*, vol. 49, pp. 575–584, 1993.

[40] Z. Q. Chen, X. D. Yu, G. Yang and B. F. Spencer, 'Wind-induced self-excited loads on bridges,' *Journal of Structural Engineering*, vol. 131, pp. 1783–1793, 2005.

[41] Q. C. Li, 'Measuring flutter derivatives for bridge sectional models in water channel,' *Journal of Engineering Mechanics*, vol. 121, pp. 90–101, 1995.

[42] B. Cao and P. P. Sarkar, 'Identification of rational functions using two-degree-of-freedom model by forced vibration method,' *Engineering Structures*, vol. 43, pp. 21–30, 2012.

[43] Y. Han, S. Liu, J. X. Hu, C. S. Cai, J. Zhang and Z. Chen, 'Experimental study on aerodynamic derivatives of a bridge cross-section under different traffic flows,' *Journal of Wind Engineering & Industrial Aerodynamics*, vol. 133, pp. 250–262, 2014.

[44] B. Siedziako, O. Øiseth and N. E. A. Rønnquist, 'Identification of aerodynamic properties of bridge decks in arbitrary motion,' in *Special Topics in Structural Dynamics, Volume 6: Proceedings of the 34th IMAC, A Conference and Exposition on Structural Dynamics 2016*, D. Di Miao, P. Tarazaga and P. Castellini, Eds., First Edition, Springer, 2016, pp. 79–85.

[45] N. D. Katopodes, *Free-Surface Flow: Environmental fluid mechanics*, First Edition. Butterworth-Heinemann, 2019.

[46] S. O. Hansen, 'Vortex-induced vibrations of structures,' in *Structural Engineers World Congress*, Bangalore, Nov. 2007.

[47] A. Larsen and A. Wall, 'Shaping of bridge box girders to avoid vortex shedding response,' *Journal of Wind Engineering & Industrial Aerodynamics*, vol. 104-106, pp. 159–165, 2012.

[48] A. Larsen and G. L. Larose, 'Dynamic wind effects on suspension and cable-stayed bridges,' *Journal of Sound and Vibration*, vol. 334, pp. 2–28, 2015.

[49] A. Larsen, S. Esdahl, J. E. Andersen and T. Vejrum, 'Storebælt suspension bridge - vortex shedding excitation and mitigation by guide vanes,' *Journal of Wind Engineering & Industrial Aerodynamics*, vol. 88, pp. 283–296, 2000.

[50] B. Isaksen, E. Strømmen and K. Gjerding-Smith, 'Suppression of vortex shedding vibrations at Osterøy suspension bridge,' in *Proceedings of the fourth Symposium on Strait Crossings*, Bergen, Sep. 2001, pp. 99–105.

[51] S. O. Hansen, R. G. Srouji, B. Isaksen and K. Berntsen, 'Vortex-induced vibrations of streamlined single box girder bridge decks,' in *14th International Conference on Wind Engineering*, Porto Alegre, Jun. 2015.

[52] O. Øiseth, A. Rönnquist and R. Sigbjörnsson, 'Simplified prediction of wind-induced response and stability limit of slender long-span suspension bridges, based on modified quasi-steady theory: A case study,' *Journal of Wind Engineering & Industrial Aerodynamics*, vol. 98, pp. 730–741, 2010.

[53] O. Øiseth and R. Sigbjörnsson, 'An alternative analytical approach to prediction of flutter stability limits of cable supported bridges,' *Journal of Sound and Vibration*, vol. 330, pp. 2784–2800, 2011.

[54] A. Selberg, 'Oscillation and aerodynamic stability of suspension bridges,' *Acta Polytechnica Scandinavia Civil Engineering and Building Construction Series*, vol. 13, 1961.

[55] G. Vairo, 'A simple analytical approach to the aeroelastic stability problem of long-span cable-stayed bridges,' *International Journal for Computational Methods in Engineering Science and Mechanics*, vol. 11, pp. 1–19, 2011.

[56] R. H. Scanlan, N. P. Jones and O. Lorendeaux, 'Comparison of taut-strip and section-model-based approaches in long-span bridge aerodynamics,' *Journal of Wind Engineering & Industrial Aerodynamics*, vol. 72, pp. 275–287, 1997.

[57] R. L. Wardlaw, 'Sectional versus full model wind tunnel testing of bridge road decks,' *Proceedings of the Indian Academy of Sciences Section C: Engineering Sciences*, vol. 3, pp. 177–198, 1980.

[58] L. Caracoglia, P. P. Sarkar, F. L. Haan, H. Sato and J. Murakoshi, 'Comparative and sensitivity study of flutter derivatives of selected bridge deck sections, part 2: Implications on the aerodynamic stability of long-span bridges,' *Engineering Structures*, vol. 31, pp. 2194–2202, 2009.

[59] P. P. Sarkar, L. Caracoglia, F. L. Haan, H. Sato and J. Murakoshi, 'Comparative and sensitivity study of flutter derivatives of selected bridge deck sections, part 1: Analysis of inter-laboratory experimental data,' *Engineering Structures*, vol. 31, pp. 158–169, 2009.

[60] K. Takeda and M. Kato, 'Wind tunnel blockage effects on drag coefficient and wind-induced vibration,' *Journal of Wind Engineering & Industrial Aerodynamics*, vol. 42, pp. 897–908, 1992.

[61] G. S. West and C. J. Apelt, 'The effects of tunnel blockage and aspect ratio on the mean flow past a circular cylinder with Reynolds numbers between between 10^4 and 10^5,' *Journal of Fluid Mechanics*, vol. 114, pp. 361–377, 1982.

93

[62] C.-K. Choi and D. Kwon, 'Wind tunnel blockage effects on aerodynamic behavior of bluff body,' *Wind and Structures*, vol. 1, pp. 351–364, 1998.

[63] S. B. Aas and S. E. Horg, 'Wind tunnel testing of bridge decks,' Master's thesis, NTNU, Jun. 2016.

[64] Y. Kubo, M. Miyazaki and K. Kato, 'Effects of end plates and blockage of structural members on drag forces,' *Journal of Wind Engineering & Industrial Aerodynamics*, vol. 32, pp. 329–342, 1989.

[65] H. J. Spurk and N. Aksel, *Fluid Mechanics*, Second Edition. Springer, 2008.

[66] B. Siedziako and O. Øiseth, 'On the importance of cross-sectional details in the wind tunnel testing of bridge deck section models,' *Procedia Engineering*, vol. 199, pp. 3145–3151, 2017.

[67] E. N. Strømmen, *Structural Mechanics: The Theory of Structural Mechanics for Civil, Structural and Mechanical Engineers*, First Edition. Springer, 2020.

[68] P. K. Larsen, *Dimensjonering av stålkonstruksjoner*, Second Edition. Fagbokforlaget, 2010.

[69] M. L. Stein, *Interpolation of Spatial Data: Some Theory for Kriging*, First Edition. Springer, 1999.

[70] C. E. Rasmussen and C. K. I. Williams, *Gaussian Processes for Machine Learning*, First Edition. The MIT Press, 2006.

[71] M. Heinonen, 'Learning with spectral kernels,' Seminar, Department of Computer Science, Aalto University, 2017.

[72] Ø. W. Petersen, 'A (very short) introduction to gaussian process regression,' Seminar, Department of Structural Engineering, NTNU, 2021.

[73] C. Archambeau, 'Gaussian processes for regression,' Lecture 1c, Department of Computer Science, University College London, 2008.

[74] E. Schulz, M. Speekenbrink and A. Krause, 'A tutorial on Gaussian process regression: Modelling, exploring, and exploiting functions,' *Journal of Mathematical Psychology*, vol. 85, pp. 1–16, 2018.

[75] R. Garnett, 'Gaussian process regression,' Lecture 9, Department of Computer Science and Engineering, Washington University in St. Louis, 2015.

[76] Y. Ding, R. Kondor and J. Eskreis-Winkler, 'Multiresolution kernel approximation for gaussian process regression,' in *Advances in Neural Information Processing Systems*, Long Beach, Dec. 2017.

[77] R. Planas, N. Oune and R. Bostanabad, 'Evolutionary gaussian processes,' *Journal of Mechanical Design*, vol. 143, p. 111 703, 2021.

[78] Norwegian Public Roads Administration, *The Coastal Highway Route E39*, Oct. 2019.

[79] Norwegian Public Roads Administration, *The Coastal Highway Route E39: Benefits for passenger cars*, Oct. 2019.

[80] Norwegian Public Roads Administration, *The Coastal Highway Route E39: Choice of technology for fjord crossings*, Mar. 2015.

[81] Norwegian Public Roads Administration, *No er det bestemt kor langenuen skal kryssast*, Sep. 2019. [Online]. Available: `https://www.vegvesen.no/Europaveg/e39stordos/nyhetsarkiv/no-er-det-bestemt-kor-langenuen-skal-kryssast`.

[82] Norconsult, *Bru over Langenuen og Søreidsvika - Skisseprosjekt*, Mar. 2020.

[83] Dr. techn. Olav Olsen, *Langenuen suspension bridge: Aluminium bridge girder alternative*, Jun. 2020.

[84] K. K. Dunham, 'Coastal Highway Route E39 - extreme crossings,' *Transportation Research Procedia*, vol. 14, pp. 494–498, 2016.

[85] Standard Norge, *Eurocode 9: Design of aluminium structures. Part 1-1: General structural rules*, May 2007.

[86] G. A. Alison, 'Evaluation of seven aluminum highway bridges after two to three decades of service,' *Transportation Research Record*, vol. 950, 1984.

[87] R. D. Cook, D. S. Malkus, M. E. Plesha and R. J. Witt, *Concepts and Applications of Finite Element Analysis*, Fourth Edition. Wiley, 2002.

[88] Dassault Systémes Simulia Corporation, *Abaqus*, 2018.

[89] M. V. Dombu and M. Gjelstad, 'Parametric modelling of a suspension bridge with an aluminium girder,' Master's thesis, NTNU, Jun. 2019.

[90] Python Software Foundation, *Python version 3.8.5*, 2020.

[91] S. Bas, N. M. Apaydin and N. Catbas, 'Considerations for finite element modeling of the Bosphorus Suspension Bridge,' in *Istanbul Bridge Conference*, Istanbul, Aug. 2016.

[92] M. Smith, *Abaqus analysis user's guide, version 6.14*, Dassault Systémes Simulia Corporation, 2014.

[93] DIAB Group, *Divinycell H: Technical manual*, Oct. 2010.

[94] The Mathworks, Inc., *MATLAB version 9.7.0.1190202 (R2019b)*, 2019.

[95] Dassault Systémes SolidWorks Corporation, *SOLIDWORKS 2021*, 2021.

[96] L. Li and R. J. Hearst, 'The influence of freestream turbulence on the temporal pressure distribution and lift of an airfoil,' *Journal of Wind Engineering & Industrial Aerodynamics*, vol. 209, p. 104 456, 2021.

[97] E. Torenbeek and H. Wittenberg, *Flight Physics: Essentials of Aeronautical Disciplines and Technology, with Historical Notes*, First Edition. Springer, 2009.

[98] H. Babinsky, 'How do wings work?' *Physics Education*, vol. 38, pp. 497–503, 2003.

[99] J. Aguilar-Cabello, P. Gutierrez-Castillo, L. Parras, C. del Pino and E. Sanmiguel-Rojas, 'On the onset of negative lift in a symmetric airfoil at very small angles of attack,' *Physics of Fluids*, vol. 32, p. 055 107, 2020.

[100] D. F. Castellon, A. Fenerci and O. Øiseth, 'A comparative study of wind-induced dynamic response models of long-span bridges using artificial neural networks, support vector regression and buffeting theory,' *Journal of Wind Engineering & Industrial Aerodynamics*, vol. 209, p. 104 484, 2021.

[101] H. Ahmadian, G. M. L. Gladwell and F. Ismail, 'Extracting real modes form complex measured modes,' in *Proceedings of the 13th International Modal Analysis Conference*, Nashville, Feb. 1995.

[102] E. Cheynet, J. B. Jakobsen and J. Snæbjörnsson, 'Buffeting response of a suspension bridge in complex terrain,' *Engineering structures*, vol. 128, pp. 474–487, 2016.

[103] H. Tang, Y. Li and K. M. Shum, 'Flutter performance and aerodynamic mechanism of plate with central stabilizer at large angles of attack,' *Advances in Structural Engineering*, vol. 21, pp. 335–346, 2018.

[104] T. Miyata and K. Yamaguchi, 'Aerodynamics of wind effects on the Akashi Kaikyo Bridge,' *Journal of Wind Engineering & Industrial Aerodynamics*, vol. 48, pp. 287–315, 1993.

[105] Y.-J. Ge, 'Aerodynamic challenge and limitation in long-span cable-supported bridges,' in *Advances in Civil, Environmental, and Materials Research (ACEM16)*, Jeju Island, Aug. 2016.

Appendix A

List of Electronic Attachments

Eleven Python scripts which generate global finite element models in Abaqus are appended. These are listed in Table A.1.

Table A.1: The electronic attachments appended to this thesis. These are Python scripts which generate finite element models in Abaqus.

I_T [m^4]	H [m]	Filename
26	4.9	Langenuen21_4900.py
	5.2	Langenuen21_5200.py
	5.5	Langenuen21_5500.py
	5.8	Langenuen21_5800.py
	6.1	Langenuen21_6100.py
31	5.5	Langenuen20_5500.py
	5.8	Langenuen20_5800.py
	6.1	Langenuen20_6100.py
	6.4	Langenuen20_6400.py
	6.7	Langenuen20_6700.py
	7.0	Langenuen20_7000.py

Appendix B

Modal Analysis

The results from the modal finite element analysis are presented in this appendix. The first 15 most relevant mode shapes for the global response of the girder are shown for each cross-section. Non-relevant mode shapes include modes which are dominated by oscillations of cables and towers. Each mode shape is described as either horizontal (H), vertical (V) or torsional (T), as well as symmetric (S) or asymmetric (A). In Figure B.1, the first 15 most relevant mode shapes from the global element model are shown for the cross-section with $H = 5.5$ m and $I_T = 26$ m^4. The natural frequency of each mode is included in the tables in this appendix, both in rad/s and Hz. The results from the cross-sections with $I_T = 26$ m^4 are presented in Tables B.1 to B.5, while the results from the cross-sections with $I_T = 31$ m^4 are presented in Tables B.6 to B.11.

(a) 1HS.

(b) 1VA.

(c) 1HA.

(d) 1VS.

(e) 2VS.

(f) 2VA.

(g) 2HS.

(h) 3VS.

(i) 3VA.

(j) 1TS.

(k) 4VS.

(l) 1TA.

(m) 2HA.

(n) 4VA.

(o) 5VS.
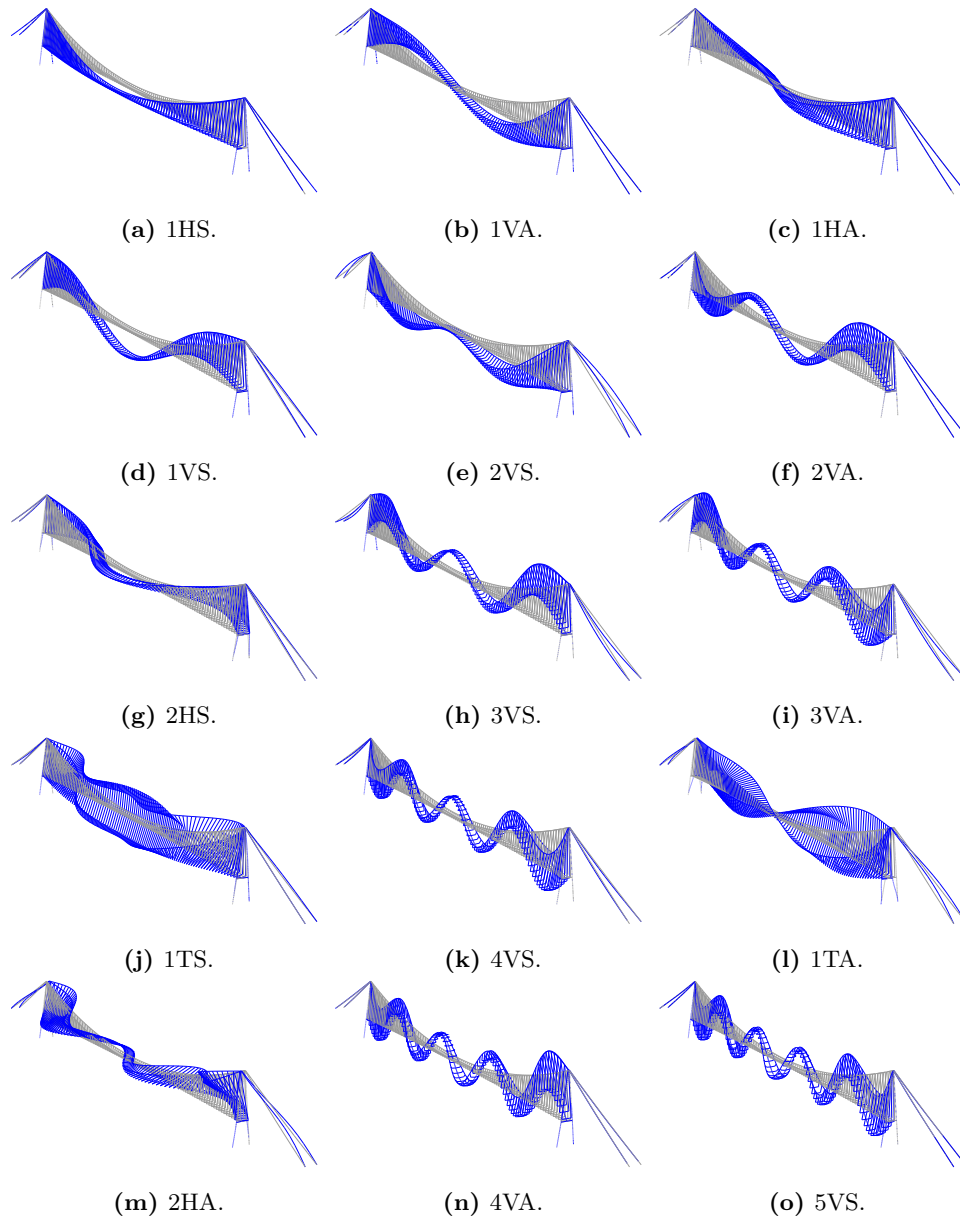
Figure B.1: The 15 first most relevant mode shapes for the global response of the girder from the finite element analysis of the cross-section with $H = 5.5$ m and $I_T = 26$ m^4.

B.1   Torsion constant $I_T = 26$ $\mathbf{m}^4$

Table B.1: Modal properties of the cross section with $H = 4.9$ m and $I_T = 26$ m^4.

Mode	Abaqus nr.	Frequency [rad/s]	[Hz]	Displacement Lateral	Vertical	Torsional
1HS	1	0.3603	0.0573			
1VA	2	0.6880	0.1095			
1VS	3	0.9042	0.1439			
1HA	4	0.9059	0.1442			
2VS	5	1.3274	0.2113			
2VA	6	1.3678	0.2177			
2HS	12	1.8010	0.2866			
3VS	13	1.8214	0.2899			
3VA	14	2.2670	0.3608			
1TS	27	2.6060	0.4148			
4VS	28	2.8013	0.4458			
1TA	31	2.9881	0.4756			
2HA	34	3.3630	0.5352			
4VA	36	3.3851	0.5388			
5VS	41	4.0429	0.6434			

Table B.2: Modal properties of the cross section with $H = 5.2$ m and $I_T = 26$ m^4.

Mode	Abaqus nr.	Frequency [rad/s]	[Hz]	Displacement Lateral	Vertical	Torsional
1HS	1	0.3600	0.0573			
1VA	2	0.6886	0.1096			
1HA	3	0.9037	0.1438			
1VS	4	0.9059	0.1442			
2VS	5	1.3285	0.2114			
2VA	6	1.3731	0.2185			
2HS	12	1.7964	0.2859			
3VS	13	1.8307	0.2914			
3VA	16	2.2831	0.3634			
1TS	27	2.6025	0.4142			
4VS	28	2.8252	0.4497			
1TA	31	2.9881	0.4756			
2HA	35	3.3567	0.5342			
4VA	36	3.4192	0.5442			
5VS	41	4.0885	0.6507			
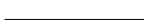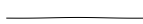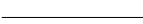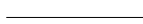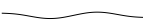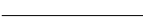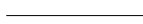
Table B.3: Modal properties of the cross section with $H = 5.5$ m and $I_T = 26$ m^4.

Mode	Abaqus nr.	Frequency [rad/s]	[Hz]	Displacement Lateral	Vertical	Torsional
1HS	1	0.3604	0.0574			
1VA	2	0.6892	0.1097			
1HA	3	0.9066	0.1443			
1VS	4	0.9073	0.1444			
2VS	5	1.3287	0.2115			
2VA	6	1.3775	0.2192			
2HS	12	1.8025	0.2869			
3VS	13	1.8385	0.2926			
3VA	16	2.2966	0.3655			
1TS	27	2.6019	0.4141			
4VS	28	2.8456	0.4529			
1TA	31	2.9895	0.4758			
2HA	35	3.3667	0.5358			
4VA	36	3.4479	0.5488			
5VS	41	4.1270	0.6568			

Table B.4: Modal properties of the cross section with $H = 5.8$ m and $I_T = 26$ m^4.

Mode	Abaqus nr.	Frequency [rad/s]	[Hz]	Displacement Lateral	Vertical	Torsional
1HS	1	0.3611	0.0575			
1VA	2	0.6896	0.1098			
1VS	3	0.9083	0.1446			
1HA	4	0.9112	0.1450			
2VS	5	1.3287	0.2115			
2VA	6	1.3809	0.2198			
2HS	12	1.8123	0.2884			
3VS	13	1.8445	0.2936			
3VA	16	2.3070	0.3672			
1TS	27	2.6005	0.4139			
4VS	29	2.8613	0.4554			
1TA	31	2.9897	0.4758			
2HA	35	3.3825	0.5383			
4VA	36	3.4701	0.5523			
5VS	41	4.1567	0.6616			

Table B.5: Modal properties of the cross section with $H = 6.1$ m and $I_T = 26$ m^4.

Mode	Abaqus nr.	Frequency [rad/s]	[Hz]	Displacement Lateral	Vertical	Torsional
1HS	1	0.3617	0.0576			
1VA	2	0.6899	0.1098			
1VS	3	0.9090	0.1447			
1HA	4	0.9158	0.1457			
2VS	5	1.3285	0.2114			
2VA	6	1.3831	0.2201			
2HS	12	1.8219	0.2900			
3VS	13	1.8485	0.2942			
3VA	16	2.3140	0.3683			
1TS	27	2.5981	0.4135			
4VS	29	2.8717	0.4570			
1TA	31	2.9861	0.4753			
2HA	35	3.3978	0.5408			
4VA	36	3.4849	0.5546			
5VS	41	4.1765	0.6647			

B.2   Torsion constant $I_T = 31$ m^4

Table B.6: Modal properties of the cross section with $H = 5.5$ m and $I_T = 31$ m^4.

Mode	Abaqus nr.	Frequency [rad/s]	[Hz]	Lateral	Vertical	Torsional
1HS	1	0.3624	0.0577			
1VA	2	0.6913	0.1100			
1HA	3	0.9111	0.1450			
1VS	4	0.9123	0.1452			
2VS	5	1.3277	0.2113			
2VA	6	1.3939	0.2218			
2HS	12	1.8138	0.2887			
3VS	13	1.8677	0.2973			
3VA	19	2.3478	0.3737			
1TS	27	2.6632	0.4239			
4VS	30	2.9211	0.4649			
1TA	32	3.1871	0.5072			
2HA	34	3.3845	0.5387			
4VA	36	3.5543	0.5657			
5VS	42	4.2689	0.6794			

Table B.7: Modal properties of the cross section with $H = 5.8$ m and $I_T = 31$ m^4.

Mode	Abaqus nr.	Frequency [rad/s]	[Hz]	Lateral	Vertical	Torsional
1HS	1	0.3626	0.0577			
1VA	2	0.6920	0.1101			
1HA	3	0.9128	0.1453			
1VS	4	0.9140	0.1455			
2VS	5	1.3286	0.2115			
2VA	6	1.3991	0.2227			
2HS	12	1.8174	0.2892			
3VS	13	1.8770	0.2987			
3VA	19	2.3631	0.3761			
1TS	27	2.6617	0.4236			
4VS	30	2.9444	0.4686			
1TA	32	3.1853	0.5070			
2HA	34	3.3902	0.5396			
4VA	36	3.5870	0.5709			
5VS	43	4.3131	0.6864			

Table B.8: Modal properties of the cross section with $H = 6.1$ m and $I_T = 31$ m^4.

Mode	Abaqus nr.	Frequency [rad/s]	[Hz]	Lateral	Displacement Vertical	Torsional
1HS	1	0.3630	0.0578			
1VA	2	0.6925	0.1102			
1VS	3	0.9153	0.1457			
1HA	4	0.9155	0.1457			
2VS	5	1.3287	0.2115			
2VA	6	1.4033	0.2233			
2HS	12	1.8233	0.2902			
3VS	13	1.8844	0.2999			
3VA	19	2.3758	0.3781			
1TS	27	2.6603	0.4234			
4VS	30	2.9634	0.4716			
1TA	32	3.1859	0.5071			
2HA	35	3.3997	0.5411			
4VA	36	3.6137	0.5751			
5VS	43	4.3482	0.6920			

Table B.9: Modal properties of the cross section with $H = 6.4$ m and $I_T = 31$ m^4.

Mode	Abaqus nr.	Frequency [rad/s]	[Hz]	Lateral	Displacement Vertical	Torsional
1HS	1	0.3637	0.0579			
1VA	2	0.6930	0.1103			
1VS	3	0.9166	0.1459			
1HA	4	0.9200	0.1464			
2VS	5	1.3288	0.2115			
2VA	6	1.4074	0.2240			
2HS	12	1.8328	0.2917			
3VS	13	1.8918	0.3011			
3VA	20	2.3884	0.3801			
1TS	27	2.6577	0.4230			
4VS	30	2.9822	0.4746			
1TA	32	3.1847	0.5069			
2HA	35	3.4147	0.5435			
4VA	36	3.6400	0.5793			
5VS	43	4.3831	0.6976			

Table B.10: Modal properties of the cross section with $H = 6.7$ m and I_T = 31 m^4.

Mode	Abaqus nr.	Frequency [rad/s]	[Hz]	Lateral	Displacement Vertical	Torsional
1HS	1	0.3643	0.0580			
1VA	2	0.6932	0.1103			
1VS	3	0.9168	0.1459			
1HA	4	0.9244	0.1471			
2VS	5	1.3284	0.2114			
2VA	6	1.4086	0.2242			
2HS	12	1.8423	0.2932			
3VS	13	1.8940	0.3014			
3VA	20	2.3921	0.3807			
1TS	27	2.6530	0.4222			
4VS	30	2.9877	0.4755			
1TA	32	3.1753	0.5054			
2HA	35	3.4294	0.5458			
4VA	36	3.6478	0.5806			
5VS	43	4.3935	0.6992			

Table B.11: Modal properties of the cross section with $H = 7.0$ m and I_T = 31 m^4.

Mode	Abaqus nr.	Frequency [rad/s]	[Hz]	Lateral	Displacement Vertical	Torsional
1HS	1	0.3652	0.0581			
1VA	2	0.6934	0.1104			
1VS	3	0.9171	0.1460			
1HA	4	0.9306	0.1481			
2VS	5	1.3280	0.2114			
2VA	6	1.4099	0.2244			
2HS	12	1.8552	0.2953			
3VS	13	1.8961	0.3018			
3VA	20	2.3959	0.3813			
1TS	27	2.6480	0.4214			
4VS	30	2.9933	0.4764			
1TA	32	3.1645	0.5037			
2HA	35	3.4489	0.5489			
4VA	36	3.6556	0.5818			
5VS	43	4.4039	0.7009			

Appendix C

Axial Stiffness of Transverse Panel Concept

Values from the calculations of the effective thickness in longitudinal and transverse direction are presented in this appendix. Elasticity modulus E and original length L_0 were 70 000 MPa and 4000 mm, respectively. Table C.1 lists values from the calculation of axial stiffness in the longitudinal direction. Table C.2 lists values from the calculation of axial stiffness in the transverse direction.

C.1 Longitudinal direction

Table C.1: Axial stiffness in the longitudinal direction.

Reaction forces N [N]	Deformation ΔL [mm]	Effective area $A = \frac{NL_0}{E\Delta L}$ [mm^2]	Effective thickness t [mm]
16448.9	$6.16 \cdot 10^{-3}$	152587.2	38.1

C.2 Transverse direction

Table C.2: Axial stiffness in the transverse direction.

Reaction forces N [N]	Deformation ΔL [mm]	Effective area $A = \frac{NL_0}{E\Delta L}$ [mm^2]	Effective thickness t [mm]
588000	0.2857	117605.9	29.4

Appendix D

Vortex Induced Vibrations

The plots from the vortex induced vibration (VIV) tests are presented in this appendix. Figures D.1 to D.5 show the results for the cross-sections with $I_T = 26$ m^4, while Figures D.6 to D.11 show the results for the cross-sections with $I_T = 31$ m^4.

D.1 Torsion constant $I_T = 26$ m^4
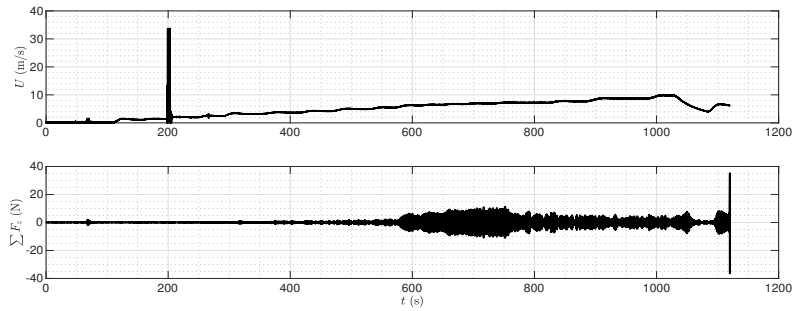
(a) Wind speed and vertical forces.
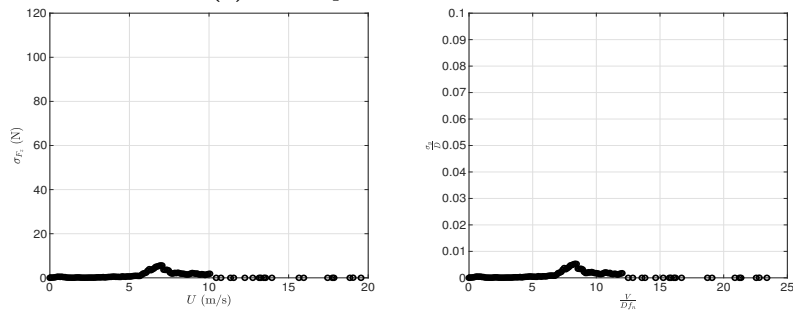
(b) Standard deviation of vertical and normalized lateral forces.

Figure D.1: Result of the VIV test for the cross-section with $H = 4.9$ m and $I_T = 26$ m^4.
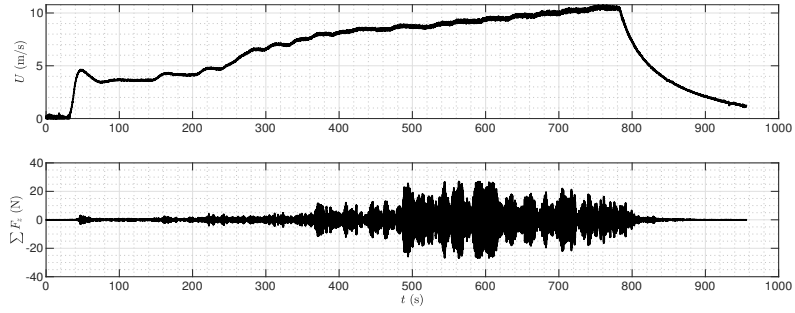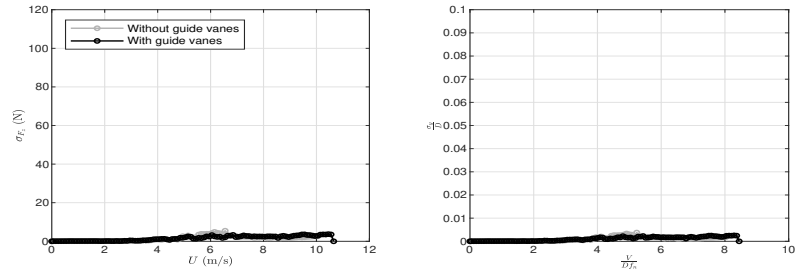
(a) Wind speed and vertical forces.
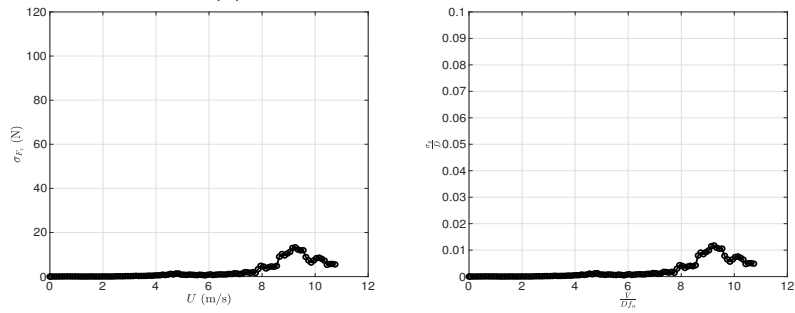
(b) Standard deviation of vertical and normalized lateral forces.

Figure D.2: Result of the VIV test for the cross-section with $H = 5.2$ m and $I_T = 26$ m^4.
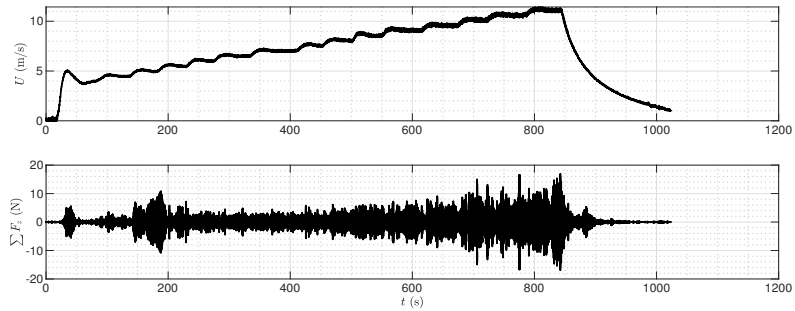
(a) Wind speed and vertical forces.
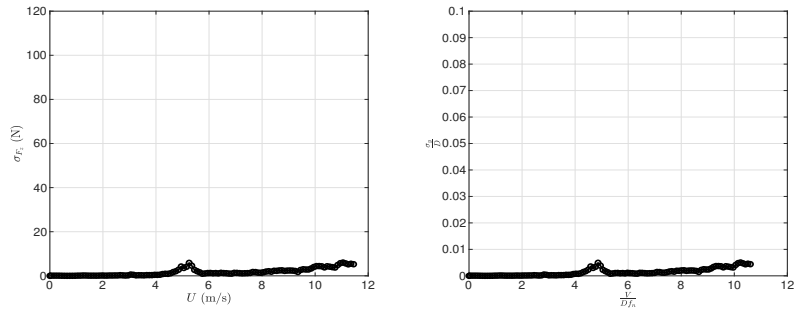
(b) Standard deviation of vertical and normalized lateral forces.

Figure D.3: Result of the VIV test for the cross-section with $H = 5.5$ m and $I_T = 26$ m^4.
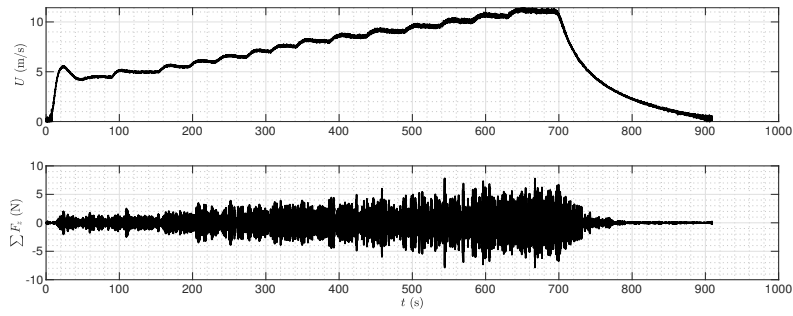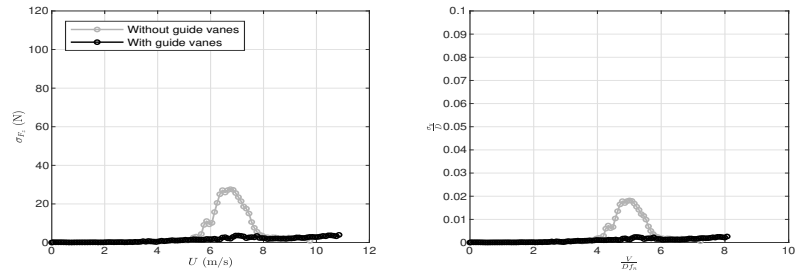
(a) Wind speed and vertical forces.
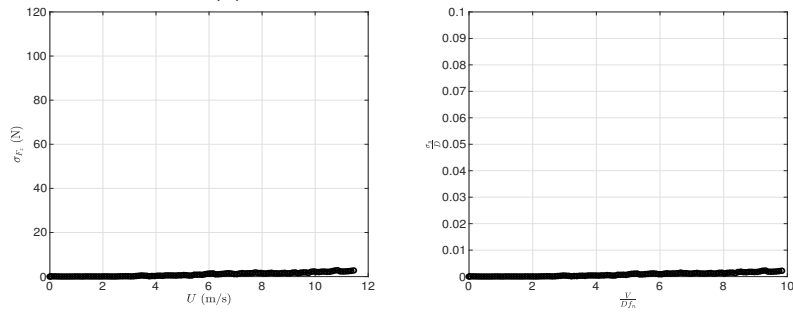
(b) Standard deviation of vertical and normalized lateral forces.

Figure D.4: Result of the VIV test for the cross-section with $H = 5.8$ m and $I_T = 26$ m^4.
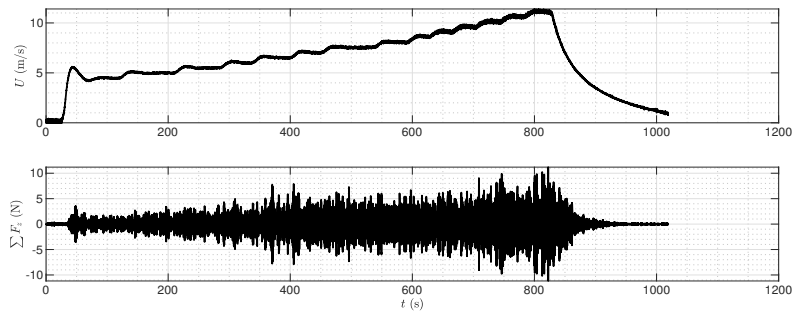
(a) Wind speed and vertical forces.
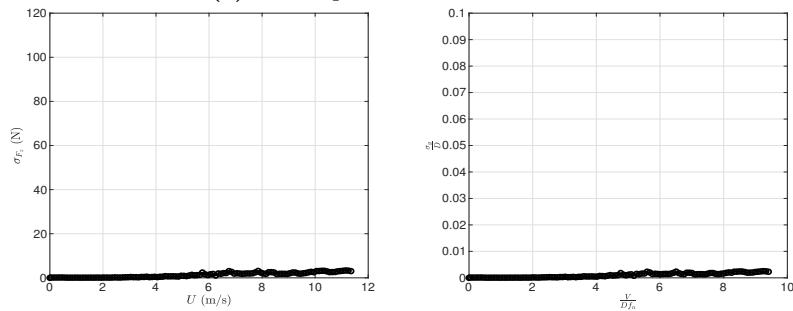
(b) Standard deviation of vertical and normalized lateral forces.

Figure D.5: Result of the VIV test for the cross-section with $H = 6.1$ m and $I_T = 26$ m^4.

D.2   Torsion constant $I_T = 31$ m^4
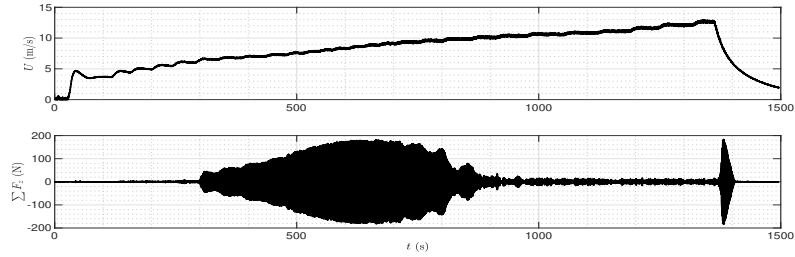
(a) Wind speed and vertical forces.
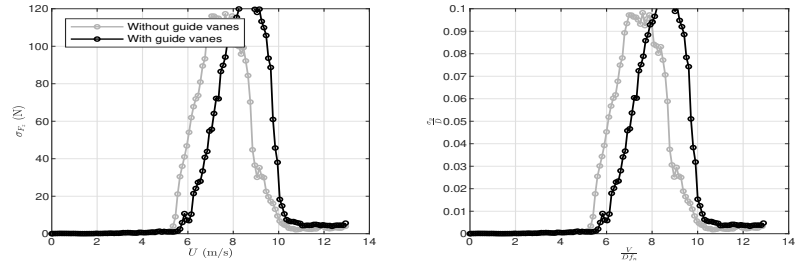
(b) Standard deviation of vertical and normalized lateral forces. Tests without guide vanes were performed the year prior to this thesis [1].

Figure D.6: Result of the VIV test for the cross-section with $H = 5.5$ m and $I_T = 31$ m^4.
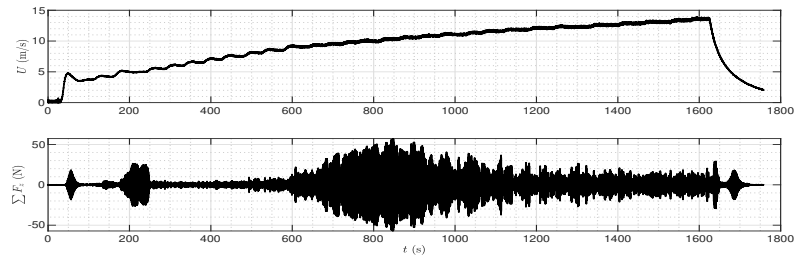
(a) Wind speed and vertical forces.
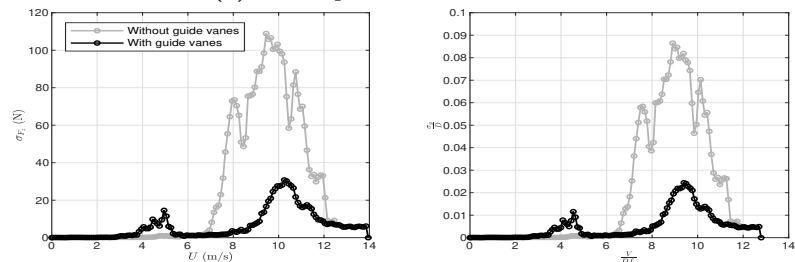
(b) Standard deviation of vertical and normalized lateral forces. Tests without guide vanes were performed the year prior to this thesis [1].

Figure D.7: Result of the VIV test for the cross-section with $H = 5.8$ m and $I_T = 31$ m^4.
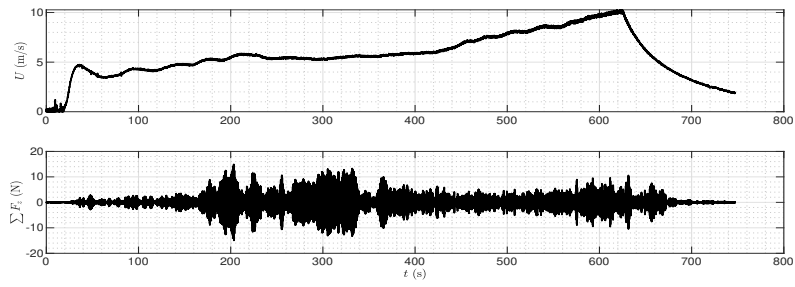
(a) Wind speed and vertical forces.
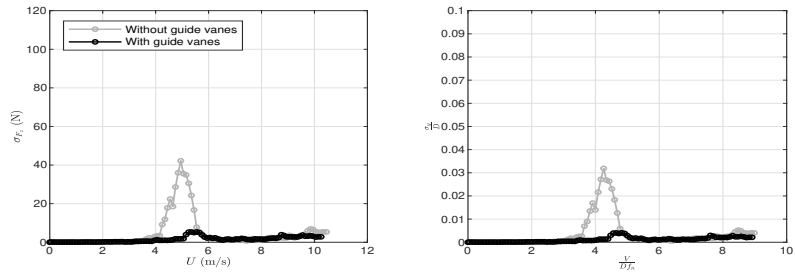
(b) Standard deviation of vertical and normalized lateral forces. Tests without guide vanes were performed the year prior to this thesis [1].

Figure D.8: Result of the VIV test for the cross-section with $H = 6.1$ m and $I_T = 31$ m^4.
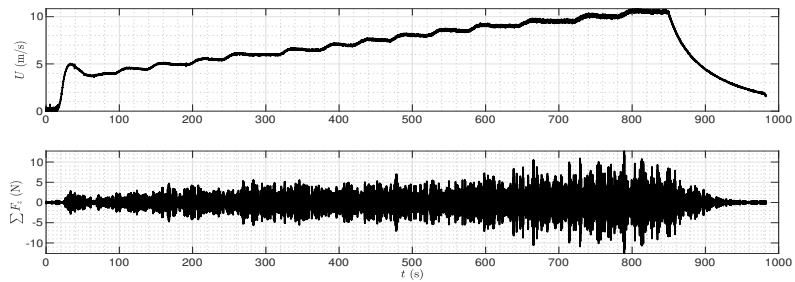
(a) Wind speed and vertical forces.
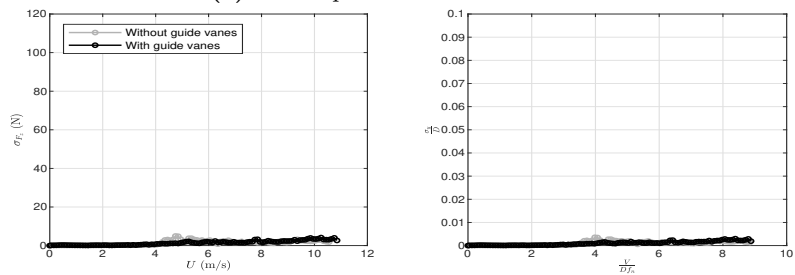
(b) Standard deviation of vertical and normalized lateral forces. Tests without guide vanes were performed the year prior to this thesis [1].

Figure D.9: Result of the VIV test for the cross-section with $H = 6.4$ m and $I_T = 31$ m^4.
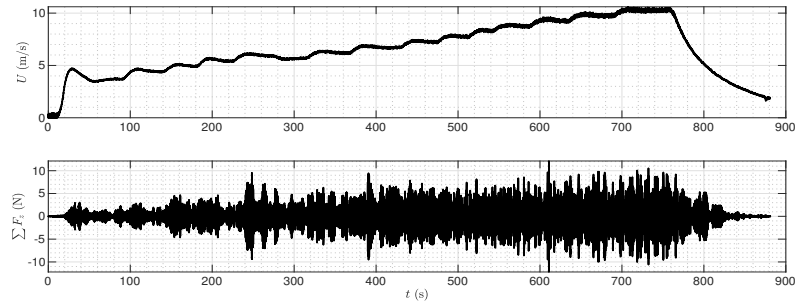
(a) Wind speed and vertical forces.

(b) Standard deviation of vertical and normalized lateral forces. Tests without guide vanes were performed the year prior to this thesis [1].

Figure D.10: Result of the VIV test for the cross-section with $H = 6.7$ m and $I_T = 31$ m^4.
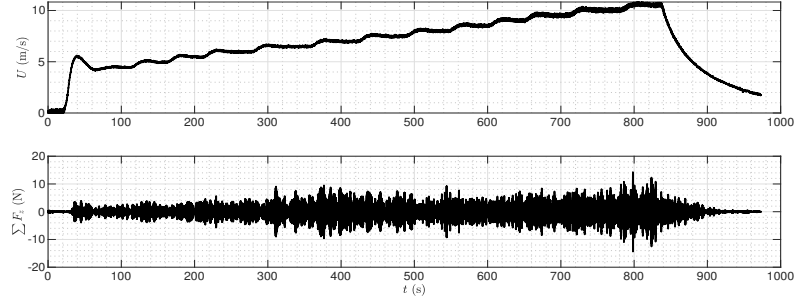
(a) Wind speed and vertical forces.

(b) Standard deviation of vertical and normalized lateral forces. Tests without guide vanes were performed the year prior to this thesis [1].

Figure D.11: Result of the VIV test for the cross-section with $H = 7.0$ m and $I_T = 31$ m^4.

Appendix E

Aerodynamic Derivatives

All 18 aerodynamic derivatives (ADs) for every cross-section are presented in this appendix. A third degree polynomial was fitted to the data points from the wind tunnel tests. The fitted curve was constrained to a constant value outside the range of the experimental observations. ADs were plotted against the reduced frequency K.

Figures E.1 to E.5 show the ADs for the cross-sections parameterized with $I_T = 26$ m^4, while Figures E.6 to E.11 show ADs for the cross-sections parameterized with $I_T = 31$ m^4.

E.1   Torsion constant $I_T = 26$ m^4
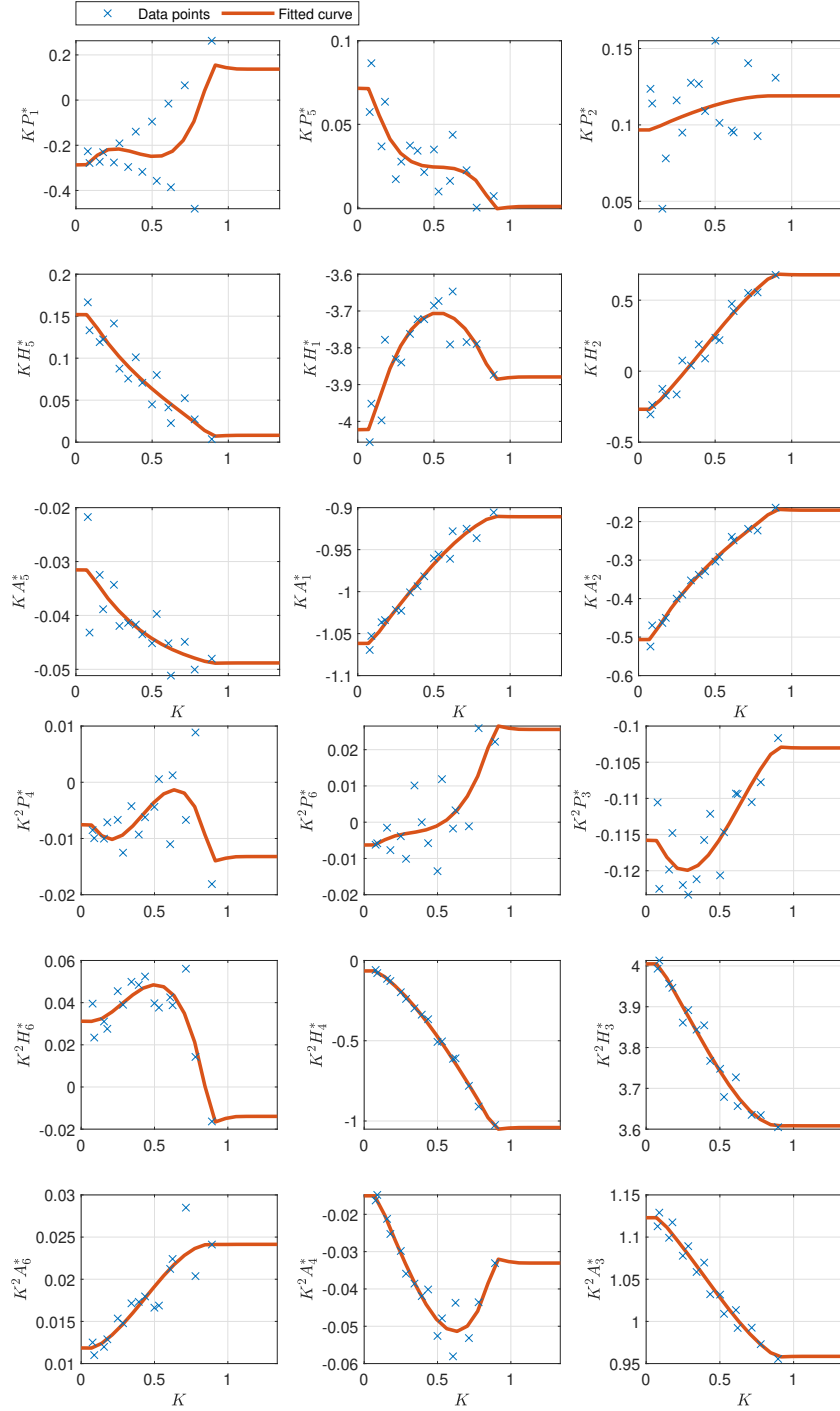
Figure E.1: ADs for the cross-section of height $H = 4.9$ m, parameterized with $I_T = 26$ m^4.
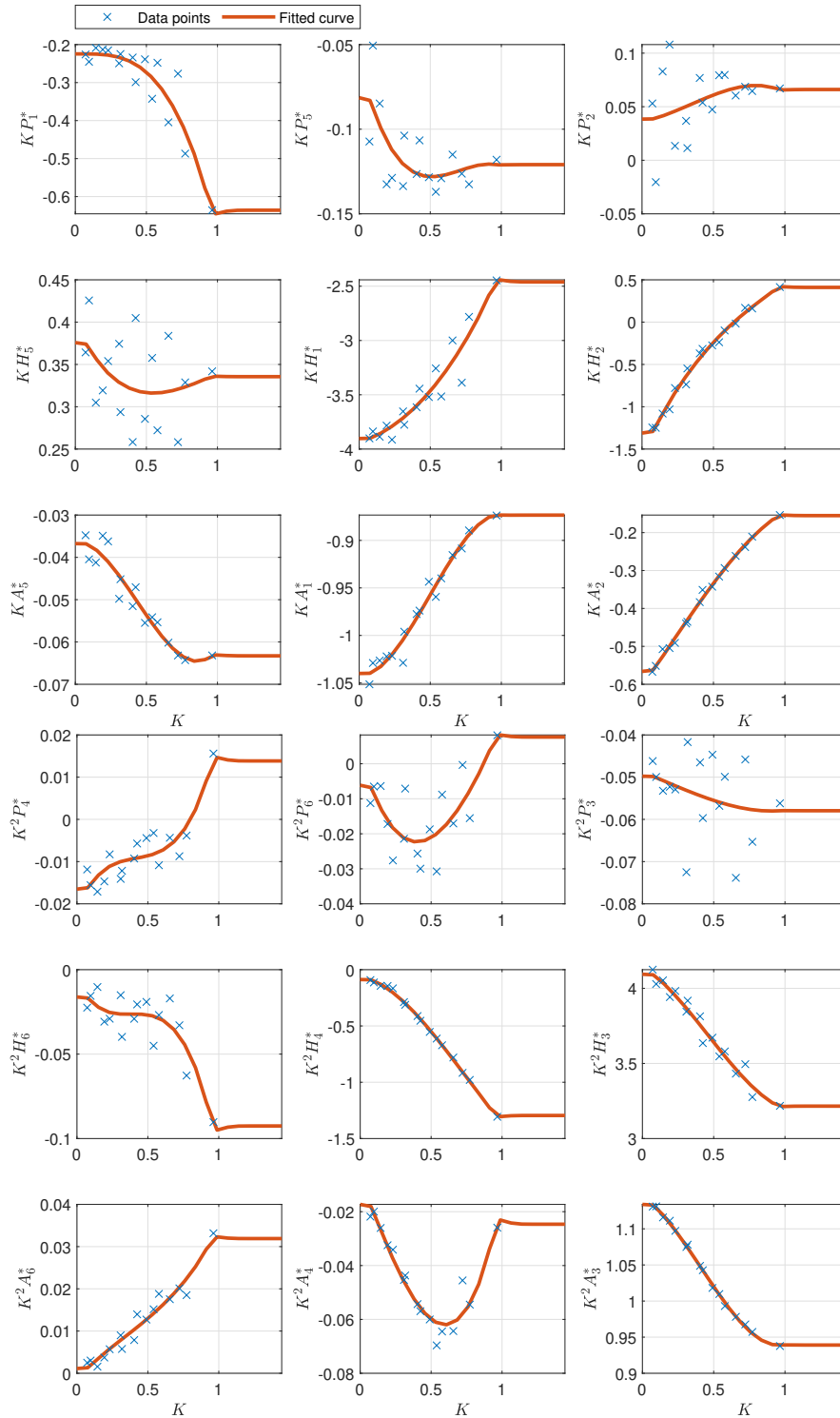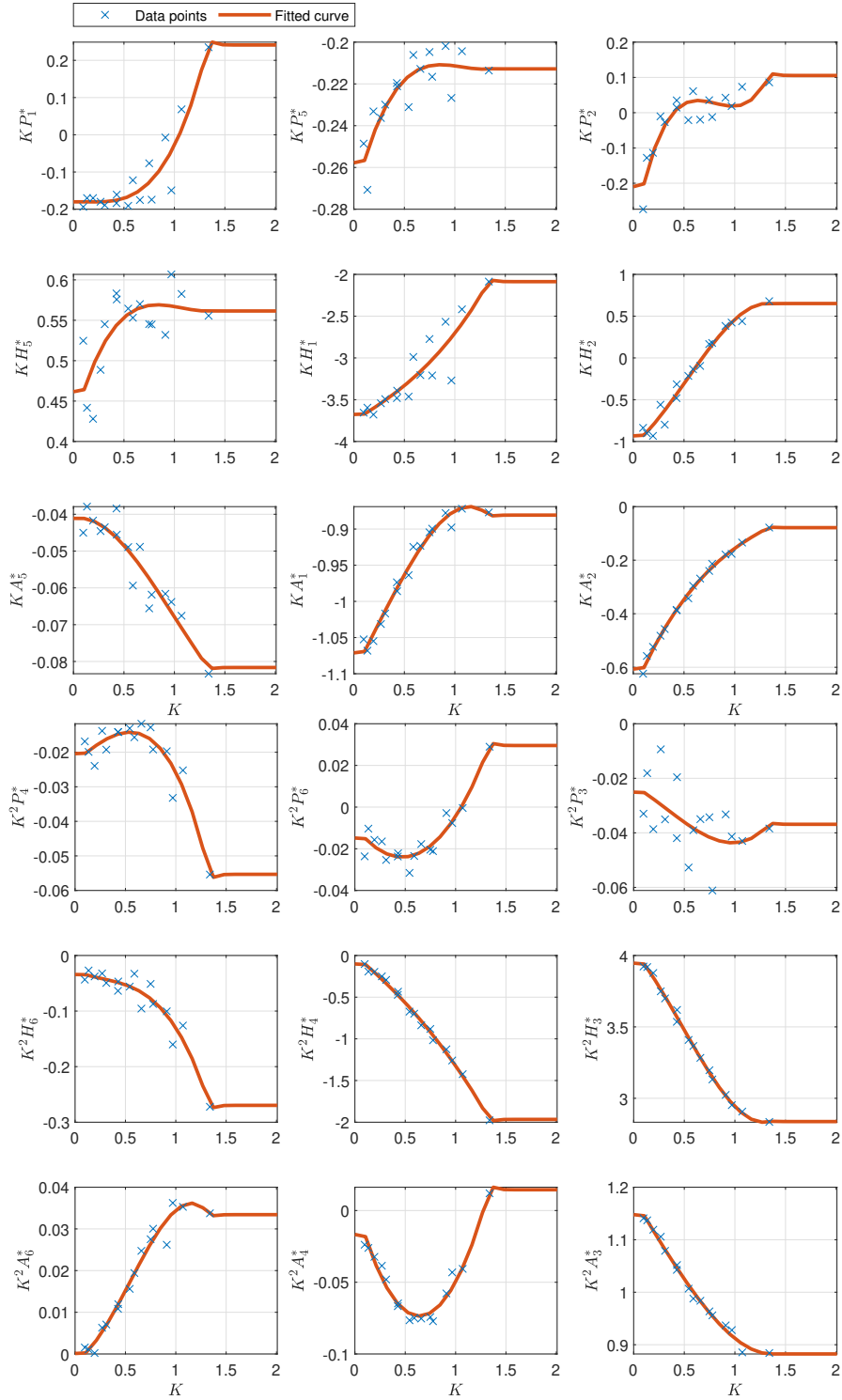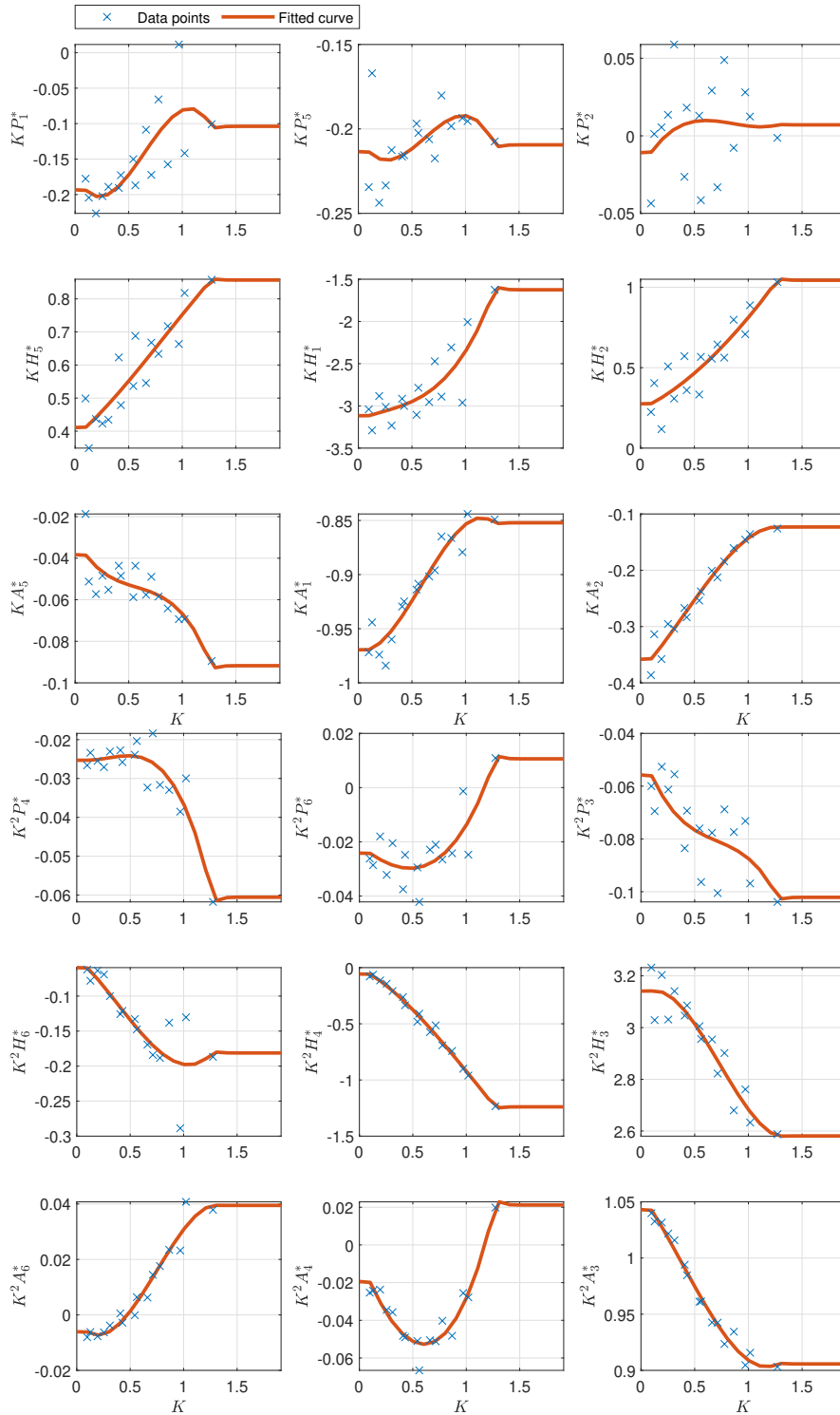
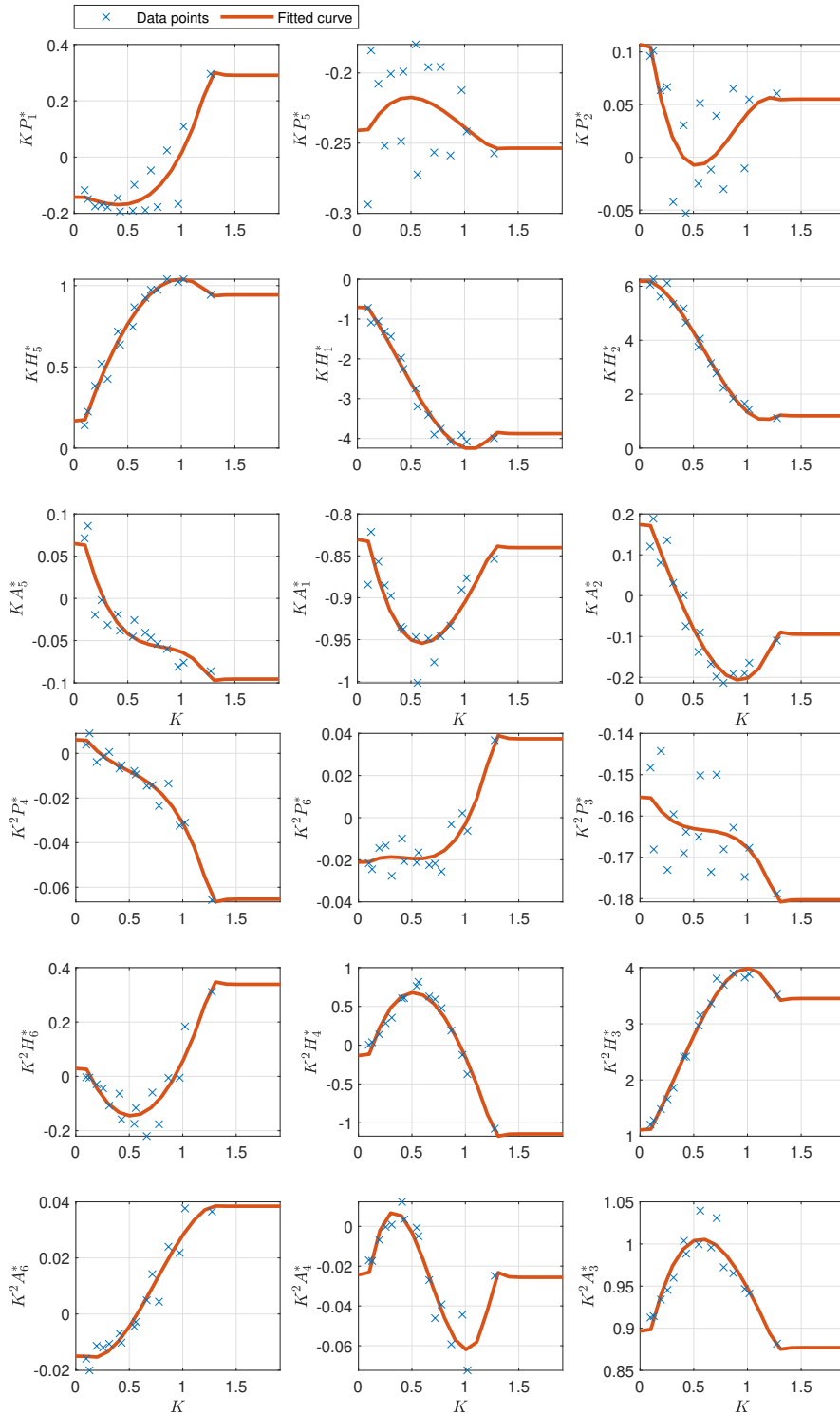**Figure E.2:** ADs for the cross-section of height $H = 5.2$ m, parameterized with $I_T = 26$ m^4.
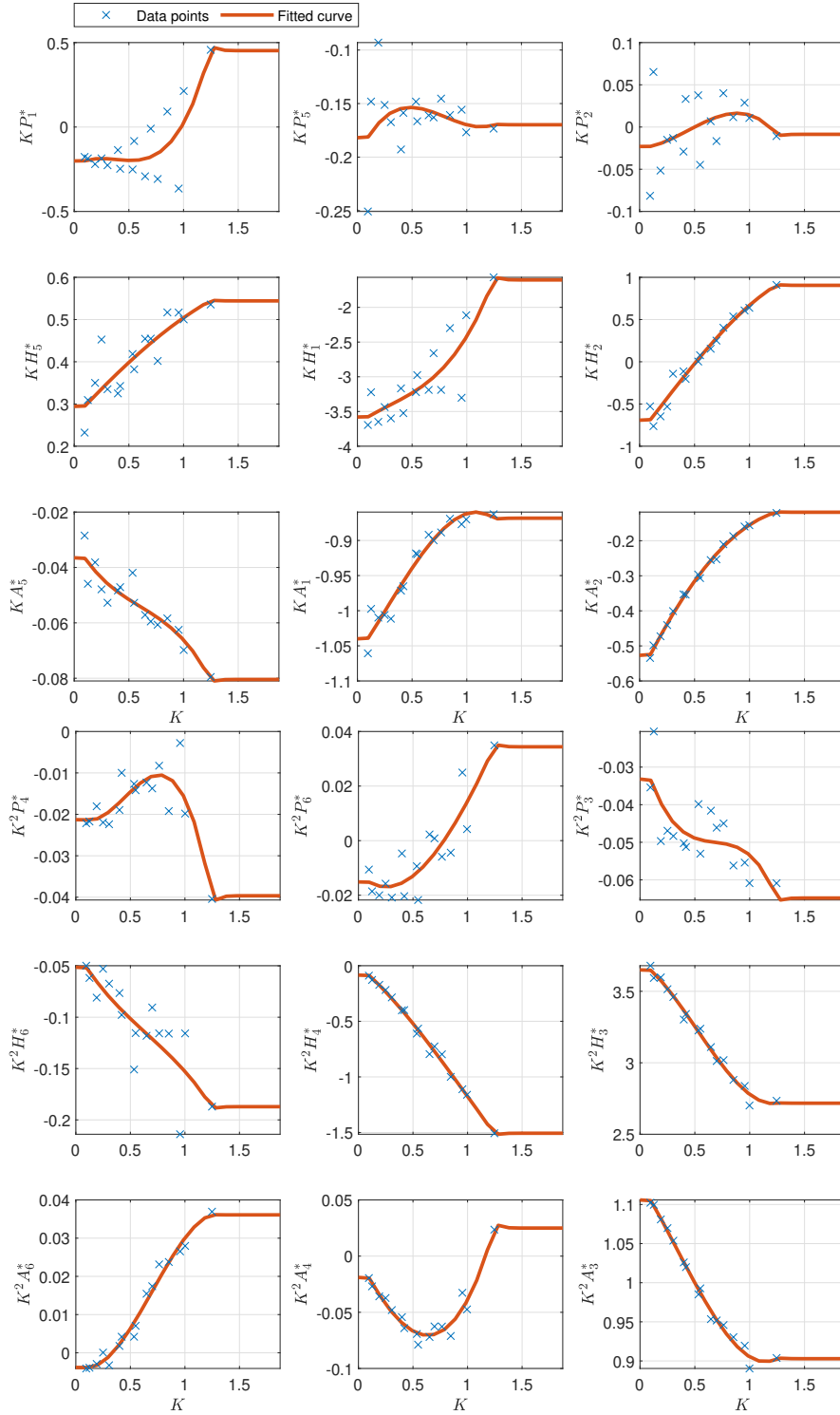
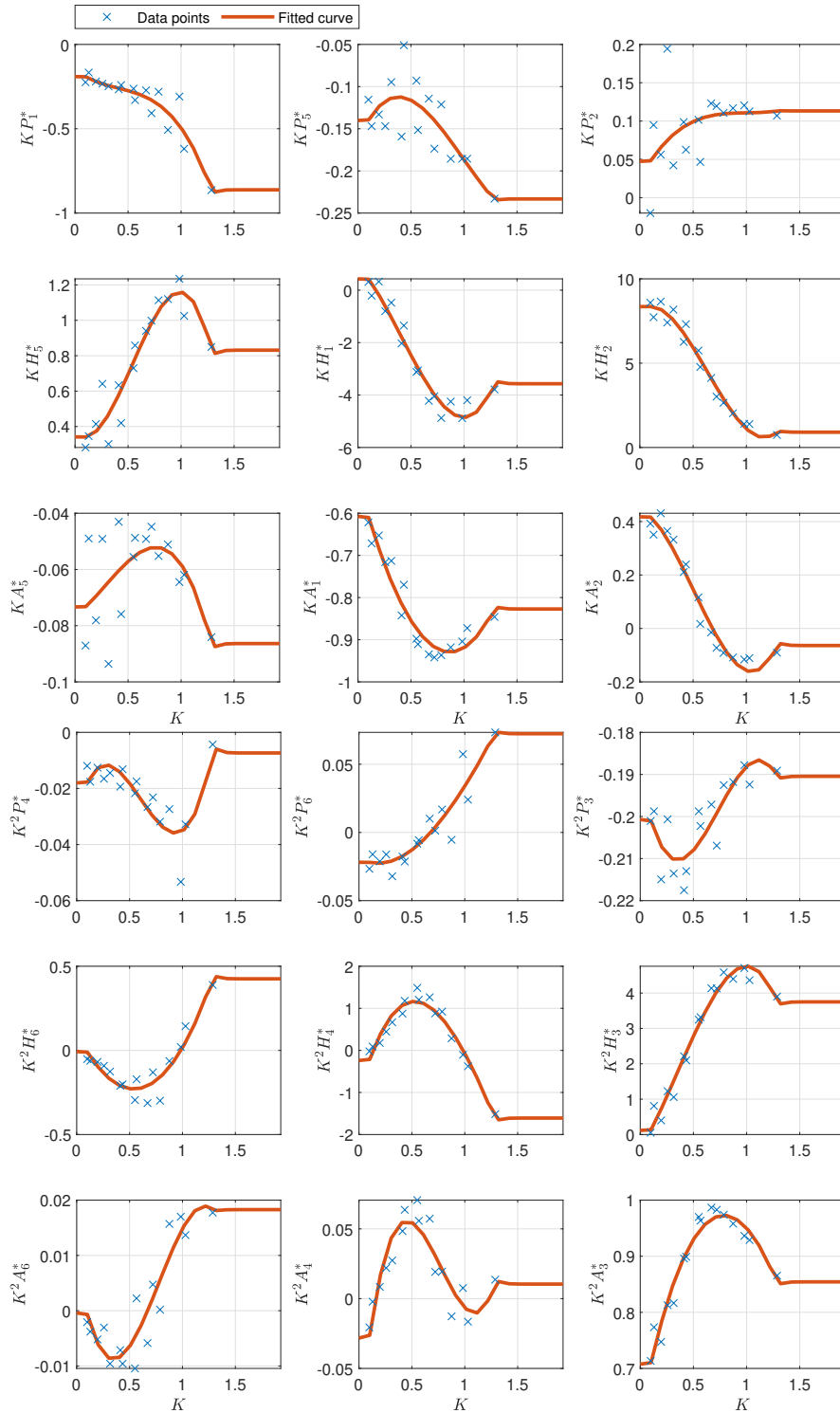**Figure E.3:** ADs for the cross-section of height $H = 5.5$ m, parameterized with $I_T = 26$ m^4.
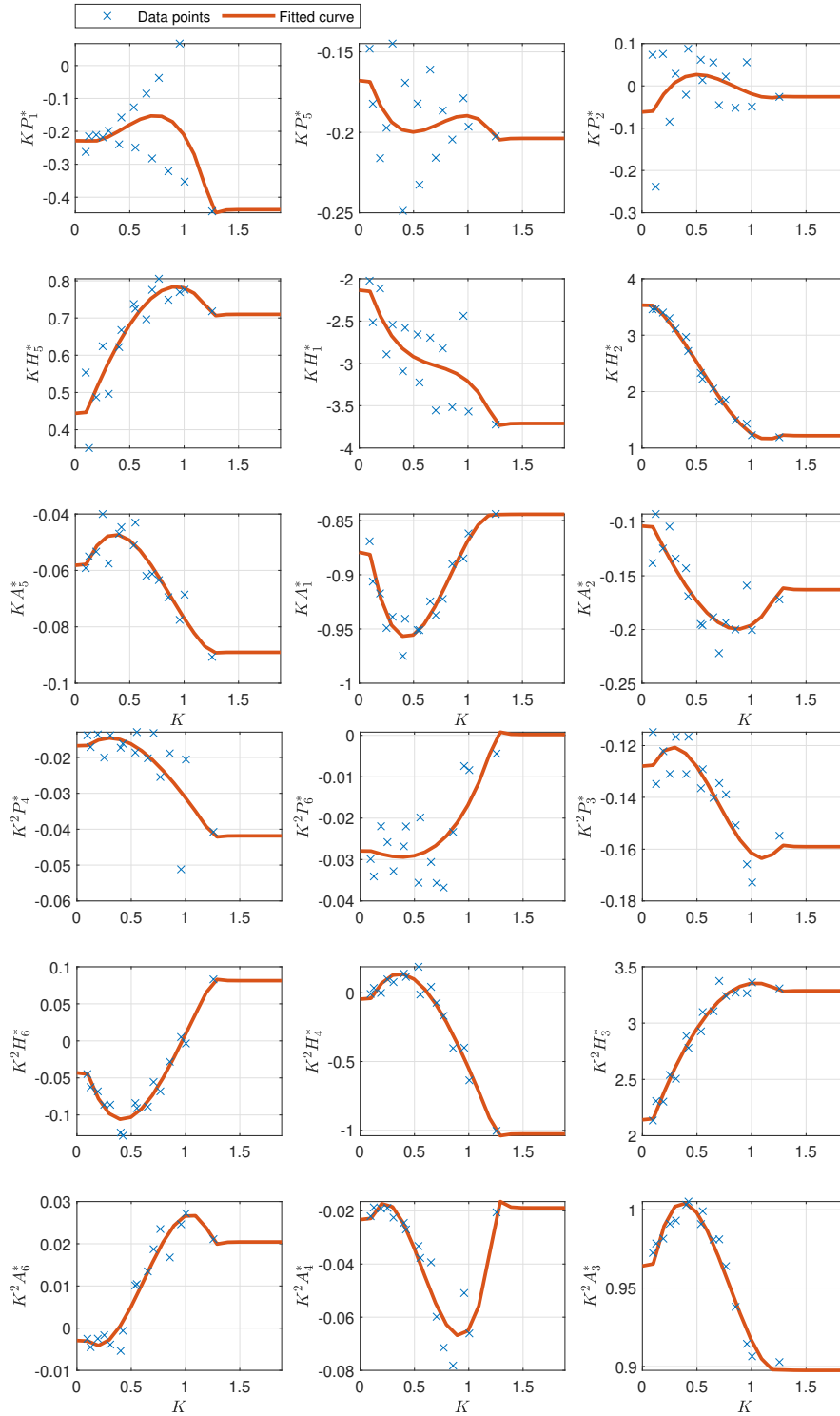
Figure E.4: ADs for the cross-section of height $H = 5.8$ m, parameterized with $I_T = 26$ m^4.
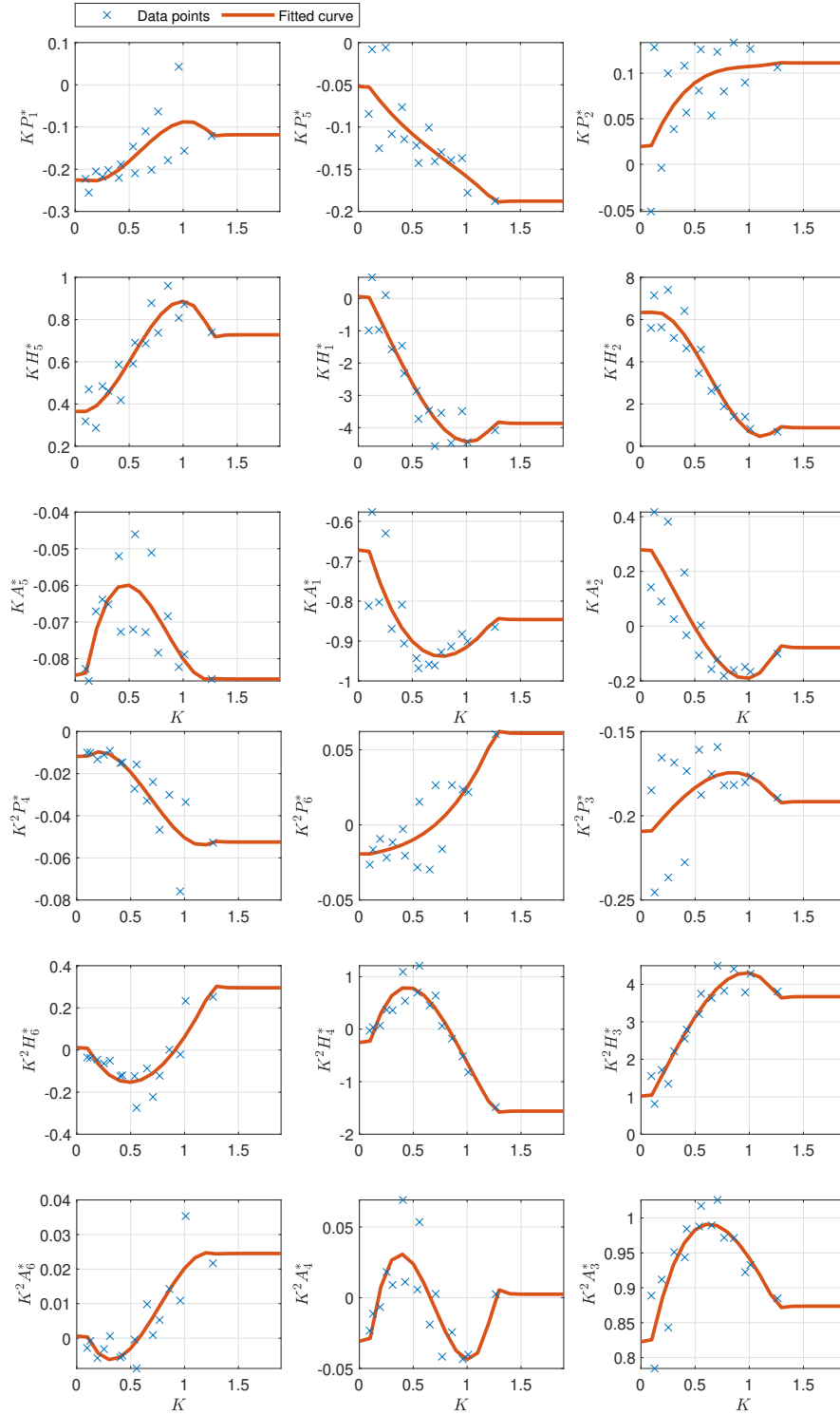
Figure E.5: ADs for the cross-section of height $H = 6.1$ m, parameterized with $I_T = 26$ m^4.

E.2   Torsion constant $I_T = 31$ m^4
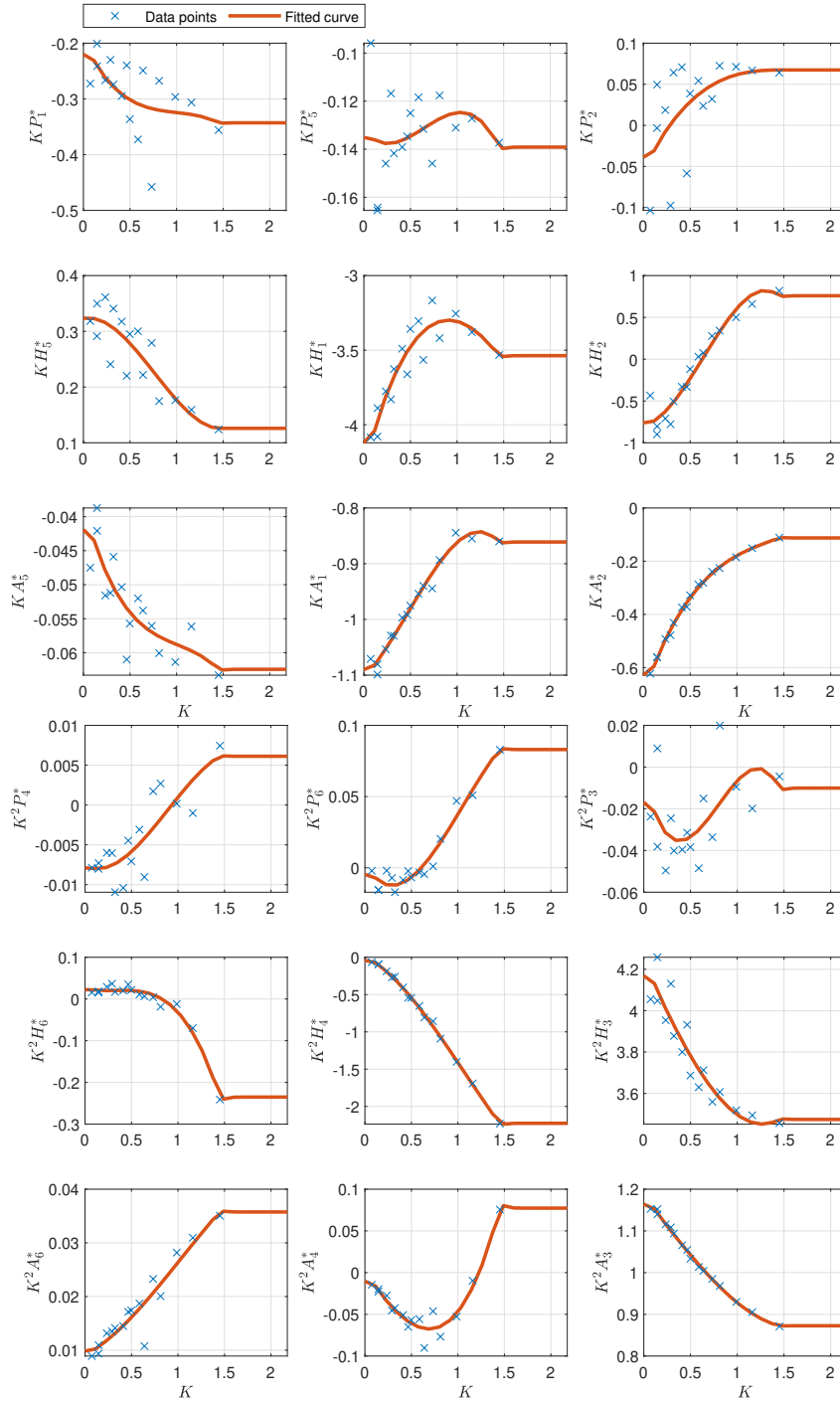
Figure E.6: ADs for the cross-section of height $H = 5.5$ m, parameterized with $I_T = 31$ m^4.

Figure E.7: ADs for the cross-section of height $H = 5.8$ m, parameterized with $I_T = 31$ m^4.

Figure E.8: ADs for the cross-section of height $H = 6.1$ m, parameterized with $I_T = 31$ m^4.

Figure E.9: ADs for the cross-section of height $H = 6.4$ m, parameterized with $I_T = 31$ m^4.

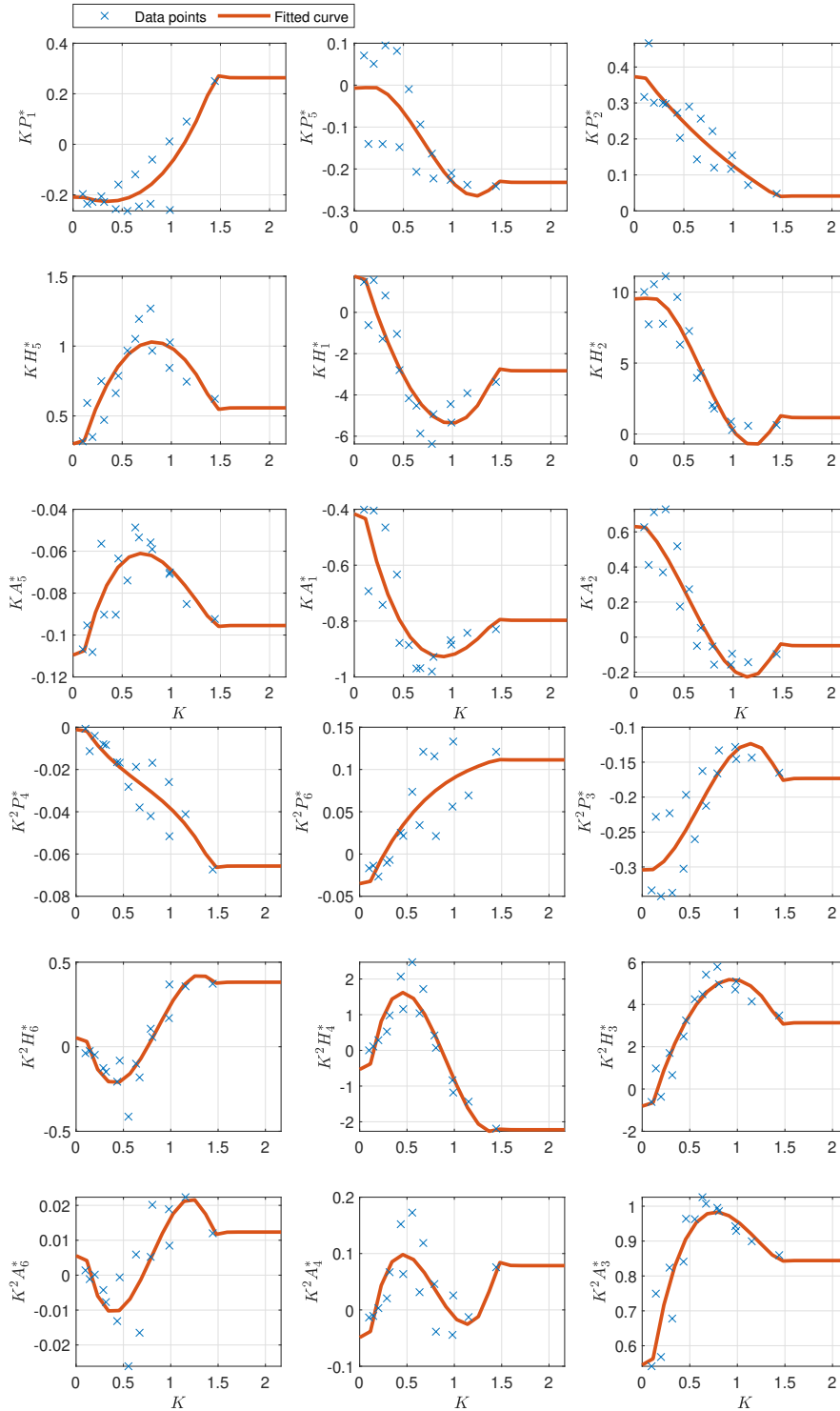**Figure E.10:** ADs for the cross-section of height $H = 6.7$ m, parameterized with $I_T = 31$ m^4.

Figure E.11: ADs for the cross-section of height $H = 7.0$ m, parameterized with $I_T = 31$ m^4.

Appendix F

Theodorsen Aerodynamic Derivatives

The aerodynamic derivatives (ADs) developed by Theodorsen [23] are compared to the polynomials which were fitted to the data points from the wind tunnel tests of ADs in this appendix. Figures F.1 to F.5 show the ADs for the cross-sections parameterized with $I_T = 26$ m^4, while Figures F.6 to F.11 show ADs for the cross-sections parameterized with $I_T = 31$ m^4.

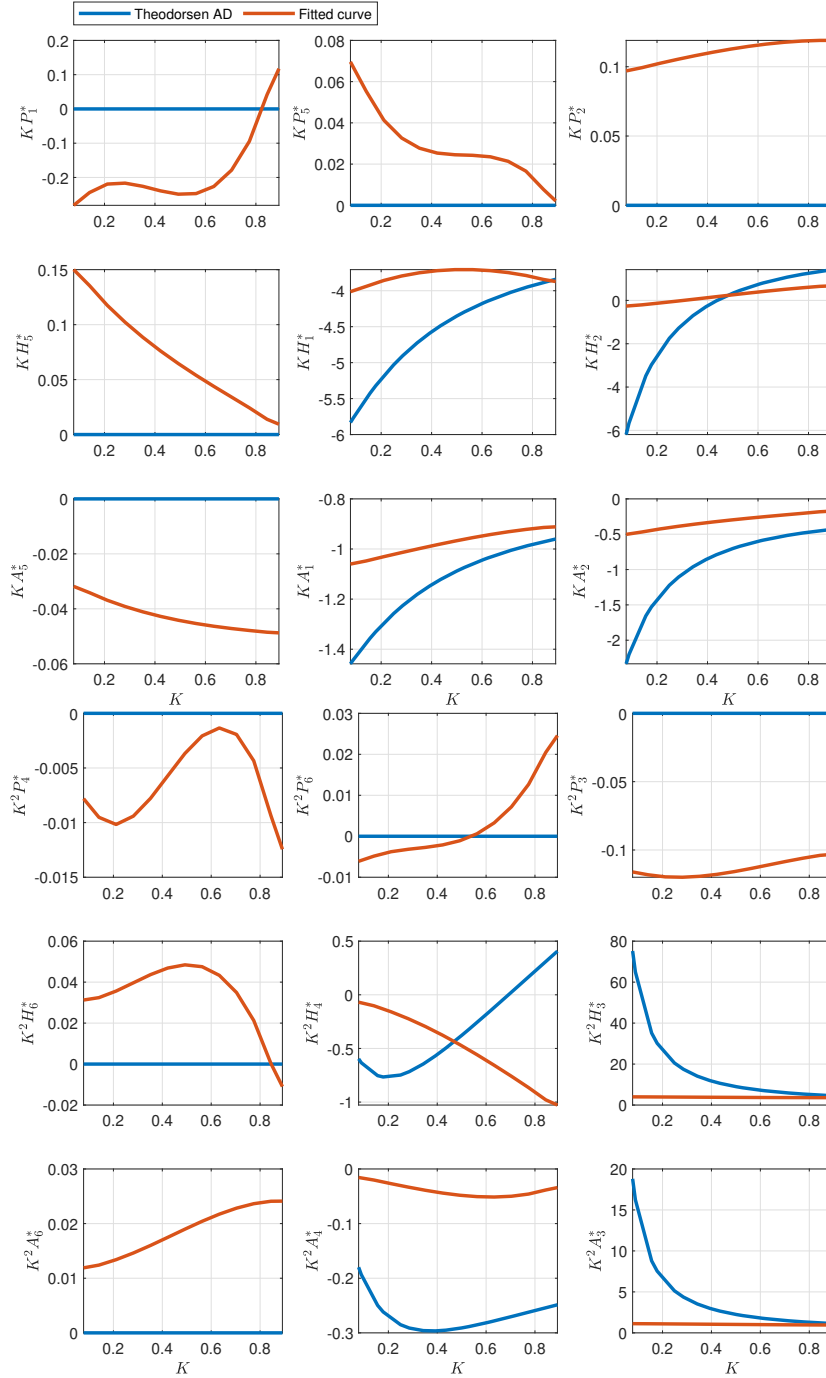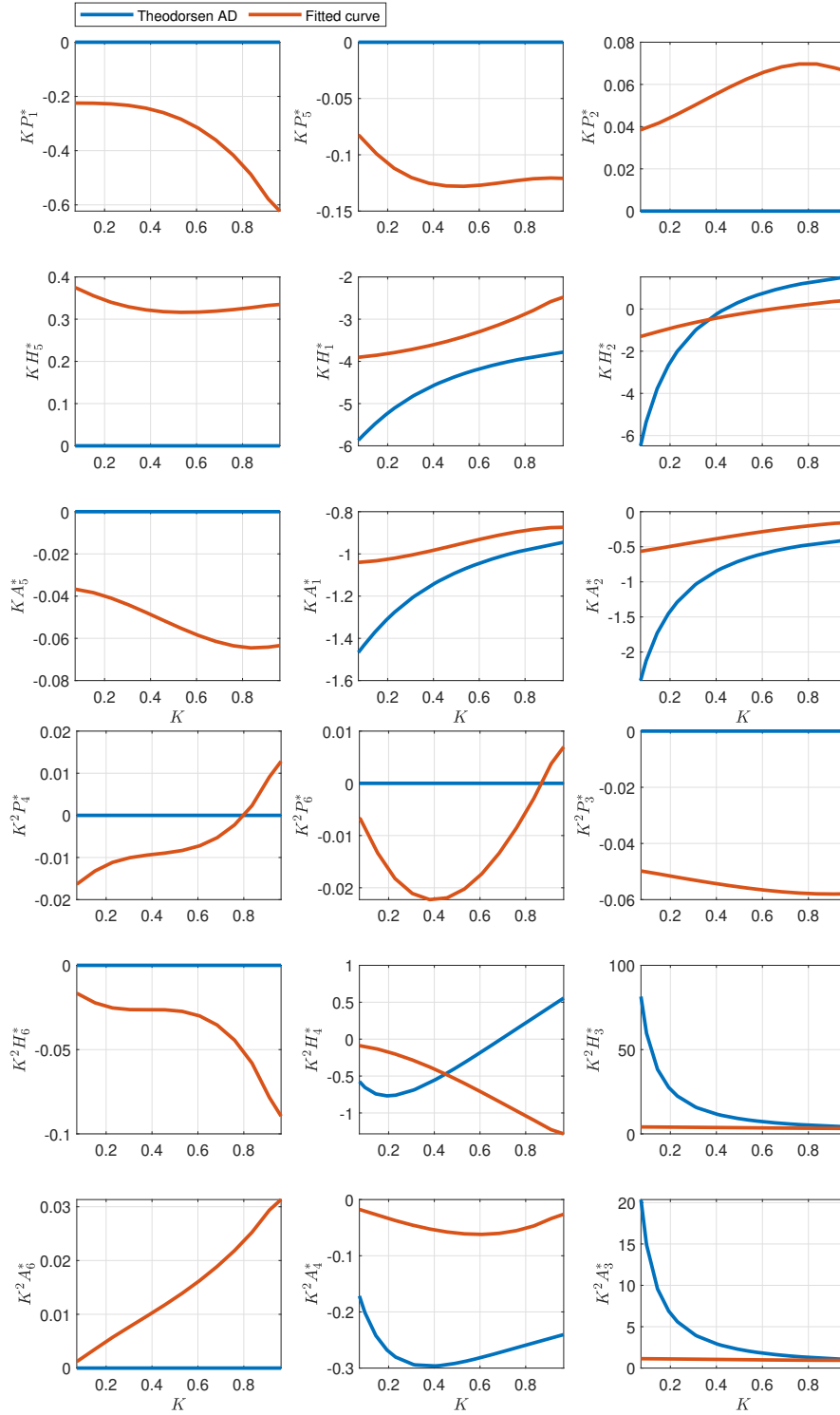## F.1 Torsion constant $I_T = 26 \text{ m}^4$

Figure F.1: Comparison of the ADs developed by Theodorsen and the polynomial which was fitted to the data points from the wind tunnel tests for the cross-section of height $H = 4.9$ m, parameterized with $I_T = 26 \text{ m}^4$.

Figure F.2: Comparison of the ADs developed by Theodorsen and the polynomial which was fitted to the data points from the wind tunnel tests for the cross-section of height $H = 5.2$ m, parameterized with $I_T = 26$ m^4.
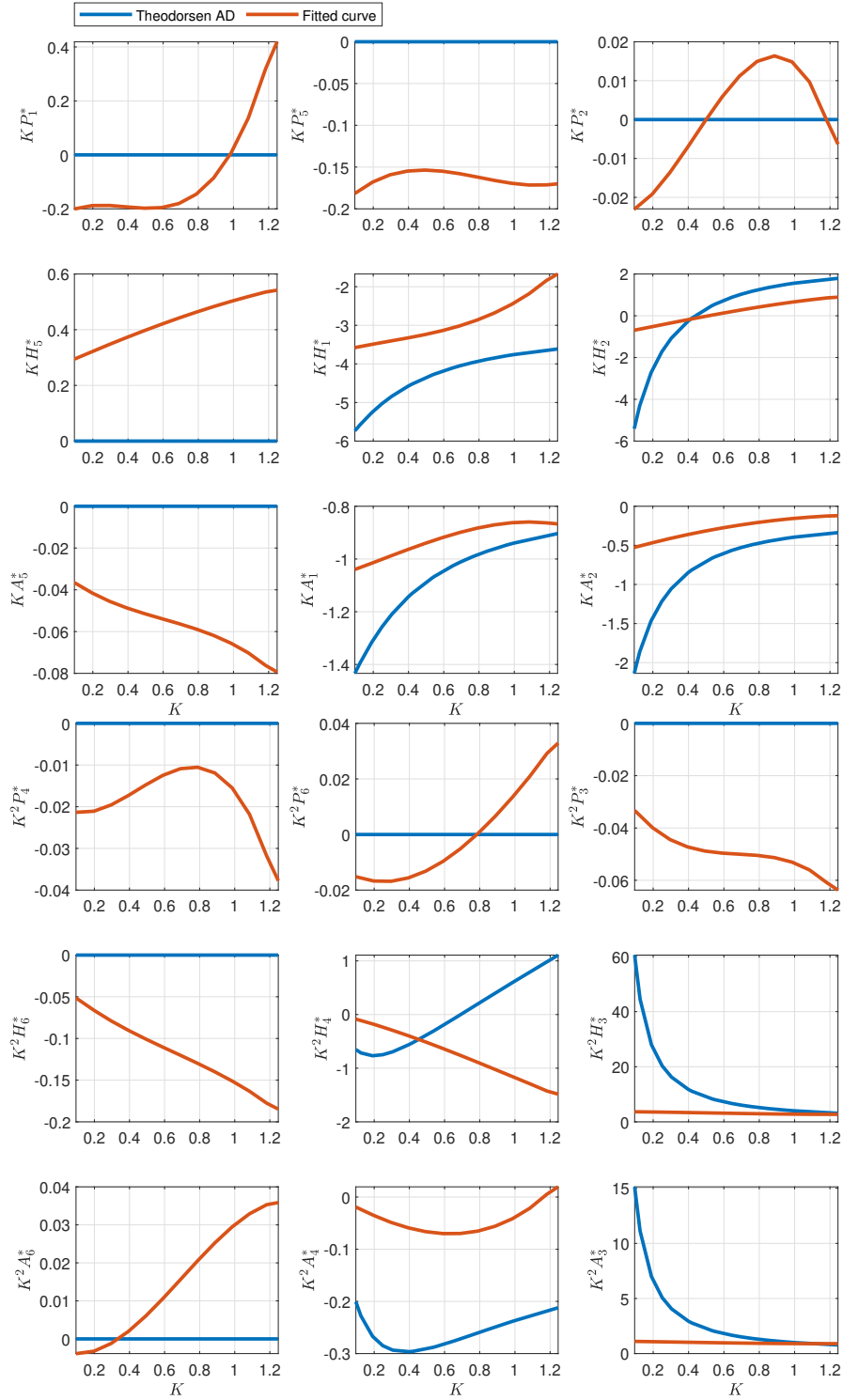
Figure F.3: Comparison of the ADs developed by Theodorsen and the polynomial which was fitted to the data points from the wind tunnel tests for the cross-section of height $H = 5.5$ m, parameterized with $I_T = 26$ m^4.

Figure F.4: Comparison of the ADs developed by Theodorsen and the polynomial which was fitted to the data points from the wind tunnel tests for the cross-section of height $H = 5.8$ m, parameterized with $I_T = 26$ m^4.
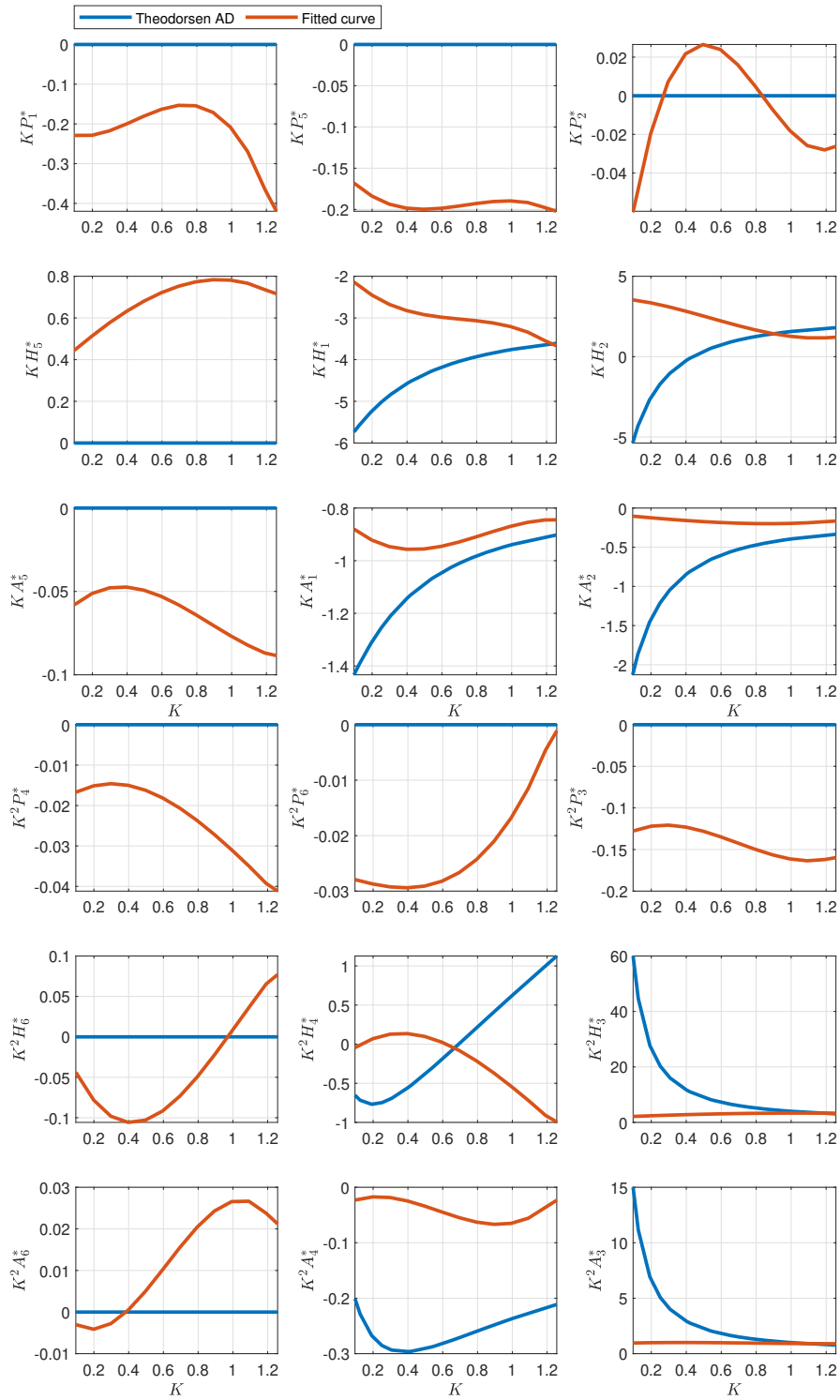
Figure F.5: Comparison of the ADs developed by Theodorsen and the polynomial which was fitted to the data points from the wind tunnel tests for the cross-section of height $H = 6.1$ m, parameterized with $I_T = 26$ m^4.

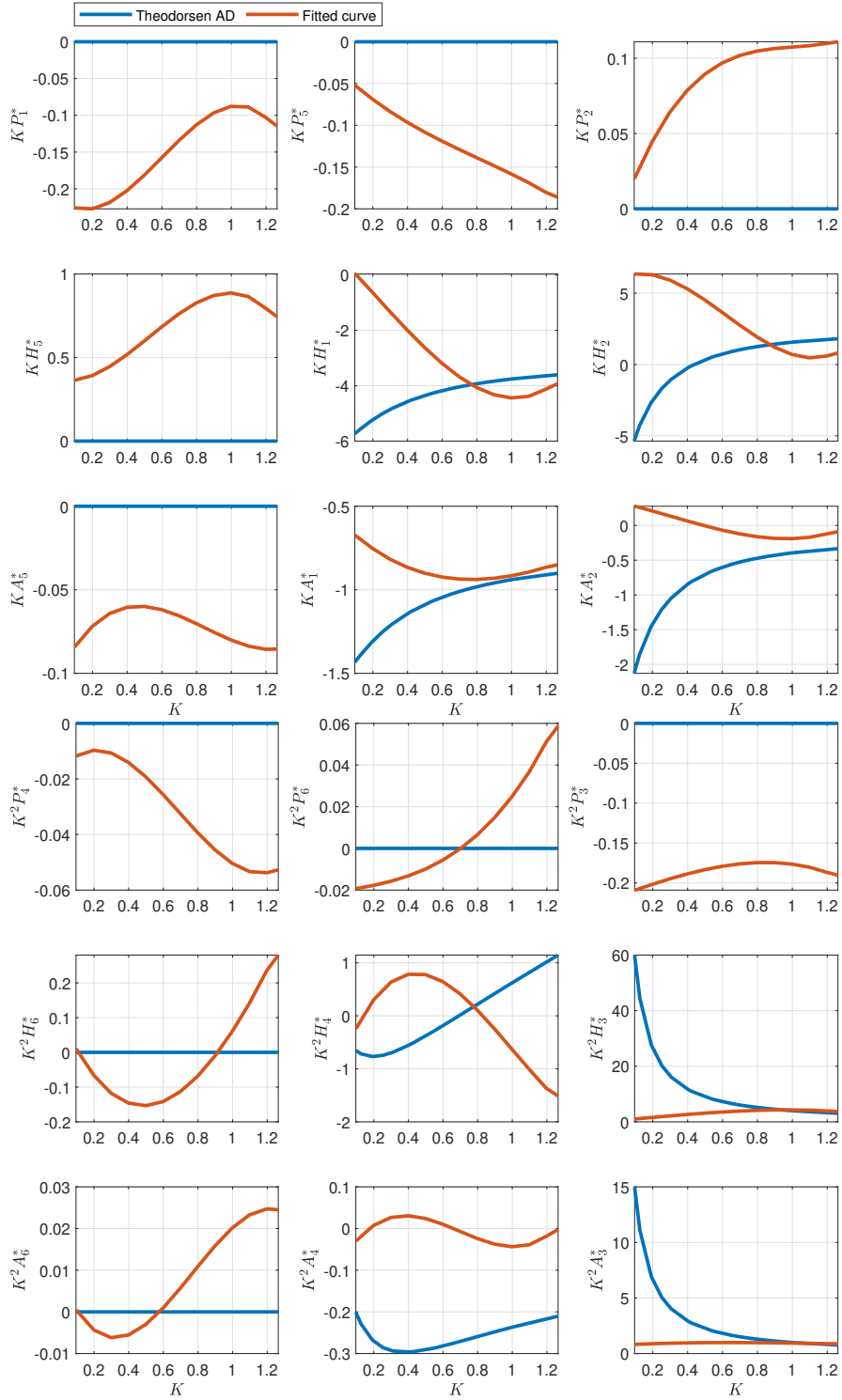## F.2   Torsion constant $I_T = 31$ m^4

Figure F.6: Comparison of the ADs developed by Theodorsen and the polynomial which was fitted to the data points from the wind tunnel tests for the cross-section of height $H = 5.5$ m, parameterized with $I_T = 31$ m^4.

Figure F.7: Comparison of the ADs developed by Theodorsen and the polynomial which was fitted to the data points from the wind tunnel tests for the cross-section of height $H = 5.8$ m, parameterized with $I_T = 31$ m^4.
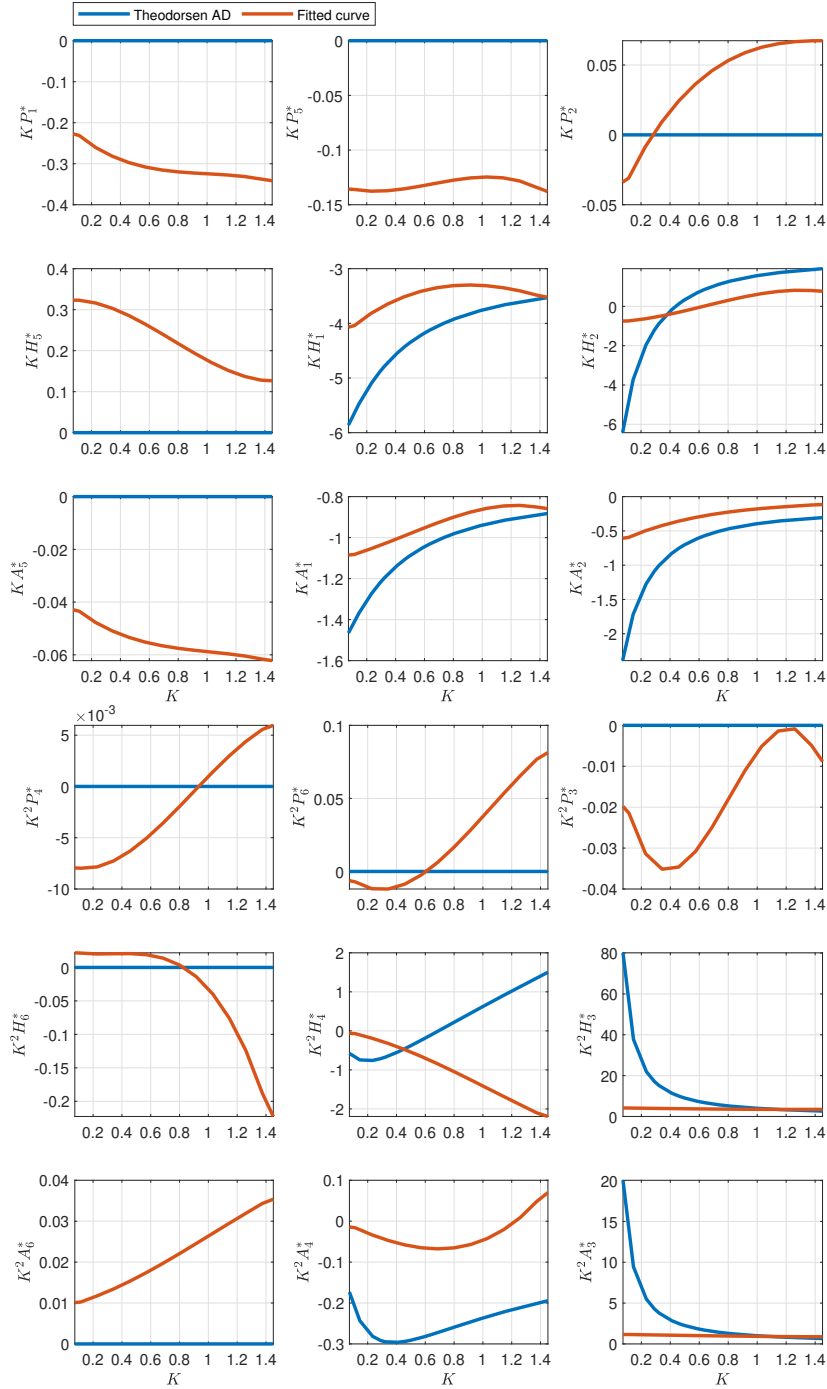
Figure F.8: Comparison of the ADs developed by Theodorsen and the polynomial which was fitted to the data points from the wind tunnel tests for the cross-section of height $H = 6.1$ m, parameterized with $I_T = 31$ m^4.
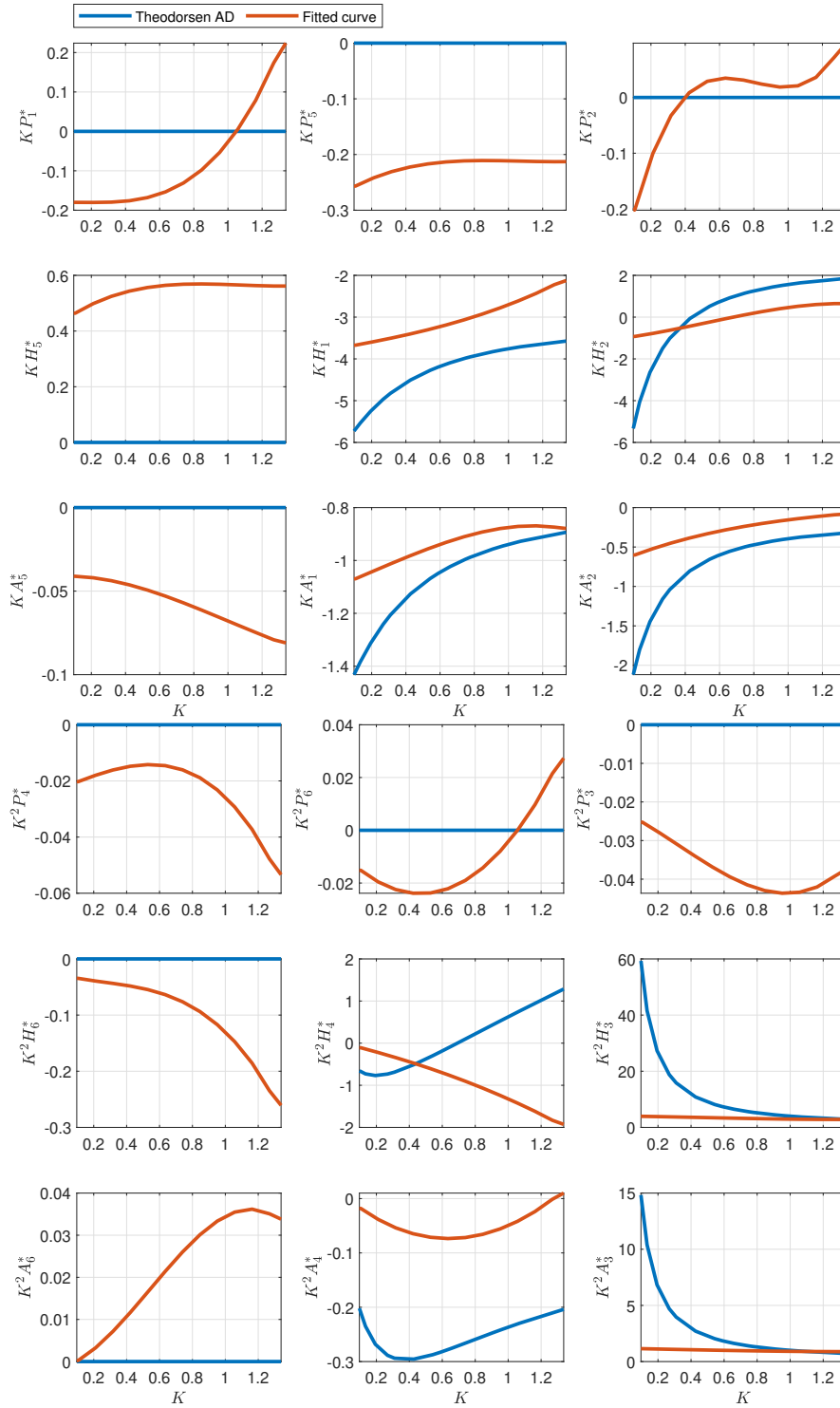
Figure F.9: Comparison of the ADs developed by Theodorsen and the polynomial which was fitted to the data points from the wind tunnel tests for the cross-section of height $H = 6.4$ m, parameterized with $I_T = 31$ m^4.

Figure F.10: Comparison of the ADs developed by Theodorsen and the polynomial which was fitted to the data points from the wind tunnel tests for the cross-section of height $H = 6.7$ m, parameterized with $I_T = 31$ m^4.
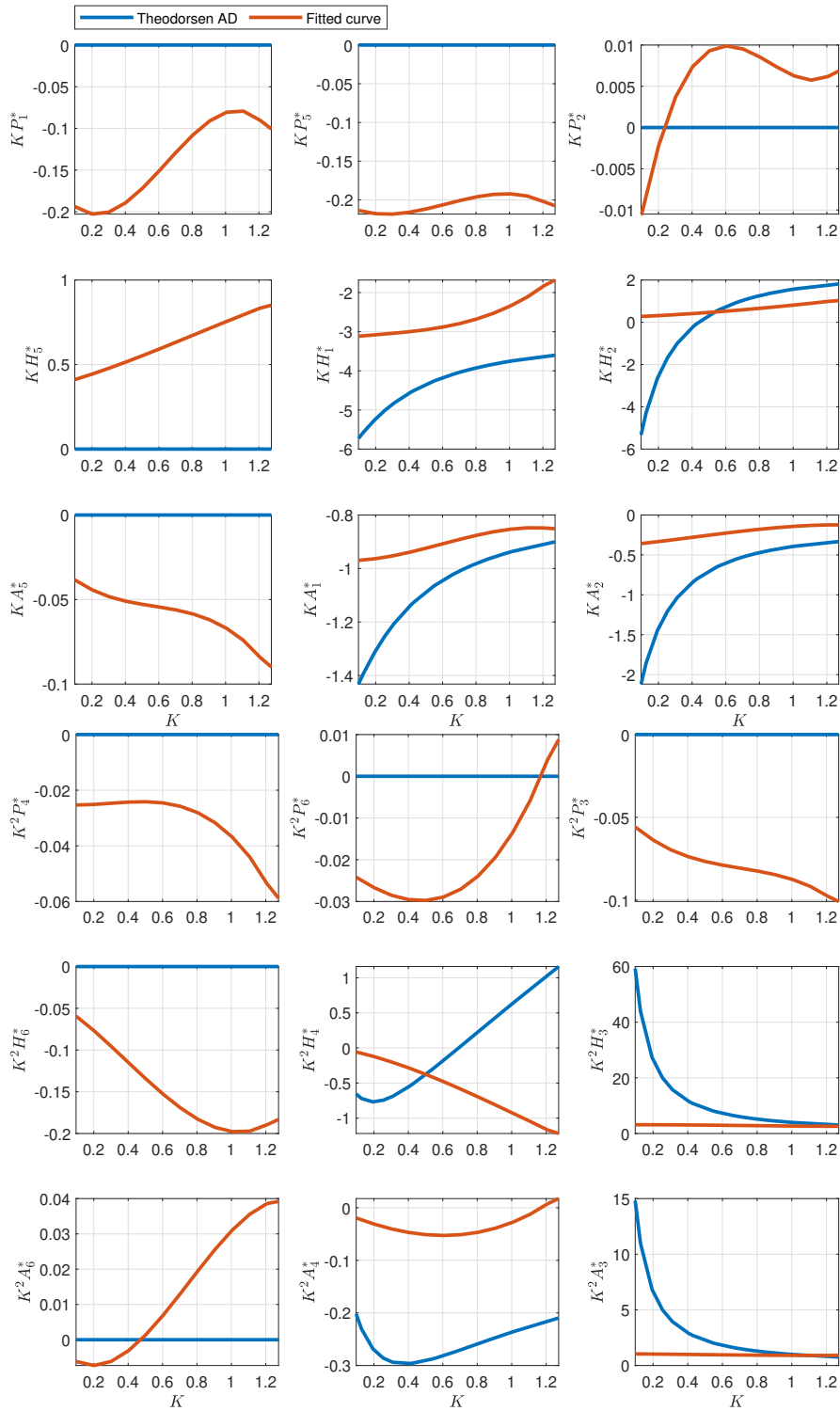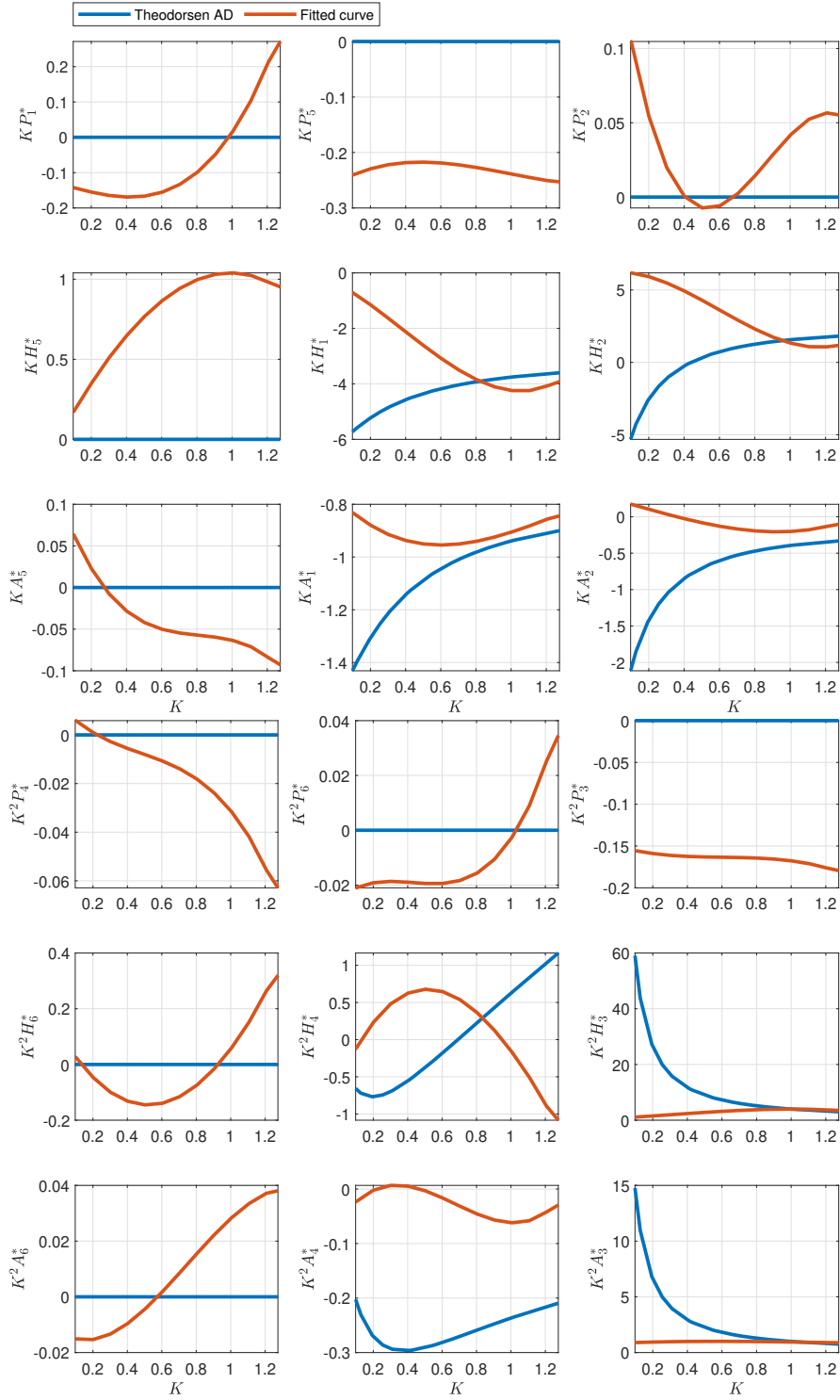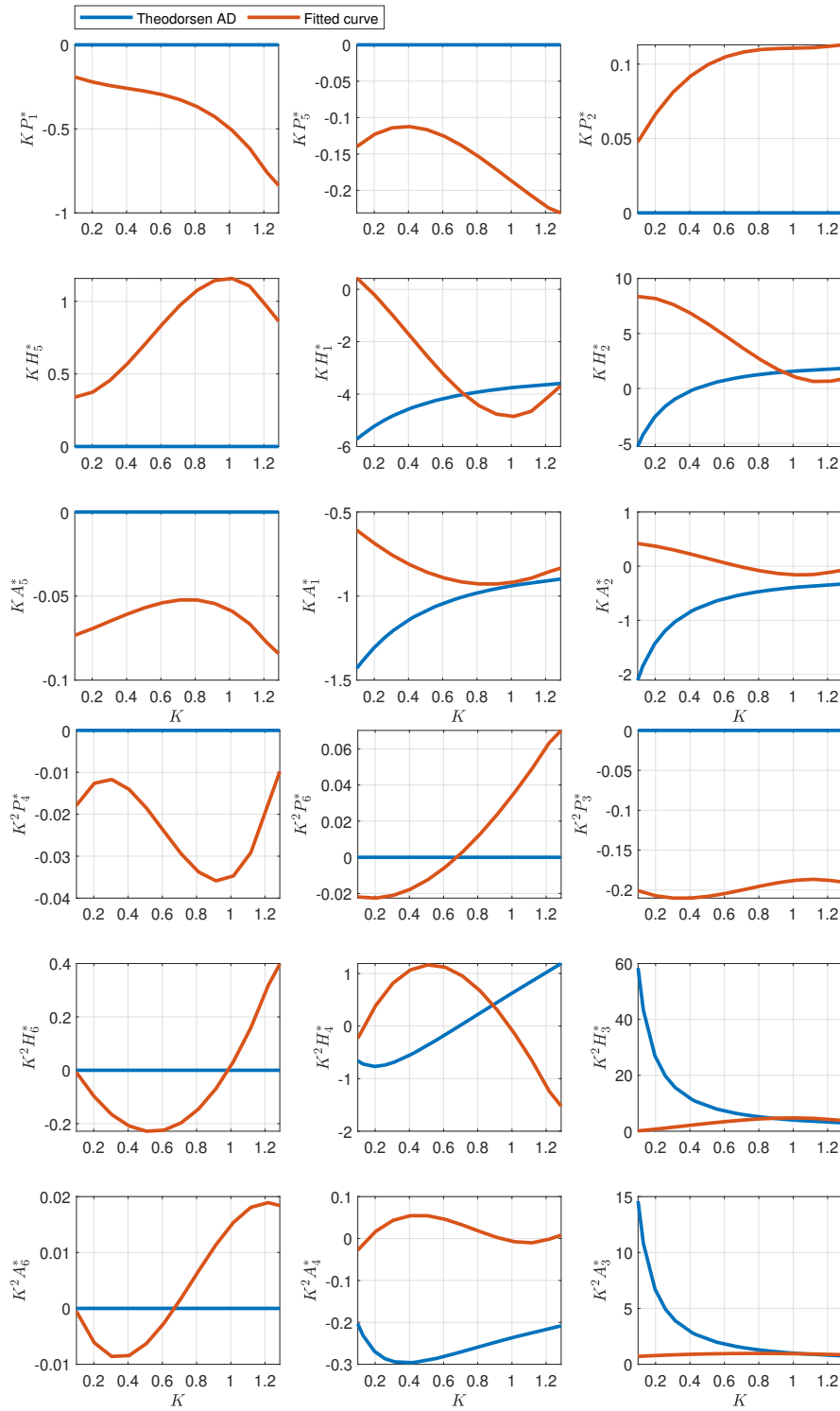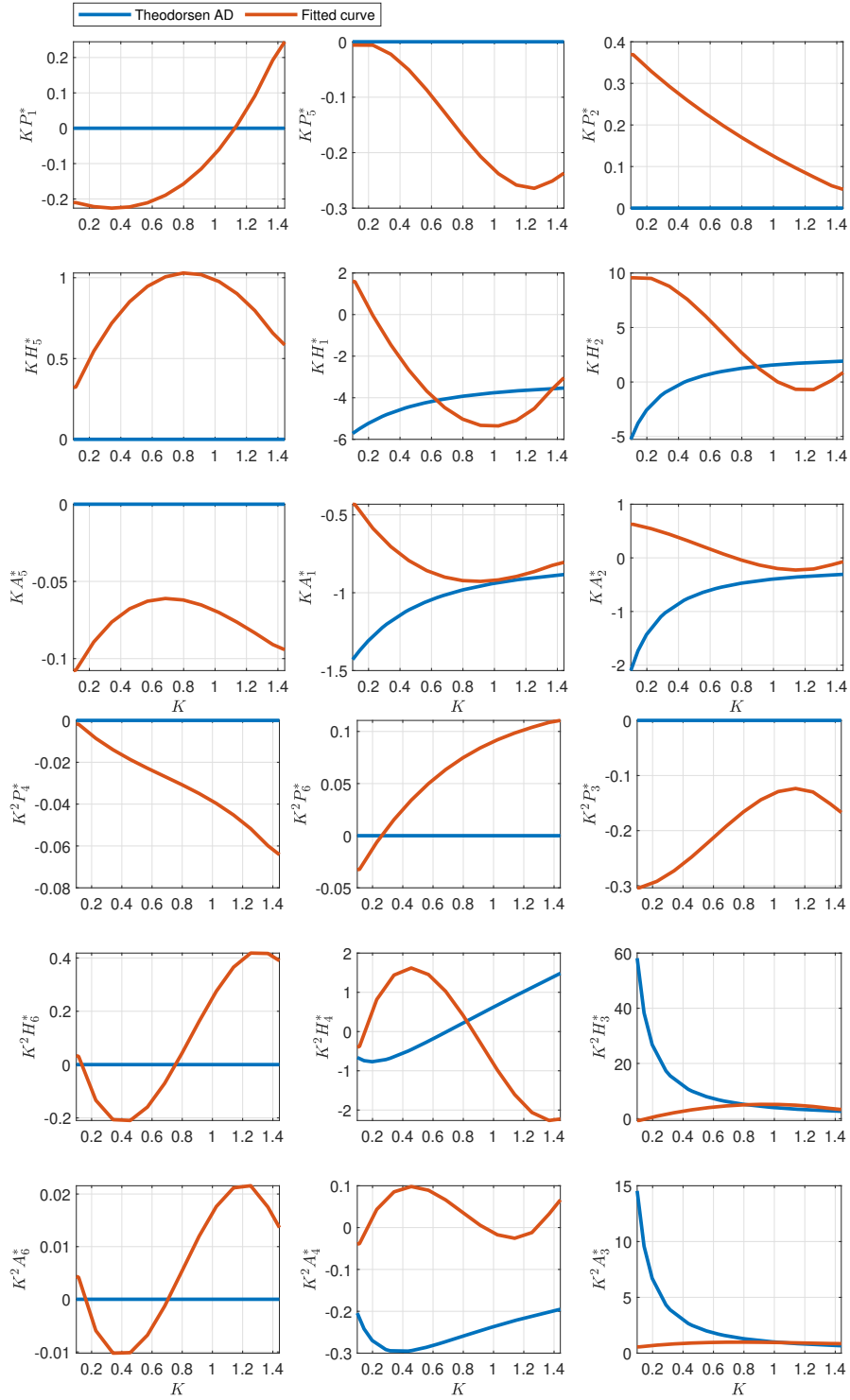
Figure F.11: Comparison of the ADs developed by Theodorsen and the polynomial which was fitted to the data points from the wind tunnel tests for the cross-section of height $H = 7.0$ m, parameterized with $I_T = 31$ m^4.

Appendix G

Gaussian Process Regression

The hyperparameters calculated by Gaussian process regression (GPR) are presented in this appendix. Four hyperparameters $\theta = \begin{bmatrix} \sigma_p & L_1 & L_2 & \sigma_n \end{bmatrix}$ were calculated for all ADs in the GPR. The lower and upper bound were $\theta_{lb} = \begin{bmatrix} 0 & 0.1 & 0 & 0 \end{bmatrix}$ and $\theta_{ub} = \begin{bmatrix} 10 & 10 & 10 & 10 \end{bmatrix}$, respectively. Table G.1 lists the hyperparameters for the cross-sections with $I_T = 26$ m^4 and Table G.2 lists the hyperparameters for the cross-sections with $I_T = 31$ m^4.

G.1   Torsion constant $I_T = 26 \text{ m}^4$

Table G.1: Hyperparameters calculated by GPR for the cross-sections with $I_T = 26 \text{ m}^4$.

AD	σ_p	L_1	L_2	σ_n
KP_1^*	0.2509	0.1007	0.6924	0.1265
KP_2^*	0.0974	0.5015	3.1861	0.0494
$K^2P_3^*$	0.1200	0.4350	3.7385	0.0139
$K^2P_4^*$	0.0207	0.8721	0.4058	0.0080
KP_5^*	0.1303	0.3504	2.1111	0.0271
$K^2P_6^*$	0.0243	0.2299	0.5946	0.0103
KH_1^*	3.0585	0.6765	0.7920	0.3968
KH_2^*	2.1946	0.4335	0.5847	0.3319
$K^2H_3^*$	2.4383	0.6857	0.6335	0.1604
$K^2H_4^*$	0.8323	0.4476	0.4379	0.0985
KH_5^*	0.3490	0.3710	0.8773	0.0569
$K^2H_6^*$	0.1110	0.3419	0.3578	0.0329
KA_1^*	0.6866	1.0852	0.9006	0.0356
KA_2^*	0.2910	0.5231	0.6325	0.0500
$K^2A_3^*$	0.6582	1.3953	0.6880	0.0171
$K^2A_4^*$	0.0381	0.4763	0.3358	0.0102
KA_5^*	0.1071	2.0396	1.1734	0.0078
$K^2A_6^*$	0.0584	1.6347	1.5230	0.0082

G.2 Torsion constant $I_T = 31$ m^4

Table G.2: Hyperparameters calculated by GPR for the cross-sections with $I_T = 31$ m^4.

AD	σ_p	L_1	L_2	σ_n
KP_1^*	0.3380	0.1000	0.8319	0.0665
KP_2^*	0.1284	0.2139	0.9174	0.0487
$K^2P_3^*$	0.1438	0.7689	0.7927	0.0221
$K^2P_4^*$	0.2561	1.0657	9.2469	0.0176
KP_5^*	0.1676	0.8637	0.9147	0.0452
$K^2P_6^*$	0.1267	0.8452	1.2852	0.0168
KH_1^*	2.7654	0.7436	0.4376	0.4642
KH_2^*	3.0065	0.3716	0.5185	0.5431
$K^2H_3^*$	2.7133	0.8012	0.5047	0.2593
$K^2H_4^*$	1.1143	0.6392	0.3396	0.1761
KH_5^*	0.4583	0.7205	0.6391	0.0950
$K^2H_6^*$	0.1829	0.3121	0.3998	0.0534
KA_1^*	0.6085	1.8090	0.5275	0.0469
KA_2^*	0.2923	0.7056	0.4523	0.0583
$K^2A_3^*$	0.6264	1.5881	0.6307	0.0309
$K^2A_4^*$	0.0534	0.7566	0.2773	0.0200
KA_5^*	0.0691	0.2687	0.5891	0.0141
$K^2A_6^*$	0.0633	1.3569	1.0513	0.0184

Appendix H

Stability Limit Calculations

Combinations of modes for each cross-section used in the stability limits calculations are presented with the corresponding critical wind speed V_{cr} in this appendix. Results from the cross-sections with $I_T = 26$ m^4 are presented in Tables H.1 to H.5, while results from the cross-sections with $I_T = 31$ m^4 are shown in Tables H.6 to H.11.

H.1   Torsion constant $I_T = 26 \text{ m}^4$

Table H.1: Calculated stability limits for the cross-section with $H = 4.9$ m and $I_T = 26$ m^4.

Mode combination	Abaqus no.	Critical wind speed V_{cr} [m/s]
1-50	1-50	79.40
1-2HS, 1-2HA, 1-5VS,	1-6, 12-14, 27-28	90.54
1-4VA, 1TS, 1TA	31, 34, 36, 41	
Symmetric combinations		
1-5VS, 1TS	3, 5, 13, 27-28, 41	90.60
1-4VS, 1TS	3, 5, 13, 27-28	90.60
1-3VS, 1TS	3, 5, 13, 27	90.56
1-2VS, 1TS	3, 5, 27	91.90
2VS, 1TS	5, 27	113.23
1VS, 1TS	3, 27	137.22
Asymmetric combinations		
1-4VA, 1TA	2, 6, 14, 31, 36	112.94
1-3VA, 1TA	2, 6, 14, 31	112.94
1-2VA, 1TA	2, 6, 31	112.94
2VA, 1TA	6, 31	186.94
1VA, 1TA	2, 31	112.94

Table H.2: Calculated stability limits for the cross-section with $H = 5.2$ m and $I_T = 26$ m^4.

Mode combination	Abaqus no.	Critical wind speed V_{cr} [m/s]
1-50	1-50	79.54
1-2HS, 1-2HA, 1-5VS,	1-6, 12-13, 16	85.75
1-4VA, 1TS, 1TA	27-28, 31, 35-36, 41	
Symmetric combinations		
1-5VS, 1TS	4-5, 13, 27-28, 41	85.32
1-4VS, 1TS	4-5, 13, 27-28	85.32
1-3VS, 1TS	4-5, 13, 27	85.30
1-2VS, 1TS	4-5, 27	86.63
2VS, 1TS	5, 27	102.35
1VS, 1TS	4, 27	123.78
Asymmetric combinations		
1-4VA, 1TA	2, 6, 16, 31, 36	116.77
1-3VA, 1TA	2, 6, 16, 31	116.77
1-2VA, 1TA	2, 6, 31	116.77
2VA, 1TA	6, 31	> 200
1VA, 1TA	2, 31	116.77

Table H.3: Calculated stability limits for the cross-section with $H = 5.5$ m and $I_T = 26$ m^4.

Mode combination	Abaqus no.	Critical wind speed V_{cr} [m/s]
1-50	1-50	37.96
1-2HS, 1-2HA, 1-5VS,	1-6, 12-13, 16	38.02
1-4VA, 1TS, 1TA	27-28, 31, 35-36, 41	
Symmetric combinations		
1-5VS, 1TS	4-5, 13, 27-28, 41	91.71
1-4VS, 1TS	4-5, 13, 27-28	91.71
1-3VS, 1TS	4-5, 13, 27	91.69
1-2VS, 1TS	4-5, 27	92.88
2VS, 1TS	5, 27	106.57
1VS, 1TS	4, 27	125.97
Asymmetric combinations		
1-4VA, 1TA	2, 6, 16, 31, 36	121.87
1-3VA, 1TA	2, 6, 16, 31	121.87
1-2VA, 1TA	2, 6, 31	121.87
2VA, 1TA	6, 31	> 200
1VA, 1TA	2, 31	121.87

Table H.4: Calculated stability limits for the cross-section with $H = 5.8$ m and $I_T = 26$ m^4.

Mode combination	Abaqus no.	Critical wind speed V_{cr} [m/s]
1-50	1-50	86.42
1-2HS, 1-2HA, 1-5VS,	1-6, 12-13, 16, 27	93.39
1-4VA, 1TS, 1TA	29, 31, 35-36, 41	
Symmetric combinations		
1-5VS, 1TS	3, 5, 13, 27, 29, 41	93.00
1-4VS, 1TS	3, 5, 13, 27, 29	93.00
1-3VS, 1TS	3, 5, 13, 27	92.98
1-2VS, 1TS	3, 5, 27	93.80
2VS, 1TS	5, 27	106.94
1VS, 1TS	3, 27	124.68
Asymmetric combinations		
1-4VA, 1TA	2, 6, 16, 31, 36	117.47
1-3VA, 1TA	2, 6, 16, 31	117.47
1-2VA, 1TA	2, 6, 31	117.47
2VA, 1TA	6, 31	> 200
1VA, 1TA	2, 31	117.47

Table H.5: Calculated stability limits for the cross-section with $H = 6.1$ m and $I_T = 26$ m^4.

Mode combination	Abaqus no.	Critical wind speed V_{cr} [m/s]
1-50	1-50	77.86
1-2HS, 1-2HA, 1-5VS,	1-6, 12-13, 16, 27	85.89
1-4VA, 1TS, 1TA	29, 31, 35-36, 41	
Symmetric combinations		
1-5VS, 1TS	3, 5, 13, 27, 29, 41	85.67
1-4VS, 1TS	3, 5, 13, 27, 29	85.67
1-3VS, 1TS	3, 5, 13, 27	85.65
1-2VS, 1TS	3, 5, 27	86.51
2VS, 1TS	5, 27	100.52
1VS, 1TS	3, 27	112.35
Asymmetric combinations		
1-4VA, 1TA	2, 6, 16, 31, 36	106.42
1-3VA, 1TA	2, 6, 16, 31	106.42
1-2VA, 1TA	2, 6, 31	106.42
2VA, 1TA	6, 31	153.54
1VA, 1TA	2, 31	106.42

H.2 Torsion constant $I_T = 31\ \mathbf{m}^4$

Table H.6: Calculated stability limits for the cross-section with $H = 5.5$ m and $I_T = 31$ m^4.

Mode combination	Abaqus no.	Critical wind speed V_{cr} [m/s]
1-50	1-50	85.03
1-2HS, 1-2HA, 1-5VS,	1-6, 12-13, 19, 27	87.18
1-4VA, 1TS, 1TA	30, 32, 34, 36, 42	
Symmetric combinations		
1-5VS, 1TS	4-5, 13, 27, 30, 42	87.00
1-4VS, 1TS	4-5, 13, 27, 30	87.00
1-3VS, 1TS	4-5, 13, 27	86.98
1-2VS, 1TS	4-5, 27	87.86
2VS, 1TS	5, 27	100.26
1VS, 1TS	4, 27	119.07
Asymmetric combinations		
1-4VA, 1TA	2, 6, 19, 32, 36	117.35
1-3VA, 1TA	2, 6, 19, 32	117.35
1-2VA, 1TA	2, 6, 32	117.35
2VA, 1TA	6, 32	> 200
1VA, 1TA	2, 32	117.37

Table H.7: Calculated stability limits for the cross-section with $H = 5.8$ m and $I_T = 31$ m^4.

Mode combination	Abaqus no.	Critical wind speed V_{cr} [m/s]
1-50	1-50	86.34
1-2HS, 1-2HA, 1-5VS,	1-6, 12-13, 19, 27	88.47
1-4VA, 1TS, 1TA	30, 32, 34, 36, 43	
Symmetric combinations		
1-5VS, 1TS	4-5, 13, 27, 30, 43	88.27
1-4VS, 1TS	4-5, 13, 27, 30	88.27
1-3VS, 1TS	4-5, 13, 27	88.27
1-2VS, 1TS	4-5, 27	89.42
2VS, 1TS	5, 27	102.86
1VS, 1TS	4, 27	121.42
Asymmetric combinations		
1-4VA, 1TA	2, 6, 19, 32, 36	121.59
1-3VA, 1TA	2, 6, 19, 32	121.59
1-2VA, 1TA	2, 6, 32	121.59
2VA, 1TA	6, 32	> 200
1VA, 1TA	2, 32	121.61

Table H.8: Calculated stability limits for the cross-section with $H = 6.1$ m and $I_T = 31$ m^4.

Mode combination	Abaqus no.	Critical wind speed V_{cr} [m/s]
1-50	1-50	87.88
1-2HS, 1-2HA, 1-5VS,	1-6, 12-13, 19, 27	90.50
1-4VA, 1TS, 1TA	30, 32, 35-36, 43	
Symmetric combinations		
1-5VS, 1TS	3, 5, 13, 27, 30, 43	90.19
1-4VS, 1TS	3, 5, 13, 27, 30	90.19
1-3VS, 1TS	3, 5, 13, 27	90.17
1-2VS, 1TS	3, 5, 27	91.10
2VS, 1TS	5, 27	104.13
1VS, 1TS	3, 27	122.47
Asymmetric combinations		
1-4VA, 1TA	2, 6, 19, 32, 36	121.34
1-3VA, 1TA	2, 6, 19, 32	121.34
1-2VA, 1TA	2, 6, 32	121.34
2VA, 1TA	6, 32	> 200
1VA, 1TA	2, 32	121.36

Table H.9: Calculated stability limits for the cross-section with $H = 6.4$ m and $I_T = 31$ m^4.

Mode combination	Abaqus no.	Critical wind speed V_{cr} [m/s]
1-50	1-50	87.31
1-2HS, 1-2HA, 1-5VS,	1-6, 12-13, 20, 27	90.65
1-4VA, 1TS, 1TA	30, 32, 35-36, 43	
Symmetric combinations		
1-5VS, 1TS	3, 5, 13, 27, 30, 43	90.36
1-4VS, 1TS	3, 5, 13, 27, 30	90.34
1-3VS, 1TS	3, 5, 13, 27	90.34
1-2VS, 1TS	3, 5, 27	91.01
2VS, 1TS	5, 27	104.46
1VS, 1TS	3, 27	115.91
Asymmetric combinations		
1-4VA, 1TA	2, 6, 20, 32, 36	115.97
1-3VA, 1TA	2, 6, 20, 32	115.97
1-2VA, 1TA	2, 6, 32	115.97
2VA, 1TA	6, 32	164.21
1VA, 1TA	2, 32	115.99

Table H.10: Calculated stability limits for the cross-section with $H = 6.7$ m and $I_T = 31$ m^4.

Mode combination	Abaqus no.	Critical wind speed V_{cr} [m/s]
1-50	1-50	77.51
1-2HS, 1-2HA, 1-5VS,	1-6, 12-13, 20, 27	81.36
1-4VA, 1TS, 1TA	30, 32, 35-36, 43	
Symmetric combinations		
1-5VS, 1TS	3, 5, 13, 27, 30, 43	81.08
1-4VS, 1TS	3, 5, 13, 27, 30	81.08
1-3VS, 1TS	3, 5, 13, 27	81.06
1-2VS, 1TS	3, 5, 27	81.69
2VS, 1TS	5, 27	92.82
1VS, 1TS	3, 27	100.17
Asymmetric combinations		
1-4VA, 1TA	2, 6, 20, 32, 36	101.36
1-3VA, 1TA	2, 6, 20, 32	101.36
1-2VA, 1TA	2, 6, 32	101.36
2VA, 1TA	6, 32	129.27
1VA, 1TA	2, 32	101.36

Table H.11: Calculated stability limits for the cross-section with $H = 7.0$ m and $I_T = 31$ m^4.

Mode combination	Abaqus no.	Critical wind speed V_{cr} [m/s]
1-50	1-50	66.63
1-2HS, 1-2HA, 1-5VS,	1-6, 12-13, 20, 27	82.10
1-4VA, 1TS, 1TA	30, 32, 35-36, 43	
Symmetric combinations		
1-5VS, 1TS	3, 5, 13, 27, 30, 43	82.04
1-4VS, 1TS	3, 5, 13, 27, 30	82.04
1-3VS, 1TS	3, 5, 13, 27	82.04
1-2VS, 1TS	3, 5, 27	82.49
2VS, 1TS	5, 27	91.24
1VS, 1TS	3, 27	97.43
Asymmetric combinations		
1-4VA, 1TA	2, 6, 20, 32, 36	83.70
1-3VA, 1TA	2, 6, 20, 32	83.70
1-2VA, 1TA	2, 6, 32	83.70
2VA, 1TA	6, 32	120.89
1VA, 1TA	2, 32	83.70

Appendix I

Buffeting Response

Buffeting response plots are presented in this appendix. The response has been calculated at three different points along the bridge; the quarter-span ($\frac{x}{L} = 0.25$), the half-span ($\frac{x}{L} = 0.50$) and the three-quarter-span ($\frac{x}{L} = 0.75$). The calculated correlation coefficients (Equation 2.33) are given for all eleven cross-sections at the three locations. Figures I.1 to I.3 show the autospectral density of the buffeting response for the cross-sections parameterized with I_T = 26 m^4, and Figures I.4 to I.6 show the autospectral density of buffeting response for the cross-sections parameterized with I_T = 31 m^4.

I.1   Torsion constant $I_T = 26$ m^4

The correlation coefficients from the buffeting analyses of the cross-sections with $I_T = 26$ m^4 were:

$$\boldsymbol{\rho}|_{H=4.9\text{m}}^{\frac{x}{L}=0.25} = \begin{bmatrix} 1.0000 & -0.0513 & 0.6495 \\ -0.0513 & 1.0000 & -0.2269 \\ 0.6495 & -0.2269 & 1.0000 \end{bmatrix}\Bigg|_{H=4.9\text{m}}^{\frac{x}{L}=0.25} \tag{I.1a}$$

$$\boldsymbol{\rho}|_{H=4.9\text{m}}^{\frac{x}{L}=0.50} = \begin{bmatrix} 1.0000 & -0.1197 & 0.6964 \\ -0.1197 & 1.0000 & -0.3059 \\ 0.6964 & -0.3059 & 1.0000 \end{bmatrix}\Bigg|_{H=4.9\text{m}}^{\frac{x}{L}=0.50} \tag{I.1b}$$

$$\boldsymbol{\rho}|_{H=4.9\text{m}}^{\frac{x}{L}=0.75} = \begin{bmatrix} 1.0000 & -0.0514 & 0.6500 \\ -0.0514 & 1.0000 & -0.2268 \\ 0.6500 & -0.2268 & 1.0000 \end{bmatrix}\Bigg|_{H=4.9\text{m}}^{\frac{x}{L}=0.75}, \tag{I.1c}$$

$$\boldsymbol{\rho}|_{H=5.2\text{m}}^{\frac{x}{L}=0.25} = \begin{bmatrix} 1.0000 & -0.0473 & 0.5698 \\ -0.0473 & 1.0000 & -0.2159 \\ 0.5698 & -0.2159 & 1.0000 \end{bmatrix}\Bigg|_{H=5.2\text{m}}^{\frac{x}{L}=0.25} \tag{I.2a}$$

$$\boldsymbol{\rho}|_{H=5.2\text{m}}^{\frac{x}{L}=0.50} = \begin{bmatrix} 1.0000 & -0.1070 & 0.6121 \\ -0.1070 & 1.0000 & -0.2831 \\ 0.6121 & -0.2831 & 1.0000 \end{bmatrix}\Bigg|_{H=5.2\text{m}}^{\frac{x}{L}=0.50} \tag{I.2b}$$

$$\boldsymbol{\rho}|_{H=5.2\text{m}}^{\frac{x}{L}=0.75} = \begin{bmatrix} 1.0000 & -0.0474 & 0.5703 \\ -0.0474 & 1.0000 & -0.2158 \\ 0.5703 & -0.2158 & 1.0000 \end{bmatrix}\Bigg|_{H=5.2\text{m}}^{\frac{x}{L}=0.75}, \tag{I.2c}$$

$$\boldsymbol{\rho}|_{H=5.5\text{m}}^{\frac{x}{L}=0.25} = \begin{bmatrix} 1.0000 & -0.0347 & 0.4995 \\ -0.0347 & 1.0000 & -0.1980 \\ 0.4995 & -0.1980 & 1.0000 \end{bmatrix}\Bigg|_{H=5.5\text{m}}^{\frac{x}{L}=0.25} \tag{I.3a}$$

$$\boldsymbol{\rho}|_{H=5.5\text{m}}^{\frac{x}{L}=0.50} = \begin{bmatrix} 1.0000 & -0.1015 & 0.5959 \\ -0.1015 & 1.0000 & -0.2542 \\ 0.5959 & -0.2542 & 1.0000 \end{bmatrix}\Bigg|_{H=5.5\text{m}}^{\frac{x}{L}=0.50} \tag{I.3b}$$

$$\boldsymbol{\rho}|_{H=5.5\text{m}}^{\frac{x}{L}=0.75} = \begin{bmatrix} 1.0000 & -0.0347 & 0.5001 \\ -0.0347 & 1.0000 & -0.1979 \\ 0.5001 & -0.1979 & 1.0000 \end{bmatrix}\Bigg|_{H=5.5\text{m}}^{\frac{x}{L}=0.75}, \tag{I.3c}$$

$$\rho\Big|_{H=5.8\text{m}}^{\frac{x}{L}=0.25} = \begin{bmatrix} 1.0000 & -0.0842 & 0.6022 \\ -0.0842 & 1.0000 & -0.2071 \\ 0.6022 & -0.2071 & 1.0000 \end{bmatrix}\Bigg|_{H=5.8\text{m}}^{\frac{x}{L}=0.25} \tag{I.4a}$$

$$\rho\Big|_{H=5.8\text{m}}^{\frac{x}{L}=0.50} = \begin{bmatrix} 1.0000 & -0.1887 & 0.6494 \\ -0.1887 & 1.0000 & -0.3252 \\ 0.6494 & -0.3252 & 1.0000 \end{bmatrix}\Bigg|_{H=5.8\text{m}}^{\frac{x}{L}=0.50} \tag{I.4b}$$

$$\rho\Big|_{H=5.8\text{m}}^{\frac{x}{L}=0.75} = \begin{bmatrix} 1.0000 & -0.0843 & 0.6028 \\ -0.0843 & 1.0000 & -0.2070 \\ 0.6028 & -0.2070 & 1.0000 \end{bmatrix}\Bigg|_{H=5.8\text{m}}^{\frac{x}{L}=0.75}, \tag{I.4c}$$

$$\rho\Big|_{H=6.1\text{m}}^{\frac{x}{L}=0.25} = \begin{bmatrix} 1.0000 & -0.0818 & 0.5522 \\ -0.0818 & 1.0000 & -0.2047 \\ 0.5522 & -0.2047 & 1.0000 \end{bmatrix}\Bigg|_{H=6.1\text{m}}^{\frac{x}{L}=0.25} \tag{I.5a}$$

$$\rho\Big|_{H=6.1\text{m}}^{\frac{x}{L}=0.50} = \begin{bmatrix} 1.0000 & -0.1896 & 0.5906 \\ -0.1896 & 1.0000 & -0.3085 \\ 0.5906 & -0.3085 & 1.0000 \end{bmatrix}\Bigg|_{H=6.1\text{m}}^{\frac{x}{L}=0.50} \tag{I.5b}$$

$$\rho\Big|_{H=6.1\text{m}}^{\frac{x}{L}=0.75} = \begin{bmatrix} 1.0000 & -0.0818 & 0.5527 \\ -0.0818 & 1.0000 & -0.2046 \\ 0.5527 & -0.2046 & 1.0000 \end{bmatrix}\Bigg|_{H=6.1\text{m}}^{\frac{x}{L}=0.75}. \tag{I.5c}$$
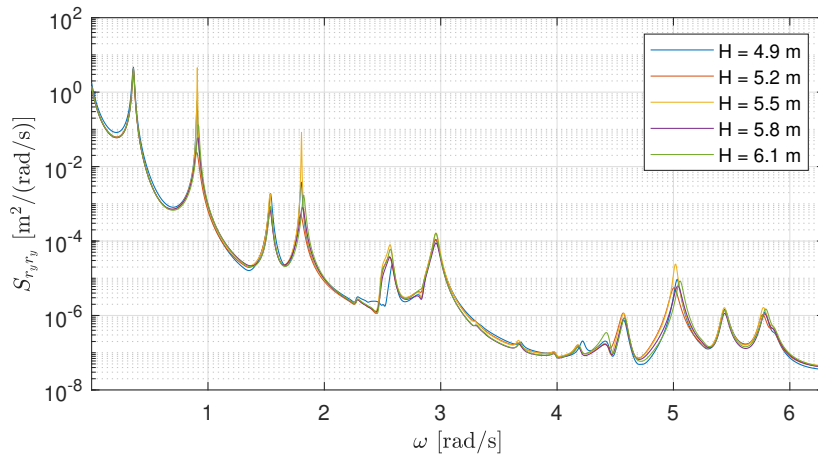
(a) Lateral direction.
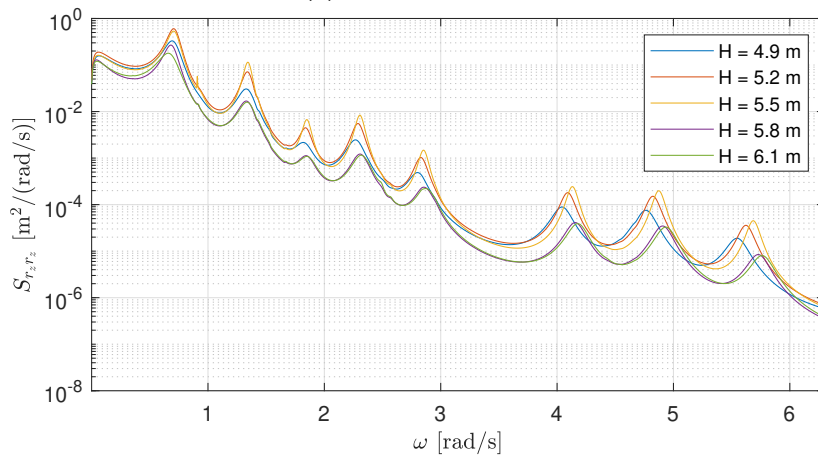
(b) Vertical direction.
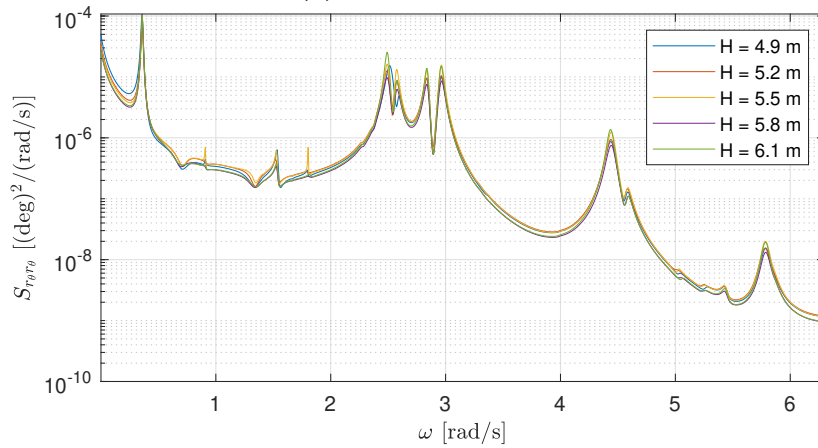
(c) Torsional direction.

Figure I.1: Autospectral densities of the buffeting response in three directions at the quarter-span for the cross-sections parameterized with $I_T = 26$ m^4.
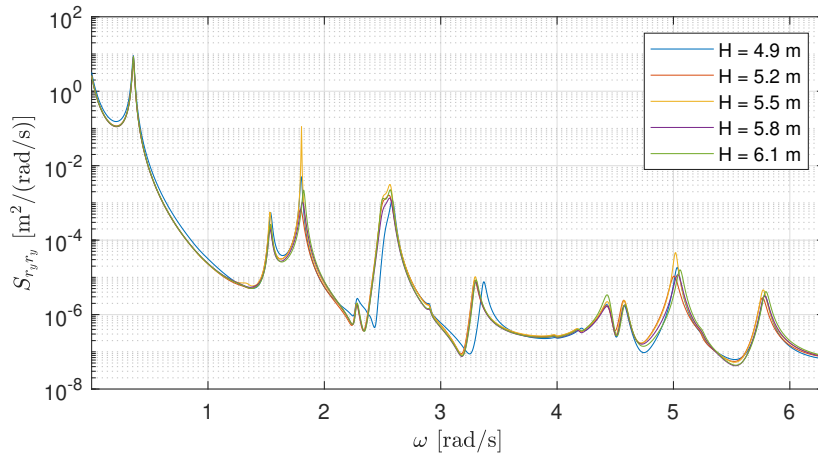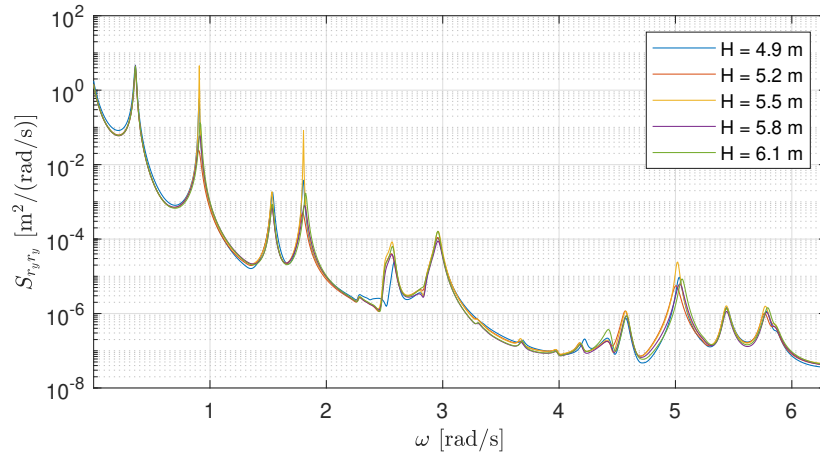
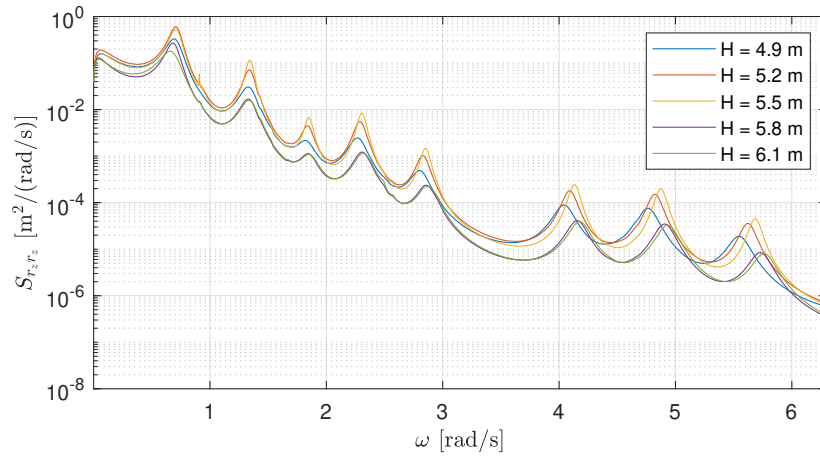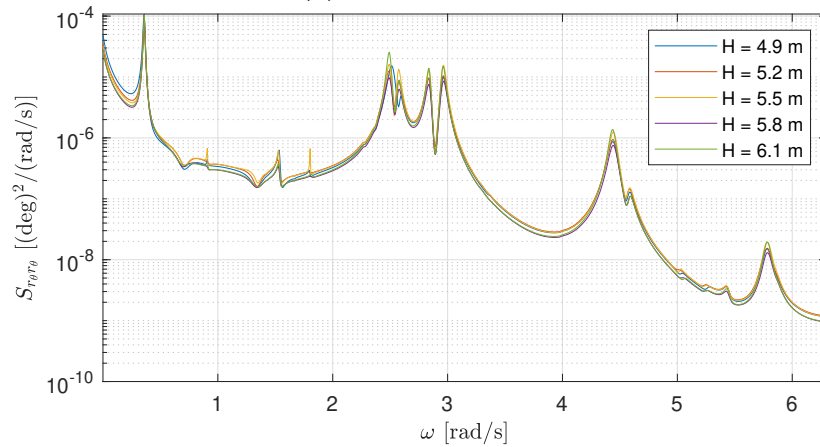**(a)** Lateral direction.
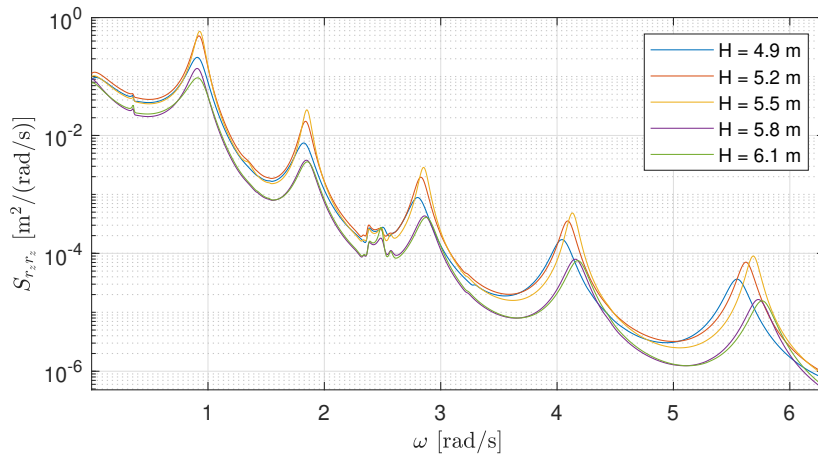
(b) Vertical direction.
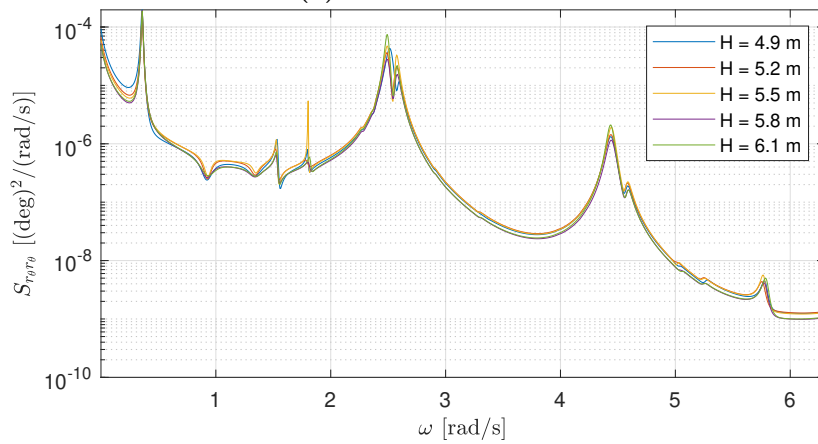
(c) Torsional direction.

Figure I.2: Autospectral densities of the buffeting response in three directions at the half-span for the cross-sections parameterized with $I_T = 26\ \mathrm{m}^4$.

(a) Lateral direction.

(b) Vertical direction.

(c) Torsional direction.

Figure I.3: Autospectral densities of the buffeting response in three directions at the three-quarter-span for the cross-sections parameterized with $I_T = 26$ m^4.

I.2 Torsion constant $I_T = 31\ \mathbf{m}^4$

The correlation coefficients from the buffeting analyses of the cross-sections with $I_T = 31\ \mathrm{m}^4$ were:

$$\boldsymbol{\rho}|_{H=5.5\mathrm{m}}^{\frac{x}{L}=0.25} = \begin{bmatrix} 1.0000 & -0.0441 & 0.5263 \\ -0.0441 & 1.0000 & -0.2139 \\ 0.5263 & -0.2139 & 1.0000 \end{bmatrix}\Bigg|_{H=5.5\mathrm{m}}^{\frac{x}{L}=0.25} \tag{I.6a}$$

$$\boldsymbol{\rho}|_{H=5.5\mathrm{m}}^{\frac{x}{L}=0.50} = \begin{bmatrix} 1.0000 & -0.1091 & 0.5729 \\ -0.1091 & 1.0000 & -0.2984 \\ 0.5729 & -0.2984 & 1.0000 \end{bmatrix}\Bigg|_{H=5.5\mathrm{m}}^{\frac{x}{L}=0.50} \tag{I.6b}$$

$$\boldsymbol{\rho}|_{H=5.5\mathrm{m}}^{\frac{x}{L}=0.75} = \begin{bmatrix} 1.0000 & -0.0442 & 0.5268 \\ -0.0442 & 1.0000 & -0.2138 \\ 0.5268 & -0.2138 & 1.0000 \end{bmatrix}\Bigg|_{H=5.5\mathrm{m}}^{\frac{x}{L}=0.75}, \tag{I.6c}$$

$$\boldsymbol{\rho}|_{H=5.8\mathrm{m}}^{\frac{x}{L}=0.25} = \begin{bmatrix} 1.0000 & -0.0488 & 0.5004 \\ -0.0488 & 1.0000 & -0.1869 \\ 0.5004 & -0.1869 & 1.0000 \end{bmatrix}\Bigg|_{H=5.8\mathrm{m}}^{\frac{x}{L}=0.25} \tag{I.7a}$$

$$\boldsymbol{\rho}|_{H=5.8\mathrm{m}}^{\frac{x}{L}=0.50} = \begin{bmatrix} 1.0000 & -0.1139 & 0.5558 \\ -0.1139 & 1.0000 & -0.2602 \\ 0.5558 & -0.2602 & 1.0000 \end{bmatrix}\Bigg|_{H=5.8\mathrm{m}}^{\frac{x}{L}=0.50} \tag{I.7b}$$

$$\boldsymbol{\rho}|_{H=5.8\mathrm{m}}^{\frac{x}{L}=0.75} = \begin{bmatrix} 1.0000 & -0.0489 & 0.5010 \\ -0.0489 & 1.0000 & -0.1868 \\ 0.5010 & -0.1868 & 1.0000 \end{bmatrix}\Bigg|_{H=5.8\mathrm{m}}^{\frac{x}{L}=0.75}, \tag{I.7c}$$

$$\boldsymbol{\rho}|_{H=6.1\mathrm{m}}^{\frac{x}{L}=0.25} = \begin{bmatrix} 1.0000 & -0.0598 & 0.5724 \\ -0.0598 & 1.0000 & -0.1839 \\ 0.5724 & -0.1839 & 1.0000 \end{bmatrix}\Bigg|_{H=6.1\mathrm{m}}^{\frac{x}{L}=0.25} \tag{I.8a}$$

$$\boldsymbol{\rho}|_{H=6.1\mathrm{m}}^{\frac{x}{L}=0.50} = \begin{bmatrix} 1.0000 & -0.1267 & 0.6232 \\ -0.1267 & 1.0000 & -0.2589 \\ 0.6232 & -0.2589 & 1.0000 \end{bmatrix}\Bigg|_{H=6.1\mathrm{m}}^{\frac{x}{L}=0.50} \tag{I.8b}$$

$$\boldsymbol{\rho}|_{H=6.1\mathrm{m}}^{\frac{x}{L}=0.75} = \begin{bmatrix} 1.0000 & -0.0598 & 0.5729 \\ -0.0598 & 1.0000 & -0.1839 \\ 0.5729 & -0.1839 & 1.0000 \end{bmatrix}\Bigg|_{H=6.1\mathrm{m}}^{\frac{x}{L}=0.75}, \tag{I.8c}$$

$$\boldsymbol{\rho}\Big|_{H=6.4\text{m}}^{\frac{x}{L}=0.25} = \begin{bmatrix} 1.0000 & -0.1001 & 0.5254 \\ -0.1001 & 1.0000 & -0.1850 \\ 0.5254 & -0.1850 & 1.0000 \end{bmatrix}\Bigg|_{H=6.4\text{m}}^{\frac{x}{L}=0.25} \tag{I.9a}$$

$$\boldsymbol{\rho}\Big|_{H=6.4\text{m}}^{\frac{x}{L}=0.50} = \begin{bmatrix} 1.0000 & -0.2353 & 0.5976 \\ -0.2353 & 1.0000 & -0.3167 \\ 0.5976 & -0.3167 & 1.0000 \end{bmatrix}\Bigg|_{H=6.4\text{m}}^{\frac{x}{L}=0.50} \tag{I.9b}$$

$$\boldsymbol{\rho}\Big|_{H=6.4\text{m}}^{\frac{x}{L}=0.75} = \begin{bmatrix} 1.0000 & -0.1001 & 0.5261 \\ -0.1001 & 1.0000 & -0.1850 \\ 0.5261 & -0.1850 & 1.0000 \end{bmatrix}\Bigg|_{H=6.4\text{m}}^{\frac{x}{L}=0.75}, \tag{I.9c}$$

$$\boldsymbol{\rho}\Big|_{H=6.7\text{m}}^{\frac{x}{L}=0.25} = \begin{bmatrix} 1.0000 & -0.1412 & 0.5463 \\ -0.1412 & 1.0000 & -0.1716 \\ 0.5463 & -0.1716 & 1.0000 \end{bmatrix}\Bigg|_{H=6.7\text{m}}^{\frac{x}{L}=0.25} \tag{I.10a}$$

$$\boldsymbol{\rho}\Big|_{H=6.7\text{m}}^{\frac{x}{L}=0.50} = \begin{bmatrix} 1.0000 & -0.3004 & 0.5854 \\ -0.3004 & 1.0000 & -0.3184 \\ 0.5854 & -0.3184 & 1.0000 \end{bmatrix}\Bigg|_{H=6.7\text{m}}^{\frac{x}{L}=0.50} \tag{I.10b}$$

$$\boldsymbol{\rho}\Big|_{H=6.7\text{m}}^{\frac{x}{L}=0.75} = \begin{bmatrix} 1.0000 & -0.1413 & 0.5469 \\ -0.1413 & 1.0000 & -0.1717 \\ 0.5469 & -0.1717 & 1.0000 \end{bmatrix}\Bigg|_{H=6.7\text{m}}^{\frac{x}{L}=0.75}, \tag{I.10c}$$

$$\boldsymbol{\rho}\Big|_{H=7.0\text{m}}^{\frac{x}{L}=0.25} = \begin{bmatrix} 1.0000 & -0.1584 & 0.5331 \\ -0.1584 & 1.0000 & -0.1564 \\ 0.5331 & -0.1564 & 1.0000 \end{bmatrix}\Bigg|_{H=7.0\text{m}}^{\frac{x}{L}=0.25} \tag{I.11a}$$

$$\boldsymbol{\rho}\Big|_{H=7.0\text{m}}^{\frac{x}{L}=0.50} = \begin{bmatrix} 1.0000 & -0.3477 & 0.5807 \\ -0.3477 & 1.0000 & -0.3202 \\ 0.5807 & -0.3202 & 1.0000 \end{bmatrix}\Bigg|_{H=7.0\text{m}}^{\frac{x}{L}=0.50} \tag{I.11b}$$

$$\boldsymbol{\rho}\Big|_{H=7.0\text{m}}^{\frac{x}{L}=0.75} = \begin{bmatrix} 1.0000 & -0.1585 & 0.5337 \\ -0.1585 & 1.0000 & -0.1565 \\ 0.5337 & -0.1565 & 1.0000 \end{bmatrix}\Bigg|_{H=7.0\text{m}}^{\frac{x}{L}=0.75}. \tag{I.11c}$$
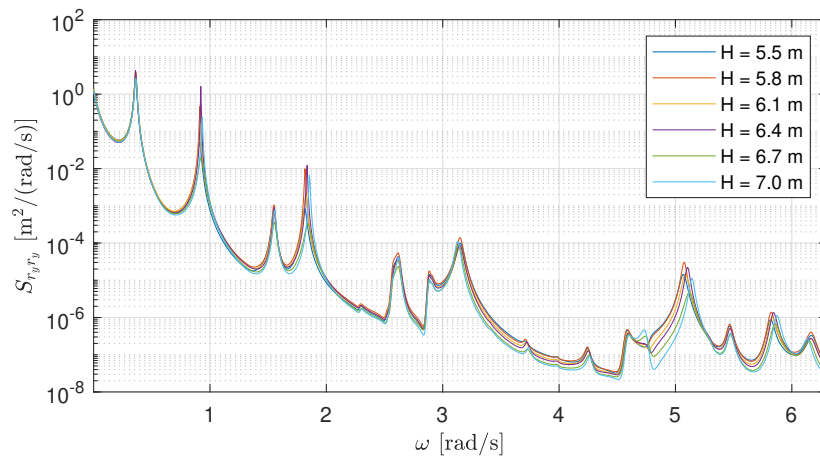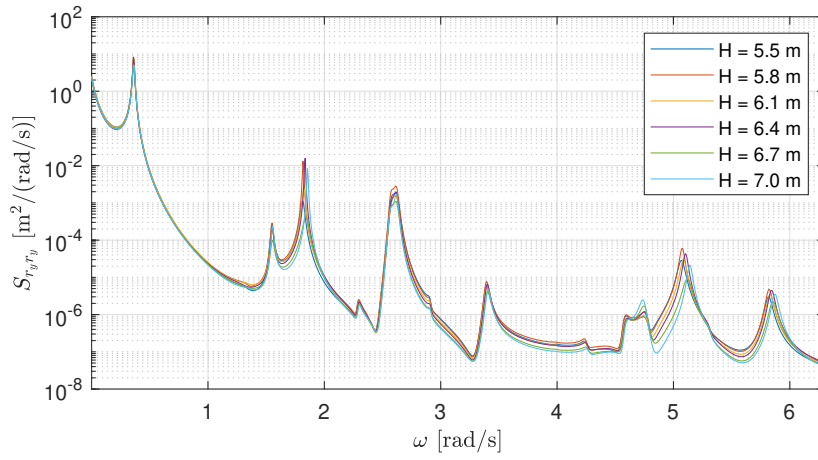
(a) Lateral direction.
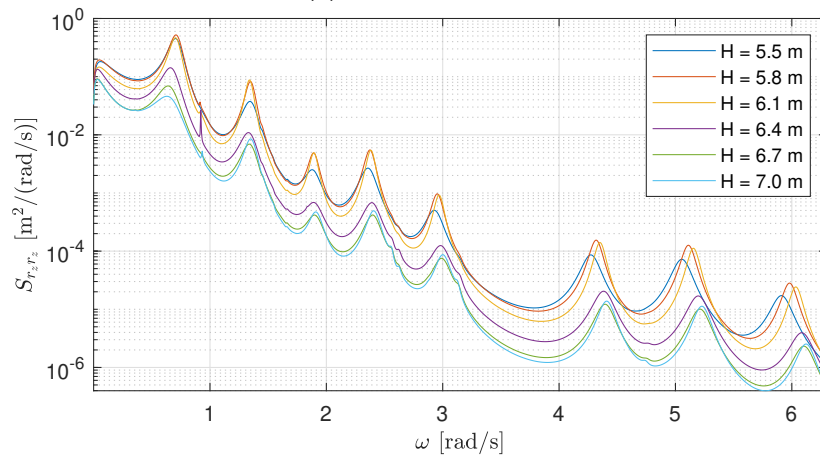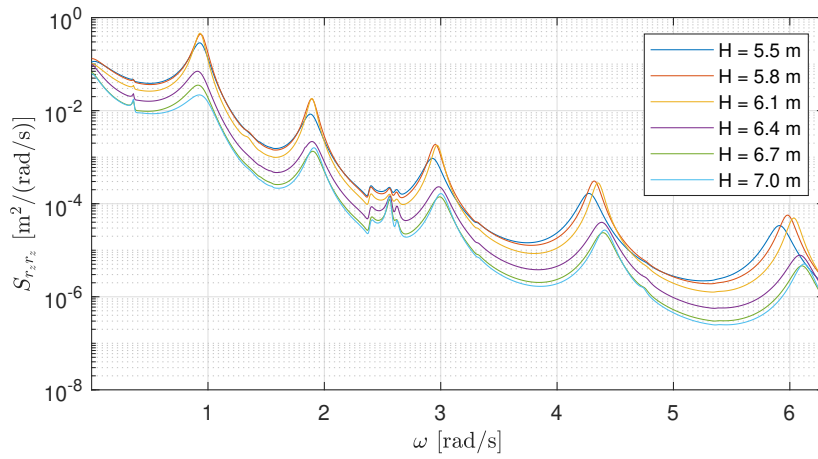
(b) Vertical direction.
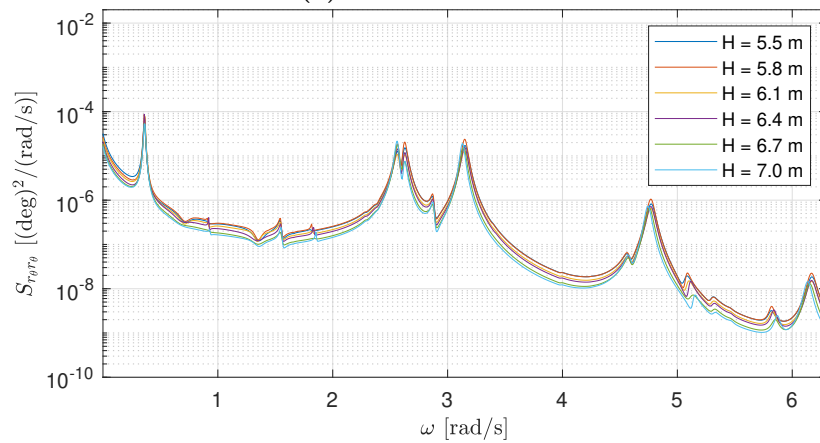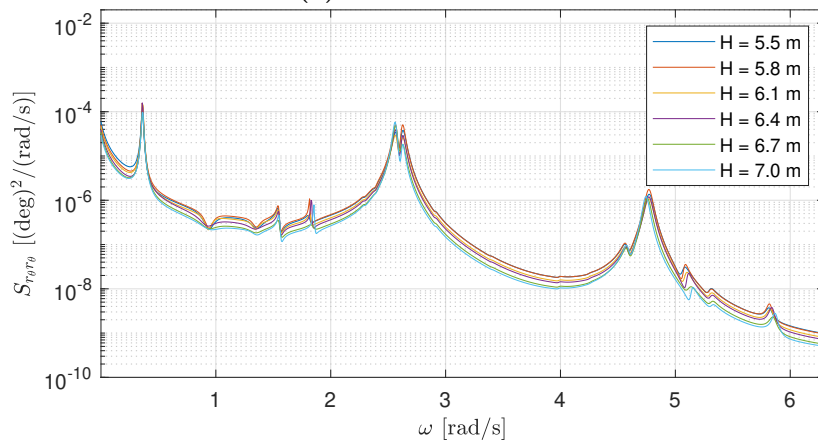
(c) Torsional direction.

Figure I.4: Autospectral densities of the buffeting response in three directions at the quarter-span for the cross-sections parameterized with $I_T = 31\ \mathrm{m}^4$.
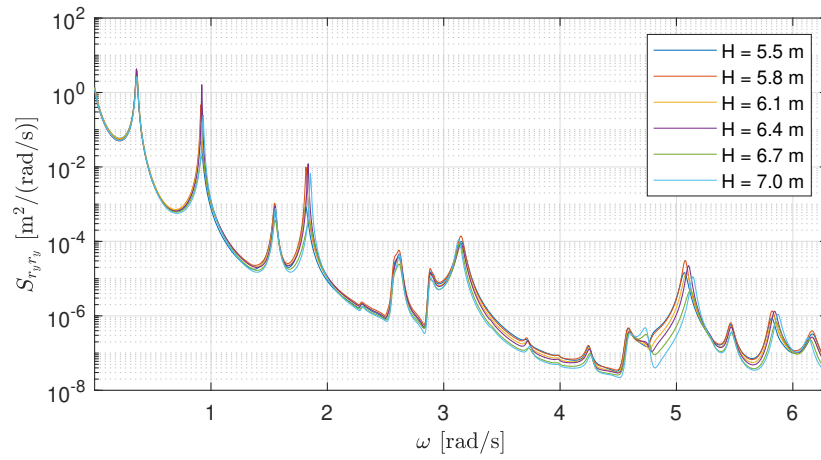
(a) Lateral direction.

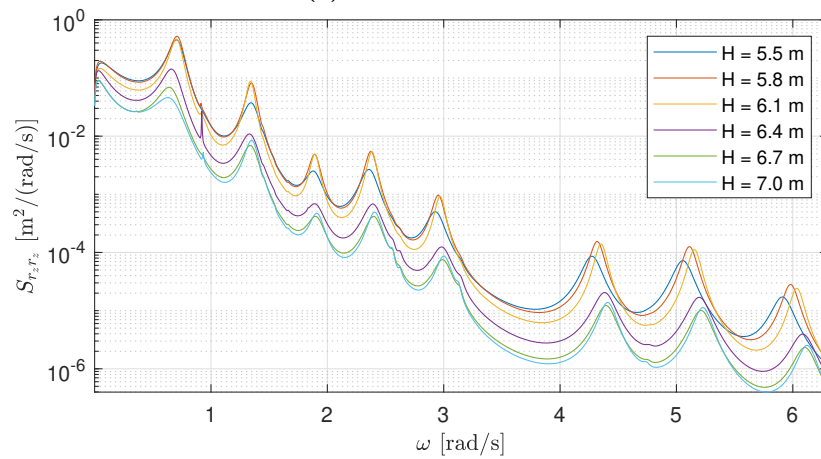**(b)** Vertical direction.
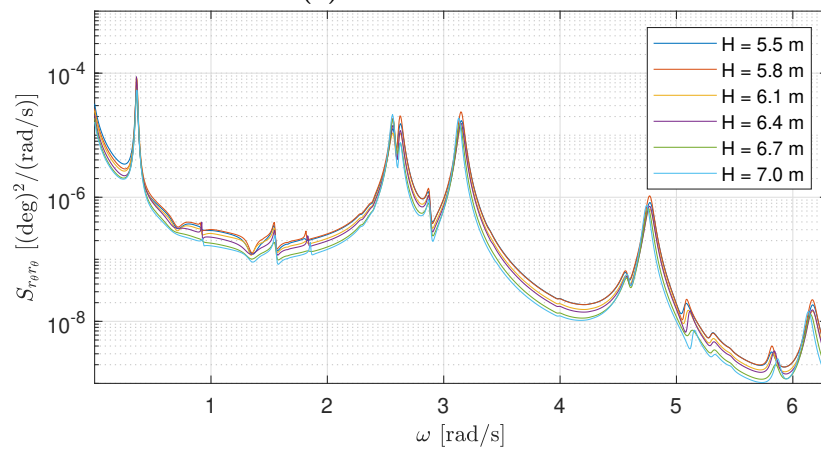

(c) Torsional direction.

Figure I.5: Autospectral densities of the buffeting response in three directions at the half-span for the cross-sections parameterized with $I_T = 31$ m^4.

(a) Lateral direction.

(b) Vertical direction.

(c) Torsional direction

Figure I.6: Autospectral densities of the buffeting response in three directions at the three-quarter-span for the cross-sections parameterized with $I_T = 31$ m^4.

Jens Petter Bergerud & Håvard Morvik Torød

Shape optimization of an aluminium girder for a long-span suspension bridge

NTNU
Norwegian University of
Science and Technology